A comparative analysis and optimisation of thermo-mechanical energy storage technologies

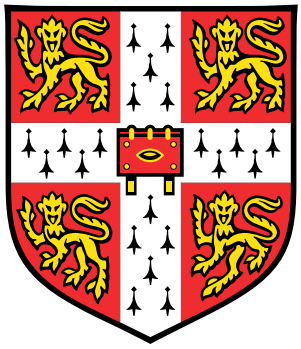

Haobai Xue

Department of Engineering

University of Cambridge

This dissertation is submitted for the degree of

Doctor of Philosophy

St Edmund's College

September 2018

This thesis is dedicated to my loving parents.

Declaration

I hereby declare that except where specific reference is made to the work of others, the contents of this dissertation are original and have not been submitted in whole or in part for consideration for any other degree or qualification in this, or any other University. This dissertation is the result of my own work and includes nothing which is the outcome of work done in collaboration, except where specifically indicated in the text. This dissertation contains approximately 64,500 words including appendices, bibliography, footnotes, tables and equations and has 98 figures.

Haobai Xue
September 2018

Acknowledgements

I would like to express my profound gratitude to my supervisor, Dr. Alexander White, for his invaluable support, continuous encouragement, enthusiastic supervision and insightful suggestions throughout this research work. His wide knowledge and rigorous attitudes towards research have been of great value for me. His mental support and patient guidance enabled me to progress smoothly with my research. Discussing the novel concepts of energy systems with him has always been a pleasure for me. I also wish to express my warm and sincere thanks to my adviser Prof. Epaminondas Mastorakos and tutor Dr. Alan Colli for their help and support throughout my time as a PhD student in Cambridge.

I am deeply indebted to my colleague Joshua McTigue for his patient and detailed explanation of his program for system modelling and optimization, and for his kind help throughout the early periods of my PhD study. I am also deeply grateful for the time and support from Pau Farres-Antunez throughout my PhD study. Without his constructive comments and important support in heat exchanger modelling, my research would have been much more difficult. I would also like to convey my thanks to the members of staff and colleagues in my department for all their time, help and support.

I gratefully acknowledges Cambridge Trust and China Scholarship Council (CSC) for the studentship which allows me to develop this research project at Cambridge University Engineering Department. I would also like to acknowledge the travel grants and bursaries from the Department of Engineering and the St. Edmund's college. I am grateful to these institutes for their generosity.

Finally, I would like to thank the people and organizations who have used their time and resources to develop open-source software. Without the use of the following programs and databases, my research would have been very different: Linux, Fortran, Gnuplot, LyX, LaTeX, Texmaker, Coolprops, gedit and LibreOffice. I would also like to thank the following commercial software for the convenience it brings to my research: Refprop and Microsoft Visio.

Abstract

Electrical Energy Storage (EES) can decouple energy production from its consumption and is urgently needed by both conventional energy system for load leveling and renewable energy system for intermittency smoothing. Currently, Pumped Hydro Energy Storage (PHES) and Compressed Air Energy Storage (CAES) are the main technologies employed, but they both suffer from high capital cost, geographical constraints and environmental issues. Therefore, many innovative concepts of EES technologies have been proposed recently, including the Adiabatic Compressed Air Energy Storage (A-CAES), Pumped Thermal Energy Storage (PTES), Isothermal Compressed Air Energy Storage (I-CAES) and Liquid Air Energy Storage (LAES). All of these EES store electricity in the forms of thermal or mechanical energy, and are most suitable for large-scale energy storage. As a result, they have received intensive treatment from both the industry and academia, but a comparative study and optimization of these large-scale thermo-mechanical energy storage systems from a thermo-economic perspective has so far been lacking, which forms the major part of this thesis.

In this thesis, a complete set of system models have been developed for each EES technology, incorporating both thermodynamic and economic factors with due consideration for the constraints and variation ranges of each parameter. Then parametric studies are carried out for each system to analyze the impact of each parameter on the system performance (e.g., efficiency and unit cost). Loss and cost distributions are given for the representative cases, and the detailed explanation and potential improvement are also provided. After that, thermo-economic optimizations are carried out for each individual system, and the trade-off between efficiency and unit cost as well as the main factors controlling this trade-off are revealed. Finally, these optimized systems are compared with each other, and new EES systems that combined the merits of existing ones are proposed as well.

Useful conclusions can be drawn from this thesis: A simplified comparison of the baseline A-CAES and PTES reveals that the PTES is more sensitive to various losses but enjoys higher energy density and more siting freedom. Then different variants of PTES are compared with each other and the variation of their system efficiencies are found to be determined by the losses of auxiliary heat exchangers. In the A-CAES, cavern and Thermal Storage System (TES) are studied in detail, and it is found that cavern parameters may affect system efficiency

through “direct” air reservoir losses and “indirect” losses of other components, and the hybrid A-CAES with low-pressure solid TES and high-pressure liquid TES tends to have the best thermo-economic performance of all A-CAES considered.

In an isothermal compressor/expander, the losses can be further divided into the aerodynamic, thermodynamic and storage losses, which are determined by the polytropic efficiency η, the combination $\dot{p}\tau$ and the heat capacity ratio C_r respectively. $\dot{p}\tau$ is a function of system frequency f and droplet diameter d, and for I-CAES with negligible droplet velocity, f and d^2 are equivalent. In the LAES, the cold TES is found to be responsible for the low system energy density, high unit storage cost and operational stability problem, and therefore, a method for maintaining system operational stability is proposed and other alternatives for avoiding the cold TES altogether are also considered.

All of these innovative EES systems are optimized and compared in the end, and the results show that A-CAES and I-CAES tend to have higher system efficiency and lower unit cost than PTES and LAES, but the PTES and LAES enjoys higher energy density and more siting freedom. Besides, the A-CAES variants with hybrid TES or underwater air reservoirs tend to be cheaper than the baseline A-CAES, and it seems difficult for the I-CAES to achieve the same thermo-economic performance with the A-CAES with the mentioned parameters and assumptions in this thesis. For the PTES and LAES, it is found that the system pressurization can significantly reduce the unit storage cost of PTES, making it comparable with the A-CAES and I-CAES, whereas the LAES can achieve slightly higher system efficiency than the PTES.

Contents

Contents xi

List of Figures xvii

List of Tables xxv

Nomenclature xxxiii

1 Introduction 1

1.1 General background to electricity storage 1
1.2 Outline description of various thermo-mechanical storage methods 2
1.3 Motivation for the comparative study 4
1.4 Scope of the present work 5
1.5 Clarification of contribution 6

2 Literature review 7

2.1 Review of the contribution of energy storage 7
2.1.1 Pumped Hydro Energy Storage 9
2.1.2 Compressed Air Energy Storage 11
2.2 Review of the thermodynamic modelling of individual technologies 13
2.2.1 Pumped Thermal Energy Storage 13
2.2.2 Adiabatic Compressed Air Energy Storage 18
2.2.3 Isothermal Compressed Air Energy Storage 23
2.2.4 Liquid Air Energy Storage 28
2.3 Review of the thermo-economic methods 32
2.3.1 Cost modelling 32
2.3.2 Multi-objective optimization 35
2.3.3 Application in EES systems 36

3 A simplified preliminary comparison of CAES and PTES **39**
3.1 Introduction . . . 39
3.2 Cycle layouts and component modelling . . . 40
3.2.1 Modelling of compressors and expanders . . . 41
3.2.2 Modelling of heat exchangers and TES systems . . . 42
3.3 Simplified analytical models of the CAES and PTES . . . 43
3.3.1 Thermodynamic model of the A-CAES . . . 43
3.3.2 Thermodynamic model of the PTES . . . 45
3.4 Results and discussion . . . 46
3.4.1 Heat transfer effects . . . 46
3.4.2 Compressor / expander effects . . . 49
3.4.3 Pressure loss effects . . . 51
3.4.4 Temperature ratio effects . . . 52
3.4.5 Energy density . . . 53
3.5 Numerical comparison of CAES and PTES . . . 55
3.5.1 Loss distribution . . . 55
3.5.2 Parametric studies . . . 56
3.6 Summary . . . 57

4 Pumped Thermal Energy Storage **59**
4.1 Introduction . . . 59
4.2 Cycle layouts . . . 60
4.2.1 Baseline PTES . . . 61
4.2.2 Precooled PTES . . . 62
4.2.3 Preheated PTES . . . 63
4.2.4 Recuperated PTES . . . 64
4.3 Overview of modelling approach . . . 65
4.3.1 Solid TES system . . . 65
4.3.2 Liquid TES system . . . 67
4.3.3 Compressor and expander . . . 68
4.3.4 Heat exchanger . . . 69
4.4 Cost modelling of components . . . 71
4.4.1 TES system costs . . . 71
4.4.2 Compressor and expander costs . . . 72
4.4.3 Heat exchanger costs . . . 74
4.5 TES materials . . . 75
4.6 Starting processes . . . 76

4.7 Parametric study . . . 77
4.7.1 Temperature ratio effect . . . 77
4.7.2 Heat exchanger effectiveness effect . . . 78
4.7.3 Polytropic efficiency effect . . . 79
4.7.4 Pressure loss effect . . . 80
4.8 Loss and cost distributions of the standard designs . . . 81
4.9 Summary . . . 83

5 Adiabatic Compressed Air Energy Storage 85
5.1 Introduction . . . 85
5.2 Cycle layouts . . . 86
5.3 Thermodynamic modeling of the air reservoirs . . . 88
5.3.1 Numerical modeling . . . 89
5.3.2 Analytical modeling . . . 90
5.4 Cost modeling of the air reservoirs . . . 92
5.4.1 Underground cavern costs . . . 92
5.4.2 Submerged accumulator costs . . . 92
5.5 Simplified analytical models of an A-CAES . . . 93
5.5.1 Modelling of an A-CAES with isobaric air reservoir . . . 94
5.5.2 Modelling of an A-CAES with isochoric and isothermal cavern . . . 94
5.5.3 Modelling of an A-CAES with isochoric and adiabatic cavern . . . 95
5.6 The impact of air reservoir on A-CAES . . . 97
5.6.1 The effect of maximum pressure on system efficiency . . . 98
5.6.2 The effect of fluctuation factor on system efficiency . . . 100
5.6.3 The effect of heat transfer coefficient on system efficiency . . . 101
5.6.4 The effect of storage loss on system efficiency . . . 104
5.6.5 The effects of cavern parameters on energy density . . . 107
5.7 Case study of the Huntorf CAES cavern . . . 109
5.8 The impact of TES on A-CAES . . . 112
5.8.1 Effect of cavern parameters . . . 112
5.8.2 Effect of heat exchanger size for liquid and hybrid systems . . . 113
5.8.3 Effect of compression and expansion efficiency . . . 113
5.8.4 Effect of packed bed parameters for solid and hybrid systems . . . 115
5.9 Comparison of the results for the nominal designs . . . 118
5.10 Summary . . . 119

6 Isothermal Compressed Air Energy Storage **121**
6.1 Introduction . . . 121
6.2 Cycle layouts . . . 122
6.3 Approximate model for the isothermal compressor/expander . . . 124
6.3.1 Thermodynamic modelling . . . 124
6.3.2 Cost modelling . . . 128
6.3.3 Estimating the impact of evaporation . . . 129
6.4 Validation and discussion of the approximated model . . . 132
6.4.1 Different forms of the injected liquid . . . 132
6.4.2 Validation of the isothermal model . . . 134
6.4.3 Temperature difference and water amount . . . 135
6.4.4 Loss analysis . . . 136
6.5 Parametric study . . . 139
6.5.1 Effect of cavern and heat exchanger parameters . . . 139
6.5.2 Effect of isothermal compressor/expander parameters . . . 141
6.5.3 Effect of compressor/expander parameters . . . 143
6.6 Loss and cost distributions of the standard designs . . . 145
6.7 Summary . . . 147

7 Liquid Air Energy Storage **149**
7.1 Introduction . . . 149
7.2 Cycle layouts . . . 150
7.3 System modelling . . . 151
7.3.1 Modelling of the heat exchanger . . . 151
7.3.2 Modelling of the cryogenic system . . . 153
7.4 System analysis . . . 154
7.4.1 Stability analysis . . . 155
7.4.2 Impact of the storage media . . . 157
7.4.3 Impact of pressure on the TES . . . 161
7.5 Impact of pressures on the system efficiency . . . 164
7.5.1 Operating pressure p . . . 164
7.5.2 Pressure ratio p_d/p_c . . . 165
7.6 Impact of TES and C/E on system efficiency . . . 166
7.6.1 Heat exchanger effectiveness ε . . . 166
7.6.2 Thermal reservoir parameters . . . 167
7.6.3 Compressor/Expander (C/E) polytropic efficiency . . . 168
7.6.4 Throttle valve and cryo-expander . . . 170

7.7 Loss and cost analysis of specific cases . . . 171
7.7.1 Loss analysis for different LAES . . . 171
7.7.2 Cost analysis and comparison . . . 173
7.8 Energy distribution and density . . . 174
7.8.1 Energy distribution of solid and liquid LAES . . . 174
7.8.2 Energy density of solid and liquid LAES . . . 175
7.9 Comparison with PTES and potential improvement . . . 176
7.10 Summary . . . 180

8 Comparison and optimisation of the technologies 183
8.1 Description of optimisation method . . . 183
8.1.1 Parent Selection . . . 185
8.1.2 Population recombination . . . 185
8.1.3 Population mutation . . . 185
8.2 Multi-objective optimisation and Pareto fronts . . . 186
8.2.1 Multi-objective archiving . . . 187
8.2.2 Archiving diversity . . . 188
8.3 Optimization study . . . 188
8.3.1 Comparison of liquid, solid and hybrid A-CAES . . . 189
8.3.2 Comparison of A-CAES and PTES . . . 194
8.3.3 Comparison of A-CAES and I-CAES . . . 200
8.3.4 Comparison of LAES and PTES . . . 206
8.3.5 Comparison of all technologies considered . . . 208
8.4 Summary . . . 211

9 Conclusions and Suggestions for Future Work 213
9.1 Conclusions of this thesis . . . 213
9.2 Suggestions for future work . . . 216

Bibliography 219

A Liquid TES systems 233

B Numerical method 237
B.1 System design . . . 237
B.2 Solid TES system . . . 240
B.3 Cavern and liquid TES system . . . 242
B.4 Compressor and expander . . . 242

B.5 Isothermal compressor and expander 244

List of Figures

2.1 Instantaneous wind generation and electricity demand in the UK from 13/08/2018 to 19/08/2018. Data from Grid Watch [1]. 8
2.2 Schematic diagram of the PHES 10
2.3 Schematic diagram of the CAES 12
2.4 Schematic diagram of the PTES during (a) charge and (b) discharge 13
2.5 T-s diagrams of the PTES variants: (a) Brayton-cycle PTES (Argon) (b) Rankine-cycle PTES (Ammonia) 15
2.6 Schematic diagram of the A-CAES 18
2.7 Schematic diagrams of the air reservoirs of Underground CAES: (a) Isochoric cavern (b) Isobaric cavern [2] 20
2.8 Photos of the air reservoirs of Underwater CAES and Above-ground CAES: (a) Underwater CAES (b) Above-ground CAES 21
2.9 Schematic diagrams of the I-CAES and the isothermal expander: (a) I-CAES (b) Isothermal expander 23
2.10 Schematic diagram of the LAES and illustration of exergy (temperature related contribution only) variation of compressed air: (a) Schematic diagram of the LAES (b) Illustration of exergy (temperature related contribution only) variation of compressed air 28
2.11 Schematic diagram of the Supercritical Compressed Air Energy Storage (SC-CAES) [3] 31
2.12 Schematic diagram and cost distribution of the A-CAES design option in Ref. [4]: (a) Schematic diagram (b) Cost distribution 35

3.1 Schematic diagrams of the A-CAES and PTES: (a) A-CAES ($N = 2$) (b) PTES 40
3.2 T-s diagrams of the A-CAES and PTES: (a) A-CAES (b) PTES 43
3.3 Sensitivity of the system efficiencies to the parameters of TES: (a) Heat exchanger effectiveness ε (b) Insulation factor κ 48

3.4 Sensitivity of the system efficiencies to the parameters of compressor/expander: (a) Polytropic efficiency η (b) Heat leakage factor α 50
3.5 Sensitivity of the system efficiencies to the system parameters: (a) Friction factor f_p (b) Temperature ratio τ (where $\varepsilon = 0.95$) 51
3.6 Exergy distribution of the CAES and PTES as functions of (a) system pressure ratio p/p_0 and (b) temperature ratio τ 53
3.7 Exergy density of the PTES and CAES as functions of (a) system pressure ratio p/p_0 and (b) temperature ratio τ 54
3.8 Losses distribution of the CAES and PTES: (a) CAES (b) PTES 56
3.9 Comparison of the system efficiencies as functions of the (a) heat exchanger effectiveness ε and (b) polytropic efficiency η 57

4.1 T-s diagram of the Rankine-cycle PTES 61
4.2 Schematic and T-s diagrams for the Baseline PTES: (a) Schematic diagram (b) T-s diagram 62
4.3 Schematic and T-s diagrams for the Precooled PTES: (a) Schematic diagram (b) T-s diagram 64
4.4 Schematic and T-s diagrams for the Preheated PTES: (a) Schematic diagram (b) T-s diagram 65
4.5 Schematic and T-s diagrams for the Recuperated PTES: (a) Schematic diagram (b) $T-s$ diagram 66
4.6 Validation of the compressor/expander cost equations 73
4.7 Schematic diagram of the indirect-contact liquid and solid TES: (a) Liquid TES operating in series (b) Indirect-contact solid TES 74
4.8 Starting processes of the PTES variants: (a) Precooled PTES (b) Preheated PTES (c) Preheated PTES (with additional heating) (d) Recuperated PTES. (c and d denotes the charging and discharging respectively.) 76
4.9 Impacts of various operating parameters on the system efficiencies of various PTES systems: (a) Charging temperature ratio τ (b) Heat transfer unit NTU (c) Polytropic efficiency η (d) Pressure loss factor f_p 79
4.10 Loss and cost distributions of different PTES with standard designs: (a) Loss distribution (b) Cost distribution 82

5.1 Schematic diagram of the hybrid A-CAES system 87

5.2 The effects of maximum pressure p_{max} on the system efficiencies χ at different number of stages N and (a) heat exchanger effectiveness ε (b) TES insulation factor κ (c) compressor/expander efficiency η (d) pressure loss factor f_p (e) fluctuation factor α 99
5.3 The system efficiencies and component losses as functions of the fluctuation factor α: (a) System efficiencies (b) Component losses at $\lambda = 5$ 101
5.4 The system efficiencies and cavern losses as functions of the dimensionless heat transfer coefficient: (a) System efficiencies (b) Cavern losses at $p_{max} = 50\,\text{bar}$ and $\alpha = 0.5$ 102
5.5 Coupled impact of the fluctuation factor α and dimensionless heat transfer coefficient λ on the cavern losses (without storage loss): (a) 3D surface graph of the cavern losses (b) Movement of the cavern heat leakage loss peak . . . 103
5.6 The impact of the inlet temperature T_{in} on the cavern losses, $T_{in} = 60\,^{\circ}\text{C}$: (a) Cavern losses at $p_{max} = 50\,\text{bar}$ and $\alpha = 0.5$ (b) 3D surface graph of the cavern losses. 104
5.7 The system efficiencies and cavern losses as functions of the dimensionless heat transfer coefficient (with cooling): (a) System efficiencies (b) Cavern losses at $\alpha = 0.5$ 105
5.8 Coupled impact of the fluctuation factor α and dimensionless heat transfer coefficient λ on the cavern losses (with storage loss): (a) 3D surface graph of the cavern losses (b) Movement of the cavern heat leakage loss peak. 106
5.9 The pressure and temperature variations within the cavern which has (a) no cooling and (b) complete cooling during storage 106
5.10 Cavern energy densities as functions of the system pressure ratio 108
5.11 Cavern energy densities as functions of the fluctuation factor 108
5.12 Cavern energy densities as functions of the dimensionless heat transfer coefficient 109
5.13 The loss distributions of the hypothetical A-CAES and Huntorf CAES cavern: (a) Hypothetical A-CAES system; (b) Huntorf CAES cavern 111
5.14 Variation of system efficiency and unit cost with cavern and heat exchanger parameters: (a) Maximum cavern pressure (b) Cavern pressure variation (c) Cavern dimensionless heat transfer rate (d) Heat exchanger NTU rating . . . 114
5.15 Variation of system efficiency and unit cost with turbomachinery efficiency and packed bed parameters: (a) Compression and expansion efficiency (b) Reservoir utilization factor (c) Effective particle diameter (d) Reservoir aspect ratio 116

5.16 Loss and cost distributions of different A-CAES with nominal designs: (a) Loss distributions (b) Cost distributions (c) TES cost distributions 117

6.1 Comparison of three methods for creating large contact area between a liquid and gas: spraying, foaming and bubbling [5] 122

6.2 Schematic diagrams of the I-CAES with heat recycling (I-CAES-HR) and the isothermal compressor: (a) I-CAES-HR (b) Isothermal compressor 123

6.3 Schematic diagrams of the I-CAES without heat recycling (Pure I-CAES) and the isothermal compressor: (a) Pure I-CAES (b) Isothermal compressor . . . 124

6.4 The impacts of temperature T and pressure p on the equivalent liquid mass for vaporisation f_l^* of (a) water and (b) dodecane ($C_{12}H_{26}$) 131

6.5 Schematic diagram of the wet aqueous foam 132

6.6 Isothermal efficiency as a function of the total droplet surface injected at different (a) droplet diameters d and (b) mass flowrate ratio ML (Lines denote the approximate results from Section 6.3.1 and points denote the accurate results from Ref. [6]) 133

6.7 Impacts of the heat capacity ratio C_r, system frequency f and droplet diameter d on the isothermal efficiency η_{iso}: (a) Contours of η_{iso} and $\dot{p}\tau$ (b) Impacts of C_r and $\dot{p}\tau$ on W_{cmp} 134

6.8 Impact of $\dot{p}\tau$ on the losses of compressor and expander: (a) Compressor with different heat capacity ratio C_r (b) Expander with different heat recycling conditions 137

6.9 Variation of $(\dot{p}\tau)_{\max}$ and $\xi_{\text{T,max}}$ with C_r at different (a) polytropic efficiency η and (b) pressure ratio β. 138

6.10 Variation of system efficiency and unit cost with various system parameters: (a) Number of stages N_{stg} (b) Cavern maximum pressure $p_{\max}$ (c) Fluctuation factor $p_{\min}/p_{\max}$ (d) Heat transfer unit NTU 140

6.11 Variation of system efficiency and unit cost with various isothermal compressor/expander parameters: (a) Heat capacity ratio C_r (b) System frequency f (c) Droplet diameter d (d) Droplet velocity u 142

6.12 Variation of system efficiency and unit cost with various compressor/expander parameters: (a) Polytropic efficiency η (b) Heat leakage factor α_{leak} (c) Pressure loss factor f_p (d) Waste heat temperature T_{f} 144

6.13 Loss and cost distributions of different I-CAES and A-CAES with standard designs: (a) Loss distributions (b) Cost distributions 146

7.1 Schematic diagram of the various air liquefaction systems: (a) Linde-Hampson system (b) Claude system . . . 150
7.2 Schematic diagram of an adiabatic LAES system . . . 155
7.3 Heat capacity of different materials (Fig. 7.3a) and thermal wave propagation of cold TES with (b) boron (B), (c) iron (Fe) and (d) lead (Pb) . . . 158
7.4 Specific heat capacity variation of (a) different thermal fluids and (b) supercritical air at different pressure levels . . . 159
7.5 Temperature distribution inside the main heat exchanger of cold TES: (a) Methanol stage during charge (b) Methanol stage during discharge (c) Propane stage during charge (d) Propane stage during discharge . . . 160
7.6 Thermal front speed $\vec{U}$ as a function of temperature at different pressure levels 162
7.7 The impact of operating pressure on the thermal front of solid TES: (a) $p_c = 50\,\text{bar}$ during charge (b) $p_d = 50\,\text{bar}$ during discharge (c) $p_c = 200\,\text{bar}$ during charge (d) $p_d = 200\,\text{bar}$ during discharge . . . 163
7.8 The impact of operating pressure on the pinch points of propane stage heat exchanger: (a) $p_c = 50\,\text{bar}$ during charge (b) $p_d = 50\,\text{bar}$ during discharge (c) $p_c = 200\,\text{bar}$ during charge (d) $p_d = 200\,\text{bar}$ during discharge . . . 164
7.9 The impact of operating pressure p on the system efficiency χ and unit cost Z of the LAES with (a) solid TES and (b) liquid TES . . . 166
7.10 The impact of pressure ratio p_d/p_c on the system efficiency χ and unit cost Z of the LAES with (a) solid TES and (b) liquid TES . . . 167
7.11 The impact of heat exchanger effectiveness ε on the system efficiency χ and unit cost Z of LAES with (a) solid TES and (b) liquid TES . . . 168
7.12 The impact of thermal reservoir parameters on the system efficiency χ and unit cost Z of LAES with solid TES: (a) Reservoir utilization factor Π (b) Reservoir particle diameter d_p (c) Reservoir aspect ratio L/D . . . 169
7.13 The impact of polytropic efficiency η on the system efficiency χ and unit cost Z of LAES with (a) solid TES and (b) liquid TES . . . 170
7.14 The impact of different air expansion devices on the system efficiency χ of liquid LAES with (a) cryogenic expander and (b) throttle valve . . . 171
7.15 Loss distributions of the solid and liquid LAES: (a) Solid LAES (b) Liquid LAES . . . 173
7.16 Cost distributions of the solid and liquid LAES: (a) Solid LAES (b) Liquid LAES . . . 174
7.17 Energy distribution between each component for (a) solid LAES and (b) liquid LAES . . . 175

7.18 Energy density of each component for (a) solid LAES and (b) liquid LAES . 176
7.19 Schematic and T-s diagrams of the combined cycle: (a) Schematic diagram (b) T-s diagrams 177
7.20 Sensitivity study of the stand-alone PTES, LAES and the combined cycle: (a) Stand-alone PTES (b) Stand-alone LAES (c) Combined cycle [7] 179

8.1 Basic structure of GA 184
8.2 Types of multi-objective optimum 187
8.3 Multi-objective archiving 188
8.4 Pareto fronts and loss and cost distributions of the three systems: (a) Pareto fronts (b) Loss distributions (c) Cost distributions (d) TES Cost distributions. (loss and cost distributions are for designs with thermodynamic round-trip efficiency $\chi = 70\%$.) 190
8.5 Pareto fronts of the liquid A-CAES with different thermal fluids 193
8.6 Pareto fronts of the liquid A-CAES systems: (a) with different cost factor scenarios (nominal, optimistic and pessimistic cases) and (b) with different stored energy W_{dis} at fixed power P using nominal cost factors. 194
8.7 Pareto fronts of different A-CAES and PTES: (a) Comparison of PTES and CAES (b) Comparison of PTES (c) Comparison of CAES (d) T-s diagram of the Recuperated CAES 196
8.8 Loss and cost distributions of different A-CAES and PTES systems: (a) Loss distribution (b) Cost distribution 198
8.9 Pareto fronts of the Baseline PTES with different working fluids 199
8.10 Pareto fronts (trade-off surfaces) for the A-CAES, Pure I-CAES and I-CAES-HR systems 200
8.11 Loss and cost distributions for the three A-CAES when $\chi = 65\%$: (a) Loss distributions (b) Cost distributions 203
8.12 Pareto fronts of the I-CAES and A-CAES: (a) with different cost factor scenarios ($k_r = 0.5$ or 1.5 for optimistic or pessimistic cases) and (b) with different nominal efficiency scenarios ($\eta_{\text{std}} = 0.90$ or 0.80 for optimistic or pessimistic cases). 204
8.13 Impacts of the system frequency f and droplet diameter d 205
8.14 Pareto fronts of the LAES and PTES 207
8.15 Loss and cost distributions for the three LAES when $\chi = 60\%$: (a) Loss distributions (b) Cost distributions 209
8.16 Pareto fronts of the representative energy storage systems 210

A.1 Schematic diagram of a typical hot TES with two stages 233

B.1 A section of the computational grid of the thermal reservoir (properties are known at nodes marked • and unknown at those marked ○) 240
B.2 Pressure and temperature profiles in the solid TES and isochoric cavern of the nominal hybrid A-CAES in Chapter 5. (a) thermal fronts in the solid TES (b) pressure and temperature variation in the cavern 241
B.3 Temperature and mass variation of the hot and cold thermal fluid tanks within the liquid TES of the nominal hybrid A-CAES in Chapter 5. (a) hot thermal fluid tanks (b) cold thermal fluid tanks 243
B.4 Comparison of calculation errors of different numerical methods 244
B.5 Illustration of the converging process of the isothermal compressor 246

List of Tables

2.1 Comparison of the PHES and CAES [8] . . . 10
2.2 Comparison of the Huntorf and McIntosh CAES [9] . . . 12

3.1 System parameters and final results of the CAES and PTES . . . 55

4.1 Constants used in the equations for the purchase cost of the components . . . 73
4.2 Thermo-economic properties of the commonly used thermal fluids [10–13] . . . 75
4.3 The standard, minimum and maximum design variable values of PTES for the parametric and optimization study . . . 77
4.4 Main results for the standard designs . . . 81

5.1 Constants used in the cost modelling of air reservoirs . . . 93
5.2 The standard, minimum and maximum design variable values of A-CAES for the sensitivity study . . . 97
5.3 The conclusions of the effects of maximum pressure on the A-CAES . . . 100
5.4 Basic parameters of the hypothetical A-CAES . . . 110
5.5 The nominal, minimum and maximum design variable values of A-CAES for the parametric and optimization study . . . 112
5.6 Main results for the nominal designs . . . 116

6.1 Comparison of three methods for creating large contact area between a liquid and gas: spraying, foaming and bubbling [5] . . . 132
6.2 The standard, minimum and maximum design variable values of I-CAES for the parametric and optimization study . . . 139
6.3 Main results for the standard designs . . . 146

7.1 The nominal, minimum and maximum design variable values of LAES for the parametric and optimization study . . . 165
7.2 Main results for the specified designs . . . 172
7.3 Comparison between the stand-alone PTES, LAES and the combined cycle [7] 178

8.1 Design variables and main results for the nominal and optimal designs indicated in Fig. 8.4a . . . 191
8.2 Main results for the 70 % efficiency cases of A-CAES . . . 191
8.3 Design variables and main results for the optimal designs indicated in Fig. 8.7b . . . 197
8.4 Main results for the 150 $/kWh cost cases of PTES . . . 198
8.5 Design variables and main results for the nominal and optimal designs indicated in Fig. 8.10 . . . 201
8.6 Main results for the 65 % efficiency cases of I-CAES and A-CAES . . . 202
8.7 Design variables and main results for the nominal and optimal designs indicated in Fig. 8.14 . . . 207
8.8 Main results for the 60 % efficiency cases of LAES and PTES . . . 208
8.9 The efficiency, unit cost and energy density of the representative energy storage systems . . . 210

Nomenclature

Roman Symbols

$\dot{p}$	Compression rate
$\dot{Q}$	Heat tranfer rate
$\dot{S}_l$	Entropy generation rate due to heat leakage loss [W/K]
$\dot{S}_p$	Entropy generation rate due to pressure loss [W/K]
$\dot{S}_t$	Entropy generation rate due to thermodynamic loss [W/K]
A	Cavern surface area; heat transfer area [m^2]
A_c	Cross-sectional inlet area [m^2]
B	Exergy [J]
b	Specific exergy [J/kg]
C	Cost [$]; energy consumption [J]
c_f	Friction coefficient
c_p	Specific heat capacity at constant pressure [$J/(kg \cdot K)$]
C_r	Heat capacity ratio
c_v	Specific heat capacity at constant volume [$J/(kg \cdot K)$]
D	Energy density [J/m^3]; diameter [m]
d	Droplet diameter [m]
E	Energy; exergy; electricity [J]

f	System frequency [Hz]
f_l	Mass of liquid [kg]
f_p	Pressure loss factor; friction factor
f_T	Temperature loss factor of the TES
G	Mass flowrate per unit area [kg/ $\left(\mathrm{m}^2 \cdot \mathrm{s}\right)$]; energy generation [J]
g	Local gravitational acceleration [$\mathrm{m/s}^2$]
H	Enthalpy [J]; elevation difference [m]
h_{eff}	Effective heat transfer coefficient [W/ $\left(\mathrm{m}^3 \cdot \mathrm{K}\right)$]
I	Chemical Engineering Plant Cost Index; Consumer Price Index
k	Cost coefficient [$\$/\mathrm{m}^3$]; isentropic index
k_r	Cost ratio
L	Length [m]; latent heat of vaporization [J/kg]
l	Reservoir length scale
M	Molecular weight [kg/mol]
m	Mass [kg]
N	Number of stages
n	Stage number
P	Energy percentage [%]; power [W]
p	Pressure [Pa]
p_s	Saturated vapour pressure [Pa]
R	System pressure ratio; gas constant [J/ $(\mathrm{kg} \cdot \mathrm{K})$]
R_g	Gas constant [J/ $(\mathrm{kg} \cdot \mathrm{K})$]
S	Entropy [J/K]; size
s	Specific entropy [J/ $(\mathrm{kg} \cdot \mathrm{K})$]

S_v	Surface area to volume ratio for particles and droplets
T	Temperature [K]
t	Time; elapsed time [s]
U	Heat transfer coefficient [W/m^2]
V	Volume [m^3]
W	Total work [J]
w	Specific work [J/kg]
x	Vapour quality
NTU	Heat Transfer Unit
Nu	Nusselt number
Pr	Prantle number
Re	Renold number
St	Stanton number
WR	Work ratio

Greek Symbols

α	Fluctuation factor; heat leakage factor
α_f	Fraction of the total time used for heat transfer
α_s	Fraction of the droplets suspended in the air
α_{leak}	Heat leakage factor
β	Pressure ratio of each stage
χ	System efficiency; roundtrip efficiency
η	Polytropic efficiency of compressor/expander
γ	Heat capacity ratio
κ	TES insulation factor

λ	Dimensionless heat transfer coefficient
ω	Mass of vapour [kg]
ϕ	Polytropic exponent
Π	Reservoir utilization factor
τ	Temperature ratio; droplet relaxation time; reservoir time scale
τ_{ins}	TES heat leakage time constant
θ	Ratio between the expander and compressor inlet temperature
ε	Heat exchanger effectiveness; reservoir void fraction
ξ	Loss [J]; percentage of loss [%]

Superscripts

’	Discharge
*	Effective value
-	Average
.	Rate

Subscripts

∞	Infinite supply
0	Ambient; base value
a	Air
ac	Compressor; actual
acc	Air accumulator
ae	Aerodynamic
C	Cold TES
c	Compressor; charge; cold TES
cave	Cavern

chg	Charge
cold	Cold thermal fluid
d	Discharge
dis	Discharge
e	Expander; electricity
ex	Expander
f	Fluid; fuel; final
fil	Fillings; packing material
g	Gas
H	Hot TES
h	Hot fluid; hot TES
HE	Heat engine
hot	Hot thermal fluid
HP	Heat pump
in	Input; inlet; import
ins	Insulation layer
iso	Isothermal
L	Liquid air
l	Liquid
leak	Heat leakage
m	Intermediate state
max	Maximum
min	Minimum
mine	Solution mining

nom	Nominal state; nominal design
out	Ouput; outlet; export
P	Isobaric
pipe	Delivery pipes
pmp	Hydraulic pump; cryogenic pump
PV	Pressure vessel
ref	Reference value; reference state
rev	Reversible
s	Solid; storage; start
std	Standard design
sys	System
tank	Thermal fluid tank
th	Thermodynamic
tot	Total
turb	Cryogenic turbine
v	Vapour
VA	Isochoric and adiabatic
VT	Isochoric and isothermal
w	Water
well	Well drilling

Acronyms / Abbreviations

A-CAES	Adiabatic Compressed Air Energy Storage
CAES	Compressed Air Energy Storage
CE	Compressor and/or Expander

COP	Coefficient of Performance
EES	Electrical Energy Storage
GA	Genetic Algorithm
GDEA	Genetic Diversity Evolutionary Algorithm
HR	Heat Recycling
HX	Heat Exchanger
I-CAES	Isothermal Compressed Air Energy Storage
ICE	Isothermal Compressor/Expander
LAES	Liquid Air Energy Storage
NSGA	Non-dominated Sorting Genetic Algorithm
PHES	Pumped Hydro Energy Storage
PTES	Pumped Thermal Energy Storage
SPEA	Strength Pareto Evolutionary Algorithm
TES	Thermal Energy Storage

Chapter 1

Introduction

1.1 General background to electricity storage

Electrical Energy Storage (EES) refers to the process of converting surplus electricity into a form that can be stored and reconverted to electricity when needed [14, 15]. Such a process enables the electricity to be generated at times of low energy demand, low generation cost or from intermittent energy sources and to be used at times of high energy demand, high generation cost or when the renewable energy sources are unavailable [14, 15]. Therefore, EES is not only needed by conventional energy systems for load leveling and peak shaving, but also by renewable energy systems for intermittency smoothing and surplus time-shifting [16]. With the increasing penetration of renewable energy sources into the power grid, EES is generally viewed as a key enabling technology and receives increasing attention from both the industry and the academia [9, 17].

EES technologies mainly include the Pumped Hydro Energy Storage (PHES), Compressed Air Energy Storage (CAES), Flow Battery, Battery, Capacitor and Supercapacitor, Flywheel and Superconducting Magnetic Energy Storage (SMES) [14, 15]. Some EES technologies (e.g., Flywheel and Supercapacitor) have very high efficiency, fast response and high power density, but are only able to supply power for short durations. They are therefore most appropriate for power quality management applications such as bridging short duration interruptions and providing voltage and frequency support during rapid supply or demand swings [18]. For energy management applications - e.g., leveling daily demand fluctuations and time-shifting the surplus renewable energy generation - PHES and CAES are the main technologies currently employed, but they both suffer from high capital cost, geographical constraints and environmental issues [18]. Therefore, many innovative concepts have been proposed recently, including Pumped Thermal Energy Storage System (PTES), Adiabatic Compressed Air Energy Storage (A-CAES), Isothermal Compressed Air Energy Storage (I-CAES), and Liquid

Air Energy Storage (LAES) systems [9].

1.2 Outline description of various thermo-mechanical storage methods

Pumped Thermal Energy Storage

Pumped Thermal Energy Storage (PTES) operates as a heat pump during charge, pumping heat from a cold store to a hot one and thus storing electricity in the form of temperature potential; whilst during discharge, this process is reversed and it operates as a heat engine, converting the stored thermal energy back into electricity [19]. According to the difference of its thermodynamic cycle, a PTES can be further categorized into a Brayton-cycle PTES and a Rankine-cycle PTES. The former was proposed simultaneously and independently by Isentropic Ltd. [20] in the UK and Saipem Ltd. [21] in the France, whilst the latter was proposed by ABB Ltd. [22] in the Switzerland. Since then, numerous variants of PTES had been proposed and investigated, and both parametric and optimization study had been carried out. However, there is little research on the comparison of different variants of PTES and on the comparison of PTES with other EES such as A-CAES, which forms the topics of Chapter 3 and Chapter 4 of this thesis.

Adiabatic Compressed Air Energy Storage

Adiabatic Compressed Air Energy Storage (A-CAES) compresses air near-adiabatically and stores the generated thermal energy separately in a Thermal Energy Storage (TES) system before storing the compressed air in an air reservoir; whilst during discharge, the compressed air is reheated in the TES and then expanded through the turbines to generate electricity [23]. The first research project on A-CAES was started in Europe on 2004 [24], and then A-CAES with both high-temperature TES (e.g. “ADELE” project [25]) and low-temperature TES (e.g. LTA-CAES [26]) were investigated in Germany. Recently, the first pilot-scale demonstration plant of A-CAES has been built and tested in Switzerland [27, 28]. All of the above projects make use of an isochoric underground cavern, but the research on Underwater CAES (UW-CAES) and the isobaric energy bags are also very active [29, 30]. Recently, an UW-CAES facility had been applied in Toronto using an underwater air storage in Lake Ontario [31]. Although numerous studies have been conducted on the thermodynamics of A-CAES, an investigation of different air reservoir and TES models on the system performance has so far been lacking, which forms the subjects of Chapter 5 of this thesis.

Isothermal Compressed Air Energy Storage

Isothermal Compressed Air Energy Storage (I-CAES) compresses air near-isothermally by continuously removing the generated thermal energy during charge, whilst during discharge, heat from the environment is continuously added to the system at near-ambient temperature [32]. Proposals of I-CAES had been published by SustainX, LightSail and General Compression [33, 34], most of which required continuous heat exchange between the air and some other substance to remove (or add) heat during compression (or expansion). Recently, a novel Ground-Level Integrated Diverse Energy Storage (GLIDES) had been proposed in the United States [35, 36], which employed solar or waste heat to approach a near-isothermal process and improve the roundtrip efficiency. Both numerical and experimental investigations were carried out for the isothermal compressor/expander. However, most models are limited to very specific cases because the complicated heat/mass transfer entails a clear definition of its geometry. A more generalized and universal heat transfer model that can be easily integrated into the I-CAES system has so far been lacking, which forms the topic of Chapter 6 in this thesis.

Liquid Air Energy Storage

Liquid Air Energy Storage (LAES) cryogenically cools and liquefies air using off-peak electricity during charge, whilst during discharge, the stored liquid air is pumped, heated and expanded in turbines to generate electricity [37]. Like PTES, LAES also stores electricity in the form of temperature potential, but it also resembles A-CAES since it is an open cycle. The concept of LAES was first proposed by Smith in 1977 [37] but was later developed by industry groups such as Mitsubishi, Hitachi and Highview [38, 39]. A key milestone for LAES was the completion and testing of a 350 kW/2.5 MWh pilot plant by Highview, whose roundtrip efficiency was measured to be 8 % [40]. Its low efficiency is mainly caused by the air liquefaction plant, which tends to be small-scale and inefficient. As a result, the concept of adiabatic LAES was proposed and numerous variants had been researched in the academia. However, most of the research were carried out separately and based on different assumption, and a fair comparison of these variants on a level playing field is still absent, which then forms the research subject of Chapter 7 in this thesis.

Summary

From the above review, it can be concluded that:

1. Most researches focused on investigation a certain kind of EES technology. However, a

comparison of different kinds of EES technologies has not been investigated thoroughly.

2. Most researches were conducted from a thermodynamic perspective. However, relatively few researches carried out thermo-economic analysis with these novel EES technologies.

3. Although increasing numbers of researches on the system optimisation have been published, there is still plenty of room for further researches on the thermo-economic optimisation of different EES technologies.

1.3 Motivation for the comparative study

A promising EES technology should have a high system efficiency whilst simultaneously minimizing the unit storage cost. The system efficiency is limited by various system irreversibility, some of which is straightforward, whilst others may require an in-depth investigation. Even if the system efficiency can be expressed as a simple function of the irreversibility of each component (e.g, η of compressor/expander or ε of heat exchanger), these irreversibility may interact with the economic factors in a complex manner. Therefore, the following expected objectives have been identified for this thesis:

1. To develop a complete set of system models for each EES technology, incorporating both thermodynamic and economic factors with due consideration for the constraints and ranges of each design parameters.

2. To conduct parametric study for each EES technology and study the impact of each design parameter on the system efficiency and unit storage cost.

3. To carry out detailed loss and cost analysis for certain designs and find out the major loss and cost of these systems.

4. To undertake thermo-economic optimization for each EES technology and compare them from a thermo-economic perspective.

5. To propose new EES systems with higher system efficiency, lower unit storage cost and more siting freedom.

1.4 Scope of the present work

Analytical and numerical study of each individual EES technology

Although some of the thermodynamic models have been proposed in the literature for certain types of EES variants, a complete set of thermo-economic models and a thorough parametric study and loss/cost analysis have so far been lacking. Therefore, the following specific tasks will be conducted and the results included in this thesis:

1. Developing a complete set of thermo-economic models for each individual component and system variant, and deriving the analytical expression of system efficiency, energy distribution and energy density.

2. Conducting parametric study and analyzing the impact of each design variable on the system efficiency and unit storage cost.

3. Performing detailed loss and cost distribution analysis for certain representative cases and find out the reason of major losses or costs.

Thermo-economic optimization and comparative study of various EES technologies

Although the feasibility and importance of system optimization has been mentioned several times in the literature, relatively few researchers have actually carried out stochastic optimizations for the energy storage systems and the researches on thermo-economic optimization are particularly scant. Therefore, the following specific tasks will be conducted and the results included in this thesis:

1. Undertaking thermo-economic optimizations for each configuration of EES technology and revealing the tradeoff between efficiency and cost.

2. Comparing different EES variants from a thermo-economic perspective and analyzing the merits and weakness of each EES technology.

Proposal of new EES systems

Although numerous EES technologies have been proposed in the literature, they all inevitably suffer from certain weakness and new variants of these EES systems are being proposed frequently. Therefore, the following specific tasks will be conducted and the results included in this thesis:

1. Proposing new methods (or configurations) for reducing the system losses and costs for the existing EES systems;

2. Proposing new EES systems that combines the merits or avoids the weakness of existing EES systems;

1.5 Clarification of contribution

The author gratefully acknowledges the contribution of his supervisor Alexander White, colleagues Joshua McTigue and Pau Farres-Antunez, and other researchers, institutes and organizations to this thesis. White [41, 42] and McTigue [43, 44] developed the Fortran codes for the segmented thermal reservoirs and the author integrated it into his A-CAES and LAES program as the solid TES. McTigue also developed the NSGA-II code in Fortran based on the paper by Dr. Kalyanmoy Deb [45] and was referenced by this author. The NSGA-II employed in this thesis was translated from the C code by Deb [46] into Fortran by the current author.

Pau Farres-Antunez first proposed the concepts of PTES with liquid TES, and the various operating strategies such as preheating, precooling, recuperating and stage repetition [47, 48]. He also conducted a thorough research on the available thermal fluids for hot and cold TES [47]. The author of this thesis referenced these results and conducted comparative study (among PTES variants and with CAES) and multi-objective optimization. Pau Farres-Antunez also developed a Matlab code for pinch point analysis of heat exchangers [49], and the author translated it into Fortran and integrated into the LAES as the liquid TES. The pressure loss correlation of heat exchangers used in this thesis is also suggested by Pau Farres-Antunez and the author gratefully acknowledge this. Finally, Pau Farres-Antunez conducted some original research on the combined cycle of PTES and LAES [7], and some conclusions of his research are included in this thesis for better comparison with each individual system.

The analytical models of air reservoir were first proposed by Yuan Zhang in Ref. [50] and the numerical models were first proposed by Michael Money in Ref. [51]. The current author developed the Fortran code and carried out parametric studies. The concept of hybrid A-CAES (A-CAES with both solid and liquid TES) was first proposed by Alexander White and the current author developed the program and conducted the research [52]. The economic models were also developed together with Alexander White and the author gratefully acknowledge this.

Chapter 2

Literature review

2.1 Review of the contribution of energy storage

Electrical Energy Storage (EES) refers to the process of converting surplus electricity during low energy demand into a storable form that can be converted back into electricity during high energy demand [14]. Such a process can decouple the energy generation from its consumption and therefore, EES is urgently needed by both conventional energy systems for energy management and renewable energy systems for power quality/reliability support [18]. To better demonstrate the benefits of EES, the fundamental law of energy conservation can be applied to energy systems of any scale:

$$\dot{G} = \dot{C} + \left(\dot{E}_{\text{out}} - \dot{E}_{\text{in}}\right) + \frac{\mathrm{d}E_{\text{CV}}}{\mathrm{d}t} \tag{2.1}$$

where $\dot{G}$ and $\dot{C}$ are the instantaneous energy generation and consumption rate respectively, $\dot{E}_{\text{in}}$ and $\dot{E}_{\text{out}}$ are the energy import and export rate with other interconnected grids, and E_{CV} refers to the total energy stored within the system. In conventional energy systems and power grids, however, there is little or no storage facilities, which means the energy production and consumption must exactly balance if there is no interconnection with other grids or if the electricity import/export is difficult [24]. Meanwhile, the energy demand or consumption always varies with time, as shown in Fig. 2.1, which entails the energy production units to be designed for the peak, rather than the average, power demand and operated at partial load most of the time. This will inevitably lead to inefficient, over-designed and expensive plants [14]. In addition, some energy production units, such as the nuclear power plants, are designed for base load operation and their power output cannot be modulated to follow the varying demand [16]. Spinning reserves, such as peak-load gas turbines, can be used to address these challenges, but they are usually inefficient and dependent on the combustion of

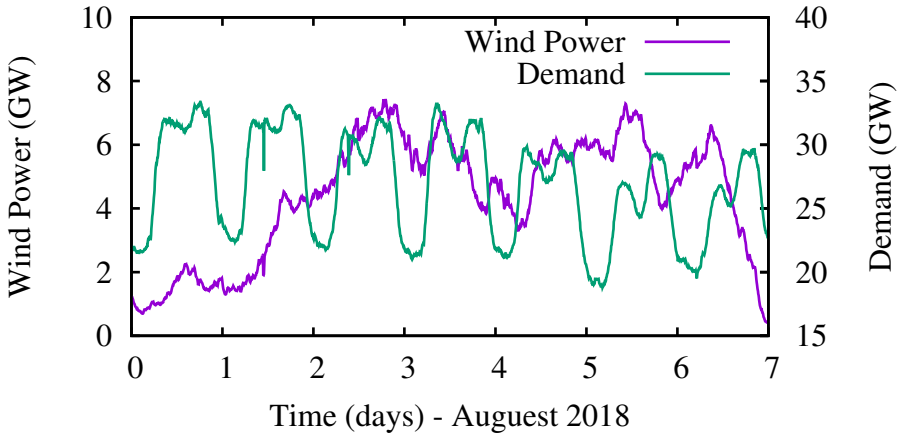

Figure 2.1: Instantaneous wind generation and electricity demand in the UK from 13/08/2018 to 19/08/2018. Data from Grid Watch [1].

fossil fuels, which results in harmful emissions [24]. Even if energy import/export is available through better grids interconnection, additional transmission facilities will be required which makes the power grid expensive and over-designed; or otherwise the transmission congestion problem may be aggravated [15].

Recently, the EES has attracted an increasing attention from both the industry and academia, mainly due to the gradual integration of renewable energies into the power grids. According to UK's target for the EU Renewable Energy Directive, more than 30 % of electricity will come from renewable energy sources by 2020 [16]. Much of this energy may be in the form of solar energy or wind (including off-shore wind) which are intermittent, difficult to predict, and uncontrollable by nature, as shown in Fig. 2.1. These characteristics pose significant challenges for the large-scale integration of renewable generation into the power grid, for which production and consumption of electricity must exactly balance. In addition, the fluctuation and intermittency of wind energy may cause frequency control problems for the grids if they are integrated in large-scale in the future [14]. There is evidence that the availability and generation of wind energy are inter-related over a large land area so that enhancing the grids interconnection across neighboring countries alone cannot completely solve these problems [8].

EES is generally perceived to be a key enabling technology for the large-scale integration

of renewable energies [17]. By time-shifting the otherwise discarded off-peak renewable energies and smoothing the power output of intermittent sources, EES can effectively address the problems of renewable energy systems. Even for conventional energy systems, EES can still provide various benefits such as energy management and power quality/reliability support. Therefore, numerous EES technologies, such as Pumped Hydro Energy Storage (PHES), Compressed Air Energy Storage (CAES), Thermal Energy Storage (TES), Flow Battery, Battery, Capacitor and Super-capacitor, Flywheel and Superconducting Magnetic Energy Storage (SMES), has been proposed [14, 15]. According to their functions, the above EES technologies can be categorized into EES for power quality and reliability support, and EES for energy managements. The former, such as Flywheel and SMES, have fast response, high efficiency and power density, but are only able to supply power for short duration. They are therefore more appropriate for bridging short duration interruptions and providing voltage and frequency support during rapid supply or demand swings. The latter, such as PHES and CAES, have large capacity, long storage period and low unit cost, but are only economical in very large scale. They are therefore more appropriate for energy management such as leveling daily demand fluctuations and serving as contingency reserve [18].

The above EES technologies can also be categorized into the electrical energy storage (e.g., Capacitors and SMES), mechanical energy storage (e.g., PHES and CAES), chemical energy storage (e.g., batteries and solar fuels) and thermal energy storage (e.g., PTES and LAES) in terms of their storage forms. In this thesis, only the large-scale thermo-mechanical energy storage systems for energy management are discussed and analyzed in details.

2.1.1 Pumped Hydro Energy Storage

Pumped Hydro Energy Storage (PHES) is the most widely implemented energy storage technology and has the highest capacity of current commercial energy storage systems [53]. PHES stores the off-peak electricity by pumping water from a lower to an upper water reservoir, and during discharge, the stored water is released through a hydroelectric turbine to generate electricity, as shown in Fig. 2.2. Hence, the electricity is stored in the form of potential energy of water which is defined by the elevation difference between the two reservoirs ΔH. The energy density of PHES can be written as:

$$D_{\mathrm{PHES}} = \rho_{\mathrm{w}} g \triangle H \tag{2.2}$$

where ρ_{w} is the density of water, g is the local gravitational acceleration, and ΔH is the elevation difference between the two reservoirs. The typical height difference of PHES is in the range of 150 to 600 m, which corresponds to an energy density of $0.5 - 1.5\,\mathrm{kWh \cdot m^{-3}}$. A

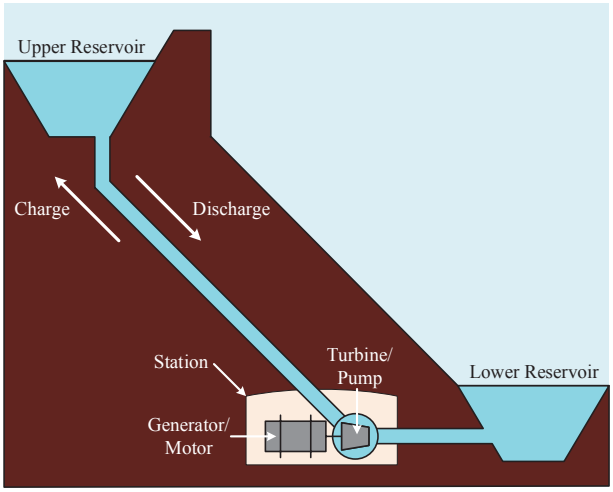

Figure 2.2: Schematic diagram of the PHES

Table 2.1: Comparison of the PHES and CAES [8]

	Efficiency (%)	Energy Density (kWh/m^3)	Power Density (kW/m^3)
PHES	70-85	0.5-1.5	5000
CAES	70-80	3-6	330
CAES - Huntorf	42	1.9	-
CAES - McIntosh	54	5.7	-

comparison with CAES is shown in Table 2.1.

As a mature technology, PHES enjoys the advantages of high efficiency, relatively fast response (typically within 1 min [54]), long storage time and large energy storage capacity. However, PHES requires special geographical conditions to build the reservoirs and dams, whilst in most developed countries there is only limited prospect for further development [16]. Besides, the construction of reservoirs and dams requires high initial investment, long construction time, and clearing and flooding large areas, which may lead to serious environmental and immigration problems.

Other variants of PHES such as underground and underwater PHES have been proposed recently [55], however, they still rely on the specific geographical conditions and suffer from the high investment and long construction due to its low energy density. In addition, they are not proven technology and may cause additional technical challenges in their future developments [56]. However, it should be noted that underground and underwater PHES are usually combined with the air reservoir of CAES to form isobaric CAES [29, 57, 58], which will be discussed in Chapter 5.

2.1.2 Compressed Air Energy Storage

Compressed Air Energy Storage (CAES) is the only other commercially available technology (besides PHES) for large-scale energy storage. During low energy demand, surplus electricity is used to compress ambient air to high pressure, and the pressurized air is then stored in an air reservoir of any kind. During high energy demand, the stored air is released through a gas turbine to generate electricity, as shown in Fig. 2.3. Thereby, the surplus electricity is stored in the form of potential energy, or more precisely exergy, of the pressurized air [17]. The energy density of CAES is given by:

$$D_{\mathrm{CAES}} = p \ln \frac{p}{p_0} - p + p_0 \tag{2.3}$$

where p is the charge pressure of air reservoir and p_0 is the ambient pressure. The typical charged pressure of air reservoir is in the range of 40 to 80 bar [14], which corresponds to an energy density of $3.0-7.5\,\mathrm{kWh}\cdot\mathrm{m}^{-3}$. Recently proposed A-CAES can deliver compressed air at sufficiently high temperatures (~650 °C) and pressures (~ 10 to 20 MPa) [24] and therefore, the energy density of CAES is generally believed to be higher than that of PHES.

CAES works on the basis of conventional gas turbine generation. It decouples the compression and expansion cycles of gas turbine into two separate processes, and thus the power output during discharge could be significantly boosted by using the pre-stored compressed air produced by surplus electricity or renewable energy. It should be noted that the CAES is not a mere storage technology, but a hybrid electricity generation and storage technology [17], which converts parts of the chemical exergy of fuel into electricity. For hybrid storage concept, the integration of additional thermal energy $Q_{\mathrm{in,f}}$, which is usually provided by combustion of nature gas or light oil, complicates the comparison of different storage technologies. Different definitions of the system efficiency have thus been suggested for the CAES: one is based on a first law analysis and considers both the input exergy of electricity $E_{\mathrm{in,e}}$ and input thermal energy of fuel $Q_{\mathrm{in,f}}$, as shown in Eq. (2.4); whilst the other is based on a second law analysis and deducts the contribution of thermal energy $Q_{\mathrm{in,f}}$ by a reference efficiency η_{ref} from the outlet exergy, as shown in Eq. (2.5) [9].

$$\chi_{\mathrm{CAES1}} = \frac{E_{\mathrm{out,e}}}{E_{\mathrm{in,e}} + Q_{\mathrm{in,f}}} \tag{2.4}$$

$$\chi_{\mathrm{CAES2}} = \frac{E_{\mathrm{out,e}} - Q_{\mathrm{in,f}} \cdot \eta_{\mathrm{ref}}}{E_{\mathrm{in,e}}} \tag{2.5}$$

CAES has several advantages such as high energy storage capacity, long storage period, high efficiency and relatively low construction cost [17, 26]. However, conventional CAES

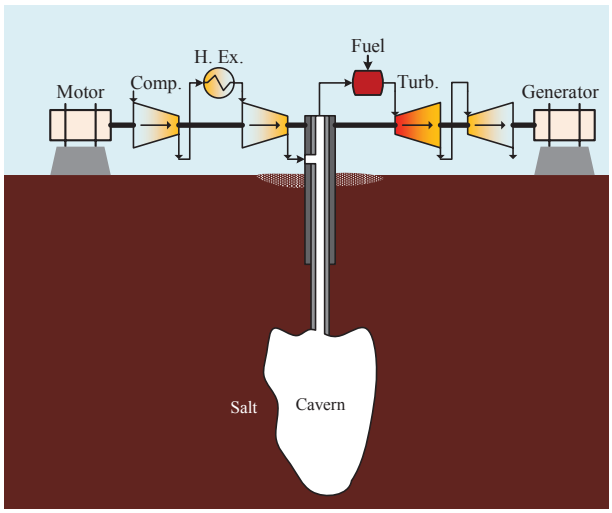

Figure 2.3: Schematic diagram of the CAES

Table 2.2: Comparison of the Huntorf and McIntosh CAES [9]

	Huntorf	McIntosh
Year of commissioning	1978	1991
Power of compression train [MW]	60	49
Duration of charging process [h]	8	41
Power provided during discharge [MW]	321	110
During of discharging at full power [h]	2	26
Volume of cavern [m^3]	310000	538000
Air pressure in cavern [bar]	43-70	46-75
Maximum air mass flow [kg/s]	417	154
Required electricity [kWh] for kWh output	0.8	0.82
Required fuel [kWh] for kWh output	1.6	1.21

does not recycle the thermal exergy generated during compression, which causes additional loss and reduces its system efficiency. Moreover, it relies on the combustion of fossil fuels and specific geological conditions, which renders it less attractive. To date, there are two commercial CAES plants in operation, namely the Huntorf CAES in Germany and the McIntosh CAES in the USA. The former was put into operation in 1978 with a rated power of 290 MW and the latter was built in 1991 with an output power of 110 MW. One major difference between the two plants is that the recuperator is applied in McIntosh for exhaust-heat recovery, which reduces the exergy losses of exhaust gas and results in higher efficiency than Huntorf CAES. However, the cost of McIntosh CAES will also rise accordingly. Other parameters of the two CAES plants are given and compared in Table 2.2 and Ref. [9, 17].

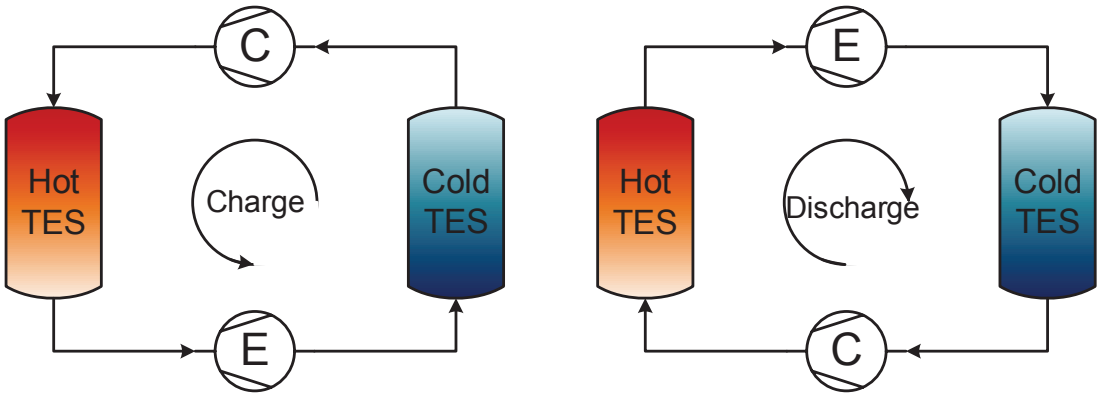

(a) charge (b) discharge

Figure 2.4: Schematic diagram of the PTES during (a) charge and (b) discharge

2.2 Review of the thermodynamic modelling of individual technologies

In recent years, many innovative concepts of large-scale EES technologies have been proposed, including Adiabatic Compressed Air Energy Storage (A-CAES), Isothermal Compressed Air Energy Storage (I-CAES), Pumped Thermal Energy Storage (PTES) and Liquid Air Energy Storage (LAES). These technologies store exergy in the form of temperature or pressure potential via different energy carriers such as natural stones, compressed or liquid air and all enjoy many advantages. However, a thorough investigation and comparison of all these technologies is still lacking and it constitutes the major part of this thesis.

2.2.1 Pumped Thermal Energy Storage

Pumped Thermal Energy Storage (PTES) effectively operates as a heat pump during charge, pumping thermal energy from a cold reservoir to a hot one; whilst during discharge, the process is reversed and it operates as a heat engine, converting the stored thermal energy back into electricity, as shown in Fig. 2.4. Therefore, electricity is stored in the form of thermal potential of the two thermal reservoirs due to the temperature difference with the environment. The thermal storage materials can be solid, such as gravel and metal oxide, which are cheap, abundant and nontoxic by nature; or liquid, which enables the system to be pressurized to reduce the cost and the thermal energy to be stored statically at a single temperature; or Phase Change Materials (PCM) which tend to enjoy much higher energy density. Therefore, the advantage of thermal storage materials is one of the main motivations behind PTES and it will be discussed in detail in Chapter 4. Even with sensible thermal energy alone, the energy den-

sity of PTES is relatively high when compared with other thermo-mechanical energy storage systems. For example, the energy density of a Thermal Energy Storage (TES) at temperature T can be expressed as:

$$D_{\mathrm{TES}} = \rho_s c_s \left(T - T_0 - T_0 \ln \frac{T}{T_0} \right) \tag{2.6}$$

where ρ_s and c_s are the density and heat capacity of the energy storage materials respectively, and T_0 is the ambient temperature. The TES temperature T of a PTES can be as high as 500 °C and as low as -150 °C, which correspond to energy densities of $130\,\mathrm{kWh \cdot m^{-3}}$ and $60\,\mathrm{kWh \cdot m^{-3}}$ respectively, if magnetite is used as the thermal storage material (Fe_3O_4 is selected here due to its relatively high heat capacity and low cost, see Ref. [59]). Therefore, the energy density of PTES is orders of magnitude higher than that of PHES and CAES, as shown in Table 2.1.

The roundtrip efficiency of PTES is not limited by the Carnot efficiency and could also reach 100 % for an ideal PTES. This is because although the thermal efficiency of an heat engine is bounded by the Carnot efficiency, which tends to be low and falls between 20 and 50 % for most heat generation systems, the Coefficient of Performance (COP) of an heat pump tends to be the reciprocal of the thermal efficiency of heat engine and hence, the combination of the two as a system becomes more attractive. For example, the roundtrip efficiency of a reversible PTES can be expressed as:

$$\chi_{\mathrm{rev}} = \mathrm{COP}_{\mathrm{HP,rev}} \cdot \eta_{\mathrm{HE,rev}} = \left(\frac{T_{\mathrm{h}}}{T_{\mathrm{h}} - T_{\mathrm{c}}} \right) \cdot \left(\frac{T_{\mathrm{h}} - T_{\mathrm{c}}}{T_{\mathrm{h}}} \right) = 1 \tag{2.7}$$

where T_{h} and T_{c} are the temperatures of hot and cold thermal reservoir respectively. From Eq. (2.7), it can be noted that the roundtrip efficiency of an ideal PTES is always 100 % despite the variation of T_{h} and T_{c}. In practice, however, the aerodynamic dissipation within the compression and expansion device, the irreversible heat transfer within the heat exchanger or thermal reservoir, and the pressure losses within each component together render the roundtrip efficiency of PTES in the range of 50 to 70 %.

In Eq. (2.7), the term $(T_{\mathrm{h}} - T_{\mathrm{c}})$ is proportional to the net work input during charge (or net work output during discharge), $w_{\mathrm{net}} \propto (T_{\mathrm{h}} - T_{\mathrm{c}}) = (T_{\mathrm{h}} - T_0) - (T_0 - T_{\mathrm{c}}) \propto w_{\mathrm{in}} - w_{\mathrm{out}}$. Therefore, it can be noted that as a closed system, there is always a portion of energy to be generated during charge, like the w_{out} in the above equation, or to be consumed during discharge, which are both against the desired direction of energy flow and reduces the net work w_{net}. Further study reveals that this portion of energy also makes the PTES more sensitive to compression and expansion losses and therefore, the ratio between w_{out} and w_{in} should be minimized. Currently, there are mainly two methods to reduce the work ratio: one is to employ the Brayton

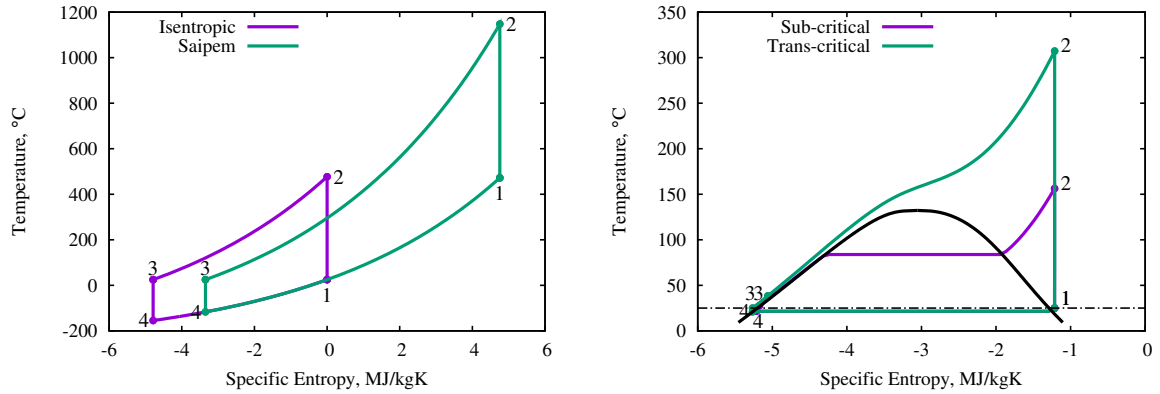

(a) Brayton-cycle PTES (Argon)

(b) Rankine-cycle PTES (Ammonia)

Figure 2.5: T-s diagrams of the PTES variants: (a) Brayton-cycle PTES (Argon) (b) Rankine-cycle PTES (Ammonia)

cycle and the other is to employ Rankine-cycle, and the PTES can be further categorized into the Brayton-cycle PTES and the Rankine-cycle PTES accordingly.

Brayton-cycle PTES

The Brayton-cycle PTES seems to have been proposed almost simultaneously and independent by Isentropic Ltd. [20] in England and Saipem Ltd. [21] in France after the companies filed their patents in 2008-2009 [18]. The T-s diagram of the Isentropic system and Saipem system are shown in Fig. 2.5a, and it can be noted that the Joule-Brayton cycle is followed in both systems. In addition, argon and solid refractories are respectively employed as the working fluid and thermal storage materials in both systems as well. However, there is no preheating in the Isentropic system so that both T_1 and T_3 are fixed at ambient temperature T_0; whilst in the Saipem system, T_1 is increased to around 480 °C by adjusting the discharging temperature ratio τ' and T_3 is fixed at ambient value, as shown in Fig. 2.5a. The maximum temperature T_2 of Saipem system is also much higher than that of the Isentropic. In addition, turbomachineries are deployed as the compression and expansion devices in Saipem system whilst reciprocating compressors and expanders are used in Isentropic system instead. In Isentropic system, the thermal reservoir is segmented to further reduce the pressure loss.

The Saipem scheme has been modelled in the literature by Desrues et al. and Ni and Caram. Desrues et al. [60] modelled the thermal reservoir with finite element method with the axial conduction and pressure loss being included, whilst Ni and Caram [61] modelled the thermal reservoir with the Schumann equations and solved with the exponential matrix method. They both model the turbomachineries with polytropic efficiency η but the effects

of heat leakage loss and pressure loss are not considered. Results show the feasibility of this process, with an estimated roundtrip efficiency of 66.7 % and key factors for improving the process performance are identified. It should be noted that the maximum reached temperature in Saipem scheme is as high as 1268 K, which is above the maximum allowable temperature of current compressors and expanders.

The Isentropic scheme is mainly researched in Cambridge by White and McTigue. White first studied the sensitivity of PTES roundtrip efficiency to various loss factors and indicated the particular susceptibility to compression and expansion losses which can be mitigated by using efficient reciprocating devices and reducing the ratio of discharged temperature between hot and cold store [18]. Then he focused on the losses of packed bed thermal reservoir with a simple numerical model based on Schumann equations and demonstrates the dependence of losses on operating temperatures, reservoir geometry and mode of operation [41]. The impact of the variation of heat capacity with temperature was also investigated in detail [59]. McTigue then integrated the packed bed model with the reciprocating compressor/expander model. Both parametric and optimization studies are carried out and a flat tradeoff between efficiency and energy density is discovered, which is mainly due to the utilization factor Π and indicates an attainable high energy density with a small penalty on efficiency [43]. Later McTigue extended the Schumann model of thermal reservoir by including the effects of axial conduction and heat leakage and carried out thermo-economic optimization for the Brayton PTES [44]. Similar researches are carried out for segmented thermal reservoir [42, 44] and radial thermal reservoir [62], and their advantages and disadvantages are revealed.

More recent papers have focused on the PTES with liquid stores and heat exchangers. Complicated techniques such as preheating, precooling and recuperating, are employed to adapt the PTES cycles to match with the temperature range of the thermal fluids, as well as increasing the roundtrip efficiency and energy density [48]. Stage repetition and system pressurization have also been proposed as ways for increasing system efficiency and reducing the unit storage cost. The research on this recent progress can be found in Ref. [48] and will be discussed in Chapter 4.

Rankine-cycle PTES

The Rankine-cycle PTES can be further categorized into the transcritical and subcritical PTES depending on the state of working fluid at high pressure side. Modern research on Rankine-cycle PTES was initiated in Switzerland by ABB Ltd. [63] but soon attracted the attention from researchers in other countries. The T-s diagram of the transcritical and subcritical PTES are shown in Fig. 2.5b, and it can be noted that the Rankine cycle is followed. Carbon dioxide, ammonia and steam are proposed as working fluids, and both pressurized liquid stores and

indirect contact thermal reservoir are proposed as the hot TES. For the cold TES, either phase change materials such as salt water ice slurry or environment are proposed because the bottom part of Rankine cycle is always a phase change process, as shown in Fig. 2.5b, which makes the sensible heat storage inappropriate here due to the serious pinch point problem. Compared with Brayton-cycle PTES, Rankine-cycle PTES enjoys higher work ratio between w_{out} and w_{in} during charge because compressing liquid usually requires less work than compressing ideal gas, as shown in Figs. 2.5a and 2.5b. However, Rankine-cycle PTES is also more prone to heat transfer losses within the hot TES due to the heat capacity variation around the critical point, and the temperature ratio of Rankine-cycle PTES tends to be low, which reduces its energy density and make it more sensitive to all kinds of irreversiblities.

The transcritical PTES with carbon dioxide as the working fluid has been first proposed by ABB Ltd. in 2011 [22]. Water is used as the hot TES materiel and ice production/melting forms the cold TES. The technical feasibility of using off-the-shelf components for a pilot-scale plant has been analyzed [22]. Mercangöz et al. [63] further developed this concept and provided more details of the suggested design. The advantages of using CO_2, water and ice slurry respectively as the working fluid, hot and cold TES materials are discussed, and the importance of matching the temperatures of working fluid and thermal storage fluid are emphasized. Morandin et al. [64] presented a modelling method based pinch analysis for a base case and alternative system configurations. They also conducted a more detailed thermo-economic optimization for the transcritical PTES with CO_2 as the working fluid and found the most sensitive design parameters are the number of intermediate storage tanks and the system pressure ratio. A similar transcritical PTES with ammonia, indirect contact thermal reservoir and environment as the working fluid, hot and cold TES respectively was proposed by Abarr et al. [65, 66] as a stand-alone energy storage system and a bottoming cycle for an integrated gas turbine system. Parametric study and baseline thermo-economic analysis was also carried out, and results shows that this transcritical PTES has relatively low system efficiency but competitive economic performance.

The subcritical (or latent) PTES with steam and ammonia as the working fluid has been studied by Steinmann and is referred to as the Compressed Heat Energy Storage (CHEST) [67]. The basic CHEST configuration used steam as the working fluid, a combination of sensible and latent storage as the hot TES, and the environment as the cold TES. The combination of sensible and latent storage can minimize the temperature difference of heat transfer caused by the pinch point problem. Steinmann also considered the cascaded cycles and the step-wise compressions. Ammonia cycle is used for low temperature compression and water cycle is employed as the high temperature compression, and therefore, the hot store of ammonia cycle also acts as the cold store of the water cycle. The roundtrip efficiency is estimated as 72.8

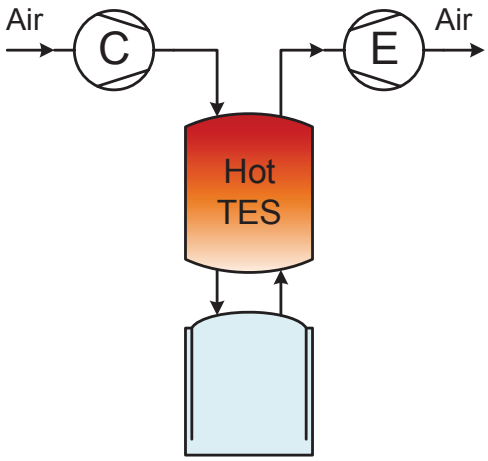

Figure 2.6: Schematic diagram of the A-CAES

% without considering the effect of heat leakage losses and pressure losses. Dietrich et al. [68] analyzed a subcritical PTES with Butane as the working fluid. Tube-in-concrete thermal reservoir and environment are still deployed as the hot and cold TES respectively. Its roundtrip efficiency and unit storage cost are estimated to be 27.3% and 56.21 ct/kWh respectively.

2.2.2 Adiabatic Compressed Air Energy Storage

Adiabatic Compressed Air Energy Storage (A-CAES) compresses air near-adiabatically during charge and then stores the generated thermal energy (colloquially the "heat of compression") separately in a TES prior to the storage of compressed air in an air reservoir; whilst during discharge, air is reheated within the TES before being expanded in turbines to generate electricity, as shown in Fig. 2.6. The electricity is thus stored in the forms of temperature potential of the TES and pressure potential of the air reservoir. Therefore, A-CAES can be viewed as a hybrid of thermal and mechanical energy storage systems. For example, the outlet exergy flow of an ideal adiabatic compressor can be written as:

$$\dot{E}_{\text{air}} = \dot{m}\left[c_p T_0\left(\frac{T}{T_0} - 1 - \ln\frac{T}{T_0}\right) + R_g T_0 \ln\frac{p}{p_0}\right] \tag{2.8}$$

where the first part of the right hand side of Eq. (2.8) refers to the temperature related contribution; whilst the second part refers to the pressure related contribution of air exergy. Dividing the specific exergy e_{air} into temperature and pressure related contribution will be helpful for analyzing the A-CAES process. For an adiabatic compressor, the temperature ratio τ and pressure ratio β after compression are related by: $\tau = \beta^{\frac{\gamma-1}{\gamma}}$, where $\tau = T/T_0$ and $\beta = p/p_0$. After substituting this relation into Eq. (2.8), it can be proved that the temperature related

contribution increases whilst the pressure related contribution decreases with the pressure ratio β, and the energy density of A-CAES is simply an weighted average of the energy density of compressed air and TES system, which can be calculated by Eq. (2.3) and Eq. (2.6) respectively. Therefore, it can be noted that both the air reservoir and TES are important to the energy density and unit cost of A-CAES.

In addition, the roundtrip efficiency of an isobaric A-CAES can be written as:

$$\chi_{\mathrm{CAES}} = \frac{\eta T'_{\mathrm{e,in}} \left(1-\tau^{-1}\right)}{T_{\mathrm{c,in}} \left(\tau-1\right)/\eta} = \eta^2 \left(1-f_{\mathrm{T}}\right) \tag{2.9}$$

where $T_{\mathrm{c,in}}$ is the compressor inlet temperature during charge, which is always T_0; whilst $T'_{\mathrm{e,in}}$ is the expander inlet temperature during discharge, $T'_{\mathrm{e,in}} = T_{\mathrm{c,out}} \left(1-f_{\mathrm{T}}\right) \approx T_0 \tau \left(1-f_{\mathrm{T}}\right)$, where f_{T} is the temperature loss factor of TES which measures the temperature drop within the TES subsystem. Since η is the isentropic efficiency of the compressor and expander, it can be noted that the roundtrip efficiency of an isobaric A-CAES is determined by the performance of TES system and compression/expansion device. Further analysis reveals that the cavern parameters also plays an important role in the performance of an isochoric A-CAES. Therefore, air reservoir, TES system and compressor/expander are all critical units for A-CAES.

The type of compressor/expander is usually determined by the rated power P and energy E of an A-CAES. For example, axial compressors/turbines are more suited for large-scale A-CAES with high mass flowrate, whilst reciprocating compressors/expanders are more suited for micro-scale A-CAES with low mass flowrate. The A-CAES can also be categorized into different variants due to their different types of air reservoirs and TES systems, which will be discussed in detail in the following parts of this section.

Air reservoir

In terms of pressure fluctuation, an air reservoir can be categorized into an isobaric or isochoric type; whilst the isochoric air reservoir can be further divided into an isothermal, intermediate or adiabatic type, according to its heat exchange with the surrounding. Similarly, an A-CAES can also be categorized into an isobaric or isochoric A-CAES according to their deployed air reservoirs. For example, in an underwater A-CAES (Fig. 2.8a) or an underground A-CAES with rock formation and water equalizing pits (Fig. 2.7b), the pressure within the air reservoir remains constant, and they are therefore categorized into the isobaric A-CAES. On the other hand, in an underground A-CAES with solution-mined cavern (Fig. 2.7a) or an above-ground A-CAES with artificial air reservoirs (Fig. 2.8b), the pressure within the air reservoir constantly varies between p_{min} and p_{max}, and they are therefore categorized into

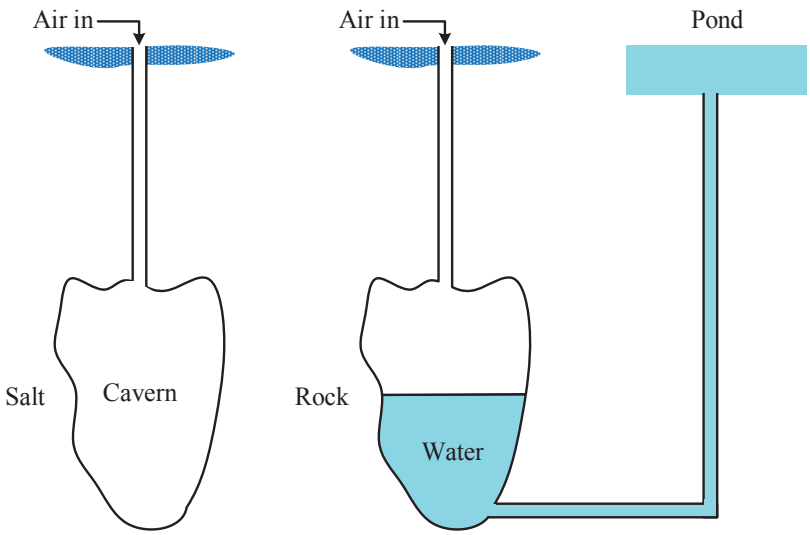

(a) Isochoric cavern (b) Isobaric cavern

Figure 2.7: Schematic diagrams of the air reservoirs of Underground CAES: (a) Isochoric cavern (b) Isobaric cavern [2]

the isochoric A-CAES. For an isobaric air reservoir with both inlet and stored air at ambient temperature T_0, it can be proved that there is no heat exchange with its surrounding so that an isothermal or adiabatic boundary makes no difference for it [50]. For an isochoric air reservoir, however, there is heat transfer across the system boundary and its amount can be adjusted by changing the mass flowrate of inlet/outlet air [2].

As a proven technology, isochoric air reservoir, such as underground solution-mined cavern and above-ground artificial air reservoir, has received intensive treatment from both the academia and the industry. In 2004, Bullough et al. [24] studied the availability of underground air reservoir and concluded that using existing cavern or solution-mined ones are both feasible options. The pressure and temperature variation within the cavern of the first CAES plant was published by Crotogino et al. [71] and based on this data, Raju et al. [72] developed an accurate simulation model for the Huntorf cavern and found the heat transfer between a cavern and its surrounding plays an important role in determining its thermodynamic behavior. Zhang et al. [50] arranged the work of other researchers and proposed a complete set of thermodynamic models for different air reservoirs and A-CAES systems. He also discovered that the impacts of air reservoir models and stage number on the system performance are significant, and these models and conclusions can be applied to above-ground artificial air reservoirs as well. In 2008, Grazzini and Milazzo [73] proposed an A-CAES with artificial air reservoir and variable configuration system. The pressure within this artificial air reservoir

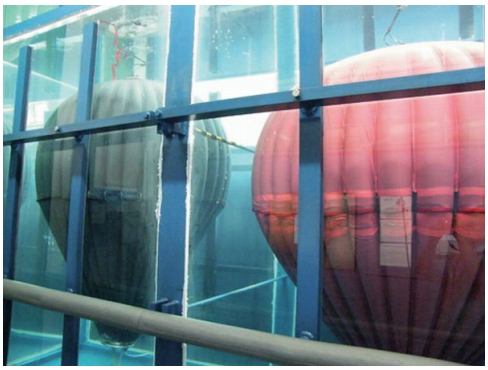

(a) Underwater CAES [69]

(b) Above-ground CAES [70]

Figure 2.8: Photos of the air reservoirs of Underwater CAES and Above-ground CAES: (a) Underwater CAES (b) Above-ground CAES

can vary continuously from 1 bar to 200 bar, thus making full use of the stored exergy. They also provided a simple theoretical method for estimating the mass of steel for the artificial air reservoir. Other more detailed study on the economics of artificial reservoirs can be found in Refs. [4] and [74].

The air reservoirs studied in the above literature are all isochoric ones. However, isobaric air reservoirs, such as underwater energy bags (Fig. 2.8a) and underground isobaric caverns (Fig. 2.7b), are also popular. The underground cavern with rock formations and water equalizing pits was first proposed in a report by Brown, Boveri (BBC) [58], and this isobaric cavern was claimed to have smaller volume and could avoid the throttle losses caused by the pressure sliding of isochoric cavern. A micro-scale isobaric air reservoir which combines CAES with PHES was proposed by Kim et al. [57], which could help the turbomachineries operate at their optimal efficiency. The research on Underwater CAES (UW-CAES) is also very active in the UK and Canada. Both numerical and experimental research has been carried out and the results can be found in Refs [30] and [29]. Recently, an underwater CAES reference facility has been applied in Toronto using an underwater air storage in Lake Ontario [31].

In spite of these numerous variants of air reservoirs, an investigation of different models and parameters of air reservoir on the system losses and efficiency has so far been lacking. This forms the subject of Chapter 5, together with a case study of the Huntorf CAES cavern. The motivation for this comparative study is to minimize the cavern losses (direct losses) and other losses due to cavern parameters (indirect losses), as well as maximizing the energy density of cavern.

TES system

In terms of temperature range, a TES can be categorized into a high-temperature (above 400 °C), medium-temperature (between 200 °C and 400 °C) or low-temperature (below 200 °C) TES, as shown in Ref. [17]. High-temperature TES is estimated to have higher system efficiency while the low-temperature TES is believed to have faster start-up and better profitability. In addition, the difference in temperature range can also be represented by the difference in heat transfer method and thermal storage materials. For example, thermal storage may be achieved by cooling the air in heat exchangers which allow the energy to be transferred to liquid tanks. Alternatively, heat may be transferred directly to a solid storage material, for example in a packed bed. The former is referred to as the liquid TES and mostly used for low-temperature TES; whilst the latter is named as the solid TES and usually deployed as high-temperature TES.

Bullough et al. [24] were the first to study and compare solid and liquid TES for A-CAES systems, proposing several suitable TES materials that cover temperatures from 50 to 650 °C. RWE Power Ltd. proposed the ADELE project in Germany which is intended to operate at high temperature (600 °C) and high pressure (100 bar), with a targeted system efficiency of 70 % [25]. Barbour et al. [75] presented a thermodynamic analysis of a two-stage solid A-CAES system and suggested that solid A-CAES is superior to its liquid counterpart because this system has no costly thermal fluid requirements and enjoys higher system efficiency and energy density. Hybrid TES with both solid and Phase Change Material (PCM) has been proposed and investigated by Peng et al. [76], and it is claimed to be more efficient than TES with single solid or PCM. These studies all propose high temperature TES systems, but there are also numerous concepts that operate in the range of 80-200 °C.

Low temperature A-CAES (LTA-CAES) was advocated by Wolf et al. [26] who highlighted several advantages: fast cycling and wide-ranging part-load capacity, and avoidance of various high-temperature challenges. These benefits come at the expense of lower efficiency, which is anticipated to be in the range of 52-60 %. Grazzini and Milazzo [73] proposed a system in which the TES comprises pressurized water at 120 °C combined with a high-pressure artificial air reservoir. The system efficiency is estimated at 72 % which clearly competes with other energy storage technologies.

Many cycle analysis studies for liquid A-CAES have been reported in the literature, including those of Luo et al. [77] for a liquid-based TES systems, who concluded that efficiency is determined mainly be compression and expansion losses and heat exchanger effectiveness. Buffa et al. [78] proposed a system under the project “ENEL Ingegneria e Innovazione”, with seven stages of compression and six stages of expansion. Due to the large number of stages, the TES temperature is low enough that ambient water can be used as the thermal fluid, but

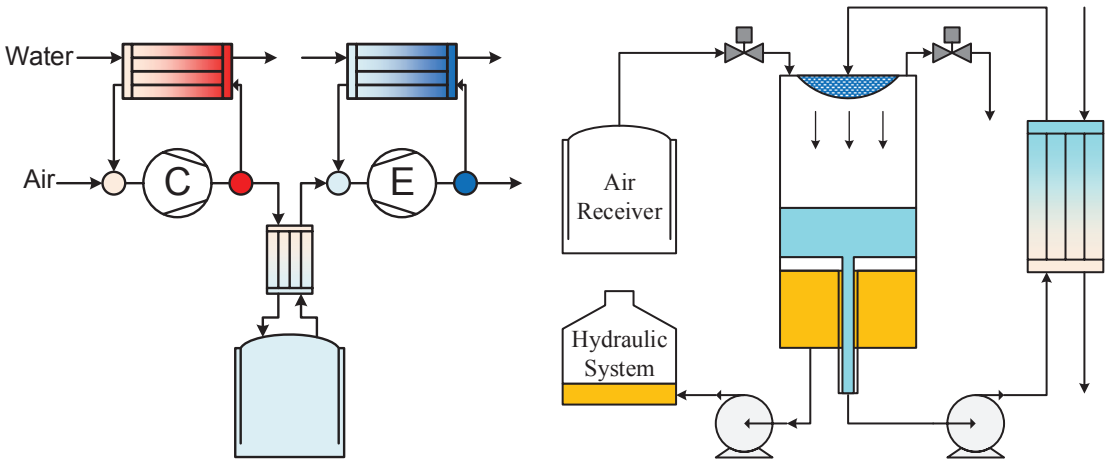

(a) I-CAES (b) Isothermal expander

Figure 2.9: Schematic diagrams of the I-CAES and the isothermal expander: (a) I-CAES (b) Isothermal expander

the system efficiency is estimated to be only 52 %.

Despite these and many other studies of different A-CAES configurations, a comparative study of liquid and solid based systems from both thermodynamic and economic perspectives has so far been lacking. This forms the subject of Chapter 5, together with the investigation of a hybrid solid-liquid system aimed at achieving high efficiency whilst reducing capital cost. The motivation for hybrid A-CAES lies in the fact that the packed bed is generally more efficient and cheaper than heat exchangers at low pressure, but becomes exorbitantly expensive at high pressures.

2.2.3 Isothermal Compressed Air Energy Storage

Isothermal Compressed Air Energy Storage (I-CAES) compresses air near-isothermally by continuously removing the generated thermal energy during charge, whilst during discharge, thermal energy is continuously added to the system at near-ambient temperature, as shown in Figs 2.9a and 2.9b. Therefore, a separate TES can be avoided and almost all its exergy is stored in the form of pressure potential of the compressed air. In practice, some of the proposed I-CAES make use of cheap and low-grade thermal storage by means of, for example, a warm water pool. The energy density of I-CAES is the same with that of the CAES, as shown in Eq. (2.3), which tends to be lower than that of a TES, as shown in Eq. (2.6). However, the unit cost of storing compressed air is much lower than that of storing thermal energy, which is the underlying motivation for developing I-CAES.

The efficiency of an I-CAES is obviously dependent on how fast it can exchange heat with

its surroundings and how close it is to ideal isothermal process. To measure this effect, the isothermal efficiency η_{iso} is introduced, which is the ratio between the ideal isothermal work w_{ideal} and the actual work w_{actual} for a compressor, $\eta_{\text{iso}} = w_{\text{ideal}}/w_{\text{actual}}$. There are generally three methods to enhance the heat transfer and increase the isothermal efficiency, which are through increasing the heat leakage factor, and enhancing the sensible and latent heat exchange with a thermal fluid respectively. To better demonstrate these effects, the infinitesimal temperature increase of compressing an air-vapor-liquid mixture that maintains thermal equilibrium can be written as [79, 80]:

$$\frac{\mathrm{d}T}{T} = \frac{1-\alpha_{\text{c}}}{\eta_{\text{c}}} \frac{R^*}{c_p^*} \frac{\mathrm{d}p}{p} \tag{2.10}$$

where η_{c} is the polytropic efficiency and α_{c} is the heat leakage factor of compressor, which quantifies the compression heat losses by $\alpha_{\text{c}} = \delta q_{\text{c}}/\delta w_{\text{c}}$. Therefore, if the heat leakage factor α_{c} is one, then the same amount of heat will be leaked out through the boundary as the compression work, which means it is an ideal isothermal process as $\delta q_{\text{c}} = \delta w_{\text{c}}$ and $\mathrm{d}T = 0$. However, increasing α_{c} is difficult to realize in practice because as shown in Ref. [81], the bottleneck in heat transfer through the boundary is the convection resistance inside the cylinder, for which few methods are available to reduce it. From Eq. (2.10), it can also be noted that increasing the polytropic efficiency η_{c} and thus reducing the aerodynamic loss can also help make the compression more isothermal.

Another method for isothermal compression is enhancing the heat transfer between the air and a thermal fluid, and the heat transfer can be further categorized into the latent and sensible heat transfer. For example, most I-CAES systems require large amount of water droplets to enhance the heat transfer, and for each kg of dry air, there will be ω kg of water vapor and f kg of liquid water with it. If the air-vapor-liquid mixture is in thermal equilibrium, then the effective heat capacity c_p^* and gas constant R^* in Eq. (2.10) can be expressed as [79, 82]:

$$c_p^* = c_{p,\text{a}} + \omega c_{p,\text{v}} + f c_{p,\text{l}} + \left(1 + \frac{M_{\text{a}}}{M_{\text{v}}}\omega\right) \frac{\omega L^2}{R_{\text{v}} T^2} \tag{2.11}$$

$$R^* = R_{\text{a}} + \omega R_{\text{v}} + \left(1 + \frac{M_{\text{a}}}{M_{\text{v}}}\omega\right) \frac{\omega L}{T} \tag{2.12}$$

where the subscripts a, v and l denote the dry air, vapor and liquid respectively, M is the molecular weight and L is the latent heat of vaporization. From Eqs. (2.11) and (2.12), it can be noted that although the mass of vapor ω is usually negligible, its contribution to the effectiveness heat capacity c_p^* and gas constant R^* may be significant because the latent heat of vaporization L is very large. This is especially the case when the pressure p is low but the

temperature T is high since both of them lead to higher vapor mass ω. It is reported that with the latent heat transfer alone, the effective isentropic index γ^* can be reduced from 1.40 to 1.12 ~ 1.16 [79, 82]. Therefore, latent heat transfer is usually employed in the inlet fog boosting of gas turbines to reduce its compression work.

Compared with gas turbines, the operating temperature of an I-CAES is much lower whilst the operating pressure is much higher, which means the mass of water vapor ω is low and the contribution of latent heat transfer is not enough to achieve near-isothermal compression alone. Therefore, sensible heat transfer is also deployed to further reduce the effective isentropic index γ^*. Since the heat capacity of water is roughly four times that of the air, the effectiveness heat capacity c_p^* of air-vapor-water mixture can increase by 400 % for each unit increase of water, as shown by Eqs. (2.11). Therefore, sensible heat transfer is widely employed in all kinds of isothermal compression and especially important in the liquid-flooded compressors because thermal oil tends to have high boiling point and thus the contribution of latent heat transfer is negligible.

Most of the current I-CAES systems employ several of the above techniques together to increase its isothermal efficiency. For example, the surface area to volume ratio of a liquid piston can be maximized by conforming its liquid to an irregular shape, and its heat leakage factor can be increased accordingly. Meanwhile, large amount of water droplets can be sprayed into the liquid piston to further enhance the heat transfer between air and water, which may occur in both sensible and latent methods. Therefore, all of the above heat transfer enhancement methods will be first reviewed separately and then their applications in I-CAES will be emphasized.

Heat leakage

For an isothermal compressor, the overall heat transfer resistance between the cylinder air and the ambient can be divided into three parts, namely the convection resistance of the cylinder air $R_{\text{conv,air}}$, the conduction resistance $R_{\text{cond,metal}}$, and the convection resistance of the ambient $R_{\text{conv,amb}}$ [81]. The conduction resistance $R_{\text{cond,metal}}$ is negligible when compared with the convection resistances, and the convection resistance of ambient $R_{\text{conv,amb}}$ can be further decreased by employing a water jacket around the cylinder. Therefore, the bottleneck in heat transfer enhancement is the convection resistance of cylinder air $R_{\text{conv,air}}$, and its value can be reduced by increasing the heat transfer area between wall and air.

Knowlen [83] was the first to investigate the effects of bore-to-stroke ratio and engine frequency on the isothermal efficiency, and concluded that small bore and low frequency were desirable for en efficient isothermal engine. He also proposed the concept of conically finned piston to further increase the heat transfer area of inner cylinder, and the simulation results

showed that significant improvement could be obtained. However, it should be noted that increasing the cylinder area or reducing the engine frequency is always accompanied by an increase in capital cost, and the potential for further improvement is very limited.

Latent heat transfer

Another method of heat transfer enhancement involves liquid evaporation and condensation within the compressor/expander. As mentioned earlier, the impact of latent heat transfer on isothermal efficiency is significant even if the mass of water vapor ω is mall due to the large latent heat of vaporization L. One example of the application of latent heat transfer is the Inlet Fog Boost (IFB) and wet compression of gas turbines, and it is reported that a 1 % water injection to air mass flow will increase the gas turbine output up to 10 % and efficiency up to a relative 3 %, with other benefits such as NOx emissions reduction. This is because of the reduction of compression work due to continuous evaporative intercooling, and the increased turbine mass flowrate and specific work due to high heat capacity of water vapor.

Zheng et al. [82] established the thermodynamic model for wet compression process and discussed the topics such as ideal and actual wet compression, inlet evaporative cooling, efficiencies of wet compression, and droplet evaporation rate and time. White and Meacock [79] studied the effect of water evaporation throughout the compressor stages, and examined the consequent off-design behavior and the potential reduction in compressor work input. Their work was initially restricted to small droplets which follows the gas-phase velocity with negligible slip, but was later extended to multi-spool gas turbine [84] and wet compression with velocity slip effects [85]. They found the overall performance of multi-spool gas turbine shows a substantial power boost and a marginal increase in thermal efficiency, and for droplet sizes of typical of fog boosting, the overall effect of slip is to slightly increase the evaporative cooling effect through the enhanced heat and mass transfer rates.

It should be noted that the wet compression is not near-isothermal compression, but the models of latent heat transfer will be used in Chapter 6 of this thesis.

Sensible heat transfer

Liquid flooded compression refers to the process of flooding a screw or scroll compressor with large quantities of lubrication oil as the air flows through it, so that the oil also operates a medium for heat exchange. Since the boiling point of lubrication oil is relatively high, the impact of latent heat transfer on isothermal efficiency is very limited. Therefore, the sensible heat transfer is critical for the isothermal efficiency of liquid-flooded compression.

Hugenroth et al. [86, 87] carried out thermodynamic analysis and experimental investi-

gation for a liquid-flooded Ericsson cycle cooler. Analytical models of liquid-flooded compression and expansion processes were developed using ideal gas, constant specific heat, and incompressible liquid assumptions. The optimum liquid flooding rate that minimized compression work was discovered as well. These models were later validated with experimental results, and it was found that the scroll compressor and expander perform pretty well considering they were not designed for the operating conditions encountered.

Coney et al. [88, 89] developed a novel reciprocating compressor, in which quasi-isothermal compression is achieved by the injection of a large quantity of water through spray nozzles inside the compressor. Due to the high density and heat capacity of the liquid water spray, the temperature increases only slightly during compression. They claimed a compression ratio of up to 1:30 can be realized in a single cylinder with a significant reduction in the power consumption.

The analytical and numerical models of sensible heat transfer have been developed by Hugenroth and Coney respectively, and will be used in Chapter 6 of this thesis.

Application in I-CAES

As mentioned earlier, all of the above techniques can be used together to increase the isothermal efficiency of an I-CAES. A good example of this kind of application is the liquid piston, which was first proposed by Van de Ven and Li [90]. Liquid piston, as its name suggests, uses liquid column to compress the air directly. Since a liquid can easily conform to an irregular shape, the surface to volume ratio and heat leakage factor of a liquid piston can be maximized. Meanwhile, the liquid can be used to enhance heat transfer and carry the "heat of compression" out of the system. Finally, a liquid piston can eliminate gas leakage and replace sliding seal friction with viscous friction. Therefore, it was found that the liquid piston could significantly reduce the compression work and increase the efficiency, whilst the friction loss did not increase much. Qin and Loth [6] investigated the concept of droplet spray heat transfer to establish near-isothermal compression. A detailed multiphase thermodynamic model was established and validated with experimental data, and the compression efficiency was increased from 71 % to 98 %. Later, they investigated this concept with detailed two-dimensional unsteady flow simulations, which uncovered the flow characteristics and strong spatial variation in droplet size and concentration [91].

Proposals of I-CAES have been published by SustainX, LightSail and General Compression [33, 34, 92], most of which require continuous heat exchange between the air and some other substance to remove (or add) heat during compression (or expansion). Water is often used as the heat-exchange fluid due to its highly suitable properties and it can be in various forms (bubbling, spraying and foaming etc.) to increase the two-phase contact area. Hence,

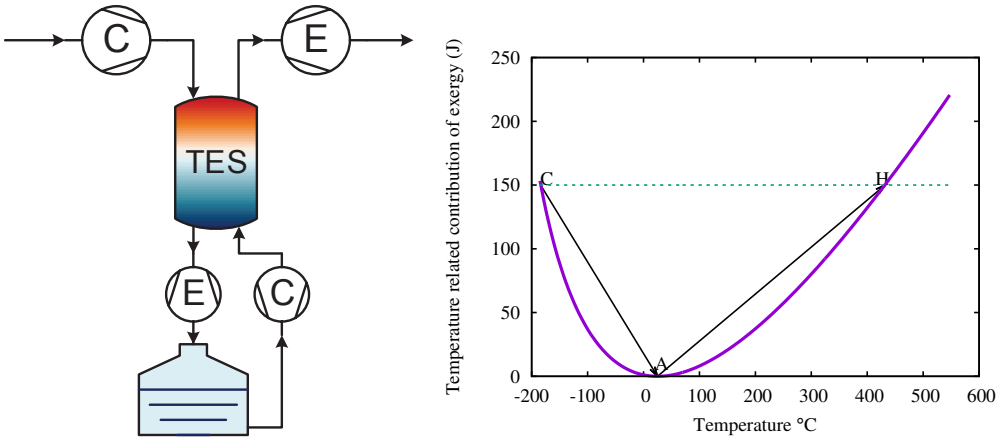

(a) Schematic of LAES (b) Illustration of exergy variation of compressed air

Figure 2.10: Schematic diagram of the LAES and illustration of exergy (temperature related contribution only) variation of compressed air: (a) Schematic diagram of the LAES (b) Illustration of exergy (temperature related contribution only) variation of compressed air

liquid piston and hydraulic pump are often deployed in I-CAES as the isothermal compressor and expander, but I-CAES based on reciprocating devices are also proposed. In 2013, SustainX has replaced spray-based exchange with foam-based heat exchange to further enhance heat transfer [5]. Experimental results showed that compression/expansion ratio as high as 200 could be achieved with only two stages of compression/expansion, with temperature variation less than 50 °C in each stage and isothermal efficiency as high as 95 %. In the same year, a novel Ground-Level Integrated Diverse Energy Storage (GLIDES) system has been proposed in the United States, which employs solar or waste heat to approach a quasi-isothermal process and improve the roundtrip efficiency [35, 36].

2.2.4 Liquid Air Energy Storage

Liquid Air Energy Storage (LAES) cryogenically cools and liquefies air using off-peak electricity during charge, whilst during discharge, the liquid air is pumped, heated and expanded in a series of turbines to generate electricity, as shown in Fig. 2.10a. Hence, the off-peak electricity is stored in the form of temperature potential of liquid air, which is pretty high (e.g., $388-444\,\mathrm{MJ/m^3}$ for saturated liquid air at $10-16\,\mathrm{bar}$) when compared with other thermo-mechanical energy storage systems. Meanwhile, LAES is not bound by specific geographic and geologic conditions, and enjoys much higher siting freedom. In these senses, LAES shares some similarities with PTES.

However, LAES is not a closed cycle and cannot be pressurized like PTES. Actually, the hot part of LAES is quite similar to an A-CAES or CAES before the compressed air is

cooled, liquefied and stored. Like CAES, baseline LAES (which is a simple combination of an air liquefaction plant and a power recovery system) cannot recycle the generated thermal energy of compression (colloquially the "heat of compression"), which increases the work input during charge and reduces the work output during discharge. In addition, baseline LAES cannot recycle the released thermal energy of liquid air (colloquially the "cold of liquid air") either, which means the compressed air could only be cooled by the flash-gas or separately expanded air during charge. This further increases the compression work during charge and reduces its roundtrip efficiency. Actually, baseline LAES usually has a low efficiency and according to Ref. [40], the roundtrip efficiency of the first pilot LAES plant is only 8 % despite that a small portion of the cold energy of liquid air has been recycled.

Since the previous LAES cannot recycle the "heat of compression" during charge and the "cold of liquid air" during discharge, it is also referred to as the Diabatic LAES in the follow part of this thesis because all this thermal energy is dissipated into the environment. To improve the efficiency of Diabatic LAES, thermal energy recycling has been proposed, and both hot and cold TES have been integrated into the Diabatic LAES. In the ideal case, all the thermal energy will be recycled and the LAES will not rely on any external supply of thermal energy. An Adiabatic LAES has thus been proposed, and depending on the type of its TES, an Adiabatic LAES can be further categorized into one with solid TES (colloquially "solid LAES") and one with liquid TES (colloquially "liquid LAES").

During discharge of an Adiabatic LAES, liquid air with exergy E_{L} is first pumped and stores its "cold exergy" E_{C} in a cold TES, then it absorbs the "hot exergy" E_{H} from a hot TES before finally being expanded in turbines to generate electricity. If the net work output is W_{net}, then the following equation should hold:

$$W_{\mathrm{net}} = E_{\mathrm{L}} - E_{\mathrm{C}} + E_{\mathrm{H}} \tag{2.13}$$

Eq. (2.13) is also valid for the charging process. It can be noted from Eq. (2.13) that the flow of "cold exergy" E_{C} is against the desired direction of exergy flow because during discharge, all the exergy is expected to be converted to electricity and fed into the grid, rather than being stored for later use.

To better illustrate the change of thermal exergy, the temperature related contribution of Eq. (2.8) as a function of temperature has been shown in Fig. 2.10b, where the heat capacity $\dot{m}c_p$ is set as unity. From Fig. 2.10b, it can be noted that after storing E_{C} at -188 °C and absorbing E_{H} at 550 °C, the temperature related contribution of exergy of compressed air almost remains unchanged, which indicates $E_{\mathrm{C}} \approx E_{\mathrm{H}}$ and $E_{\mathrm{L}} \approx W_{\mathrm{net}} \approx E$, where E is the rated energy of the LAES system. Therefore, roughly the same exergy as the designed capacity is stored in the liquid air, which has very high energy density. However, the energy density of

LAES plant is not be as high as the liquid air, because the volume of hot TES and cold TES reduces the system energy density, which will be discussed in Chapter 7.

In terms of roundtrip efficiency, an Adiabatic LAES may have lower efficiency than an A-CAES due to its additional losses within the cold TES. However, an Adiabatic LAES has a high work ratio between w_{out} and w_{in} during discharge since pumping liquid air requires much less work than compressing gas, which makes it competitive when compared with PTES. Considering its geographical independence and relatively high energy density, Adiabatic LAES is still a promising energy storage system, and its comparison with other energy storage systems will be discussed in Chapter 8.

Diabatic LAES

The concepts of LAES was first proposed by Smith in 1977 [37] but was later developed by industry groups such as Mitsubishi [38], Hitachi [39] and Highview [40]. Early concept of LAES is no more than a simple combination of air liquefaction unit and power recovery unit with little thermal energy recovery between them. Therefore, the low-temperature thermal energy required for air liquefaction is either provided by the flash-gas (unliquefied air vapor) or the separately expanded air. The cycles deployed by these two methods are referred to as the Linde-Hampson cycle and Claude cycle respectively. It is generally believed that the Claude cycle is more efficient than Linde cycle and more suited for large scale air liquefaction, but this is because in a stand-alone air liquefaction unit, there is no low-temperature thermal exergy available, which is not the case in a LAES system.

Early this century, an integrated LAES and gas turbine (GT) system was proposed to reduce the GT compression work by compressing liquid rather than ambient air [38]. The liquid air in this case was obtained by the Linde process (exploiting off-peak electricity) in an air liquefaction unit, and the power output of the GT was more than doubled relative to that of a conventional cycle. Later on, a subcritical LAES using a combined Linde and Rankine cycle was analyzed by Ameel et al. [93]. This combined cycle relies on external supply on liquid air and only a fraction of the low-temperature thermal exergy can be recycled, and its system efficiency is estimated to be 43 %.

A key milestone for LAES was the completion and testing of a 350 kW/2.5 MWh demonstration plant by Highview [40], which is based on the Claude liquefaction cycle (charge) and the Rankine cycle (discharge). During discharge, some of the exergetic content of the liquid air can be stored for later use, but the rest (roughly 50 %) is still provided by the expansion of compressed air. Therefore, its roundtrip efficiency is only 8 % and future plans for enhancing its cold recovery are proposed.

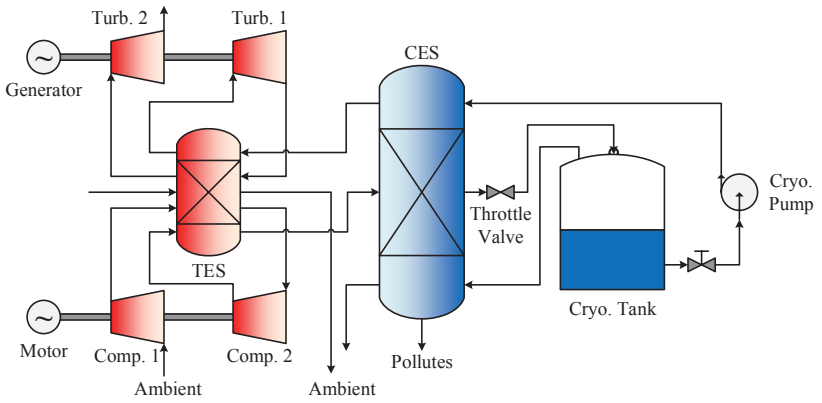

Figure 2.11: Schematic diagram of the Supercritical Compressed Air Energy Storage (SC-CAES) [3]

Adiabatic LAES with solid TES

Since the recovery of "cold" and "hot" thermal energy is so important for the efficiency of LAES, modern research on LAES all deploy TES systems to recycle the cold of liquid air and even the heat of compression. Depending on the types of TES deployed, an Adiabatic LAES can be further categorized into Solid LAES (LAES with solid TES) and Liquid LAES (LAES with liquid TES), as mentioned before. For example, a series of packed beds filled with quartzite based river shingles are used in the Highview LAES plant to recycle the cold thermal exergy, therefore, this TES can be classified as a solid TES [40]. Besides, it is also an indirect-contact solid TES because the stored cold is first transferred to a circulation fluid and then supplied to the main "cold box" (multi-steam heat exchanger), therefore, there is no direct contact between the working fluid and thermal storage media. On the other hand, in the Hitachi LAES proposed by Chino et al. [39], cold is stored in steel pipes filled with small pebbles, and the compressed air efficiently changes its heat by direct contact with the media. Therefore, it is referred to as an direct-contact solid TES.

Another example of solid LAES is the Supercritical Compressed Air Energy Storage (SC-CAES). It was first proposed by Chen et al. [3] by combining the characteristics of A-CAES and LAES, as shown in Fig. 2.11. Both the heat of compression and cold of liquid air are stored respectively in a hot and cold TES which could be packed beds filled with rocks. Guo et al. [94] built the thermodynamic model and carried out exergetic analysis for the SC-CAES, and estimated its efficiency to be 67.4 % and its energy density 18 times higher than a conventional CAES. He also proposed a concise analytical solution for SC-CAES, conducted sensitivity and exergetic analysis based on this model, and proved that the system efficiency varies linearly with the isentropic efficiency, heat exchanger effectiveness and pressure loss factor [95]. The cryogenic energy storage characteristics of a packed bed filled with granite

pebbles were investigated experimentally at pressure of 0.1 MPa and 6.5 MPa by Chai et al. [96], and it is found that the temperature distribution varies significantly at different pressures. Sciacovelli et al. [97] built the thermodynamic model for a LAES with packed bed and evaluated its dynamic behavior. The packed bed model was validated with experimental data and the system efficiency was estimated to be 50 %.

Adiabatic LAES with liquid TES

In addition to the solid LAES, the research on liquid LAES is also very active. The use of common refrigerants as thermal fluids was first proposed by Li [98], and R218 and methanol are selected as the high-grade and low-grade cold thermal storage medium respectively. Pinch point may arise within the heat exchangers due to the heat capacity variation of supercritical air, and Li combined Pinch Analysis with Genetic Algorithm and carried out thermo-economic optimization for the cold TES and LAES plant [99]. The integration of LAES with both nuclear and renewable generation are also conducted and can be found in Ref. [100, 101]. The thermodynamic analysis of liquid LAES with methanol and propane as the cold storage medium has been carried out independently by Guizzi [102] and Krawczyk et al. [103], with the former focusing on the pinch point analysis and loss distribution whilst the latter on the parametric study. The estimated roundtrip efficiencies are both in the range of 50 - 60 %.

The integration of LAES with other energy storage systems is also a heated research area. Usually the cold TES can be got rid of through this method, and as a result, the system energy density can be increased whilst the unit storage cost can be reduced, as shown in Eq. (2.13). Kantharaj et al. [104, 105] proposed a hybrid energy storage system combining features of the high-efficiency CAES and low-cost LAES. A heat pump (engine) is used to convert the compressed (liquid) air into liquid (compressed) air, and the system efficiency is estimated to be 42 %. More recently, a combined cycle of LAES and PTES has been proposed by Farres-Antunez et al. [7], and the system efficiency and energy density are estimated to be 60.4 % and 65.7 $\mathrm{kWh/m^3}$ respectively.

2.3 Review of the thermo-economic methods

2.3.1 Cost modelling

In a world with finite natural resources and ever growing energy demand, it is becoming even more critical for thermal engineers to develop efficient and cost-effective energy systems. The second law of thermodynamics combined with economics represents a powerful tool for dealing with these challenges, and this combination leads to the formation of a relatively new

field of thermo-economics [106]. The pioneering work in thermo-economics started in the 1960s and gradually developed into a systematic technique during the 1980s. For the purposes of parametric and optimization study, it is necessary to derive the physical and cost models of the energy systems as the first step. The physical model can be established through the application of thermodynamics, as discussed in the previous literature review; whilst the cost model can be obtained through the ratio and proportion estimation technique. For example, the "rule of six-tenths" has been developed over the years as a rule of thumb, which can given satisfactory results when only an approximate cost within plus or minus 30 % is required [107]. This concept was developed by Roger Williams in 1947 [108] and based on the assumption that approximate costs can be obtained if the cost of a similar item of different size or capacity is known. At any rate, the "rule of six-tenth" can be expressed as:

$$C_B = C_A \left(\frac{S_B}{S_A} \right)^{0.6} \tag{2.14}$$

where C_B is the approximate cost of equipment having size S_B, and C_A is the known cost of equipment having corresponding size S_A. The dimensionless ratio S_B/S_A is known as the size factor whilst the index less than unity implies the increasing returns due to economies of scale. The index 0.6 can be viewed as a generalization from the typical equipments - tanks and pipe. An analysis of the cost of individual equipment shows that the size factor's exponent will vary from 0.3 to unity, but the average is very near to 0.6 [109]. If a higher degree of accuracy is required, the index 0.6 in Eq. (2.14) should be replaced by N which could be obtained from the size exponent table in Ref. [107, 110].

The ratio and proportion estimation technique can be used for a quick and approximate capital cost estimation for some components. For example, the heat exchanger cost can be estimated from its heat transfer area A, which is a function of mass flowrate $\dot{m}$ and heat transfer unit NTU. Therefore, the heat exchanger cost increases with the mass flowrate $\dot{m}$ and heat transfer unit NTU (or heat exchanger effectiveness ε), which is an appropriate approximation of reality. However, for some other components, such as compressors and expanders, it is not appropriate to estimate their capital costs from the rated power P because the rated power P of any energy storage system is usually fixed at a given value. As a result, the compressor/expander cost will also be fixed according to the N exponent method, which leaves no room for optimization. In this case, more detailed estimate with higher level of accuracy should be employed, and the CGAM problem offers a good example for this type of estimation.

In 1990, a group of concerned specialists in the filed of thermo-economics decided to compared their methodologies by solving a predefined and simple problem of optimization:

the CGAM problem, which was named after the first initials of the participating investigators [106]. The objectives of the CGAM problem is to show how different thermo-economic methods and concepts are applied and unified, and it is still used as a standard test case for thermo-economic analysis and comparison today. In CGAM, the capital costs of air compressors and gas turbine increases with the mass flowrate $\dot{m}$, system pressure ratio p/p_0 and the isentropic efficiency of air compressor η_{AC} and gas turbine η_{GT}, which is a reasonable approximation of reality. The economic model has been validated with the cost data collected from Gas Turbine World, with an estimation error within $\pm 20\%$. These cost equations was further developed by Traverso and Massardo [111], and integrated into their thermoeconomic analysis software called WIDGET-TEMP. The updated cost equations not only enjoys wider power range validity but also considers the effects of non-conventional fluids, such as gas and water/steam mixtures. More than 22 parameters are employed to improve accuracy and the estimation errors are reduced to within $\pm 15\%$. However, the accuracy of these cost equations highly depends on these 22 parameters, which are obtained through the data-fitting method. If large quantities of cost data are not available, or the type and scale of the compressors/expanders are not precisely known before the calculation, it will be difficult or inappropriate to use this type of definitive and detailed cost equations. Therefore, it can be noted that there is a tradeoff between the accuracy and complexity of the economic model, and it is critical to choose the right level of accuracy.

In 2010, Galanti and Massardo [112] adapted the cost equations of CGAM to the micro gas turbine field. Since there is only small amount of data available in the literature to validate the cost equations, the established cost equations are much simpler than the ones for large-scale gas turbines. However, they still take into account of the effect of non-conventional fluids and extend its validity range by replacing the isentropic efficiency with the polytropic one. Furthermore, there is only one coefficient in each cost equation that requires adjustment and therefore, the uncertainty caused by cost equations can be easily estimated. Finally, the cost equations are more compatible with the thermodynamic model in this thesis and as a result, the forms of their equations are adopted for the economic model in Chapter 4 but the coefficients are adjusted to align with the data collected from Refs. [4, 111].

The cost equations for TES and cavern are absent from the CGAM problem but they are both very important components for A-CAES. Therefore, a more definitive and detailed cost estimates based on the summation of each part are employed. As suggested by Refs. [42, 44], the TES costs are made up of three main components: storage materiel costs (i.e., liquid or solid), insulation costs and containment vessel (or tank) costs. The storage material cost data can be obtained from the literature [11, 13], the websites (or reports) of commercial companies [12] and even commercial software such as CES EduPack Materials Selector [113]. As shown

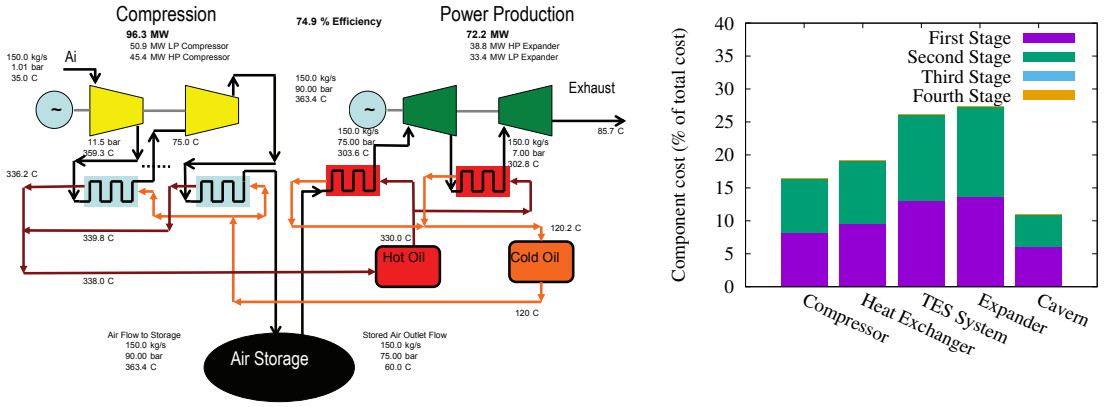

(a) Schematic diagram (b) Cost distribution

Figure 2.12: Schematic diagram and cost distribution of the A-CAES design option in Ref. [4]: (a) Schematic diagram (b) Cost distribution

by Ref. [4]., the cost of a solution-mined cavern can be divided into the well cost and the solution-mining cost, and the proportion of these two parts as well as other details of solution-mined caverns can be obtained from the reports by the commercial companies or governments.

Although cost equations obtained from linear regression are occasionally used in the literature, they are not employed in this thesis. All cost equations are adjusted through a test case proposed in Ref. [4]. The cost distribution and schematic diagram of this conceptual A-CAES are shown in Fig. 2.12. The cost data provided in Ref. [4] are estimated by experts based on the case of McIntosh Plant.

Finally, all capital costs which are not based on the present value of dollars must be adjusted to the current price through the following equations [107]:

$$C = C_0 \left(\frac{I}{I_0} \right) \tag{2.15}$$

where C and I are the current cost and index respectively; whilst C_0 and I_0 are the base cost and index respectively. More information on Chemical Engineering Plant Cost Index (CEPCI) can be obtained from Refs [114, 115], whilst in this thesis, the Consumer Price Index (CPI) is used an instead since it is easily accessible on the Internet. In this thesis, all the costs have been adjusted to the current cost, which refers to the cost in 2018.

2.3.2 Multi-objective optimization

Although the thermo-economic analysis has been well established before the millennium, the application of genetic algorithms, especially the multi-objective genetic algorithms, in thermo-

economic optimization has been a relatively recent development dating back to 2002. Earlier thermo-economic optimization attempts include the work by Massardo in 2000 [116], where the tradeoff between efficiency, specific work and cost are revealed through parametric study with respective to each input parameters. Toffolo and Lazzaretto [117] were among the first to introduce multi-objective genetic algorithm for thermo-economic optimization. In their study, the CGAM problem was simultaneously optimized for exergetic efficiency and total cost rate. Their study was later extended to incorporate an environmental objective [118]. Researchers have went on to apply the multi-objective approach to other types of thermal energy systems, such as combined cycle power systems [119], and components, like heat pumps and heat recovery steam generators. The rapid developments in multi-objective genetic algorithms during that period also facilitate its application in thermo-economic optimization [45, 120].

2.3.3 Application in EES systems

The application of genetic algorithm-type optimization technique to energy storage systems has been relatively limited to date. Among the few studies, Borghi et al. [121] optimized a high temperature superconducting magnetic energy storage device based on the amount of conductor and the device volume. An evolution strategy minimization algorithm was applied for two different optimization methods. Morandin et al. [64] applied a multi-objective genetic algorithm optimization to the design of a thermo-electric energy storage system, where investment costs were minimized and round-trip efficiency maximized. Cheung et al. [30] carried out multi-objective optimization on an Underwater Compressed Air Energy Storage (UWCAES) and provided high-level details for system performance, energy losses and costs, as well as the balance between them.

Other studies on the thermo-economic optimization of energy storage systems originated at the University of Cambridge, and has focused on the optimization of Brayton-cycle PTES. McTigue et al. [43] first integrated the packed bed model with compression/expansion devices that were modelled by polytropic efficiency η, pressure loss factor f_p and heat leakage factors α_{leak}. Both parametric study and multi-objective optimization were carried out and the importance of utilization factor Π in controlling the tradeoff between efficiency and energy density was revealed: high utilization factor Π leads to high energy density but low efficiencies. Their work was later extended to the thermo-economic optimization of Brayton PTES, with the objectives of maximizing the system efficiency χ whilst minimizing the unit storage cost C simultaneously [44]. The authors then went on to apply the multi-objective optimization to the segmented axial thermal reservoir and radial thermal reservoirs, and the difference in their Pareto fronts (or trade-off surfaces) are revealed and analyzed [42, 62].

More recently, parametric and optimization study have been conducted for the solid, liquid and hybrid A-CAES systems and the results suggest that the hybrid A-CAES has thermodynamic and economic advantages over the other two [52]. The trade off between efficiency and cost and the factors affecting this trade off are also investigated. Mineral oil was found to be the best thermal fluid for liquid TES due to its relatively high allowable temperature and low unit cost.

Chapter 3

A simplified preliminary comparison of CAES and PTES

3.1 Introduction

The available energy (exergy) of a simple compressible system can be divided into the temperature and pressure related contributions, as mentioned in Chapter 2 and Refs. [17, 122]. For any thermo-mechanical energy storage system, its available energy is either stored in the form of temperature potential or pressure potential between the system and the environment. Therefore, Compressed Air Energy Storage (CAES) and Pumped Thermal Energy Storage (PTES) can be viewed as two representatives of all thermo-mechanical energy storage systems because they respectively store electricity in the forms of pressure and temperature potential. Other types of thermo-mechanical energy storage systems, such as Isothermal CAES (I-CAES) and Liquid Air Energy Storage (LAES), can be considered as variants of CAES and PTES respectively. Recently, both CAES and PTES have received a lot of attention from industry and academia. However, a comparative study of these two representatives has so far been lacking, and this forms the major part of this chapter.

In this chapter, a simple analytical model has been built for both the CAES and PTES systems. The A-CAES with an isobaric air reservoir and Brayton-cycle PTES without preheating, precooling and recuperating have been chosen as the baseline systems. The expressions of system efficiency, energy distribution and energy density have been derived for these systems, and their sensitivities to various loss parameters have been analyzed individually. After that, case studies and comparisons of the Baseline A-CAES and PTES with more realistic parameters have been conducted. The loss distribution and parametric study are also provided, in the hope of achieving a better understanding of the advantages and disadvantages of each system and

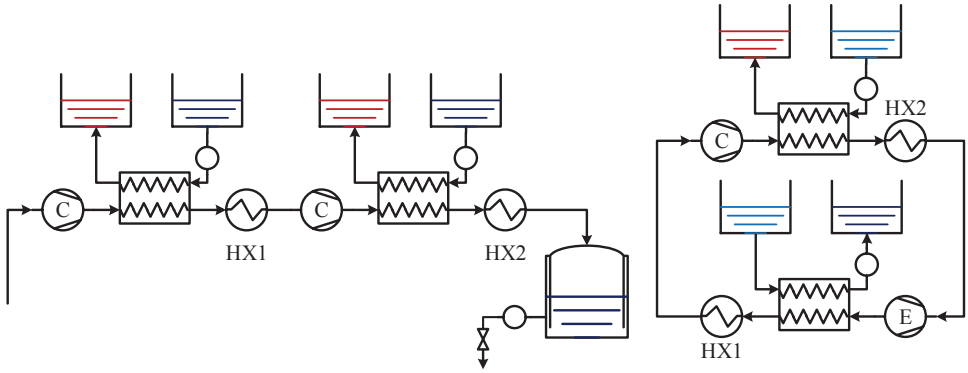

(a) A-CAES ($N = 2$) (b) PTES

Figure 3.1: Schematic diagrams of the A-CAES and PTES: (a) A-CAES ($N = 2$) (b) PTES

laying foundations for more detailed analysis in Chapter 4 and Chapter 5.

3.2 Cycle layouts and component modelling

The schematic diagram of an A-CAES system is shown in Fig. 3.1a. It can be noted from Fig. 3.1a that there are two stages ($N = 2$) in this system, with each having the same pressure ratio β. The cavern is assumed isobaric for the baseline A-CAES to make it more comparable with the baseline PTES where there is no pressure variation. Isobaric air reservoirs can be realized in the forms of underwater air accumulators or an underground cavern with an above-ground water equalizing pit, which will be discussed in Chapter 5. Therefore, the pressure ratio of each stage β is:

$$\beta = \left(\frac{p}{p_0}\right)^{\frac{1}{N}} \tag{3.1}$$

In each stage, air at ambient temperature T_0 is first compressed with a pressure ratio of β_c during charge. Then it stores its thermal energy in the Thermal Energy Storage (TES) through a heat exchanger. Finally, the compressed air with low temperature flows through an auxiliary heat exchanger to further reduce its temperature to ambient so as to prevent the inlet temperature of next stages becoming too high. Since the waste heat is not recycled but simply dissipated in the auxiliary heat exchangers, a high water flow rate (hence a low heat capacity ratio C_r) is usually adopted and the outlet temperature of air is almost T_0. Therefore, the analytical expression of the system efficiency of A-CAES with N stages can be easily derived. In order to study the impact of pressure loss (for example, those generated by heat exchangers and along the pipes) in a simple and general manner, a loss factor of f_p is assumed for each

stage. Therefore, the actual compression ratio of each compressor is $\beta_c = \beta_i/(1-f_p)$, whilst the expansion ratio of each expander is $\beta_e = \beta_i(1-f_p)$.

The schematic diagram of a baseline PTES system is shown in Fig. 3.1b. This PTES system consists of two compressors/expanders, two TES systems and two auxiliary heat exchangers. It is the simplest layout of a typical PTES system. During charge, the working fluid at ambient pressure p_0 and temperature T_0 is first compressed by a compressor, then it flows into the main heat exchanger to store its thermal energy in a hot TES. Afterwards, it is further cooled to ambient temperature T_0 by an auxiliary heat exchanger (HX2 in Fig. 3.1b) before flowing into an expander. After expansion, the working fluid at ambient pressure p_0 but much lower temperature stores its thermal energy in a cold TES and then heated back to ambient temperature T_0 by an auxiliary heat exchanger (HX1 in Fig. 3.1b) for the next cycle. Air is chosen as the working fluid here for better comparison with the A-CAES. In reality, PTES can use different gases (e.g., argon and ammonia) as the working fluids and the whole system can be pressurized to reduce the cost. This is because unlike A-CAES, the PTES employed a closed thermodynamic cycle for energy conversion. However, for a simple analytical comparison here, the same working fluids and operating parameters are chosen, and the study on the impacts of different working fluids and system pressurization will be postponed to Chapter 8. During discharge, the above process is reversed and the stored thermal energy is converted back into electricity.

In the baseline PTES, the inlet pressures of the compressor are p_0 and p respectively, so that the system pressure ratio is also p/p_0. The inlet temperatures of the compressor are fixed at ambient T_0 during charge, as shown by the T_1 and T_3 in Fig. 3.2b; whilst the inlet temperature of hot and cold TES is fixed at T_0 during discharge. This PTES is chosen as the baseline because it enjoys more design freedom (e.g., its discharging and charging temperature ratio are independent), simplicity and close relevance to other PTES variants.

3.2.1 Modelling of compressors and expanders

The simplest method of modelling compressors and expanders is by using an isentropic efficiency. However, isentropic efficiency is always associated with a pressure ratio, therefore, it is erroneous to equate two systems with the same isentropic efficiency but different pressure ratios. The polytropic efficiency, also known as the infinitesimal stage efficiency, is independent of the pressure ratio and thus a better solution for this comparison. Furthermore, the effects of heat leakage and irreversibility can be distinguished by combining a heat leakage factor (defined as the ratio between the instantaneous heat transfer and work transfer $\alpha_{leak} = \delta q/\delta w$) with a polytropic efficiency (defined as $\eta_c = -v\mathrm{d}p/\delta w$ for compression or $\eta_e = -\delta w/v\mathrm{d}p$ for expansion), as shown in Ref. [80]. Then the outlet temperature and specific work of

compressor can be calculated by:

$$T_{\text{out}} = T_{\text{in}} \beta_{\text{c}}^{\phi_{\text{c}}} \tag{3.2}$$

$$w_{\text{c}} = \frac{c_p T_{\text{in}}}{1-\alpha_{\text{c}}} \left(\beta_{\text{c}}^{\phi_{\text{c}}} - 1 \right) \tag{3.3}$$

where c_p is the heat capacity of the air, the subscripts in and out denote the inlet and outlet of the compressor respectively, ϕ_{c} is the polytropic exponent, given by $\phi_{\text{c}} = \frac{\gamma-1}{\gamma} \frac{1-\alpha_{\text{c}}}{\eta_{\text{c}}}$. Equivalent expressions to Eqs. (3.2) and (3.3) can be derived for the expansion process, with η_{c} replaced by η_{e}^{-1} and α_{c} by α_{e}. The heat leakage factor α_{leak} is usually negligible for the turbomachinery due to its high rotational speed but can become important for reciprocating devices.

3.2.2 Modelling of heat exchangers and TES systems

For liquid TES, heat is transferred between the working fluid and the thermal fluid via the main heat exchanger. To minimize the losses associated with irreversible heat transfer, a counter flow heat exchanger with $C_r = 1$ (i.e., balanced flow) is employed and the well-established $\varepsilon - \text{NTU}$ method is used for the simulation. The heat exchanger effectiveness $\varepsilon = |T_{\text{in}} - T_{\text{out}}| / \left(T_{\text{in,hot}} - T_{\text{in,cold}} \right)$ is then the only parameter needed to evaluate thermal performance and heat exchanger outlet temperatures are given by:

$$\begin{pmatrix} T_{\text{out,a}} \\ T_{\text{out,f}} \end{pmatrix} = \begin{pmatrix} 1-\varepsilon & \varepsilon \\ \varepsilon & 1-\varepsilon \end{pmatrix} \begin{pmatrix} T_{\text{in,a}} \\ T_{\text{in,f}} \end{pmatrix} \tag{3.4}$$

where the subscripts a and f denote air and (storage) fluid respectively.

In order to quantitatively analyze the effect of heat leakage of the thermal fluid tanks, an insulation factor κ is introduced in this chapter, which is defined as the ratio of the internal energy of the thermal fluids E'_{tank} after storage to E_{tank} before storage. After some simplification, the temperature of the thermal tank after the storage process can be derived, which is:

$$T'_{\text{tank}} = \kappa T_{\text{tank}} + (1-\kappa) T_0 \tag{3.5}$$

From the above equation, it can be noted that if $\kappa = 1$, then $T'_{\text{tank}} = T_{\text{tank}}$, the storage tanks are ideally insulated, without any heat leakage; however, if $\kappa = 0$, then $T'_{\text{tank}} = T_0$, the storage tanks are not insulated at all, unable to store any thermal energy.

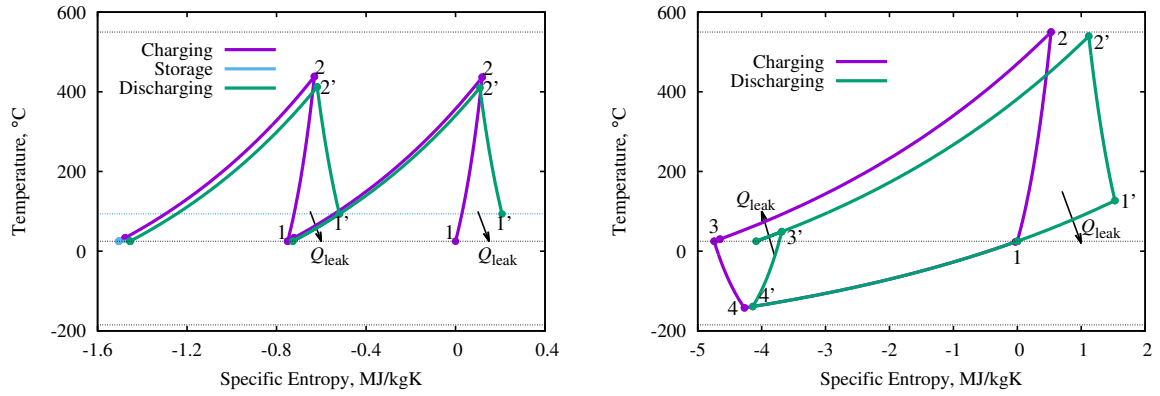

(a) A-CAES (b) PTES

Figure 3.2: T-s diagrams of the A-CAES and PTES: (a) A-CAES (b) PTES

3.3 Simplified analytical models of the CAES and PTES

In order to compare the baseline A-CAES and PTES analytically, the expressions of system efficiency χ, stored available energy B and energy density D will be derived in this section and used to support the results of numerical model in the following parts.

3.3.1 Thermodynamic model of the A-CAES

The T-s diagram of the baseline A-CAES is shown in Fig. 3.2a. Due to its isobaric cavern, the thermodynamics of baseline A-CAES is simple because the pressure (or temperature) ratio of each stage does not change during operation, therefore, the specific work consumed (or generated) of each stage and the temperature of the hot thermal fluid tank are also constant as a result. If we assume the maximum and minimum volume of the isobaric cavern are V and 0 respectively, then the mass of compressed air stored in the cavern is:

$$m = \frac{p_{\max} V}{R_g T_0} \tag{3.6}$$

Based on the analysis of compressors/expanders in Section 3.2, the specific work consumed during charge can be calculated by:

$$w_c = N \frac{c_p T_0}{1-\alpha_c} \left(\beta_c^{\phi_c} - 1 \right) \tag{3.7}$$

During discharge, the thermal energy stored in the hot TES is used to preheat the compressed air, and the inlet temperature of the expander can be can be calculated from Eqs. (3.4)

and (3.5):

$$T'_{\mathrm{e,in}} = \kappa\varepsilon T_0 \beta_{\mathrm{c}}^{\phi_{\mathrm{c}}} + \left(1 - \kappa\varepsilon^2\right) T_0 \tag{3.8}$$

and the specific expansion work generated during discharge can be calculated by:

$$w'_{\mathrm{e}} = N \frac{c_p T'_{\mathrm{e,in}}}{1 - \alpha'_{\mathrm{e}}} \left(1 - \beta_{\mathrm{e}}^{-\phi'_{\mathrm{e}}}\right) \tag{3.9}$$

Therefore, the system efficiency of baseline A-CAES system could be expressed as:

$$\chi_{\mathrm{CAES}} = \frac{w'_{\mathrm{e}}}{w_{\mathrm{c}}} = \frac{1 - \alpha_{\mathrm{c}}}{1 - \alpha'_{\mathrm{e}}} \frac{T'_{\mathrm{e,in}}}{T_0} \frac{1 - \beta_{\mathrm{e}}^{-\phi'_{\mathrm{e}}}}{\beta_{\mathrm{c}}^{\phi_{\mathrm{c}}} - 1} \tag{3.10}$$

The exergy of A-CAES is stored in both the hot TES and the cavern, therefore, it is necessary to find out the energy density of each component and the whole system. The energy density is defined as the ratio between the stored exergy and the volume of the component. Therefore, for an isobaric cavern with volume V and pressure ratio p/p_0, its stored exergy and the exergy density are respectively:

$$B_{\mathrm{air}} = pV \ln \frac{p}{p_0} \tag{3.11}$$

$$D_{\mathrm{air}} = p \ln \frac{p}{p_0} \tag{3.12}$$

By comparing Eq. (3.12) with Eq. (2.3) in Chapter 2, it can be noted that the extra exergy $(p - p_0)V$ stored in the volume V is actually the flow work of compressed air, which is provided by a water column of height ΔH, as shown in Eq. (2.2). Therefore, the total stored exergy of an isobaric cavern, as shown in Eq. (3.11), is actually provided by both the compressed air of volume V and the water pit of volume V, and the energy density of an isobaric air reservoir should be:

$$D_{\mathrm{cavern}} = \frac{p}{2} \ln \frac{p}{p_0} \tag{3.13}$$

However, since the water pit is above ground and relatively cheap compared to the cavern, the water volume is ignored and Eq. (3.12) is used as the air reservoir density instead. This treatment is particularly reasonable for Underwater CAES (UW-CAES), where the water is provided by the ocean for free. In fact, due to the technical immaturity of system shown in Fig. 2.7b, it is mainly the UW-CAES that is considered for the isobaric CAES in this thesis.

It should be noticed in Eqs. (3.11) and (3.12) that isobaric cavern is always isothermal and kept at ambient temperature T_0. For the hot TES, since there are N stages in the baseline A-CAES, the total stored exergy and the exergy density of each TES can be calculated by:

$$B_{\mathrm{TES}} = N m_{\mathrm{TES}} c_{\mathrm{TES}} T_0 \left(\beta^{\phi} - 1 - \phi \ln \beta\right) \tag{3.14}$$

$$D_{\mathrm{TES}} = \rho_{\mathrm{TES}} c_{\mathrm{TES}} T_0 \left(\beta^{\phi} - 1 - \phi \ln \beta\right) \tag{3.15}$$

3.3.2 Thermodynamic model of the PTES

The T-s diagram of the baseline PTES system is shown in Fig. 3.2b. From Fig. 3.2b and the analysis in Section 3.2, it can be found that the charging and discharging processes of PTES are more complicated than the CAES, with each process including a compression, an expansion and two heat exchange process. For the baseline PTES, the inlet temperatures of both compressor and expander are assumed to be fixed at T_0 during charge, as discussed in Section 3.2, then the consumed compression work and generated expansion work during charge can be calculated by the following equations:

$$w_{\mathrm{c}} = N \frac{c_p T_0}{1 - \alpha_{\mathrm{c}}} \left(\beta_{\mathrm{c}}^{\phi_{\mathrm{c}}} - 1\right) \tag{3.16}$$

$$w_{\mathrm{e}} = N \frac{c_p T_0}{1 - \alpha_{\mathrm{e}}} \left(1 - \beta_{\mathrm{e}}^{-\phi_{\mathrm{e}}}\right) \tag{3.17}$$

After compression (or expansion), the heated (or cooled) working fluid will store its thermal exergy into the hot TES (or cold TES) which is placed after the compressor (or expander). During discharge, the stored thermal exergy of the hot (or cold) TES will be used to preheat (or precool) the working fluid before expansion (or compression). According to Eqs. (3.4) and (3.5), the inlet temperatures of compressor and expander during discharge are respectively:

$$T'_{\mathrm{c,in}} = \kappa \varepsilon^2 T_0 \beta_{\mathrm{c}}^{\phi_{\mathrm{c}}} + \left(1 - \kappa \varepsilon^2\right) T_0 \tag{3.18}$$

$$T'_{\mathrm{e,in}} = \kappa \varepsilon^2 T_0 \beta_{\mathrm{e}}^{-\phi_{\mathrm{e}}} + \left(1 - \kappa \varepsilon^2\right) T_0 \tag{3.19}$$

and accordingly, the generated expansion work and consumed compression work during discharge can be calculated by:

$$w'_{\mathrm{e}} = \frac{c_p T'_{\mathrm{e,in}}}{1 - \alpha'_{\mathrm{e}}} \left(1 - \beta_{\mathrm{e}}^{-\phi'_{\mathrm{e}}}\right) \tag{3.20}$$

$$w'_{\mathrm{c}} = \frac{c_p T'_{\mathrm{c,in}}}{1-\alpha'_{\mathrm{c}}} \left(\beta_{\mathrm{c}}^{\phi'_{\mathrm{c}}} - 1\right) \tag{3.21}$$

Therefore, the system efficiency of the PTES system can be expressed as:

$$\chi_{\mathrm{PTES}} = \frac{w'_{\mathrm{e}} - w'_{\mathrm{c}}}{w_{\mathrm{c}} - w_{\mathrm{e}}} = \frac{1-\alpha}{1-\alpha'} \left(\kappa\varepsilon^2 - 1 + \kappa\varepsilon^2 \frac{\beta_{\mathrm{c}}^{\phi_{\mathrm{c}}} + \beta_{\mathrm{e}}^{-\phi_{\mathrm{e}}} - \beta_{\mathrm{c}}^{\phi'_{\mathrm{c}}} \beta_{\mathrm{e}}^{-\phi_{\mathrm{e}}} - \beta_{\mathrm{c}}^{\phi_{\mathrm{c}}} \beta_{\mathrm{e}}^{-\phi'_{\mathrm{e}}}}{\beta_{\mathrm{c}}^{\phi_{\mathrm{c}}} + \beta_{\mathrm{e}}^{-\phi_{\mathrm{e}}} - 2} \right) \tag{3.22}$$

where the heat leakage factors of the compressor and expander are assumed to be the same for both the charge and the discharge process: $\alpha_{\mathrm{c}} = \alpha_{\mathrm{e}} = \alpha$ and $\alpha'_{\mathrm{c}} = \alpha'_{\mathrm{e}} = \alpha'$. Besides, it can be further assumed that $\alpha' = -\alpha$ since the directions of the heat transfer and the work transfer are the same during discharge.

The exergy of baseline PTES is also stored in two components, namely the hot and cold TES. The stored exergy B_{hot} and energy density D_{hot} of the hot TES are the same as Eqs. (3.14) and (3.15), whereas the number of stages N is 1. For the cold TES, the expressions of B_{cold} and D_{cold} are also similar with Eqs. (3.14) and (3.15), with the pressure ratio β replaced by β^{-1}.

3.4 Results and discussion

In this section, the sensitivity of system efficiency χ to each of the various loss parameters will be considered in the ideal limit. The ideal limit means the whole system is reversible and free from any loss, which equals $f = 0$ (no friction loss), $\alpha_{\mathrm{leak}} = 0$ (no heat leakage loss), $\eta = 1$ (no aerodynamic loss), $\varepsilon = 1$ (no heat transfer loss) and $\kappa = 1$ (no storage loss) in this chapter. The sensitivity analyses for baseline PTES with solid and liquid TES have been carried out by White [18] and Farres-Antunez [47] respectively. However, similar analysis for A-CAES and the comparison of the two systems are still absent, which will become the major parts of this section. In addition, the variation of energy distribution and energy density with system pressure will also be provided at the end of this section.

3.4.1 Heat transfer effects

In order to analyze the effects of the TES on the system performance, both the losses of the compressor/expander and the friction loss are neglected in this section. In other words, $f = 0$, $\alpha = 0$, and $\eta = 1$ are assumed for the compressor/expander, then the system efficiencies of

the CAES and PTES could be simplified to:

$$\chi_{\mathrm{CAES}} = \tau^{-1} + \kappa\varepsilon^2\left(1-\tau^{-1}\right) \tag{3.23}$$

$$\chi_{\mathrm{PTES}} = 2\kappa\varepsilon^2 - 1 \tag{3.24}$$

where τ is the isentropic temperature ratio, which is given by: $\tau = \beta^{(\gamma-1)/\gamma}$.

From Eqs. (3.24), it can be noted that if the heat exchanger effectiveness ε falls below ~70 %, then the system efficiency of the PTES will drop below 0 %, whilst for the CAES, even if the TES is completely removed (ε = 0 in Eqs. (3.23)), the system efficiency is still:

$$\chi_{\mathrm{CAES}}|_{\kappa,\mathrm{Cr\,or}\,\varepsilon=0} = \tau^{-1} \tag{3.25}$$

From the above results, it can be noted that the heat exchanger effectiveness ε and the TES insulation factor κ are far more important to the PTES than to the CAES. For CAES, a satisfactory system efficiency (e.g., $\chi = 82\,\%$ at $\tau = 1.22$ or $\beta = 2$) is still achievable even without the TES, whilst for the PTES, heat exchangers of 70 % effectiveness will render the whole system useless. This is because all the available energy is stored in the TES for the PTES, whilst for the CAES, only a small portion is stored in the TES.

If we then analyze the sensitivity of the system efficiency χ of the PTES and CAES to the heat exchanger effectiveness ε on condition that all losses are zero, then the following expressions will be obtained:

$$\left.\frac{\partial\chi}{\partial\varepsilon}\right|_{\mathrm{CAES}} = 2\kappa\varepsilon\left(1-\tau^{-1}\right) = 2\left(1-\tau^{-1}\right) \tag{3.26}$$

$$\left.\frac{\partial\chi}{\partial\varepsilon}\right|_{\mathrm{PTES}} = 4\kappa\varepsilon = 4 \tag{3.27}$$

From the above results, it can be noted that the sensitivity of the PTES system efficiency χ to the heat exchanger effectiveness ε is more than twice that of the CAES system. That is:

$$\left.\frac{\partial\chi}{\partial\varepsilon}\right|_{\mathrm{PTES}} > 2\left.\frac{\partial\chi}{\partial\varepsilon}\right|_{\mathrm{CAES}} \tag{3.28}$$

Fig. 3.3a illustrates the relative sensitivity of the roundtrip efficiency χ of CAES and PTES to the heat exchanger effectiveness ε on conditions that all the losses are zero. In Fig. 3.3a, the solid line denotes the analytical solution from Section 3.3, and the discrete dots denote the numerical solution which will be used for more detailed analysis later. It can be noted that the analytical solution matches very well with the numerical ones, which lends credibility to both

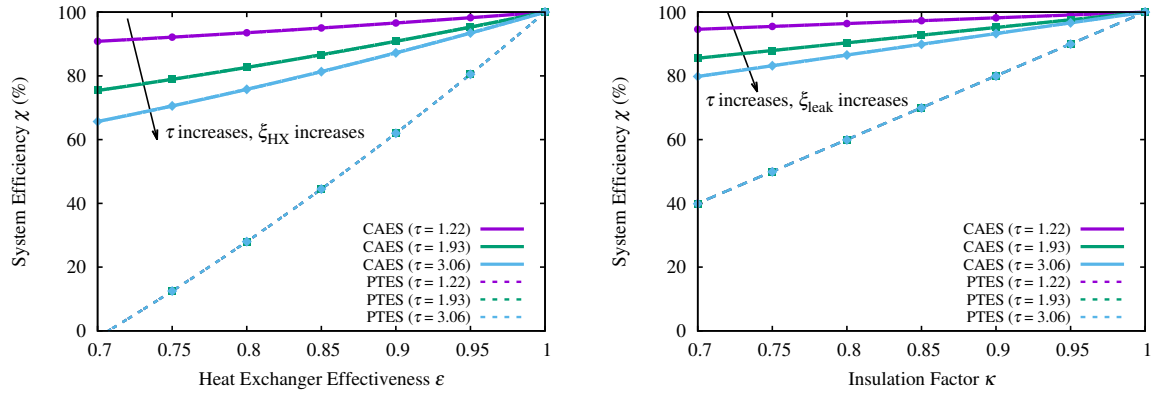

(a) Heat exchanger effectiveness ε

(b) Insulation factor κ

Figure 3.3: Sensitivity of the system efficiencies to the parameters of TES: (a) Heat exchanger effectiveness ε (b) Insulation factor κ

of the results. From Fig. 3.3a, it can be clearly seen that the sensitivity of the PTES system efficiency to the heat exchanger effectiveness ε is always more than twice that of the CAES, which verifies the conclusion of Eqs. (3.28). In addition, it can be seen from Fig. 3.3a that the sensitivity of CAES system efficiency increases with the temperature ratio τ, from 0 when τ is one to 2 when τ approaches infinity, whilst for PTES system, the sensitivity of system efficiency to heat exchanger effectiveness ε is independent of τ and always 4 for the ideal case.

From Eqs. (3.23) and Eqs. (3.24), it can be noted that κ and ε have different effects on χ, therefore, the effect of κ will be analyzed in detail. Similar to the above analysis, all the losses are assumed zero to analyze the sensitivity of the system efficiency χ to the TES insulation factor κ, then the following expressions could be obtained:

$$\left.\frac{\partial \chi}{\partial \kappa}\right|_{\text{CAES}} = \varepsilon^2 \left(1-\tau^{-1}\right) = 1-\tau^{-1} \tag{3.29}$$

$$\left.\frac{\partial \chi}{\partial \kappa}\right|_{\text{PTES}} = 2\varepsilon^2 = 2 \tag{3.30}$$

From the above results, it can be noted that the sensitivity of the PTES system efficiency χ to the heat leakage factor κ is more than twice that of the CAES system.

$$\left.\frac{\partial \chi}{\partial \kappa}\right|_{\text{PTES}} > 2\left.\frac{\partial \chi}{\partial \kappa}\right|_{\text{CAES}} \tag{3.31}$$

Besides, it can be found that for both energy storage systems, the sensitivity of the system efficiency χ to the heat exchanger effectiveness ε is always twice the sensitivity to the heat

leakage factor κ.

$$\left.\frac{\partial \chi}{\partial \varepsilon}\right|_{\mathrm{ES}} = 2 \left.\frac{\partial \chi}{\partial \kappa}\right|_{\mathrm{ES}} \tag{3.32}$$

Fig. 3.3b compares Eqs. (3.29) and (3.30) graphically, from which it can be noted that the sensitivity of the CAES system efficiency χ to the heat leakage factor κ increases with the temperature ratio τ, from 0 when τ is one to 1 when τ approaches infinity, whilst for the PTES, the sensitivity of system efficiency χ is always 2 in the ideal limit. Therefore, it can be concluded that the PTES is twice more sensitive to κ than the CAES, which verifies the conclusion of Eqs. (3.31), and for the CAES whose efficiency χ is dominated by the heat transfer losses, it is always beneficial to reduce the temperature ratio τ to increase the system efficiency.

3.4.2 Compressor / expander effects

In the ideal limit, the sensitivity of round-trip efficiency χ to compression and expansion efficiency η is:

$$\left.\frac{\partial \chi}{\partial \eta}\right|_{\mathrm{CAES}} = \frac{2\ln\tau}{\tau - 1} \tag{3.33}$$

$$\left.\frac{\partial \chi}{\partial \eta}\right|_{\mathrm{PTES}} = \frac{4\ln\tau}{\tau + \tau^{-1} - 2} \tag{3.34}$$

From the above results, it can be noted that the partial derivative of the PTES system efficiency with respect to the polytropic efficiency η is twice more larger than that of the CAES, which is:

$$\left.\frac{\partial \chi}{\partial \eta}\right|_{\mathrm{PTES}} > 2 \left.\frac{\partial \chi}{\partial \eta}\right|_{\mathrm{CAES}} \tag{3.35}$$

Fig. 3.4a shows the relative sensitivity of the system efficiencies χ of the CAES and PTES to the polytropic efficiency η on conditions that all the losses are zero. It can be noted that both of the two partial derivatives decrease with the temperature ratio τ, from 2 to 0 for the CAES and from infinity to 2 for the PTES system as τ increases from 1 to infinity. Therefore, for both CAES and PTES whose system efficiency χ is mainly dominated by the polytropic efficiency η, it's always beneficial to increase the temperature ratio τ. However, it should be noted that the PTES is much more sensitive to the polytropic efficiency η than the CAES when the temperature ratio τ is low, which explains why the CAES is usually operated in stages whilst the PTES is not.

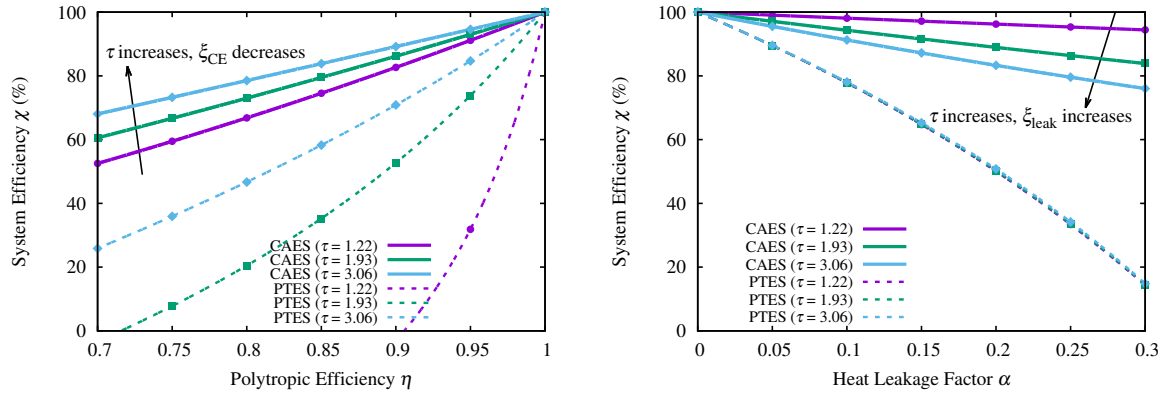

(a) Polytropic efficiency η (b) Heat leakage factor α

Figure 3.4: Sensitivity of the system efficiencies to the parameters of compressor/expander: (a) Polytropic efficiency η (b) Heat leakage factor α

Then if we calculate the partial derivatives of the system efficiency χ with respect to the heat leakage factor α_{leak} for both CAES and PTES on condition that the polytropic efficiency η of the compressor/expander is one, then the following expressions will be obtained:

$$\left.\frac{\partial \chi}{\partial \alpha}\right|_{\text{CAES}} = -2 + \frac{2\ln\tau}{\tau - 1} \tag{3.36}$$

$$\left.\frac{\partial \chi}{\partial \alpha}\right|_{\text{PTES}} = -2 \tag{3.37}$$

From the above results, it can be noted that the partial derivative of the PTES system efficiency χ with respect to heat leakage factor α is larger than that of the CAES, which means:

$$\left.\frac{\partial \chi}{\partial \alpha}\right|_{\text{PTES}} > \left.\frac{\partial \chi}{\partial \alpha}\right|_{\text{CAES}} \tag{3.38}$$

Fig. 3.4b illustrates the relative sensitivity of the system efficiency of CAES and PTES to the heat leakage factor α on conditions that all the losses are zero. From Fig. 3.4b, it can be noted that the partial derivative of the CAES system efficiency with respect to the heat leakage factor α decreases with the temperature ratio, from 0 when τ is 1 to -2 when τ approaches infinity, whilst for the PTES, this derivative is almost constant and equal to -2 when α is low. Therefore, it can be concluded that for the CAES it's beneficial to reduce the temperature ratio τ to reduce the heat leakage losses, whilst for the PTES system there is no such benefits. It can also be noted from Fig. 3.4b that the partial derivative of the PTES system efficiency increases with the heat leakage factor α increasing, which is different from both the heat

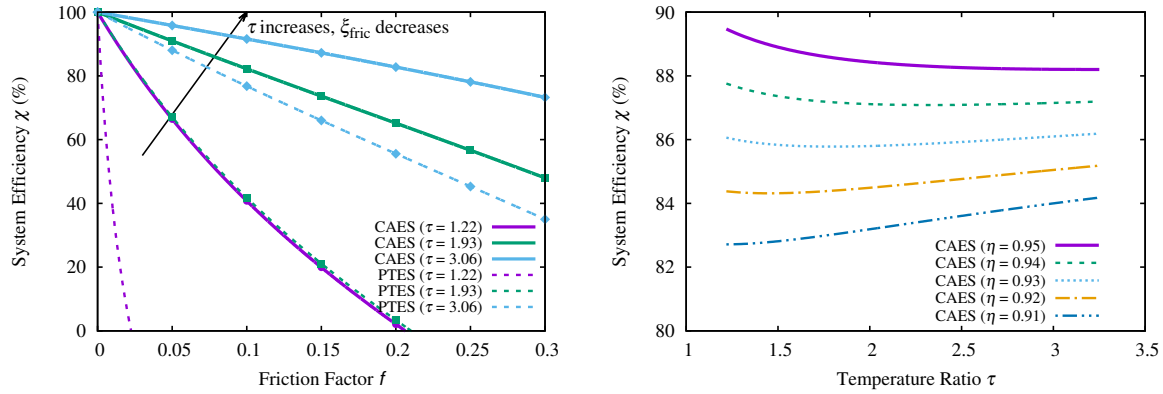

(a) Friction factor f_p

(b) Temperature ratio τ (where $\varepsilon = 0.95$)

Figure 3.5: Sensitivity of the system efficiencies to the system parameters: (a) Friction factor f_p (b) Temperature ratio τ (where $\varepsilon = 0.95$)

exchanger effectiveness ε and the insulation factor κ.

3.4.3 Pressure loss effects

In the ideal limit, the sensitivity of round-trip efficiency χ to pressure loss factor f_p is:

$$\left.\frac{\partial \chi}{\partial f}\right|_{\text{CAES}} = -\frac{2k}{\tau - 1} \tag{3.39}$$

$$\left.\frac{\partial \chi}{\partial f}\right|_{\text{PTES}} = -\frac{4k}{\tau + \tau^{-1} - 2} \tag{3.40}$$

From the above results, it can be noted that the PTES efficiency is twice more sensitive to the pressure loss factor f_p than the CAES efficiency, which is given by:

$$\left.\frac{\partial \chi}{\partial f}\right|_{\text{PTES}} > 2 \left.\frac{\partial \chi}{\partial f}\right|_{\text{CAES}} \tag{3.41}$$

Fig. 3.5a shows the relative sensitivity of the system efficiencies χ of the CAES and PTES to the pressure loss factor f_p on conditions that all the other losses are zero. From Fig. 3.5a, it can be clearly seen that the sensitivity of the PTES system efficiency χ to the pressure loss factor f_p is more than twice that of the CAES, which verifies the conclusion of Eqs. (3.41). In addition, it can also be seen from Fig. 3.5a that both of the two partial derivatives of the system efficiency increase with the temperature ratio τ and both from minus infinity when τ is 1 to 0 when τ approaches infinity. Therefore, for both CAES and PTES whose system efficiency are dominated by the friction loss, it's always beneficial to increase the temperature ratio τ.

3.4.4 Temperature ratio effects

The effects of temperature ratio τ on the system efficiency χ depends largely on the loss distribution of the components. For example, if the system efficiency χ is dominated by the heat transfer (leakage) loss stemming from temperature heterogeneity (such as those caused by the heat exchanger effectiveness ε, insulation factor κ or heat leakage factor α), then it's always beneficial to reduce the temperature ratio for the CAES system, whilst for the PTES system it makes no difference, as shown in Fig. 3.3a, Fig. 3.3b and Fig. 3.4b. On the other hand, if the system efficiency is dominated by the mechanical loss stemming from the aerodynamic and flow friction effects (such as those caused by the polytropic efficiency η and the pressure loss factor f_p), then a high temperature ratio τ is always preferred for both CAES and PTES, as shown in Fig. 3.4a and Fig. 3.5a. It can also be noted from Fig. 3.4a that increasing the temperature ratio τ can have a much more significant effect on the PTES, therefore, it is always beneficial to increase the temperature ratio τ in order to increase system efficiency χ for PTES.

For the CAES system, whether to adopt a high pressure ratio or a low one depends on the tradeoff of the heat transfer loss and the mechanical loss. For better understanding of this tradeoff, the analytical expression of the heat exchanger loss and compressor/expander loss as a fraction of the compression work are shown in Eqs. (3.42) and (3.43) respectively.

$$\xi_{\mathrm{HX}} = \frac{\varepsilon\left(1-\varepsilon\right)\left(\tau+\tau^{-1}-2\right)}{\tau^{1/\eta}-1} \tag{3.42}$$

$$\xi_{\mathrm{CE}} = \frac{\left(\eta^{-1}-1\right)\ln\tau}{\tau^{1/\eta}-1} \tag{3.43}$$

from which it can be noted that the heat exchanger loss ξ_{HX} increases with the temperature ratio τ, whilst the compressor/expander loss ξ_{CE} decreases monotonically with it, which is in accord with the above discussions.

Fig. 3.5b illustrates the tradeoff of the heat transfer loss and the mechanical loss of the CAES system. The heat exchanger effectiveness ε is fixed at 0.95 whilst the polytropic efficiency increases from 0.91 to 0.95. It can be noted from Fig. 3.5b that as the polytropic efficiency increases from 0.91 to 0.95, the mechanical loss decreases, therefore, the CAES system gradually turns from a system dominated by the mechanical loss into one dominated by the heat transfer loss. As a result, the system efficiency firstly increases monotonically with the pressure ratio, but finally decreases monotonically with pressure ratio, whilst in the middle, it decreases at first, reaching a minimum, and then increases afterwards.

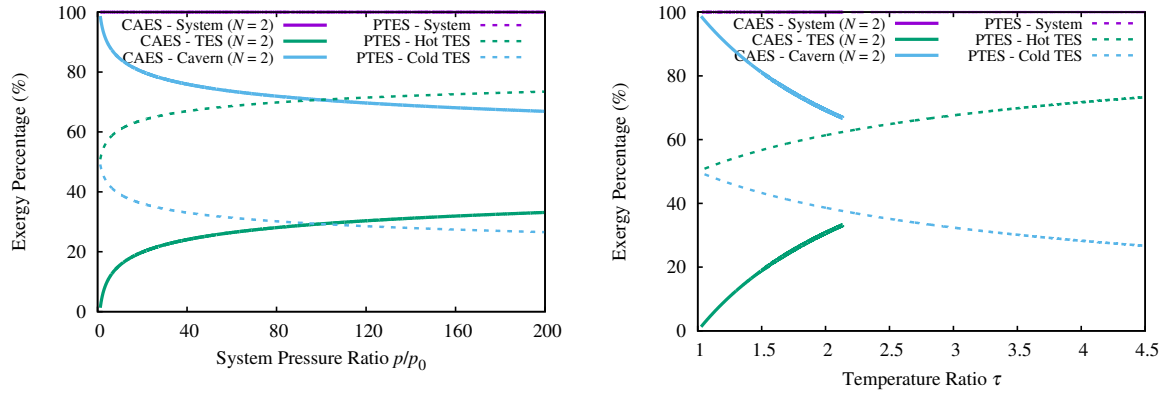

(a) system pressure ratio p/p_0 (b) temperature ratio τ

Figure 3.6: Exergy distribution of the CAES and PTES as functions of (a) system pressure ratio p/p_0 and (b) temperature ratio τ

3.4.5 Energy density

The expressions of stored available energy and energy density in each individual component have been derived in Section 3.3. From Eqs. (3.11) and (3.14), it can be noted that the stored available energy B_i all increase with the system pressure ratio p/p_0. However, it's still unknown how the distributions of the stored available energy B_i vary with the pressure ratio p/p_0. Therefore, the concept of stored exergy proportion P_i is proposed, which is defined by:

$$P_i = \frac{B_i}{\sum_{i=1}^{n} B_i} \tag{3.44}$$

where B_i refers to the available energy stored in component i, n refers to the number of types of components where the available energy is stored. For CAES, available energy is stored in two components ($n = 2$), namely the cavern and the TES (which includes N stages). After substituting Eqs. (3.11) and Eqs. (3.14) Into Eqs. (3.44), the exergy distributions of the CAES and PTES could be obtained and are shown in Fig. 3.6.

Fig. 3.6 illustrates the exergy distribution of the CAES and PTES as a function of temperature ratio τ (or system pressure ratio p/p_0). From Fig. 3.6, it can be clearly seen that as the temperature ratio τ increases, more exergy is stored in the hot TES for both CAES and PTES, whilst the sum of the exergy proportion P_i of each component are always 100 %. In other words, as the temperature ratio τ increases from 1 to infinity, the exergy proportion of the cavern decreases from 100 % to 0 % for the CAES; whilst the exergy proportion of the cold TES decreases from 50 % to 0 % for the PTES. It can also be noted from Fig. 3.6 that with the stage number N increasing, the temperature ratio τ of the CAES decreases accordingly, which

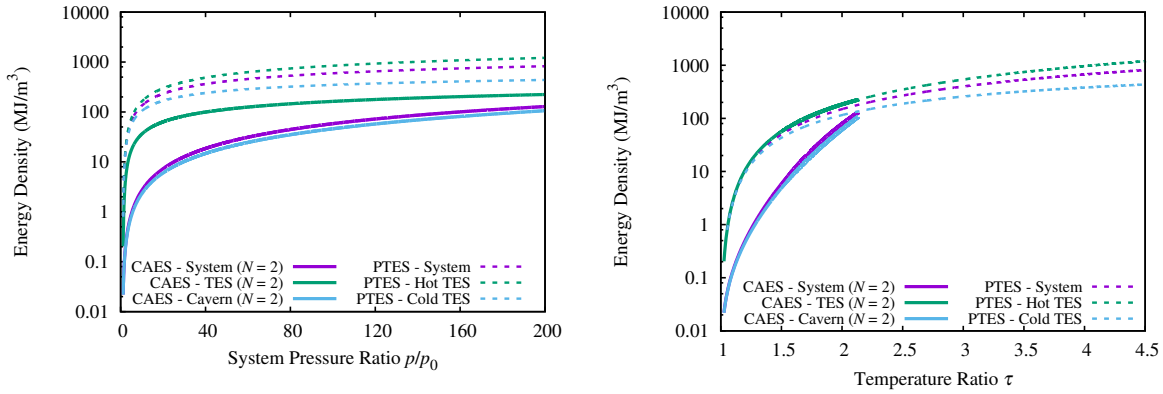

(a) system pressure ratio p/p_0 (b) temperature ratio τ

Figure 3.7: Exergy density of the PTES and CAES as functions of (a) system pressure ratio p/p_0 and (b) temperature ratio τ

leads to more exergy stored in the cavern and less in the hot TES.

After comparing the exergy distribution of CAES and PTES, it is necessary to further analyze the energy density of the two systems. Since the exergy is stored in different components, the concepts of component energy density D_i and system energy density D_{sys} are introduced here, which are defined as:

$$D_i = \frac{B_i}{V_i} \tag{3.45}$$

$$D_{\text{sys}} = \frac{\sum_{i=1}^{n} B_i}{\sum_{i=1}^{n} V_i} \tag{3.46}$$

where D_i refers to the component energy density and D_{sys} refers to the system energy density, V_i is the volume of the i-th component.

Fig. 3.7 illustrates the component and system energy density of the CAES and PTES as functions of temperature ratio τ (or system pressure ratio p/p_0). It can be noted from Fig. 3.7 that the component and system energy density of both CAES and PTES increases monotonically with the temperature ratio τ. For a typical CAES and PTES, the temperature ratio τ is in the range of 2.0 to 3.0, therefore, the energy density of PTES falls within the range of 100 to 1000 MJ/m^3; whilst the energy density of CAES is always less than 100 MJ/m^3 and decreases with the stage number N. Therefore, the energy density of CAES is an order of magnitude lower than that of the PTES. From Fig. 3.7, it can also be noted that the system energy density is a weighted average of the component energy density, and therefore the low

Table 3.1: System parameters and final results of the CAES and PTES

System	Fluid	N	β	ε	κ	η	α	f	$\chi\,(\%)$	$D\left(\mathrm{MJ/m^3}\right)$
CAES	Air	2	10	0.90	0.99	0.90	0.02	0.02	75.54	49.8
PTES	Air	1	10	0.98	0.99	0.98	0.02	0.02	71.18	125.0
PTES	Argon	1	10	0.98	0.99	0.98	0.02	0.02	75.51	254.8

system energy density of CAES is mainly due to the large cavern volume.

3.5 Numerical comparison of CAES and PTES

3.5.1 Loss distribution

In the above sections, analytical expressions of the system efficiency and energy density have been derived for both CAES and PTES. However, despite the fact that analytical solutions have many advantages, such as fast calculation and straightforward expressions, they cannot be used to calculate the loss distributions under realistic scenarios because otherwise it would be too complicated. Therefore, the numerical models, which have been verified by the analytical results, are used in this section to study the loss distributions of CAES and PTES. For this comparative study, a hypothetical 50 MW, 400 MWh A-CAES and a 2 MW, 16 MWh PTES are employed because they both correspond to realistic systems in the world [19]. The schematic diagram of the A-CAES and PTES are shown in Fig. 3.1 and the system parameters as well as the final results are summarized in Table 3.1.

In Table 3.1, a pressure ratio per stage $\beta = 10$ (which corresponds to a temperature ratio $\tau = 1.93$ for air) is assumed for both CAES and PTES. However, there are two stages in the CAES but only one in the PTES. The heat exchanger effectiveness ε and the polytropic efficiency η are set as 0.90 for CAES because it corresponds to the value of a typical turbomachinery and heat exchanger, whilst for the PTES, these two values are both 0.98 because it is reported that a novel high-efficiency reciprocating compressor/expander has been developed by the Isentropic Inc. and a more compact, segmented thermal reservoir is used for thermal storage. Under these assumptions, it can be noted from Table 3.1 that the system efficiencies of the PTES and CAES are relatively similar whilst the energy density of the PTES system is 5 times as high as that of the CAES system. It can also be noted from Table 3.1 that the system efficiency of PTES could be improved by replacing air with argon. This is because for the same pressure ratio β, argon corresponds to a higher temperature ratio $\tau = 2.52$ and thus lower compressor/expander losses.

Fig. 3.8 illustrates the losses distribution of the CAES and PTES system respectively.

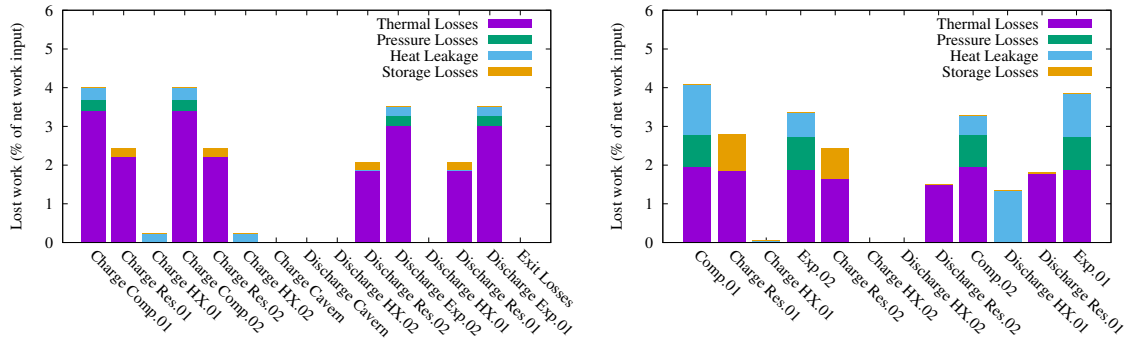

(a) A-CAES (b) PTES

Figure 3.8: Losses distribution of the CAES and PTES: (a) CAES (b) PTES

By comparing the two figures, it can be noted that the losses of CAES mainly consist of the thermodynamic loss whilst those of PTES are more determined by the heat leakage loss, which confirms the conclusion that PTES is more susceptible to heat transfer (leakage) loss. From Fig. 3.8a, it can also be noted that the expander losses during discharge is slightly lower than the compressor losses during charge, which can be proved analytically for CAES, whilst for PTES, the compressor/expander losses during charge and discharge are almost the same. In addition, it can be noted from Fig. 3.8 that the cavern has no losses. That's because this cavern is an isobaric one and its temperature and pressure remains constant during operations, therefore, there are no thermodynamic and heat leakage losses within it.

3.5.2 Parametric studies

After the case studies, it is necessary to carry out a parametric study for these realistic cases and compare the results with those of the ideal ones. The nominal operating parameters of the CAES and PTES are summarized in Table 3.1. Parts of the parametric study results are shown in Fig. 3.9a and Fig. 3.9b, from which it can be noted that under realistic scenarios, the system efficiencies χ of both CAES and PTES are less sensitive to the heat exchanger effectiveness ε and the polytropic efficiency η than those of the ideal cases. This conclusion is valid for all the other parameters previously studied, but the trends of the ideal cases and the real cases are generally very similar. It can also be noted from Fig. 3.9a and Fig. 3.9b that after using the high efficiency reciprocating device and segmented thermal reservoir, it's possible to make the efficiency of the PTES comparable to that of the CAES. This finding combined with the fact that the energy density of PTES system is always much higher that of A-CAES and that its construction is independent of certain geology requirements make PTES competitive with

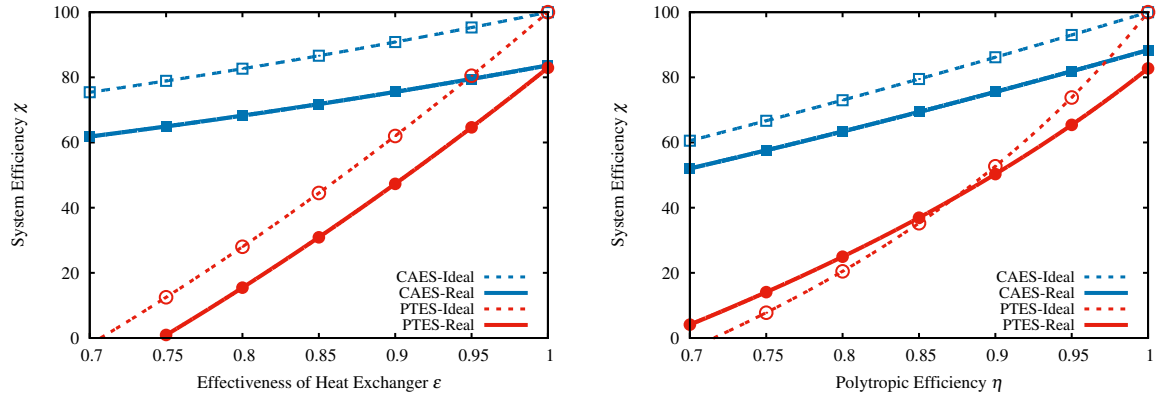

(a) heat exchanger effectiveness ε (b) polytropic efficiency η

Figure 3.9: Comparison of the system efficiencies as functions of the (a) heat exchanger effectiveness ε and (b) polytropic efficiency η

CAES.

3.6 Summary

CAES and PTES systems are compared with each other from an analytical and numerical perspective. Expressions of the system efficiency χ, exergy distribution P and energy density D are derived and the sensitivity of the system efficiency χ to various parameters are analyzed. More realistic cases of comparisons are conducted and the corresponding parametric study are carried out for the nominal design. It can be concluded from this chapter that:

1. the PTES system is much more sensitive to all kinds of losses and thus has a lower system efficiency when compared with the CAES system;

2. the PTES system efficiency χ increases monotonically with the temperature ratio τ, whilst for the CAES system, it depends on the tradeoff of the losses of the compressor/expander and the TES subsystem;

3. with the temperature ratio τ increasing, more exergy will be stored in the hot TES for both the PTES and CAES;

4. the energy densities of CAES and PTES both increases with the temperature ratio τ, however, the energy density of PTES is usually an order of magnitude higher than that of the CAES system.

Chapter 4

Pumped Thermal Energy Storage

4.1 Introduction

As mentioned in Chapter 2, Pumped Thermal Energy Storage (PTES) operates with a closed thermodynamic cycle and thus enjoys more design freedom than other energy storage systems. For example, various strategies such as precooling, preheating and recuperating can be employed to increase the roundtrip efficiency of a PTES [7, 48] and these variants are referred to as the precooled, preheated and recuperated PTES in this thesis. In this chapter, the cycle layouts and working principles of these PTES variants are introduced first. Then both thermodynamic and economic models are developed for various system components, which are common to other energy storage systems and will still be employed in later chapters. An introduction to the TES materials and starting processes of these PTES variants is also included. Finally, some simple parametric studies are carried out to compare the thermodynamic behaviors of these PTES variants, and the loss and cost distributions are provided for the nominal design. It should be noted that the effects of different working fluids, system pressurization and components re-usage are not considered in this chapter. This is because their effects on the capital cost are significant and subject to high levels of uncertainty. Therefore, their impacts on the thermo-economic performance are postponed until Chapter 8. In this chapter, air is still used as the working fluid and the minimum system pressure is ambient p_0. The optimization of these PTES variants and the comparison with other thermo-mechanical energy storage systems are also postponed until Chapter 8.

4.2 Cycle layouts

Compared with the CAES, PTES usually enjoys more design freedom due to its closed-cycle characteristics. For example, the PTES can deploy different gases, such as helium, neon and argon, as the working fluid, whilst the CAES can only use air. In addition, the charging and discharging temperature ratio can be different for PTES systems, and the whole system can be pressurized to reduce its compressor/expander cost. As shown in Ref. [18], in cases where compression and expansion losses dominate, the round-trip efficiency can be approximately by:

$$\chi = \frac{\eta w'_{\mathrm{e}} - w'_{\mathrm{c}}/\eta}{w_{\mathrm{c}}/\eta - \eta w_{\mathrm{e}}} = \frac{\mathrm{WR}\cdot\eta^2 - 1}{\mathrm{WR} - \eta^2} \tag{4.1}$$

where WR is the work ratio, $\mathrm{WR} = w'_{\mathrm{e}}/w'_{\mathrm{c}} = w_{\mathrm{c}}/w_{\mathrm{e}}$, whilst η is the average isentropic efficiency. From Eq. (4.1), it can be noted that for a given compression/expansion efficiency η, the system efficiency χ increases monotonically with the work ratio WR, and increasing WR thus becomes an important criteria for developing efficient PTES. One common method to increase WR for PTES is to use Rankine-cycle rather than the Brayton-cycle because compressing liquid requires far less work than compressing gas, as shown in Fig. 4.1. However, the Rankine-cycle will inevitable result in more losses in the heat exchangers due to the phase change of the working fluid. Besides, it may also cause damage to the liquid expander due to the cavitation problem associated with two-phase flow, which will reduce its lifespan or increase the maintenance cost. Therefore, only the Brayton-cycle PTES are studied in detail in this chapter, whilst the results on Rankine-cycle PTES can be found in other research papers, such as Refs. [63, 64, 67].

For the Brayton-cycle PTES as shown in Fig. 4.2b, it can be further proved that:

$$\mathrm{WR} = \frac{T_1\left(\tau - 1\right)}{T_3\left(1 - \tau^{-1}\right)} = \frac{\tau}{\theta} \tag{4.2}$$

where τ is the charging isentropic temperature ratio, $\tau = \beta^{(\gamma-1)/\gamma}$; θ is the ratio between the expander and compressor inlet temperature during charge, $\theta = T_3/T_1 = T'_{\mathrm{H}}/T'_{\mathrm{C}}$, where T'_{H} and T'_{C} refer to the the discharged temperature of the hot and cold TES respectively.

From Eq. (4.2), it can be noted that the work ratio WR of baseline PTES is relatively low due to its large θ, as its T_3 and T_1 are both fixed at ambient value due to the two auxiliary heat exchangers (HX1 and HX2 in Fig. 4.2a). This makes the baseline PTES vulnerable to the compressor/expander losses, and sensitive to the charging temperature ratio τ, as shown in Eqs. (4.1) and (4.2). In order to mitigate this problem, θ can be reduced by either reducing T_3 below ambient or increasing T_1 above ambient. This can be achieved by precooling the

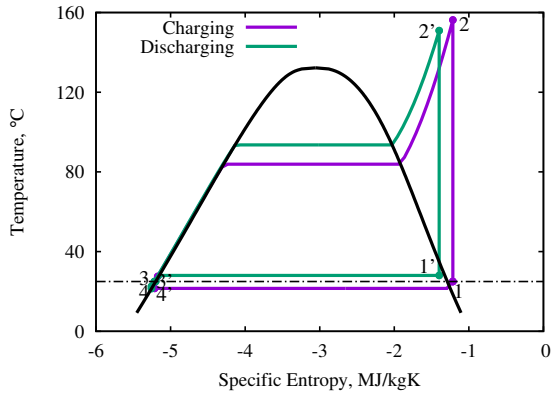

Figure 4.1: T-s diagram of the Rankine-cycle PTES

expander inlet air, as shown in Figs. 4.3a and 4.3b; or preheating the compressor inlet air, as shown in Figs. 4.4a and 4.4b; or through the employment of recuperation, as shown in Figs. 4.5a and 4.5b [48]. Accordingly, these new variants of baseline PTES are referred to as the precooled, preheated and recuperated PTES respectively.

4.2.1 Baseline PTES

The schematic and T-s diagrams of a baseline PTES are shown in Figs. 4.2a and 4.2b respectively. As mentioned before, there are two auxiliary heat exchangers within the baseline PTES to counter the effects of irreversibility. Therefore, the inlet temperatures of compressor T_1 and expander T_3 are both fixed at T_0 during charge, whilst during discharge, the inlet air temperatures of hot and cold TES are both fixed at T_0. As a result, the discharged temperature of hot and cold TES, T'_{H} and T'_{C}, are also fixed at T_0. The baseline PTES thus enjoys more design freedom than other PTES variants. For example, the discharging temperature ratio τ' of baseline PTES can be independent of its charging one τ. In addition, these two auxiliary heat exchangers make it possible for the packed bed thermal reservoir to be used as the TES, the temperature of which usually cannot be adjusted easily. The heat transfer area of thermal reservoir can be easily increased by reducing its particle diameter, which is ideal for PTES since it is very sensitive to the heat transfer losses, as discussed in Chapter 3. However, the packed bed thermal reservoir usually requires direct-contact heat transfer, which prevents PTES from being pressurized, because otherwise the pressure vessel cost will rise significantly.

As discussed before, the work ratio WR of baseline PTES is relatively low due to its large θ. This characteristic makes baseline PTES sensitive to the polytropic efficiency η and temperature ratio τ, as shown in Eqs. (4.1) and (4.2). Actually as the temperature ratio τ reduces, the round-trip efficiency χ drops to zero quickly (e.g, $\chi = 0$ at $\tau = 1/\eta^2 \approx 1.56$ if $\eta = 0.8$).

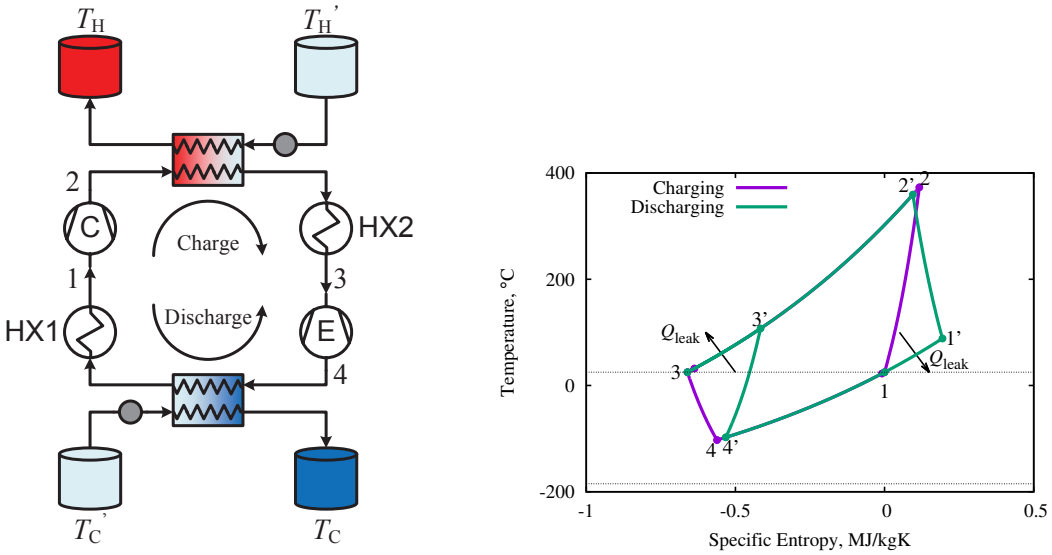

(a) Schematic diagram (b) T-s diagram

Figure 4.2: Schematic and T-s diagrams for the Baseline PTES: (a) Schematic diagram (b) T-s diagram

Like CAES, PTES can also be operated in stages. For example, there can be multiple stages N_{hot} (or N_{cold}) operating in series for hot storage (or cold storage) within any PTES system. However, since the exergy of PTES is solely stored in the form of temperature potential, it is usually unnecessary for PTES to have multiple stages if it can reach the maximum T_{max} and minimum temperature T_{min} through other methods, such as recuperation. Meanwhile, higher stage number N leads to lower temperature ratio τ, which makes PTES more sensitive to the polytropic efficiency η and pressure loss factor f_p, as discussed in Chapter 3. In addition, since the PTES is usually pressurized to its maximum pressure p_{max} to minimize the cost, increasing the stage number will inevitably reduce the average system pressure and increase the unit storage cost Z and system complexity. Therefore, it is usually beneficial for PTES to have single stage of hot and cold TES, especially after optimization.

4.2.2 Precooled PTES

The schematic and T-s diagrams of a precooled PTES are shown in Figs. 4.3a and 4.3b respectively, from which it can be noted that the expander inlet temperature T_3 is cooled down below ambient T_0 during charge. This can be realized by precooling the discharged hot TES to $T_{\text{H}}' < T_0$, and removing the auxiliary heat exchanger after the hot TES (HX2 in Fig. 4.2a). By adjusting T_{H}', the expander outlet temperature T_4 could be reduced to and fixed at the lowest allowable temperature T_{min} despite the variation of τ, η and ε. For example, if the heat transfer

loss is negligible and $\varepsilon = 1$, then the discharged hot TES temperature T'_{H} can be calculated by:

$$T'_{\mathrm{H}} = T_{\min}\tau^{\eta} \tag{4.3}$$

During discharge, however, the outlet temperature of compressor T'_3 shall not exceed T'_{H} because otherwise, it will be impossible to bring the discharged hot TES temperature back to its original value T'_{H} and the precooling effect will gradually cease to exist. Therefore, T'_{H} places an upper limit for the discharging temperature ratio τ'. For example, if the heat transfer loss is negligible and $\varepsilon = 1$, then $T_3 = T'_{\mathrm{H}}$ and $T_4 = T'_{\mathrm{H}}\tau^{-\eta}$. Since there is no heat leakage loss with the cold TES, $T'_4 = T_4$ and the outlet temperature of compressor during discharge is $T'_3 = T'_4\tau'^{1/\eta}$. Applying the upper temperature limit T'_{H} to the compressor outlet temperature T'_3 leads to:

$$\tau' = \tau^{\eta^2} \tag{4.4}$$

where τ' is the maximum allowable temperature ratio during discharge. The actual τ' could be lower than this value, however, it will incur unnecessary losses during storage, as the discharged hot TES temperature need to be heated back to its original value T'_{H} for steady operation. Hence, this maximum τ' will be used as the actual τ' in the following parametric and optimization study. From Eqs. (4.3) and (4.4), it can be noted that both T'_{H} and τ' are not independent variables, but functions of τ, η and ε, and should be determined numerically for the steady operation of the precooled PTES system.

4.2.3 Preheated PTES

The schematic and T-s diagrams of the preheated PTES are shown in Figs. 4.4a and 4.3b respectively, from which it can be noted that the compressor inlet temperature T_1 is above ambient T_0 during charge. This can be achieved by preheating the discharged cold TES to $T'_{\mathrm{C}} > T_0$, and removing the auxiliary heat exchanger after the cold TES (HX1 in Fig. 4.2a). By adjusting T'_{C}, the compressor outlet temperature T_2 can be increased to and fixed at the maximum allowable temperature $T_{\max}$ despite the variation of τ, η and ε. For example, if the heat transfer loss is negligible and $\varepsilon = 1$, then the discharged cold TES temperature T'_{C} can be calculated by:

$$T'_{\mathrm{C}} = T_{\max}\tau^{-1/\eta} \tag{4.5}$$

During discharge, however, the outlet temperature of expander T'_1 shall not drop below T'_{C} for similar reasons with the Precooled PTES. Therefore, T'_{C} places a lower limit for the

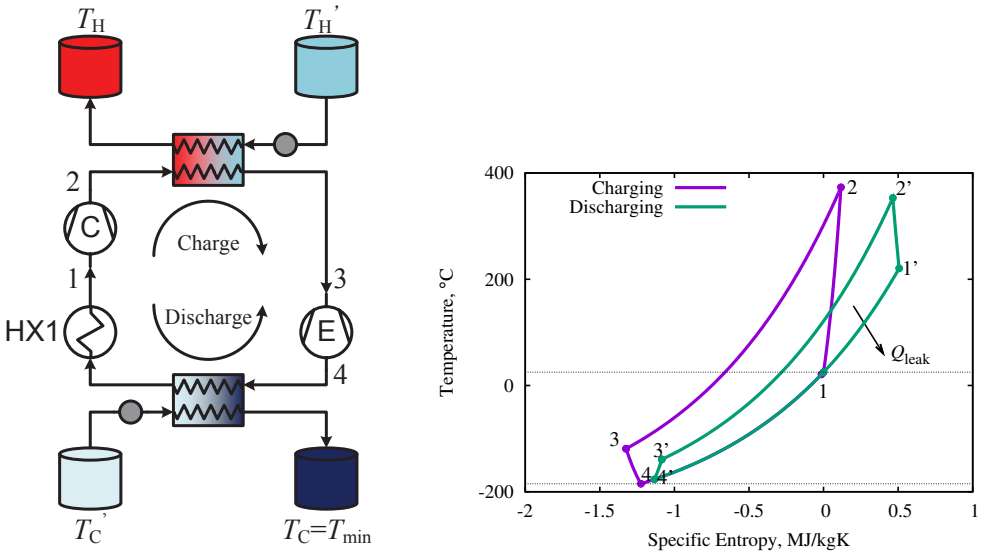

(a) Schematic diagram (b) T-s diagram

Figure 4.3: Schematic and T-s diagrams for the Precooled PTES: (a) Schematic diagram (b) T-s diagram

expander outlet temperature T_1' but an upper limit for the discharging temperature ratio τ'. For example, if $\varepsilon = 1$, then applying the lower temperature limit T_C' to the compressor outlet temperature T_1' results in:

$$\tau' = \tau^{1/\eta^2} \tag{4.6}$$

where τ' is still the maximum allowable temperature ratio due to the upper limit placed by T_C'.

From Eqs. (4.4) and (4.6), it can be noted that the maximum discharging temperature ratio τ' of the Preheated PTES is much higher than that of the Precooled PTES, and it is allowable to employ the same temperature ratio for the charge and discharge process, $\tau' = \tau$. The waste heat (or irreversibility) of the Preheated PTES is dissipated into the environment via the auxiliary heat exchanger before the hot TES (HX2 in Fig. 4.2a) because its temperature T_3' is above ambient, whilst the waste heat (or irreversibility) of the Precooled PTES is dissipated via the auxiliary heat exchanger before the cold TES (HX1 in Fig. 4.2a) because its temperature T_1' is above ambient.

4.2.4 Recuperated PTES

In addition to the Precooled and Preheated PTES, the work ratio WR can also be enhanced through recuperation, as shown in Figs. 4.5a and 4.5b. With recuperation, the outlet temperature of the compressor T_2 and expander T_4 during charge can be fixed at the maximum T_{max}

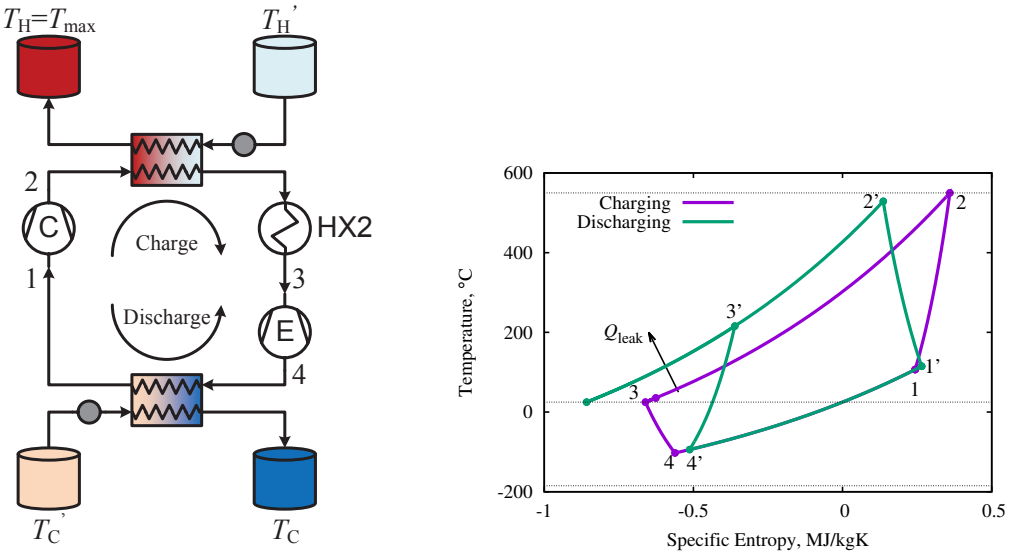

(a) Schematic diagram (b) T-s diagram

Figure 4.4: Schematic and T-s diagrams for the Preheated PTES: (a) Schematic diagram (b) T-s diagram

and minimum allowable temperature T_{min} simultaneously, thus making full use of the allowable temperature range. In Fig. 4.5b, there are two recuperators: one for the hot side and the other for the cold side recuperation. The waste heat (or irreversibility) is dissipated into the environment through the auxiliary heat exchangers between the two recuperators. T'_H and T'_C should be set by Eqs. (4.3) and (4.5) respectively, and τ' by the stricter constraint of Eq. (4.4).

4.3 Overview of modelling approach

The governing equations of major system components will be summarized below, and the numerical methods for solving these equations will be described in Appendix B.

4.3.1 Solid TES system

Solid TES is assumed to be provided by packed-bed thermal reservoirs. Equations governing the behavior of such reservoirs have been presented many times in the literature, for example, Refs [41, 123, 124]. The model used here is that described in Ref. [41] and is based on the well-established Schumann model. With a number of minor assumptions (see Ref. [41]), the governing equations for gas and solid temperature variations take the form:

$$\frac{\partial T_g}{\partial z} = \frac{T_s - T_g}{l} \tag{4.7}$$

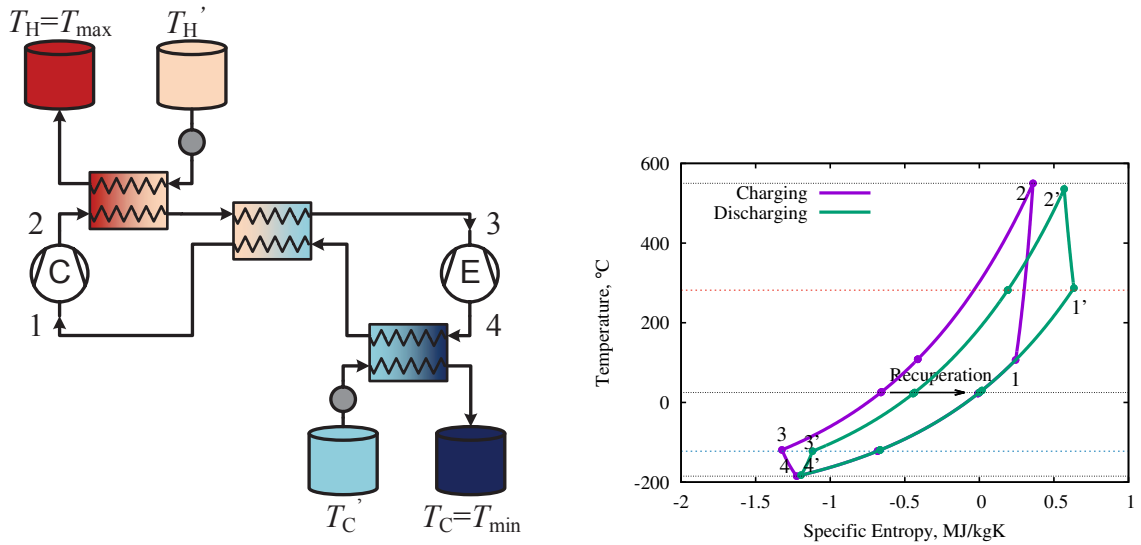

(a) Schematic diagram (b) T-s diagram

Figure 4.5: Schematic and T-s diagrams for the Recuperated PTES: (a) Schematic diagram (b) $T-s$ diagram

$$\frac{\partial T_s}{\partial t} = \frac{T_g - T_s}{\tau} \tag{4.8}$$

where l and τ are length and time scales as given in Ref. [41]. The pressure loss along the thermal reservoir is also considered and calculated from:

$$\frac{dp}{dz} = -\frac{S_v(1-\varepsilon)c_f G^2}{2\varepsilon^3 \rho_g} \tag{4.9}$$

where S_v is the particle surface-to-volume ratio and c_f is the friction coefficient, which is obtained from the Carman correlation given in Ref. [125].

Three parameters are used to model the performance of the thermal reservoir, they are respectively the utilization factor Π, particle size d_p and the aspect ratio L/D. The utilization factor Π is defined as the ratio of the actual charge time t_{chg} to the nominal charge time t_{nom}, $\Pi = t_{chg}/t_{nom}$. It is approximately equal to the stored energy as a fraction of its full-charge value and is used to determine the size of the thermal reservoir. The particle size d_p has a direct impact on the particle surface-to-volume ratio S_v (for spherical particles, $S_v = 6/d_p$) and hence determines the thermal and pressure losses. The aspect ratio L/D is essentially the length-to-diameter ratio, and determines the shape of the thermal reservoir.

Since the thermal reservoir is assumed adiabatic and there is no heat leakage loss to its surroundings, the major loss of thermal reservoir is caused by the irreversible heat transfer

between the gas and solid. The entropy generation rate associated with this process is [41, 42]:

$$\dot{S}_t = \int \left(\frac{1}{T_s} - \frac{1}{T_g} \right) \mathrm{d}\dot{Q}_z = \dot{m} c_p \int_0^L \frac{\left(T_g - T_s\right)^2}{T_g T_s} \frac{\mathrm{d}z}{l} \tag{4.10}$$

and the thermal loss can be determined by integrating the entropy generation rate over the duration of charge or discharge, $\xi_T = \int_0^t T_0 \dot{S}_t \mathrm{d}t$.

The entropy generation rate due to pressure loss can be calculated by:

$$\dot{S}_p = \dot{m} R_g \ln \frac{p_{in}}{p_{out}} \tag{4.11}$$

where the pressure drop $\Delta p = p_{in} - p_{out}$ is determined by integrating Eq. (4.9). The expressions of pressure loss for other components are similar to Eq. (4.11) and thus omitted for the sake of simplicity.

4.3.2 Liquid TES system

In liquid A-CAES, the governing equations of thermal fluid tanks are essentially the mass and energy conservation equations, which can be written as:

$$\frac{\mathrm{d}m_f}{\mathrm{d}t} = \dot{m}_{in} - \dot{m}_{out} \tag{4.12}$$

$$\frac{\mathrm{d}T_f}{\mathrm{d}t} = \frac{1}{m_f c_f} \left[\dot{Q} + \dot{m}_{in} c_f T_{in} - \dot{m}_{out} c_f T_f - \frac{\mathrm{d}m_f}{\mathrm{d}t} c_f T_f \right] \tag{4.13}$$

where m_f and T_f are the mass and temperature of the thermal fluid respectively. In this thesis, the thermal fluid tanks are assumed adiabatic during charge and discharge, $\dot{Q} = 0$. Therefore, the thermal loss of liquid TES is due to the mixing of inlet fluid with the stored fluid which is generally at a different temperature. The entropy generation rate associated with this process is:

$$\dot{S}_t = \dot{m}_{in} c_f \left(\frac{T_{in}}{T} - 1 - \ln \frac{T_{in}}{T} \right) \tag{4.14}$$

In order to quantitatively analyze the effect of heat leakage during storage, an insulation factor κ is introduced, which is the ratio of the internal energy after storage E'_{TES} to that before storage E_{TES} :

$$E'_{TES} = \kappa E_{TES} \tag{4.15}$$

The definition of the internal energy here uses ambient temperature T_0 as the reference

value, therefore:

$$E_{\mathrm{TES}} = m_{\mathrm{f}} c_{\mathrm{f}} \left(T_{\mathrm{TES}} - T_0\right) \tag{4.16}$$

After some simplification, the temperature of the thermal tank after storage can be derived, which is:

$$T'_{\mathrm{TES}} = \kappa T_{\mathrm{TES}} + (1-\kappa)\, T_0 \tag{4.17}$$

Thus if $\kappa = 1$, then $T'_{\mathrm{TES}} = T_{\mathrm{TES}}$, the storage tanks are ideally insulated, without any heat leakage; however, if $\kappa = 0$, then $T'_{\mathrm{TES}} = T_0$,they are not insulated at all, losing all its stored thermal energy to the environment. Actually, if we apply the lumped-capacity heat transfer model to the liquid TES, it can be proved that $\kappa = \exp\left(t/\tau_{\mathrm{ins}}\right)$, where t is the elapsed storage time and τ_{ins} is the heat leakage time constant which will be discussed in detail in Section 4.4.1.

4.3.3 Compressor and expander

The compressors and expanders are modelled by means of a simple polytropic or "infinitesimal stage" efficiency, defined as $\eta_{\mathrm{c}} = -v\mathrm{d}p/\delta w$ for compression or $\eta_{\mathrm{e}} = -\delta w/v\mathrm{d}p$ for expansion, and a heat leakage factor, defined as $\alpha_{\mathrm{leak}} = \delta q/\delta w$, as shown in Ref. [80]. The use of polytropic efficiencies is deemed preferable to the isentropic efficiencies which yield anomalies when, for example, compression and expansion are divided into multiple stages. The heat leakage factor, on the other hand, is used to distinguish the losses caused by the heat leakage and aerodynamic irreversibility. Compressor exit temperature T_{out} and specific work w_{c} are thus computed from:

$$T_{\mathrm{out}} = T_{\mathrm{in}} \beta_{\mathrm{c}}^{\phi_{\mathrm{c}}} \tag{4.18}$$

$$w_{\mathrm{c}} = \frac{c_p T_{\mathrm{in}}}{1-\alpha_{\mathrm{c}}} \left(\beta_{\mathrm{c}}^{\phi_{\mathrm{c}}} - 1\right) \tag{4.19}$$

where c_p is the heat capacity of the air, the subscripts in and out denote the inlet and outlet of the compressor respectively, ϕ_{c} is the polytropic exponent, $\phi_{\mathrm{c}} = \frac{\gamma-1}{\gamma}\frac{1-\alpha_{\mathrm{c}}}{\eta_{\mathrm{c}}}$. Equivalent expressions to Eqs. (4.18) and (4.19) can be derived for the expansion process, with η_{c} replaced by η_{e}^{-1} and α_{c} by α_{e}. The heat leakage factor α_{leak} is usually negligible for the turbomachinery due to its high rotational speed but can become important for reciprocating devices. Amongst the various thermal-mechanical energy storage systems, reciprocating devices are mainly employed by some variants of PTES and most I-CAES systems. Therefore, the effects of heat

leakage factor are only considered in Chapter 3 for a preliminary comparison of PTES and CAES and in Chapter 6 for the efficiency enhancement of I-CAES systems.

Since the losses within the compressor/expander are caused by fluid viscosity instead of temperature difference, they are referred to as the aerodynamic loss in Chapter 6 but still considered as the thermal losses. On the other hand, the losses caused by the irreversible heat transfer or mixing within an isothermal compressor/expander are referred to as the thermodynamic loss which also belong to the thermal losses. For conventional compressor, the entropy generation rate of the irreversible compression is:

$$\dot{S}_t = \dot{m} R_g \left(\frac{1}{\eta_c} - 1 \right) \ln \beta_c \tag{4.20}$$

Equivalent expressions to Eq. (4.20) can be derived for the expansion process, with $1/\eta_c - 1$ replaced by $1 - \eta_e$. It should be noted that the aerodynamic loss is independent of the heat leakage factor and the air inlet temperature. The entropy generation rate of the heat leakage process is:

$$\dot{S}_l = \dot{m} c_p \frac{\alpha_c}{1 - \alpha_c} \left(\tau_{out} - \tau_{in} - \ln \frac{\tau_{out}}{\tau_{in}} \right) \tag{4.21}$$

where τ is the temperature ratio between the compressor inlet/outlet and the ambient. Equivalent expressions to Eq. (4.21) can be derived for the expansion process, with α_c replaced by α_e.

4.3.4 Heat exchanger

For liquid TES heat is transferred between the working fluid and the thermal fluid via a heat exchanger. To minimize losses associated with irreversible heat transfer, a counter flow heat exchanger with $C_r = 1$ (i.e., balanced flow) is employed and the well-established $\varepsilon - \mathrm{NTU}$ method is used for the simulation. The heat exchanger effectiveness $\varepsilon = |T_{in} - T_{out}| \,/\, \left(T_{in,hot} - T_{in,cold}\right)$ is then the only parameter needed to evaluate thermal performance and heat exchanger outlet temperatures are given by:

$$\begin{pmatrix} T_{out,a} \\ T_{out,f} \end{pmatrix} = \begin{pmatrix} 1-\varepsilon & \varepsilon \\ \varepsilon & 1-\varepsilon \end{pmatrix} \begin{pmatrix} T_{in,a} \\ T_{in,f} \end{pmatrix} \tag{4.22}$$

where the subscripts in and out denote the inlet and outlet of the heat exchanger respectively; the subscripts a and f denote air and the storage fluid respectively.

For a counter-flow heat exchanger with $C_r = 1$ the effectiveness is related to the "number

of thermal units" (NTU $= UA/C_{\min}$) by (see [126]):

$$\varepsilon = \frac{\mathrm{NTU}}{\mathrm{NTU}+1} \tag{4.23}$$

Knowing the NTU enables an estimate of the heat exchanger cost and the pressure loss, the latter being determined from (see [127]):

$$\Delta p = \frac{G^2}{\bar{\rho}} \frac{c_f}{\mathrm{St}} \mathrm{NTU} \tag{4.24}$$

where $\bar{\rho}$ is the average density of the inlet and outlet, c_f/St is a constant, which equals $2\mathrm{Pr}^{\frac{2}{3}}$ for turbulent flow (see [127]). The mass flowrate per unit area G is set as $37\,\mathrm{kg}/\left(\mathrm{m}^2\mathrm{s}\right)$ so that the corresponding Reynolds number Re is ~6000, which is above the turbulence threshold 3000; the inner diameter of the heat exchanger tubes is set as 3.0 mm, which is the smallest size available commercially from multiple sources [128].

The G and Re provided above are mainly served as an example of all feasible values. They are neither optimized nor the limiting cases. Actually, even if the G is fixed, the pressure loss Δp still varies significantly with the average pressure $\bar{p}$ and temperature $\bar{T}$ since $\bar{\rho} = \bar{p}/\left(R_g \bar{T}\right)$. From Eq. (4.11), it can be noted that the entropy generation $\dot{S}_p$ is mainly determined by the pressure loss factor $f_p = \Delta p/p$ rather than the absolute value of Δp. Therefore, it is easy to prove that f_p drops rapidly with $\bar{p}$ increasing and since most heat exchangers in the A-CAES, LAES and pressurized PTES are operated at high pressures, their f_p are usually less than 1 % and their impacts on the system efficiency are negligible. Actually, an upper limit of 1 % is placed on the f_p of all heat exchangers, but this limit is only exercised within the cold TES of unpressurized PTES in Chapter 8 where $p_{\min} = p_0$. This limit is employed to avoid the otherwise excessive Δp interfering the thermodynamic cycles and is feasible because laminar flow can also be used for heat exchangers [126].

The above thermodynamic model is mainly for the heat exchanger within the liquid TES, whose function is to recycle the thermal exergy generated during charge. The entropy generation rate of a balanced flow heat exchanger with $C_r = 1$ can be calculated by [49]:

$$\dot{S}_t \approx \dot{m} c_p \varepsilon \left(1-\varepsilon\right)\left(\tau + \tau^{-1} - 2\right) \tag{4.25}$$

where τ is the temperature ratio of the hot fluid to the ambient value, $\tau = T_{\mathrm{hot}}/T_0$.

For the auxiliary heat exchanger placed after each liquid TES, its main function is to dissipate the waste heat into the environment rather than recycling it. Therefore, a high water flow rate (hence a low heat capacity ratio C_r) is usually adopted to reduce the heat exchanger

size and cost. The effectiveness of any heat exchanger with $C_r = 0$ is given by:

$$\varepsilon = 1 - \exp(-\mathrm{NTU}) \tag{4.26}$$

Hence, a relatively high effectiveness ε of 0.86 can be attained with NTU as low as 2.0. Since the waste heat is not recycled but simply dissipated, there is only heat leakage loss in the auxiliary heat exchangers, the entropy generation rate of which can be calculated by:

$$\dot{S}_l = \dot{m} c_p (\tau - 1 - \ln \tau) \tag{4.27}$$

where τ is the temperature ratio of inlet air to the ambient value, $\tau = T_{\mathrm{in}}/T_0$.

4.4 Cost modelling of components

The objective here is to provide a reasonable comparison between the initial capital costs of different energy storage systems. Cost equations for the major system components are therefore set out and justified in this section. Although efforts have been made to ensure the cost equations are as accurate as possible, it should be noted that they are still subject to significant uncertainty and should be treated accordingly with caution. Furthermore, only costs that have a direct impact on the following parametric and optimization study are included. Other costs such as electrical and control costs, materials, labor, operating and indirect costs are not included.

4.4.1 TES system costs

The TES system all consist of similar components and the capital cost can be estimated from the following correlation proposed in Ref. [44]:

$$Z_{\mathrm{TES}} = k_{\mathrm{fil}} V_{\mathrm{fil}} + k_{\mathrm{ins}} V_{\mathrm{ins}} + k_{\mathrm{PV}} pV \tag{4.28}$$

where k_{fil} and k_{ins} are costs per unit volume of the filling (storage material) and insulation respectively, whilst k_{PV} is the cost of the pressure vessel (including material and fabrication) per bar per unit volume. The coefficients used in Eq. (4.28) are summarized in Table 4.1.

Determining the required thickness of insulation is based on the fractional energy loss per day, which can be estimated from the simple lumped-capacity heat transfer model [42]:

$$\frac{\mathrm{d}E_{\mathrm{fil}}}{\mathrm{d}t} = \frac{E_{\mathrm{fil}}}{\tau_{\mathrm{ins}}} \tag{4.29}$$

where $\tau_{\text{ins}} = \rho_{\text{fil}} c_{\text{fil}} / U_{\text{ins}} S_{\text{TES}}$ is a heat leakage time constant and S_{TES} is a surface-to-volume ratio of the TES subsystem. U_{ins} is an overall heat transfer coefficient. For instance, setting the fractional energy loss rate to 0.5 % per day corresponds to a time constant τ_{ins} of 200 days, and for the nominal design ($S_{\text{TES}} = 2/D$ including hemispherical ends and setting L/D to 1), then the overall heat transfer coefficient $U_{\text{ins}} = \rho_{\text{fil}} c_{\text{fil}} D / 8\tau_{\text{ins}} \approx 0.12\,\text{W}/\left(\text{m}^2 \cdot \text{K}\right)$. U_{ins} is mainly determined by the thermal resistance λ_{ins} and thickness δ_{ins} of the insulation layer, and therefore δ_{ins} can be estimated from the following cylindrical heat conduction equation:

$$\delta_{\text{ins}} = \frac{D}{2}\left[\exp\left(\frac{2\lambda_{\text{ins}}}{D U_{\text{ins}}}\right) - 1\right] \tag{4.30}$$

However, the lumped capacity model is only valid if the temperature distribution are radially uniform within the storage media. This is a good assumption for liquid TES due to mixing, but for solid systems the Biot numbers are likely to be sufficient to cause significant non-uniformity that would invalidate the use of the 1-D Schumann-style model [42]. An additional constraint is thus placed on the temperature drop that would occur at the outer edge of the storage material, which effectively limits the Biot number and hence the maximum allowable overall heat transfer coefficient U_{ins}. Details of how this is implemented are provided in Ref. [42].

4.4.2 Compressor and expander costs

The equations for estimating the capital cost of the compressors and expanders are taken from the well-known CGAM problem, which was developed by a group of concerned specialists in the field of thermo-economics (C. Frangopoulos, G. Tsatsaronis, A. Valero, M. von Spakovsky, and co-workers) in the early 90s. This has been used as the standard test case for the comparison of different thermo-economic optimisation methods ever since [106]. The cost equations are adapted here to make them more compatible with the polytropic processes and the coefficients are adjusted to the data provided by Schainker (2008) [4] to account for inflation. Costs of both the compressors and the expanders are estimated from:

$$Z_{\text{CE}} = \sum_{i=1}^{N} \frac{\sqrt{R_{\text{g}}/R_{\text{ref}}}}{p_{\text{in}}} \frac{C_{\text{c/e}} \dot{m} \ln \beta_i}{\eta_{\max} - \eta} \tag{4.31}$$

where η and $\dot{m}$ are the polytropic efficiency and the mass flowrate respectively (η_{c} and $\dot{m}_{\text{chg}}$ for compressors, η_{e} and $\dot{m}_{\text{dis}}$ for expanders). R_{g} and R_{ref} are the actual and reference (air) gas constant respectively, and p_{in} is the system inlet pressure. $\eta_{\max}$ is set as 0.92 in accord with to Refs. [106, 116] and by comparison with data, as shown in Fig. 4.6. Eq. (4.31) encapsulates the increase in compressor / expander cost with mass flowrate $\dot{m}$, system pressure ratio p/p_0

Table 4.1: Constants used in the equations for the purchase cost of the components

Components	Constants	
Compressor	$C_c = 670\,\$/\,(\mathrm{kg/s})$	$\eta_{max} = 0.92$
Expander	$C_e = 1116\,\$/\,(\mathrm{kg/s})$	$\eta_{max} = 0.92$
Heat Exchanger	$C_h = 38880\,\$/\,(\mathrm{kg/s})^{0.6}$	
Thermal Reservoir	$k_{PV} = 250\,\$/\mathrm{bar}\cdot\mathrm{m}^3$	$k_{fil} = 200\,\$/\mathrm{m}^3$
	$k_{ins} = 1500\,\$/\mathrm{m}^3$	
Thermal Fluid Tanks	$k_{hot} = 500\,\$/\mathrm{m}^3$	$k_{cold} = 100\,\$/\mathrm{m}^3$

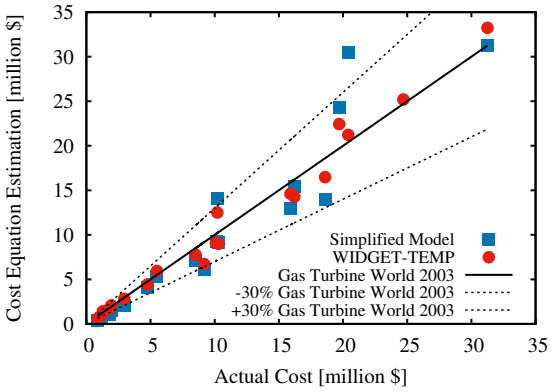

Figure 4.6: Validation of the compressor/expander cost equations

and component efficiency η. It suggests that the total cost is independent of how the system pressure ratio is distributed between each stage. The coefficients used in Eq. (4.31) are based on the centrifugal compressor and turbo-expander [4] and are summarized in Table 4.1. As with heat exchangers, both pessimistic (30 % overestimation of the cost) and optimistic (30 % underestimation of the cost) cases are given to account for the uncertainty inherent in all cost modelling.

Compressor and expander costs estimated from the above simplified model are compared in Fig. 4.6 with actual costs and with costs estimated from the considerably more complex "WIDGET-TEMP" model described in Ref. [111]. The solid line denotes estimated cost equal to actual cost, which is unlikely to be achieved by any model given fluctuations in actual cost. It is notable that the simplified model tends to underestimate costs in the low-power range and overestimate them at high power. This is because marginal costs tends to decrease with increasing power output (also referred to as the "economies of scale"), and this is not accounted for in the model. Nevertheless, estimates generally fall within $\pm 30\,\%$ of actual values and Eq. (4.31) is much simpler than the "WIDGET-TEMP" approach, which requires 22 input parameters.

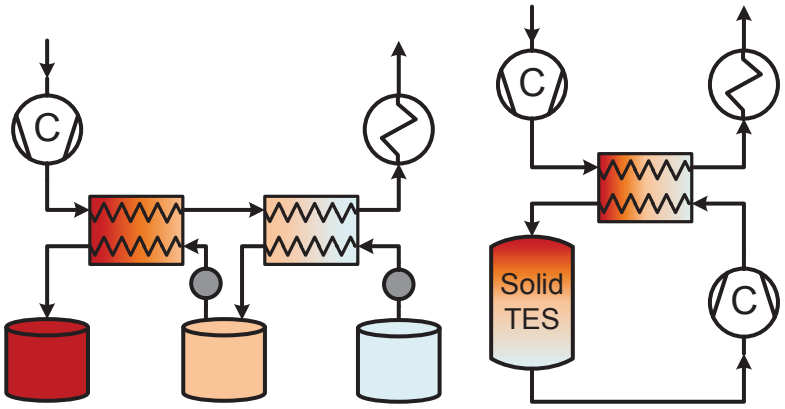

(a) Liquid TES operating in series (b) Indirect-contact solid TES

Figure 4.7: Schematic diagram of the indirect-contact liquid and solid TES: (a) Liquid TES operating in series (b) Indirect-contact solid TES

4.4.3 Heat exchanger costs

For a counter-flow concentric tube heat exchanger with $C_r = 1$, the effectiveness ε is related to the "number of thermal units" (NTU $= UA/C_{\min}$) by:

$$\varepsilon = \frac{\text{NTU}}{\text{NTU} - 1} \tag{4.32}$$

Since the NTU is proportional to heat transfer area of the heat exchanger, it is also used in this study to estimate the capital cost through:

$$Z_{\text{HEX}} = \sum_{i=1}^{N} C_{\text{hex}} \left(\dot{m} \cdot \text{NTU}_i\right)^{0.6} \tag{4.33}$$

This relation is also taken from the CGAM problem, adapted to the cost data provided by Schainker [4]. It indicates cost increasing with both flowrate and NTU because increasing either of these calls for larger heat transfer area. The index 0.6 is based on the "rule of the six-tenths" which can give an approximate cost within $\pm 20\,\%$ [108]. The coefficients used in Eq. (4.33) are summarized in Table 4.1. The pessimistic (30 % overestimation of the cost) and optimistic (30 % underestimation of the cost) scenarios are also considered for the heat exchanger cost model.

Table 4.2: Thermo-economic properties of the commonly used thermal fluids [10–13]

	C (\$/t)	ρ (kg/m^3)	c_p (J/kg · K)	Temperature (°C)
Water	1.0	1000	4174	0~100
P. Water (20 bar)	1.0	960	4210	0~213
Mineral Oil	2642	770	2600	-30~340
Therminol VP	5000	1060	1780	12~257
Solar Salt	1000	1850	1550	230~550
Saltstream XL	1000	1870	1450	120~500
Methanol	550	827	2499	-97~64
Propane	550	657	2078	-187~-42

4.5 TES materials

In the following part of this thesis, the maximum and minimum allowable temperature are set as $T_{\max} = 550$ °C and $T_{\min} = -185$ °C respectively, considering both the temperature range of the thermal fluids and the limitation of the turbomachineray. This wide temperature range can be achieved by operating multiple heat exchangers in series, each with a different kind of thermal fluid, as shown in Fig. 4.7a. For example, mineral oil ($-30 \sim 300$ °C) and solar salt ($230 \sim 550$ °C) can be used to cover the temperature range of the hot TES; whilst methanol ($-97 \sim 64$ °C) and propane ($-187 \sim -42$ °C) can be used for the cold TES. The discussion and selection of suitable thermal fluids for energy storage can be found in various literature sources, such as Ref. [10–13]. The thermo-economic properties of the thermal fluids used in this thesis are summarized in Table 4.2. More detailed analysis on the heat exchangers in series for the hot liquid TES can be found in Appendix A.

The solid TES (packed bed) can also be used for thermal energy storage, since the solid materials, such as quartz and magnetite, usually have wider operating temperature range than the thermal fluids. However, the pressure vessel of the solid TES tends to become unacceptably expensive when its operating pressure is high. Therefore, an indirect contact solid TES, as shown in Fig. 4.7b, can be deployed instead. It combines the merits of solid TES (wide operating temperature range) and liquid TES (relatively cheap at high pressure) and is suitable for the PTES systems discussed in Section 4.2. For the most part, the thermodynamics of solid-based and liquid-based PTES are the same, and therefore the descriptions are mainly given for the liquid-based PTES. The difference required for modelling solid-based systems can be found in Ref. [8].

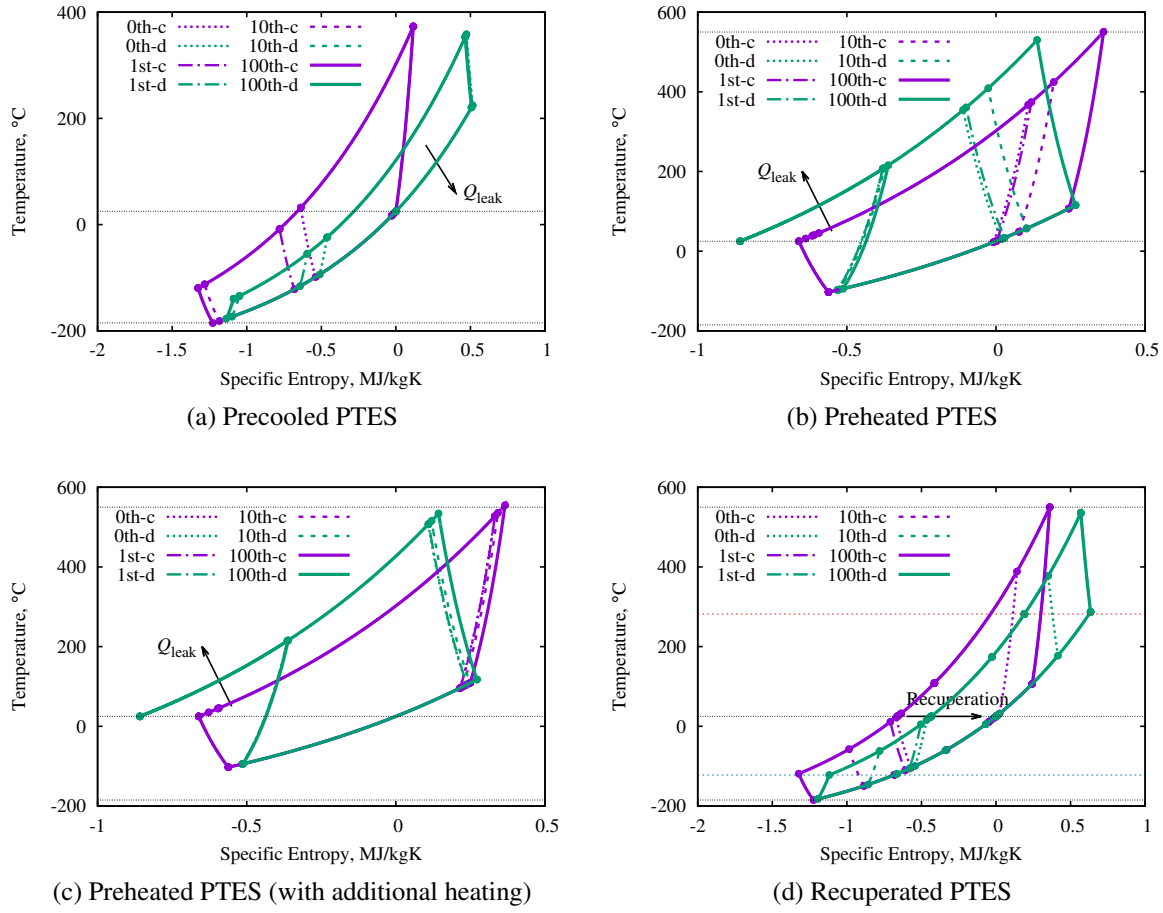

(a) Precooled PTES

(b) Preheated PTES

(c) Preheated PTES (with additional heating)

(d) Recuperated PTES

Figure 4.8: Starting processes of the PTES variants: (a) Precooled PTES (b) Preheated PTES (c) Preheated PTES (with additional heating) (d) Recuperated PTES. (c and d denotes the charging and discharging respectively.)

4.6 Starting processes

The starting processes of the precooled, preheated and recuperated PTES are shown in Figs. 4.8a, 4.8b and 4.8d respectively, from which it can be noted that the precooled PTES reaches its stable state very quickly, in roughly 10 cycles of operation, whilst for the recuperated and preheated PTES, it takes much longer time. The preheated PTES is particularly slow in reaching equilibrium, but it is possible to employ additional heating to shorten this period, as shown in Fig. 4.8c where the cold TES is heated to 100 °C prior to the starting process. Waste heat, solar energy and electric resistance heating can all be employed for the task, and although the speed of converging is not accelerated, the starting process of preheated PTES can become closer to its stable state. It is very quick for the hot TES of recuperated PTES to reach its maximum allowable temperature 550 °C, in just 2 cycles, and after that, the additional

Table 4.3: The standard, minimum and maximum design variable values of PTES for the parametric and optimization study

	R_c	R_d	T'_C	T'_H	NTU	η	f_p
Standard	10.0	10.0	1.50	0.50	49.00	0.85	0.00
Minimum	5.00	5.00	1.00	0.20	24.00	0.80	0.00
Maximum	30.0	30.0	5.00	1.00	99.0	0.90	0.10

thermal energy must be dissipated into the environment via an auxiliary heat exchanger to prevent overheating. On the other hand, it is relatively slow for the cold TES of recuperated PTES to reach equilibrium, as shown in Fig. 4.8d. However, after 10 cycles of operation, the T-s diagram of the recuperated PTES is already very close to its stable one, so that its efficiency would not be seriously affected. All these PTES variants reaches the stable states within 100 cycles, which demonstrates that the PTES has the ability to reach equilibrium by itself. The underlying force for driving this convergence is the difference in the charging and discharging temperature ratio.

4.7 Parametric study

Since the discharging temperature ratio τ', discharged hot TES temperature T'_H and the discharged cold TES temperature T'_C are all set by the charging temperature ratio τ, maximum T_{max} and minimum allowable temperature T_{min} in this study, these variables are not independent ones. As a result, only the impacts of charging temperature ratio τ, heat exchanger effectiveness ε, polytropic efficiency η, as well as the pressure loss factor f_p on the system performance are analyzed in this section, and the results are shown in Fig. 4.9a to Fig. 4.9d respectively. The number of stages of all PTES is set as $N = 1$ and the variation range of other design variables are summarized in Table 4.3. As mentioned before, the maximum and minimum allowable temperature are set as $T_{max} = 550$ °C and $T_{min} = -185$ °C respectively. In this chapter, ambient air is used as the working fluid and all PTES are not pressurized. The effects of different working fluid and pressurization on the system performance will be dealt with in Chapter 8.

4.7.1 Temperature ratio effect

Fig. 4.9a shows the impacts of charging temperature ratio τ on the system efficiency χ. Different lines refer to different PTES systems, as introduced in Section 4.1. From Fig. 4.9a, it can be clearly noted that the system efficiency χ of the precooled, recuperated and baseline

PTES all increases with the charging temperature ratio τ, and the baseline PTES is more sensitive to τ than the other two systems. This is because the baseline PTES has the lowest work ratio WR of all PTES systems, as shown in Eq. (4.1). This characteristic makes the baseline PTES most vulnerable to compressor/expander losses when the temperature ratio τ is low, as discussed in Section 4.2, whilst for other PTES systems, even if the charging temperature ratio τ approaches one, the work ratio WR is still large enough (due to its high θ) to avoid any significant impairment of efficiency.

Meanwhile, as indicated by Eqs. (4.4) and (4.6), the discharging temperature ratio τ' of the precooled, preheated, and recuperated PTES all increases with its charging temperature ratio τ. However, the auxiliary losses (losses generated in the auxiliary heat exchangers) of the precooled PTES and TES losses (including the losses of the two recuperators) of recuperated PTES decrease with τ' increasing, as shown in Fig. 4.3b and Fig. 4.5b where T_1' decreases with τ'; whilst the auxiliary losses of the preheated PTES increases with τ' increasing, as shown in Fig. 4.4b where T_3' increases with τ'. This phenomenon reduces the system efficiency of χ of preheated PTES as its charging temperature ratio τ increases, as shown in Fig. 4.9a.

4.7.2 Heat exchanger effectiveness effect

The impacts of the heat exchanger effectiveness ε on the system efficiencies χ of different PTES systems are shown in Fig. 4.9b, from which it can be found that the system efficiencies χ of all PTES systems increase with the effectiveness ε, whereas the precooled PTES is more sensitive to ε than any other system. This is because for precooled PTES system, its compressor outlet temperature during discharge T_3' should be lower than (or equal to if $\varepsilon = 1$) the expander inlet temperature during charge T_3, as discussed in Section 4.1 and shown in Fig. 4.3b. In addition, the lower the heat exchanger effectiveness ε is, the lower T_3' and τ' should become in order to counter the irreversibility of the heat transfer process. This, however, will inevitably increase the auxiliary losses of the precooled PTES and impairs its efficiency, as shown in Fig. 4.3b, where T_1' increases with τ' decreasing.

On the other hand, for the Preheated PTES system, the expander outlet temperature during discharge T_1' should be higher than the compressor inlet temperature during charge T_1 for similar reasons, as shown in Fig. 4.4b. However, higher T_1' means lower discharging temperature ratio τ' and compressor outlet temperature T_3', which will reduce the auxiliary losses of the preheated PTES and offset the increasing heat transfer losses of the heat exchangers to some extent. Therefore, the precooled PTES is most sensitive to ε, whilst the preheated PTES is least sensitive to it.

For the recuperated PTES, although its discharging temperature ratio τ' also decreases with the heat exchanger effectiveness ε reducing, just like the precooled PTES, the waste energy

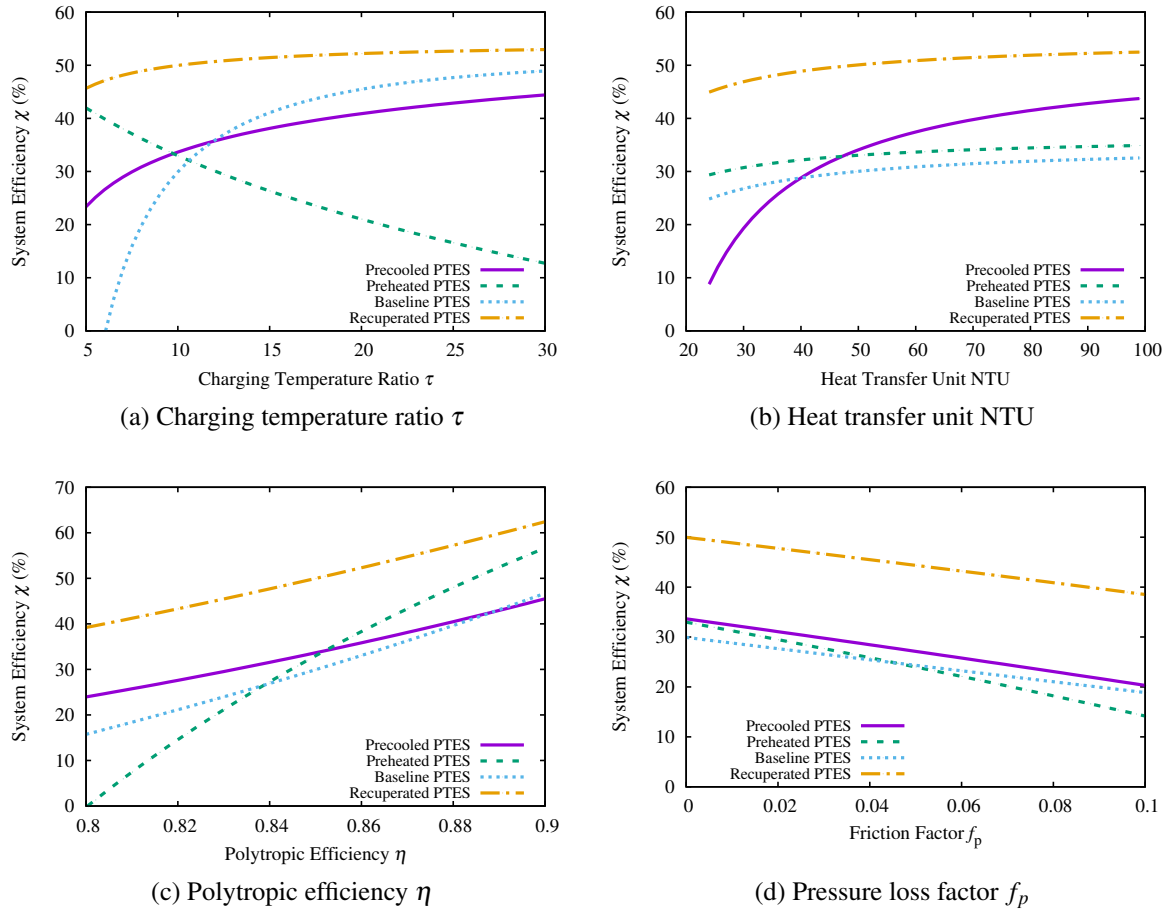

(a) Charging temperature ratio τ

(b) Heat transfer unit NTU

(c) Polytropic efficiency η

(d) Pressure loss factor f_p

Figure 4.9: Impacts of various operating parameters on the system efficiencies of various PTES systems: (a) Charging temperature ratio τ (b) Heat transfer unit NTU (c) Polytropic efficiency η (d) Pressure loss factor f_p

carried by the exhaust gas of expander during discharge is recuperated and recycled within the recuperated PTES, instead of being dissipated in the auxiliary heat exchanger like precooled PTES. Therefore, the recuperated PTES is not sensitive to the effectiveness ε either.

4.7.3 Polytropic efficiency effect

Fig. 4.9c shows the impacts of polytropic efficiency η on the system efficiencies χ of different PTES systems. Opposite to the impacts of effectiveness ε shown in Fig. 4.9b, the preheated PTES is the most sensitive PTES with respect to polytropic efficiency η, whilst the precooled PTES is the least sensitive one, as shown in Fig. 4.9c. This is because the discharging temperature ratio τ' of the preheated PTES is always higher than its charging one τ, as shown in Eq. (4.6), and as the polytropic efficiency η increases, the discharging temperature ratio τ' begins

to reduce and get close to τ. This decreasing τ', however, reduces the T_3' in Fig. 4.4b and the associated auxiliary losses, which in conjunction with the reduction of compressor/expander losses, causes the system efficiency χ to rise rapidly with η increasing.

Similarly, for the precooled PTES, its discharging temperature ratio τ' is always lower than its charging one τ, as shown in Eq. (4.4), and as the polytropic efficiency η increases, the discharging temperature ratio τ' begins to increase and get close to τ. This increasing τ', however, increases T_1' in Fig. 4.3b and the associated axillary losses, which offsets the reduction of compressor/expander losses to some extent and cause the system efficiency χ to rise slowly with η. The lines of the recuperated and precooled PTES are very similar because their discharging temperature ratio τ' are both set by the discharged temperature of the hot TES T_{H}'.

4.7.4 Pressure loss effect

The impacts of the pressure loss factor f_p on the system efficiencies χ of various PTES systems are shown in Fig. 4.9d, from which it can be noted that the precooled, preheated and recuperated PTES are all more sensitive to the pressure loss factor f_p than the baseline PTES system. This is because the pressure loss factor f_p not only increases the pressure loss, but also increases the auxiliary losses of the above three PTES systems. For example, in the precooled PTES system shown in Fig. 4.3b, although the discharging temperature ratio τ' is still set by the discharging compressor and constrained by the charging expander inlet temperature T_3 or the discharged hot TES temperature T_{H}', the actual expansion ratio during discharge is much lower due to the throttling of compressor outlet and expander inlet. Therefore, the expander outlet temperature T_1' and the auxiliary losses increase accordingly.

Similarly, in the preheated PTES shown in Fig. 4.4b, the discharging temperature ratio τ' is still set by the discharging expander and constrained by the charging compressor inlet temperature T_1 or the discharged cold TES temperature T_{C}', the actual compression ratio is much higher due to the throttling of compressor outlet and expander inlet. Therefore, the compressor outlet temperature T_3' and the auxiliary losses increases accordingly.

From Fig. 4.9d, it can also be noted that the preheated PTES is much more sensitive to f_p than the precooled PTES. This is because the impacts of pressure loss factor f_p on the T_3' in the preheated system is much more significant than on the T_1' in the precooled system, as indicated in Eqs. (4.4) and (4.6).

Table 4.4: Main results for the standard designs

	Precooled	Preheated	Baseline	Recuperated
System Efficiency	33.7 %	33.0 %	29.9 %	50.0 %
Cost per kWh	360 $/kWh	392 $/kWh	512 $/kWh	300 $/kWh
Capital Cost	62 M$	64 M$	86 M$	74 M$
Net Output Work	171 MWh	162 MWh	168 MWh	247 MWh
Net Input Work	507 MWh	492 MWh	564 MWh	494 MWh

4.8 Loss and cost distributions of the standard designs

In order to better understand the reasons for the performance difference of various PTES systems, the loss and cost distribution of all PTES variants at standard design are shown in Figs. 4.10a and 4.10b respectively. The main results of the standard designs for all PTES variants are summarized in Table 4.4. It is notable that the system efficiencies of the standard designs are relatively low (typically below 50 %) and much lower than the advocated 60 - 70 % in the references [19, 43, 60, 128]. This is because most published Brayton-cycle PTES employ solid TES (such as segmented thermal reservoir [19, 44]) rather than liquid ones due to their sensitivity to heat transfer losses, and it is much easier for solid TES to achieve larger heat transfer area and lower losses. Besides, most published Brayton-cycle PTES employ compression and expansion devices with either super high polytropic efficiency (such as the reciprocating devices designed by Isentropic [19, 43]) or super high temperature ranges (such as turbomachineray proposed by Saipem [21, 60]). These components are either unavailable or untested, and thus avoided in this thesis. Finally, the standard designs typically use parameters right in the middle of their feasible ranges, but parameters selected this way may severely deviate from their respective optimum, and the sensitivity of PTES to various losses further aggravate this scenario. Therefore, all these above-mentioned factors together contribute to the low system efficiency of PTES with standard designs. Since the Brayton-cycle PTES with liquid TES is a relatively new concept, there is few published cost estimates. Laughlin [128] made an estimation for a similar pressurized PTES and found the cost to be roughly 150 $/kWh, which is unsurprisingly much lower than the nominal cases. This is because his PTES is so pressurized that the cost is dominated by the heat exchangers, and similar PTES will be studied later in Chapter 8.

The loss distributions of all PTES variants are shown in Fig. 4.10a, from which it can be noted that the precooled PTES has the highest auxiliary losses (heat leakage losses generated in the auxiliary heat exchangers) whilst the recuperated PTES has the lowest ones. This is because unlike the precooled PTES where the waste heat is dissipated into the environment

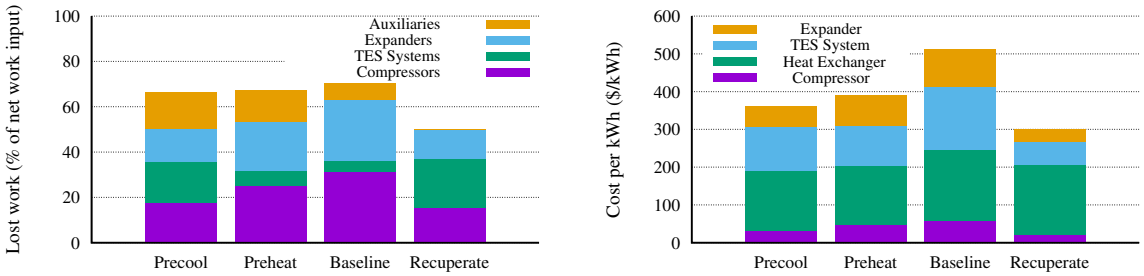

(a) Loss Distribution

(b) Cost Distribution

Figure 4.10: Loss and cost distributions of different PTES with standard designs: (a) Loss distribution (b) Cost distribution

via auxiliary heat exchangers, this energy is recycled in the recuperated PTES, as discussed in Section 4.2. Therefore, the recuperated PTES has the lowest auxiliary losses but the highest TES losses due to its large storage loss. From Fig. 4.10a, it can also be noted that the baseline PTES has the highest compressor/expander losses and the lowest TES losses. This is because the baseline PTES has the lowest temperature ranges and specific net work input due to its absence of preheating, precooling and recuperating.

The cost distributions of all PTES variants are shown in Fig. 4.10b, from which it can be noted that the compressor/expander costs form a small percentage of the total cost and this percentage can be further reduced with pressurization. As a result, the TES and heat exchanger costs will become dominant after the PTES is pressurized. From Fig. 4.10b, it can be noted that the baseline PTES has the highest TES cost whilst the recuperated PTES has the lowest one. This is because the temperature difference and energy density of the recuperated PTES is the highest whilst those of the baseline PTES is the lowest. It can also be noted that the recuperated PTES enjoys much lower compressor/expander costs than the baseline PTES due to its high specific net work input, and therefore, the unit storage cost of recuperated PTES is much lower than that of the baseline PTES despite its two extra recuperators. However, it should be noted that this conclusion is only valid for the nominal case and the optimal designs for all PTES variants as well as their comparisons will be dealt with in Chapter 8.

4.9 Summary

In this chapter, thermodynamic and economic models are built for each component and variant of PTES. Parametric studies are carried out for each PTES variant to study their relative sensitivity to each operating parameter. Comparisons are made and reasons are provided for their difference in performance. The loss and cost distributions are also provided for the nominal cases. From this chapter, it can be concluded that:

1. Baseline PTES is most sensitive to the temperature ratio τ but is least sensitive to the pressure loss factor f_p. It can also have independent temperature ratio for the charge and discharge process.

2. Precooled PTES is most sensitive to the heat exchanger effectiveness ε but is least sensitive to the polytropic efficiency η. It also has the highest auxiliary heat exchanger losses of all the PTES variants.

3. Preheated PTES is most sensitive to the polytropic efficiency η but is least sensitive to the heat exchanger effectiveness ε. Unlike other PTES variants, its round-trip efficiency χ decreases with the temperature ratio τ;

4. Recuperated PTES usually has the highest round-trip efficiency χ with the same ε and η. It also has the lowest auxiliary loss but the highest TES losses of all the PTES variants.

Chapter 5

Adiabatic Compressed Air Energy Storage

5.1 Introduction

In Adiabatic CAES (A-CAES), ambient air is first compressed near-adiabatically and its thermal energy is then stored separately in some forms of Thermal Energy Storage (TES). Depending on the number of stages N_{stg}, this process is repeated several times before storing the pressurized air in an air reservoir. Therefore, electricity is stored in the forms of temperature potential of the TES and pressure potential of the air reservoir, and as a result, the TES and air reservoir become the central components for A-CAES.

Depending on the types of air reservoir, A-CAES can be categorized into isobaric A-CAES, such as underwater A-CAES, which stores the compressed air at constant pressure in a series of submerged air accumulators; or an isochoric A-CAES, such as underground A-CAES, which stores the compressed air at constant volume in an solution-mined cavern. In addition to the air reservoirs, an A-CAES can also be categorized as a solid, liquid or hybrid A-CAES depending on the types of its TES. For example, the thermal energy of compressed air may be transferred to liquid tanks by cooling it through a heat exchanger as the thermal fluids circulate within it. Alternatively, it may be transferred directly to a solid storage materials, for example in a packed bed. However, despite these and many other studies of different A-CAES configurations, a comparative study of liquid and solid based systems from a thermo-economic perspective is relatively scant. This work has been conducted by Xue and White in Ref. [52] and the results are included in this chapter.

In this chapter, the layout of a typical A-CAES is introduced first, and then both the analytical and numerical models of an air reservoir are built and integrated into the A-CAES.

Analytical expressions of the system efficiency and energy density are derived for specific cases and validated with the numerical results of A-CAES. Then the impacts of various cavern parameters on the losses of cavern ("direct losses") and other components ("indirect losses") are analyzed individually. A case study of the Huntorf CAES cavern is carried out and the actual losses are estimated from the validated heat transfer correlations. After that, parametric studies are conducted for A-CAES with solid, liquid and hybrid TES, and their results are compared with each other. The economical models for different air reservoirs are also built, and the loss and cost distributions for the nominal design are provided.

5.2 Cycle layouts

A general A-CAES configuration comprises N stages of compression/expansion, with some form of TES between each stage, and an air-storage cavern or accumulator. The TES need not be the same for all stages: for example, for the system shown in Fig. 5.1, there is one stage of solid TES and liquid TES. This system is referred to as the hybrid A-CAES and within it the pressure ratio is the same for each like stage. If there are n solid TES and $N-n$ liquid TES in the hybrid A-CAES, then the pressure ratio of each stage is given by:

The first n stages with solid TES:

$$\beta_i = \left(\frac{p_\mathrm{m}}{p_0}\right)^{\frac{1}{n}} \quad (i \leq n) \tag{5.1}$$

The rest $N-n$ stages with liquid TES:

$$\beta_i = \left(\frac{p}{p_\mathrm{m}}\right)^{\frac{1}{N-n}} \quad (i > n) \tag{5.2}$$

where p, p_m and p_0 refer to the cavern pressure, the intermediate pressure between solid and liquid TES stages, and the ambient pressure respectively. For a solid only system $p_\mathrm{m} = p$, whereas for a liquid only system $p_\mathrm{m} = p_0$. The heat transfer between the compressed air and the liquid media is usually achieved through the main heat exchangers, for which the heat transfer losses are inversely related to the size and cost of the device. This indirect contact separates the working fluid from the liquid media, and thus enables the cost of liquid TES to be independent of the operating air pressure. For solid TES, on the other hand, it is easier (though not essential) to exploit direct-contact heat transfer between the air and solid media. For example, a packed-bed thermal reservoir can fulfill this function, and the heat transfer losses can be decreased by reducing the particle size, without increasing the capital cost simultaneously. However, direct-contact heat transfer requires the operating pressure of

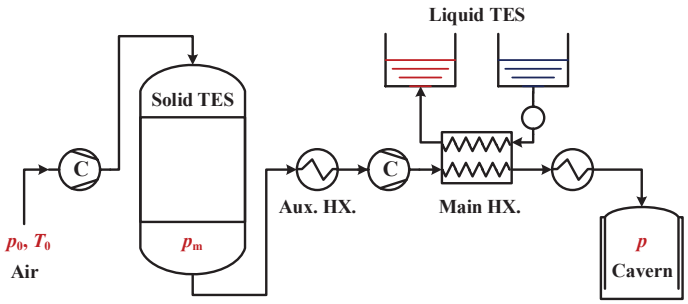

Figure 5.1: Schematic diagram of the hybrid A-CAES system

the solid TES to be the same as that of the air, thus the capital cost of solid TES (dominated by the pressure vessel) is more or less proportional to the operating pressure. However, solid TES benefits from a wider temperate range and as a result it is usually operated at higher temperature, such as ~600 °C. Liquid storage is generally operated at temperature up to ~300 °C, depending on the storage fluid and storage pressure. It is assumed here that all forms of storage (i.e., solid or liquid) have the same maximum allowable temperature and hence the pressure ratio is equally partitioned amongst each like stage (see Eqs. (5.1) and (5.2))

Auxiliary heat exchangers are included in the cycle after each TES, as shown in Fig. 5.1, to further cool the air to ambient temperature T_0. This prevents the inlet temperature of the next stages becoming too high if the solid TES is small (such that thermal fronts emerge from their exit) or the liquid TES is inefficient. Since the waste heat is not recycled but simply dissipated in the auxiliary heat exchangers, a high water flow rate (hence a low heat capacity ratio C_r) is usually adopted to reduce the heat exchanger size and cost. The effectiveness of any heat exchanger with $C_r = 0$ is given by $\varepsilon = 1 - \exp(-\text{NTU})$ [126], so with the "number of thermal units" as low as NTU $= 2$, an effectiveness ε of 0.86 is attained. This type of auxiliary heat exchanger is used for each TES and its cost added into the total.

In the absence of pressure losses (as in many cycle analyses) the stage pressure ratios during compression (charge) and expansion (discharge) are the same so that $\beta_c = \beta_e = \beta_i$. However, in order to study the impact of pressure losses (for example, those generated by heat exchangers and packed beds) in a simple and general manner, a pressure loss factor f_p is applied to each stage. Thus the actual stage compression ratio becomes $\beta_c = \beta_i / (1 - f_p)$, whilst stage expansion ratio is $\beta_e = \beta_i (1 - f_p)$. In practice, the pressure loss factors are dominated by viscous effects in heat exchangers and packed beds.

After N stages of compression, the compressed air is finally stored in an air reservoir, as shown in Fig. 5.1. Although artificial air reservoirs have been proposed by many researchers, the size for a large-scale CAES cavern (400 - 800 MWh) is in the range of 150,000 to 500,000 m^3. Solution mining or the use of existing natural caverns are therefore the most feasible

options. In this chapter, the energy and power of the A-CAES are set as 400 MWh and 100 MW respectively and the cavern volume is calculated from the energy distribution between the cavern and each TES. The cavern is isochoric by nature and therefore, the pressure fluctuates within a range of $p_{\min}$ to $p_{\max}$. The value of $p_{\max}$ is constrained by the geological conditions (e.g., the depth of the cavern) whilst $p_{\min}$ is determined by the extent of discharge and the minimum pressure required to maintain the cavern's integrity. Storage density and round-trip efficiency will generally depend on both $p_{\max}$ and the ratio $p_{\min}/p_{\max}$. The concepts of maximum pressure ratio $R_c = p_{\max}/p_0$ and fluctuation factor $\alpha = p_{\min}/p_{\max}$ are thus introduced to measure these two effects. Therefore, if the system pressure ratio of an A-CAES is equally partitioned among the N stages, then as the system pressure ratio varies from αR_c to R_c during charge, the pressure ratio of each stage varies from $\alpha^{1/N}\beta_c$ to β_c. The economic models of other air reservoirs, such as underwater air accumulators, are also provided in this chapter, but their impacts on the system performance will be dealt with in Chapter 8.

The TES subsystems all include the following three components: storage material (i.e. liquid or solid), containment vessel (or tank) and insulation layer. For the solid TES, the commonly used packing materials are natural stones, ceramic and metal oxides, which are generally very cheap and have wide temperature range. Materials selection essentially becomes finding the one with the largest volumetric heat capacity because cost tends to be dominated by the pressure vessel. On the basis of work reported in [59], magnetite (Fe_3O_4) has been used as the solid storage medium for the analysis presented here, and the maximum temperature is set at 600 °C. For liquid TES, mineral oil, molten salt and water are the most widely used thermal fluids. Their selection, however, is less straightforward due to the vast differences of cost, heat capacity and operating temperature range. A simple multi-objective optimization has therefore been carried out in Chapter 8, from which mineral oil is selected as the best option. The maximum allowable temperature is accordingly set as 340 °C [10, 11].

5.3 Thermodynamic modeling of the air reservoirs

In this section, the thermodynamic models of different air reservoirs will be given. These models will then be integrated with other component models in Section 5.5 to establish a complete set of thermodynamic models for different A-CAES systems. Both numerical and analytical models will be developed and the analytical results will then be used to support the numerical ones in Section 5.6.

5.3.1 Numerical modeling

The dynamics of the cavern (or air reservoir) must satisfy the conservation equations for mass and energy, which have been given in the literature [50, 77]. For a constant volume (isochoric) cavern of volume V, these may be written:

$$\frac{\mathrm{d}m}{\mathrm{d}t} = \dot{m}_{\mathrm{in}} - \dot{m}_{\mathrm{out}} \tag{5.3}$$

$$\frac{\mathrm{d}T}{\mathrm{d}t} = \frac{1}{mc_v}\left[\dot{Q} + \dot{m}_{\mathrm{in}} c_p T_{\mathrm{in}} - \dot{m}_{\mathrm{out}} c_p T - \frac{\mathrm{d}m}{\mathrm{d}t} c_v T\right] \tag{5.4}$$

where m and T are the mass and temperature of the cavern respectively. These equations are completed by equations of state which, for the present analysis, are based on perfect gas relations. The heat transfer rate to the cavern from the surroundings, $\dot{Q}$, is quantified by the dimensionless heat transfer coefficient λ:

$$\lambda = \frac{\dot{Q}}{\dot{m} c_p (T - T_0)} = \mathrm{St}\frac{A}{A_{\mathrm{c}}} \tag{5.5}$$

where A and A_{c} are the cavern surface area and cross-sectional inlet area respectively, and St is the Stanton number, $\mathrm{St} = U/\left(\dot{G}c_p\right)$, with U being the heat transfer coefficient. As the dimensionless heat transfer coefficient λ increases from 0 to infinity, the behavior of the cavern changes from adiabatic to isothermal. Natural caverns lie somewhat in the intermediate range and a nominal value of $\lambda = 10$ has been used for most calculations, but the effect of different values on the cost and efficiency is explored in Sections 5.6 and 5.8.

The exergetic losses of a cavern (or an air reservoir) includes thermal loss, heat leakage loss and the storage loss. The thermal loss is caused by the mixing of the inlet air and the cavern air, which are often at different temperatures. The entropy generation rate associated with this process is:

$$\dot{S}_t = \dot{m}_{\mathrm{in}} c_p \left(\frac{T_{\mathrm{in}}}{T} - 1 - \ln\frac{T_{\mathrm{in}}}{T}\right) \tag{5.6}$$

As cavern leaks heat into its surroundings, there is a loss of exergy with this heat flow, and its entropy generation rate can be calculated by:

$$\dot{S}_l = \dot{Q}\left(\frac{1}{T_0} - \frac{1}{T}\right) = UA\frac{(T - T_0)^2}{T_0 T} \tag{5.7}$$

In addition to the thermal and heat leakage losses (during charge and discharge), the cavern may also have storage loss if the storage process lasts for a long time and the cavern gradually

cools down towards the ambient temperature T_0. If all the thermal exergy stored within the cavern is lost, the associated rate of work loss is:

$$\xi_s = m\left[b\left(T, v\right) - b\left(T_0, v\right)\right] \tag{5.8}$$

5.3.2 Analytical modeling

The analytical model of a cavern (or an air reservoir) has been analyzed in details in Ref. [50], however, some important conclusions are included here for the sake of completeness. According to the characteristics such as pressure variation and thermal insulation, an air reservoir can be further categorized into an isobaric air reservoir, isochoric and isothermal air reservoir, and isochoric and adiabatic air reservoir. It has been proved in Ref. [50] that for an isobaric air reservoir, if the temperature of inlet and cavern air are both at the ambient value T_0, then there is no heat exchange between the isobaric cavern and its surroundings. In this circumstance, the increment of cavern mass could be expressed as:

$$\mathrm{d}m = \frac{p_{\max}}{R_g T_0}\mathrm{d}V \tag{5.9}$$

In Eq. (5.9), both the inlet and the cavern temperature are at the ambient value T_0. This assumption is warranted since there is always an efficient auxiliary heat exchanger (or "after-cooler") at the cavern inlet for protection and the cavern is usually operated at ambient temperature.

For an isochoric cavern, it can be noted from Eq. (5.3) that $\dot{m}_{\mathrm{in}} = \mathrm{d}m/\mathrm{d}t$ for the charge; whilst $\dot{m}_{\mathrm{out}} = -\mathrm{d}m/\mathrm{d}t$ for the discharge. Therefore, if we further assume $\lambda_{\mathrm{p}} = \dot{Q}/\left(\dot{m}c_v\right)$ and make use of the equation of state, then Eq. (5.4) can be simplified to:

$$\mathrm{d}m = \frac{V}{R_g}\frac{\mathrm{d}p}{\lambda_p + \gamma T_0} \tag{5.10}$$

for the charge; whilst for the discharge, the T_0 in Eq. (5.10) should be replaced by T. In addition, it can be proved that for an isothermal cavern, $\lambda_{\mathrm{p}} = \left(1-\gamma\right)T_0$; whilst for an adiabatic cavern, $\lambda_{\mathrm{p}} = 0$. Therefore, for an isothermal cavern, the following expression of mass increment can be derived:

$$\mathrm{d}m = \frac{V}{R_g T_0}\mathrm{d}p = m_0 N \beta^{N-1}\mathrm{d}\beta \tag{5.11}$$

where β is the instantaneous pressure ratio of each stage, which varies from β_{d} to β_{c}; and m_0 is the mass of the air when the cavern is at ambient pressure, which is given by $m_0 = p_0 V/\left(R_g T_0\right)$. In this thesis, the boundary of an isothermal cavern is assumed to be at ambient

temperature T_0, without any energy storage capability and maintains sufficient heat exchange with the air within the cavern.

For an adiabatic cavern, the expressions of the mass increment are different for charge and discharge. During charge, we have:

$$\mathrm{d}m = \frac{V}{\gamma R_g T_0}\mathrm{d}p = \frac{m_0}{\gamma} N\beta^{N-1}\mathrm{d}\beta \tag{5.12}$$

whilst during discharge, the equation becomes:

$$\mathrm{d}m = \frac{V}{\gamma R_g T}\mathrm{d}p = \frac{m_0}{\gamma}\frac{T_0}{T} N\beta^{N-1}\mathrm{d}\beta \tag{5.13}$$

It can be noted from Eq. (5.13) that the cavern temperature T is a function of the cavern pressure p, therefore, this equation cannot be used directly for integration. Instead, the charged and discharged temperature ratios of the cavern must be calculated first, which are respectively $\tau_\mathrm{c} = T_\mathrm{c}/T_0$ and $\tau_\mathrm{d} = T_\mathrm{d}/T_0$. By integrating Eq. (5.12) from the discharged state to the charged one, and then integrating Eq. (5.13) from the charged state to the discharged one, the following equations can be derived respectively:

$$\frac{\tau_\mathrm{d}}{\tau_\mathrm{c}} = \alpha\frac{\tau_\mathrm{d} - \gamma}{\tau_\mathrm{c} - \gamma} \tag{5.14}$$

$$\frac{\tau_\mathrm{d}}{\tau_\mathrm{c}} = \alpha^{\frac{\gamma-1}{\gamma}} \tag{5.15}$$

Then by solving Eqs. (5.14) and (5.15), the expression of charged temperature ratio τ_c is as follows:

$$\tau_\mathrm{c} = \gamma\frac{1-\alpha^{\frac{1}{\gamma}}}{1-\alpha} \tag{5.16}$$

In addition, according to Eq. (5.15), the temperature T at pressure p is:

$$\frac{T}{T_\mathrm{c}} = \left(\frac{p}{p_\mathrm{c}}\right)^{\frac{\gamma-1}{\gamma}} \tag{5.17}$$

After substituting Eqs. (5.16) and (5.17) into Eq. (5.13), the following equations could be derived after rearranging:

$$\mathrm{d}m = \frac{m_0}{\gamma}\frac{T_0}{T_\mathrm{c}}\beta_\mathrm{c}^{Nk} N\beta^{N(1-k)-1}\mathrm{d}\beta \tag{5.18}$$

where k is the isentropic exponent, $k = (\gamma-1)/\gamma$.

The above equations, such as Eqs. (5.9), (5.11), (5.12) and (5.18), will be used to calculate the analytical expression of the system efficiency χ and energy density D of different types of A-CAES systems in Section 5.6.

5.4 Cost modeling of the air reservoirs

In this section, the cost equations of underground cavern and submerged air accumulator will be provided. The former is developed on the basis of the cost data provided in Ref. [4] whilst the latter is cited from Ref. [30]. Although efforts have been made to ensure these cost equations are as accurate as possible, they are developed separately and not designed for a rigorous comparison. Therefore, the conclusions derived from these cost equations should be treated with caution.

5.4.1 Underground cavern costs

The cost of a cavern depends largely on its source, type and geological condition. In this chapter, only the cost equation of solution-mined caverns is employed, mainly due to their technical maturity, wide availability and relatively low capital cost. The solution-mined cavern cost can be divided into the well cost and the solution-mining cost, both of which are proportional to the cavern depth (because deeper caverns call for more drilling and pumping). In addition, the well cost is proportional to the diameter of the bore hole whilst the mining cost is proportional to the cavern volume V. Since the rated power of all A-CAES considered here is close to that of the McIntosh plant, the size of the bore hole is considered as constant and not taken into account in this cost equation. The cavern depth, according to Ref. [129], is proportional to the maximum cavern pressure $p_{\max}$. The following cost relation is thus applied:

$$Z_{\text{cave}} = (C_{\text{well}} + C_{\text{mine}} V)\, p_{\max} \tag{5.19}$$

where C_{well} and C_{mine} are coefficients corresponding to drilling and solution mining respectively, values of which (corrected for inflation) are inferred from the McIntosh CAES plant costs in Ref. [4] and are summarized in Table 5.1.

5.4.2 Submerged accumulator costs

In an Under Water CAES (UW-CAES) systems, air is stored at constant pressure in a series of submerged air accumulators placed near the beds of deep water bodies. Air stored this way is

Table 5.1: Constants used in the cost modelling of air reservoirs

Components	Constants	
Underground Cavern	$C_{\text{well}} = 41275\,\$/\text{bar}$	$C_{\text{mine}} = 0.11\,\$/\text{bar}\cdot\text{m}^3$
Underwater Accumulator	$C_{\text{p1}} = 3.6\,\$/\text{m}$	$C_{\text{p2}} = 0.00864\,\text{m}^{-1}$
	$C_{\text{acc}} = 6500\,\$$	

bounded hydrostatically to the pressure exerted by the water at depth z, which is given by the following equation:

$$p_{\text{max}} = p_0 + \rho_{\text{w}} g z \tag{5.20}$$

where p_{max} is the pressure of the isobaric accumulators and ρ_{w} is the density of water. The unit volume of each air accumulator is usually fixed at V_{acc} and the number of air accumulators is simply calculated by $N_{\text{acc}} = V/V_{\text{acc}}$, where V is the total volume of the stored air which is determined by the rated energy E of an UW-CAES system. Hence, the cost of these submerged air accumulators can be simply calculated by:

$$Z_{\text{acc}} = C_{\text{acc}} N_{\text{acc}} \tag{5.21}$$

The cost of the long air delivery pipes connecting the offshore submerged air accumulators and the onshore energy conversion and thermal recovery components is proportional to the length L_{pipe} and depends on the diameter D_{pipe} of the pipes, which, according to Ref. [30], is given by:

$$Z_{\text{pipe}} = C_{\text{p1}} L_{\text{pipe}} \exp(C_{\text{p2}} D_{\text{pipe}}) \tag{5.22}$$

where the length of the pipe L_{pipe} is determined by the depth z of the air accumulators, whilst its diameter D_{pipe} is determined by the mass flowrate $\dot{m}$. In the following parametric and optimization study, the power input is fixed at $P = 100\,\text{MW}$, and as a result, a constant pipe diameter is assumed, $D_{\text{pipe}} = 500\,\text{mm}$. These data are obtained from Ref. [30] and are summarized in Table 5.1.

5.5 Simplified analytical models of an A-CAES

In this section, the analytical models for A-CAES with isobaric air reservoir, isothermal and adiabatic cavern will be developed. The isobaric A-CAES model can be applied to Underwater A-CAES and underground CAES with water equalizing pits, as mentioned in Chapter 2. The

isochoric A-CAES models with isothermal and adiabatic caverns can be used to determine the ranges of an actual underground A-CAES. In addition, the analytical results of these models will be shown as dots in Section 5.6 to support the results of numerical models.

5.5.1 Modelling of an A-CAES with isobaric air reservoir

The A-CAES with an isobaric air reservoir is essentially the baseline A-CAES in Chapter 3. Its thermodynamic models have been provided in Section 3.3.1 and are thus omitted here to avoid repetition.

5.5.2 Modelling of an A-CAES with isochoric and isothermal cavern

Unlike the A-CAES with an isobaric air reservoir, the A-CAES with an isochoric cavern has a varying pressure ratio, therefore, both the specific work of each stage and the TES temperature varies accordingly. In order to calculate the total work consumed during charge, one feasible method is by integrating the product of the mass increment of cavern air dm (see Eq. (5.11)) and the specific work of N compressors (see Eq. (4.19)) from the discharged state to the charged one:

$$\begin{aligned} W_{\mathrm{ac}} &= \int_{\beta_{\mathrm{d}}}^{\beta_{\mathrm{c}}} N^2 m_0 c_p T_0 \left(\beta^{\phi_{\mathrm{ac}}} - 1\right) \beta^{N-1} \mathrm{d}\beta \\ &= N m_0 R_{\mathrm{c}} \left(1-\alpha\right) c_p T_0 \left(\mathrm{A}\beta^{\phi_{\mathrm{ac}}} - 1\right) \end{aligned} \tag{5.23}$$

where β is the instantaneous pressure ratio of each stage, which varies from $\alpha^{\frac{1}{N}}\beta_{\mathrm{c}}$ to β_{c}, and A is given by:

$$\mathrm{A} = \frac{N}{N+\phi_{\mathrm{ac}}} \frac{1-\alpha^{\frac{N+\phi_{\mathrm{ac}}}{N}}}{1-\alpha}$$

The total mass of compressed air can be calculated by:

$$m = \int_{\beta_{\mathrm{d}}}^{\beta_{\mathrm{c}}} \mathrm{d}m = m_0 R_{\mathrm{c}} \left(1-\alpha\right) \tag{5.24}$$

It is difficult to devise a thermocline system for liquid TES, therefore, as the thermal fluids with different temperature mix with each other, the average TES temperature at the end of the charging process is:

$$T_{\mathrm{TES}} = \frac{\int_{\beta_{\mathrm{d}}}^{\beta_{\mathrm{c}}} \left[\varepsilon T_0 \beta^{\phi_{\mathrm{ac}}} + (1-\varepsilon) T_0\right] \mathrm{d}m_{\mathrm{f}}}{\int_{\beta_{\mathrm{d}}}^{\beta_{\mathrm{c}}} \mathrm{d}m_{\mathrm{f}}}$$
$$= \varepsilon T_0 \beta_{\mathrm{c}}^{\phi_{\mathrm{ac}}} \mathrm{A} + (1-\varepsilon) T_0 \tag{5.25}$$

During discharge, the inlet temperature of the expanders is:

$$T_{\mathrm{ex}} = \kappa \varepsilon^2 T_0 \beta_{\mathrm{c}}^{\phi_{\mathrm{ac}}} \mathrm{A} + \left(1 - \kappa \varepsilon^2\right) T_0 \tag{5.26}$$

By using similar integrating methods with the compressors, the total generated work of N expanders during discharge can be calculated by:

$$W_{\mathrm{ex}} = \int_{\beta_{\mathrm{d}}}^{\beta_{\mathrm{c}}} m_0 N^2 c_p T_{\mathrm{ex}} \left(1 - \beta^{-\phi_{\mathrm{ex}}}\right) \beta^{N-1} \mathrm{d}\beta$$
$$= N m_0 R_{\mathrm{c}} (1-\alpha) c_p T_{\mathrm{ex}} \left(1 - \mathrm{B} \beta_{\mathrm{c}}^{-\phi_{\mathrm{ex}}}\right) \tag{5.27}$$

where B is given by

$$\mathrm{B} = \frac{N}{N - \phi_{\mathrm{ex}}} \frac{1 - \alpha^{\frac{N-\phi_{\mathrm{ex}}}{N}}}{1-\alpha}$$

Therefore, the system efficiency χ of the A-CAES with isochoric and isothermal caverns could be expressed as:

$$\chi_{\mathrm{VT}} = \frac{W_{\mathrm{ex}}}{W_{\mathrm{ac}}} = \frac{T_{\mathrm{ex}}}{T_0} \frac{1 - \mathrm{B} \beta_{\mathrm{ex}}^{-\phi_{\mathrm{ex}}}}{\mathrm{A} \beta_{\mathrm{ac}}^{\phi_{\mathrm{ac}}} - 1} \tag{5.28}$$

5.5.3 Modelling of an A-CAES with isochoric and adiabatic cavern

Of all the A-CAES discussed in this chapter, the A-CAES with an isochoric and adiabatic cavern is the most complicated case, however, the analyzing method remains similar. By integrating the product of the mass increment of cavern air dm (see Eq. (5.12)) and the specific work of N compressors (see Eq. (4.19)) from the discharged state to the charged one, the total work consumed during charge can be expressed as:

$$
\begin{aligned}
W_{\mathrm{ac}} &= \int_{\beta_{\mathrm{d}}}^{\beta_{\mathrm{c}}} \frac{m_0}{\gamma} N^2 c_p T_0 \left(\beta^{\phi_{\mathrm{ac}}} - 1\right) \beta^{N-1} \mathrm{d}\beta \\
&= N \frac{m_0}{\gamma} R_{\mathrm{c}} \left(1-\alpha\right) c_p T_0 \left(\mathrm{A}\beta^{\phi_{\mathrm{ac}}} - 1\right)
\end{aligned} \tag{5.29}
$$

Similarly, as the pressure ratio increases from $\alpha^{\frac{1}{N}}\beta_{\mathrm{c}}$ to β_{c}, the total mass of compressed air can be calculated by:

$$
m = \int_{\beta_{\mathrm{d}}}^{\beta_{\mathrm{c}}} \mathrm{d}m = \frac{m_0}{\gamma} R_{\mathrm{c}} \left(1-\alpha\right) \tag{5.30}
$$

By comparing Eqs. (5.29) and (5.30) with Eqs. (5.23) and (5.24), it can be noted that the total compression work W_{ac} and the total mass of compressed air m of the A-CAES with an isochoric and isothermal cavern is γ times that of the A-CAES with an isochoric and adiabatic cavern. It is also notable that the average specific compression work are the same, whilst the only difference is the mass of air stored in the isothermal and adiabatic caverns.

By using the similar method in Section 5.5.2, the average TES temperature at the end of the charge process is:

$$
\begin{aligned}
T_{\mathrm{TES}} &= \frac{\int_{\beta_{\mathrm{d}}}^{\beta_{\mathrm{c}}} \left[\varepsilon T_0 \beta^{\phi_{\mathrm{ac}}} + \left(1-\varepsilon\right) T_0\right] \mathrm{d}m_{\mathrm{f}}}{\int_{\beta_{\mathrm{d}}}^{\beta_{\mathrm{c}}} \mathrm{d}m_{\mathrm{f}}} \\
&= \varepsilon T_0 \beta_{\mathrm{c}}^{\phi_{\mathrm{ac}}} \mathrm{A} + \left(1-\varepsilon\right) T_0
\end{aligned} \tag{5.31}
$$

By comparing Eq. (5.31) with Eq. (5.25), it can be noted that the T_{TES} of A-CAES with isothermal and adiabatic caverns are the same. However, the T_{TES} of both cases are lower than that of an isobaric A-CAES, but the difference is not significant enough to change the energy distribution between the cavern and TES.

During discharge, the inlet temperature of the expanders is the same with Eq. (5.26). Therefore, by integrating the product of the mass decrement of cavern air dm (see Eq. (5.18)) and the specific work of N expanders (see Eq. (4.19)) from the charged state to the discharged one, the total generated work W_{ex} can be expressed as follows:

Table 5.2: The standard, minimum and maximum design variable values of A-CAES for the sensitivity study

	N_{stg}	$p_{\max}$	$p_{\min}/p_{\max}$	λ	ε	η	f_p
Standard	1	50	0.55	1000	1.00	1.00	0.00
Minimum	1	10	0.10	0.001	0.70	0.70	0.00
Maximum	3	150	0.99	1000	1.00	1.00	0.30

$$\begin{aligned} W_{\text{ex}} &= \int_{\beta_{\text{d}}}^{\beta_{\text{c}}} \frac{m_0}{\gamma}\frac{T_0}{T_{\text{c}}}\beta_{\text{c}}^{Nk}N^2 c_p T_{\text{ex}}\left(1-\beta^{-\phi_{\text{ex}}}\right)\beta^{N(1-k)-1}\mathrm{d}\beta \\ &= Nm_0R_{\text{c}}\frac{T_0}{T_{\text{c}}}\left(1-\alpha^{\frac{1}{\gamma}}\right)c_p T_{\text{ex}}\left(1-\mathrm{C}\beta^{-\phi_{\text{ex}}}\right) \end{aligned} \tag{5.32}$$

where C is given by

$$\mathrm{C} = \frac{N}{N-\gamma\phi_{\text{ex}}}\frac{1-\alpha^{\frac{N-\phi_{\text{ex}}}{N\gamma}}}{1-\alpha^{\frac{1}{\gamma}}}$$

Therefore, after dividing the total expansion work W_{ex} by the total compression work W_{ac}, then the system efficiency χ of an A-CAES with isochoric and adiabatic caverns can be expressed as:

$$\chi_{\text{VA}} = \frac{W_{\text{ex}}}{W_{\text{ac}}} = \frac{T_{\text{ex}}}{T_0}\frac{1-\mathrm{C}\beta_{\text{ex}}^{-\phi_{\text{ex}}}}{\mathrm{A}\beta_{\text{ac}}^{\phi_{\text{ac}}}-1} \tag{5.33}$$

5.6 The impact of air reservoir on A-CAES

After the theoretical analysis in Section 5.5, numerical models of A-CAES have been built by integrating the numerical model of cavern in Section 5.3.1 with those of other components in Section 4.3. Then parametric study will be carried out in this section to study the effect of each cavern parameter on the system performance. The standard, minimum and maximum values of each parameter has been been summarized in Table 5.2. As each parameter varies from its minimum to maximum, all the other parameters are hold constant at their standard value. The theoretical results of the previous sections are shown as solid dots whilst the numerical results are shown as solid lines. The dashed lines, if not otherwise specified, denote the sum of the system efficiency χ and all the various losses ξ, which are mainly used to make sure there is no loss omitted and the calculation results are correct.

5.6.1 The effect of maximum pressure on system efficiency

The effects of maximum pressure $p_{\max}$ on the system efficiency are highly dependent on the loss distribution of the system components. For example, if all the components are free from any loss and the cavern is isobaric, then the system efficiency is always 100 %, which is independent of the maximum pressure $p_{\max}$. However, if the A-CAES is dominated by a certain type of loss ξ_i, then the system efficiency χ may increase or decrease with the maximum pressure $p_{\max}$ due to the variation of this loss ξ_i, as $\chi \approx 1 - \sum \xi_i$. To find out how each component loss ξ_i varies with the maximum pressure $p_{\max}$ and stage number N, each of the parameters in Table 5.2 varies individually within the range and the results are shown in Fig. 5.2 and Table 5.3.

From Figs. 5.2a and 5.2b, it can be noted that when ε and κ are fixed, the system efficiency χ decreases with the maximum pressure $p_{\max}$ but increases with the stage number N. This is because all these losses are heat transfer losses which stem from temperature difference. Since a low maximum pressure $p_{\max}$ and a high stage number N correspond to a low pressure ratio per stage β, therefore, it can be concluded that in order to reduce the irreversible heat transfer loss stemming from temperature difference, the pressure ratio per stage β should be reduced.

From Figs. 5.2c and 5.2d, it can be noted that when η and f_p are fixed, then the system efficiency χ increases with the maximum pressure $p_{\max}$ but decreases with the stage number N. This is because these losses are mechanical losses which stem from viscosity. Since a high maximum pressure $p_{\max}$ and a low stage number N corresponds to a high pressure ratio per stage β, therefore, it can be concluded that in order to reduce the mechanical losses due to viscosity, the pressure ratio per stage β should be increased.

From Fig. 5.2e, it can be noted that the system efficiency χ increases with the fluctuation factor α, whilst when α is fixed, the system efficiency χ increases with both the maximum pressure $p_{\max}$ and the stage number N. This is because the main losses caused by the fluctuation factor α are the cavern losses (direct losses), TES loss and the system exit loss, all of which decrease with α but increase with $p_{\max}$. However, with $p_{\max}$ increasing, the compression work increases much faster than the losses, which then reduces the percentage of losses and increases the system efficiency. Meanwhile, larger stage number N means less pressure variation within one stage, which can significantly reduce the TES thermal loss and system exit loss. Therefore, the losses caused by pressure fluctuation can be mitigated by using higher maximum pressure $p_{\max}$ and larger number of stages N.

The conclusions of the above analysis are summarized in Table 5.3. From Table 5.3, it can be clearly seen that the heat transfer loss stemming from temperature difference and the mechanical loss due to viscosity have shown opposite trends. Therefore, in an A-CAES dominated by the heat transfer losses, it is beneficial to reduce the pressure ratio per stage β,

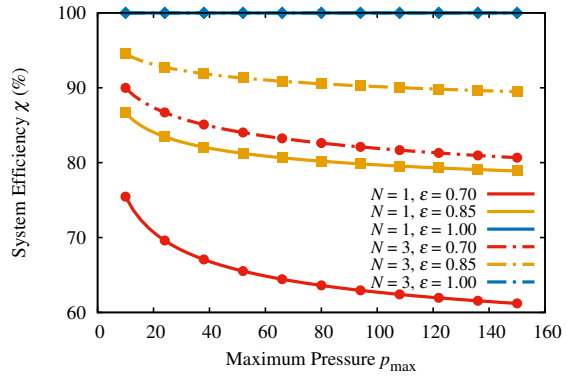

(a) heat exchanger effectiveness ε

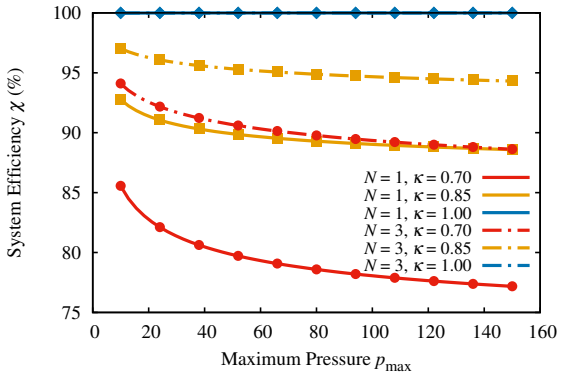

(b) TES insulation factor κ

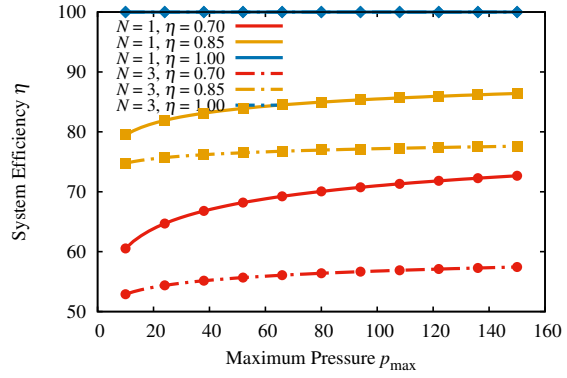

(c) compressor/expander efficiency η

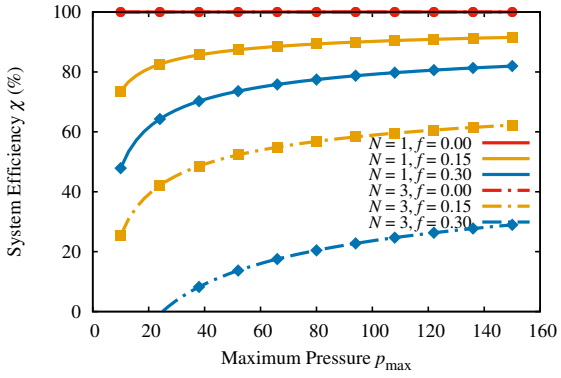

(d) pressure loss factor f_p

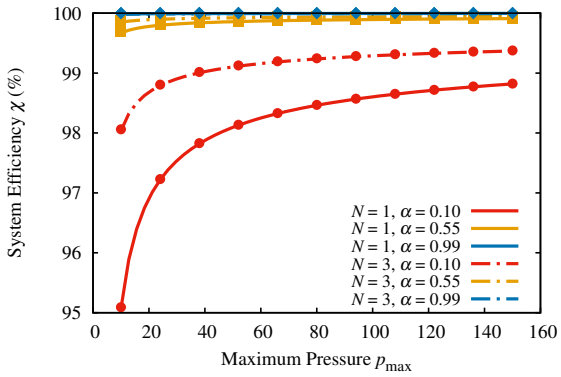

(e) fluctuation factor α

Figure 5.2: The effects of maximum pressure p_{max} on the system efficiencies χ at different number of stages N and (a) heat exchanger effectiveness ε (b) TES insulation factor κ (c) compressor/expander efficiency η (d) pressure loss factor f_p (e) fluctuation factor α

Table 5.3: The conclusions of the effects of maximum pressure on the A-CAES

	System Efficiency χ	Maximum Pressure $p_{\max}$	Stage Number N
H. Ex. Effectiveness ε	increase ($\uparrow$)	decrease ($\downarrow$)	increase ($\uparrow$)
TES Insulation Factor κ	increase ($\uparrow$)	decrease ($\downarrow$)	increase ($\uparrow$)
Polytropic Efficiency η	increase ($\uparrow$)	increase ($\uparrow$)	decrease ($\downarrow$)
Friction Factor f_p	increase ($\uparrow$)	increase ($\uparrow$)	decrease ($\downarrow$)
Fluctuation Factor α	increase ($\uparrow$)	increase ($\uparrow$)	increase ($\uparrow$)

whilst in an A-CAES dominated by the mechanical losses, it is better to increase the β. It can also be noted from Table 5.3 that the losses caused by fluctuation factor α has different trends from the other ones, which makes the analysis of isochoric A-CAES even more complicated. For example, as α increases, the average pressure ratio $\bar{\beta}$ also increases, which may further affect the losses of other components.

5.6.2 The effect of fluctuation factor on system efficiency

From the last section, we know that the system efficiency χ increases with the fluctuation factor α. However, it is still unclear how the losses are generated and how they vary with α. To focus on the effect of pressure fluctuation on the system efficiency, all the other components are assumed to be ideal and free from any loss. Both theoretical (shown as dots) and numerical (shown as lines) results are shown in Figs. 5.3a and 5.3b.

Fig. 5.3a shows the system efficiencies of A-CAES as functions of the fluctuation factor α under different cavern insulation conditions. The maximum pressure $p_{\max}$ is at standard value ($p_{\max} = 50\,\text{bar}$) for each case and it can be noted from Fig. 5.3a that all the system efficiencies increase monotonically with α and converge to 100 % eventually. The solid dots denote the theoretical results calculated from Eq. (5.28) and Eq. (5.33); the solid lines denote the numerical result whilst the dashed lines denote the sum of the system efficiency and all the losses. From Fig. 5.3a, it can be noted that the A-CAES with an isothermal cavern always has higher system efficiency than the one with an adiabatic cavern. It can also be noted that the A-CAES with an intermediate cavern ($\lambda = 5$) has the lowest system efficiency of the three when α is larger than 0.15, which reveals the joint effect of α and λ on the system efficiency. The various losses of the intermediate case as functions of the fluctuation factor are shown in Fig. 5.3b.

From Fig. 5.3b, it can be noted that the losses caused by the fluctuation factor α mainly consist of the cavern total losses (e.g., all the direct cavern losses), the TES thermal loss (due to mixing), the auxiliary heat exchanger loss and the system exit loss (e.g., energy carried by

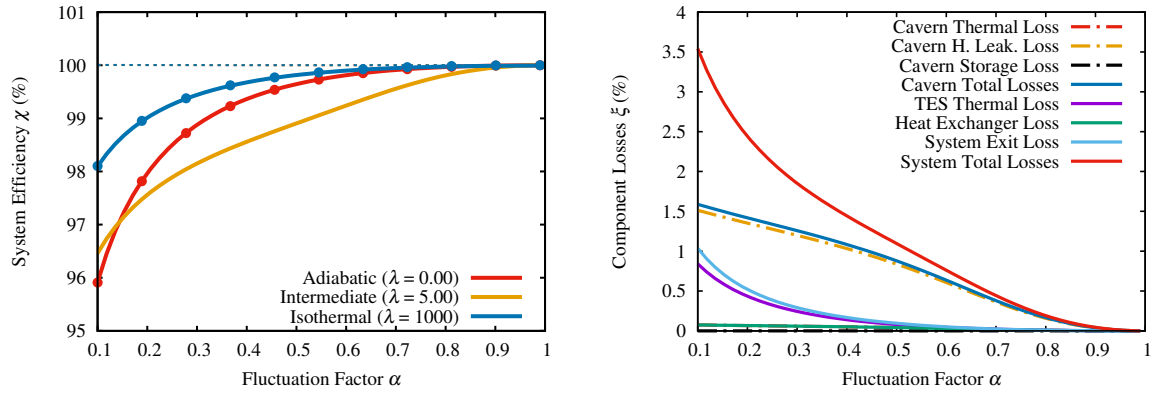

(a) System efficiencies

(b) Component losses at $\lambda = 5$

Figure 5.3: The system efficiencies and component losses as functions of the fluctuation factor α: (a) System efficiencies (b) Component losses at $\lambda = 5$

exhaust air). The cavern total losses can be further divided into the cavern thermal loss (due to mixing), cavern heat leakage loss (due to heat leakage) and the cavern storage loss (due to long time of storage, which is zero in this case). All the losses decrease monotonically with the fluctuation factor α and converge to zero eventually. This is because all these losses are caused by the cavern pressure variation, and the less the cavern pressure varies, the less these losses become. For example, the TES thermal loss is caused by the irreversible mixing of thermal fluids with different inlet temperature. Therefore, when α approaches 1, the inlet temperatures of thermal fluids are almost the same and the TES mixing loss diminishes accordingly. Similarly, the system exit loss is caused by the mismatch between the constant TES temperature and the varying expansion ratio β_{ex}. As α increases to 1, the inlet temperature of expander matches well with the expansion ratio, which means the outlet temperature is close to ambient and the exit loss is zero. The various cavern losses (e.g., mixing and heat leakage loss) and the auxiliary heat exchanger loss are essentially the outcome of cavern temperature variation. If the cavern is isobaric or isothermal, then there is no such losses.

5.6.3 The effect of heat transfer coefficient on system efficiency

From Section 5.3.2, we know that the cavern insulation condition is measured by the dimensionless heat transfer coefficient λ. Therefore, the effects of λ on the system efficiency and the cavern losses are analyzed and the results are shown in Figs. 5.4a and 5.4b respectively.

Fig. 5.4a shows the system efficiencies as functions of the dimensionless heat transfer coefficient λ at different maximum pressure p_{max}. The fluctuation factor α is 0.5 for each case and it is notable that the system efficiencies of all cases first decrease with λ until the

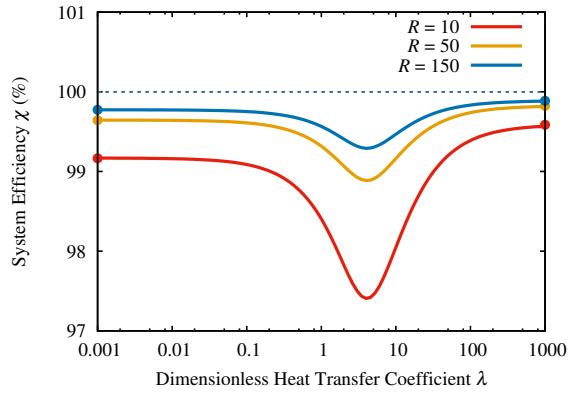

(a) System efficiencies

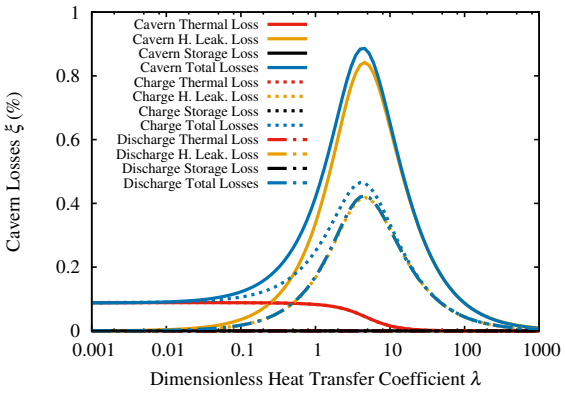

(b) Cavern losses at $p_{\max} = 50\,\text{bar}$ and $\alpha = 0.5$

Figure 5.4: The system efficiencies and cavern losses as functions of the dimensionless heat transfer coefficient: (a) System efficiencies (b) Cavern losses at $p_{\max} = 50\,\text{bar}$ and $\alpha = 0.5$

coefficient reaches its critical value somewhere between 1 and 10, then the system efficiencies increase with λ until the isothermal state is reached. The system efficiency of the isothermal state is always higher than that of the adiabatic one, which is in accord with the theoretical results (shown as dots) calculated from Eqs. (5.28) and (5.33). However, it is unexpected that there is a minimum between the adiabatic and isothermal states, and in order to figure out the reason for this minimum, the various cavern losses as functions of λ are shown in Fig. 5.4b.

Fig. 5.4b shows the various cavern losses as functions of the dimensionless heat transfer coefficient λ. The maximum pressure $p_{\max}$ is 50 whilst the fluctuation factor α is 0.5 in this case. It has been proved that the TES thermal loss and the system exit loss are independent of λ and are thus omitted here. From Fig. 5.4b, it can be noted that the cavern thermal loss decreases rapidly between $\lambda = 1$ and $\lambda = 10$, and the thermal loss only exists during charge because of the irreversible mixing. It is also notable that the heat leakage loss is the dominant loss, which first increases from 0 to its maximum when λ reaches the critical value, and then decreases back to 0 when λ approaches infinity. This is because when λ is close to 0, there is no heat leakage to the environment and thus no heat leakage loss, whilst when λ is close to infinity, the cavern is almost isothermal and there is no temperature difference and available energy with the leaked heat. Therefore, the heat leakage loss reaches its maximum when λ is neither too high nor too low. It can also be noted from Fig. 5.4b that the heat leakage loss of the charge almost overlaps with that of the discharge, which shows the similarity of the heat leakage mechanism between the two processes.

From the above analysis, it can be noticed that the impact of fluctuation factor α and heat transfer coefficient λ on the cavern losses are strongly coupled, and in order to better demonstrate this coupled effect, the 3D surface graph of the cavern losses as functions of α

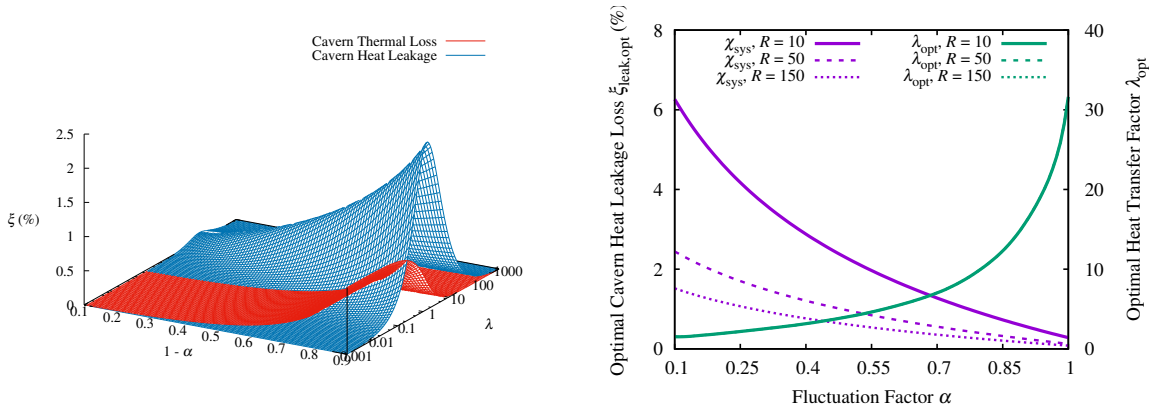

(a) 3D surface graph of the cavern losses

(b) Movement of the cavern heat leakage loss peak

Figure 5.5: Coupled impact of the fluctuation factor α and dimensionless heat transfer coefficient λ on the cavern losses (without storage loss): (a) 3D surface graph of the cavern losses (b) Movement of the cavern heat leakage loss peak

and λ are shown in Fig. 5.5a. From Fig. 5.5a, it can be noted that with the fluctuation factor α increasing, both the thermal loss and heat leakage loss of cavern decrease monotonically. In addition, it can be noticed that the optimal heat transfer coefficient λ_{opt} for the peak of cavern heat leakage loss increases with fluctuation factor α. This movement of cavern heat leakage loss peak is also shown in Fig. 5.5b, from which it can be seen that the optimal heat transfer coefficient λ_{opt} increases with α whilst the optimal cavern heat leakage loss $\xi_{\text{leak,opt}}$ decreases with it, which are in accord with the previous analysis. In addition, the impact of maximum pressure p_{max} on the movement of cavern heat leakage loss peak is also shown in Fig. 5.5b, from which it can be noted that the pressure ratio p_{max} almost have no effect on the optimal heat transfer coefficient λ_{opt} whilst the optimal cavern heat leakage loss decreases with the system pressure ratio p_{max}. This is mainly because the compression work increases more rapidly with p_{max} than the cavern heat leakage loss.

The impact of cavern inlet temperature T_{in} on the cavern losses are shown in Fig. 5.6, where Fig. 5.6a shows the various cavern losses as functions of the dimensionless heat transfer coefficient λ at condition $p_{\text{max}} = 50\,\text{bar}$, $\alpha = 0.5$ and $T_{\text{in}} = 60\,^{\circ}\text{C}$, whereas Fig. 5.6b illustrate the coupled impact of fluctuation factor α and heat transfer coefficient λ on the losses of a cavern with $p_{\text{max}} = 50$ and $T_{\text{in}} = 60\,^{\circ}\text{C}$. The variation of cavern inlet temperature T_{in} can be caused by the inefficiency of the auxiliary heat exchanger (or "after cooler") and variation of pressure ratio p_{max}, therefore, the variation of T_{in} might be quite common in practice.

From Fig. 5.6b, it can be noted that the higher inlet temperature T_{in} has completely twisted the cavern thermal losses. At lower α, the cavern thermal losses firstly decreases with λ but then increases with it, resulting in a minimum in cavern thermal loss, as shown in Fig. 5.6b;

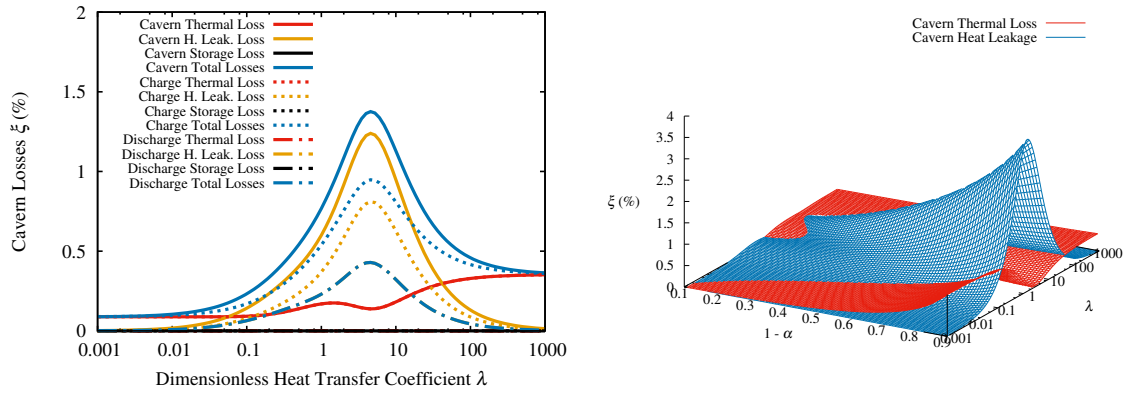

(a) Cavern losses at $p_{max} = 50\,\text{bar}$ and $\alpha = 0.5$

(b) 3D surface graph of the cavern losses

Figure 5.6: The impact of the inlet temperature T_{in} on the cavern losses, $T_{in} = 60\,°\text{C}$: (a) Cavern losses at $p_{max} = 50\,\text{bar}$ and $\alpha = 0.5$ (b) 3D surface graph of the cavern losses.

whilst at higher α, as shown in Fig. 5.6a, the cavern thermal loss generally increase with λ but only decrease slightly around the λ_{opt} of cavern heat leakage loss ξ_{leak}. In addition, from Fig. 5.6a it can be found that the higher inlet temperature T_{in} significantly increases the heat leakage loss during charge, resulting in a large difference in the cavern heat leakage loss during charge and discharge.

5.6.4 The effect of storage loss on system efficiency

In the above sections, only the charge and discharge process are considered. However, during the normal operations of A-CAES, storage process is also included and during that time, heat is leaked to the environment. This heat leakage loss is termed as the storage loss which is not only dependent on the insulation condition of the cavern but also on the elapsed time of the storage process, which is determined by the requirement of the power grid and thus highly unpredictable. Therefore, in order to simplify this analysis, only two extreme cases are considered in this section. One is the system with infinitely short storage time so that there is no storage loss at all, and the other is the system with infinitely long storage time, of which the cavern is thoroughly cooled to the ambient temperature and all the thermal energy stored in the cavern will be lost. The former case has already been discussed in the last section, therefore, in this section, complete cooling process is included in the numerical model.

Fig. 5.7a shows the system efficiencies of A-CAES with thorough cooling during storage as functions of the heat transfer coefficient λ, from which it can be noted that all the system efficiencies increase monotonically with λ, which is different from the A-CAES without cooling during storage. In order to figure out what kind of loss has changed the shape of the system

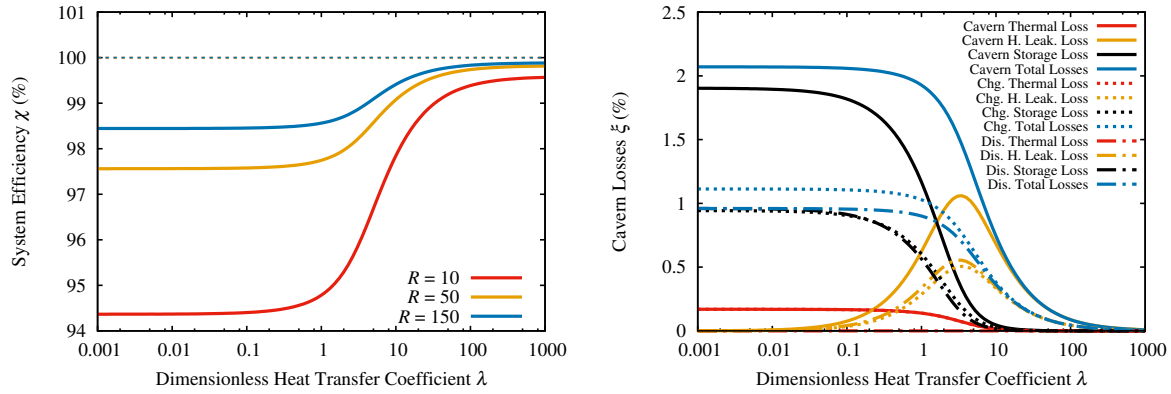

(a) System efficiencies (b) Cavern losses at $\alpha = 0.5$

Figure 5.7: The system efficiencies and cavern losses as functions of the dimensionless heat transfer coefficient (with cooling): (a) System efficiencies (b) Cavern losses at $\alpha = 0.5$

efficiency curves, the various cavern losses as functions of λ are shown in Fig. 5.7b.

Fig. 5.7b shows the various cavern losses as functions of the heat transfer coefficient λ. The maximum pressure $p_{\max}$ and fluctuation factor α are still 50 bar and 0.5 respectively. From Fig. 5.7b, it can be noted that the cavern losses are dominated by the cavern storage loss this time, which decreases rapidly between $\lambda = 0.1$ and $\lambda = 10$. When λ is low, the cavern storage loss is much larger than the cavern thermal loss and heat leakage loss combined, which results in the low system efficiency of the adiabatic state. It is also notable that the heat leakage loss during discharge is slightly higher than that during charge, mainly due to the temperature change caused by the cooling during storage.

The coupled impact of fluctuation factor α and heat transfer coefficient λ on the cavern losses are shown in Fig. 5.8a. Like other cavern losses, the cavern storage loss also decreases monotonically with α. In addition, the cavern storage loss increases the peak of cavern heat leakage loss $\xi_{\text{leak,opt}}$ but simultaneously decreases the optimal heat transfer coefficient λ_{opt} for this peak, as shown in Figs. 5.5b and 5.8b. The maximum pressure $p_{\max}$ still has no effect on the λ_{opt} of cavern heat leakage loss.

Finally, the cavern pressure and temperature of an A-CAES without cooling and with complete cooling during storage as functions of the time are shown in Figs. 5.9a and 5.9b respectively. For both cases, the cavern is assumed adiabatic during charge and discharge. The maximum pressure $p_{\max}$ and fluctuation factor α are 50 and 0.5 respectively, therefore, the cavern pressure varies within a range of 25 to 50 bar.

In Fig. 5.9a, the analytical results of the maximum and minimum cavern temperature calculated from Eqs. (5.15) and (5.16) are also included and it can be noted that the numerical results and the analytical results match very well. The temperature ratio of charged state to

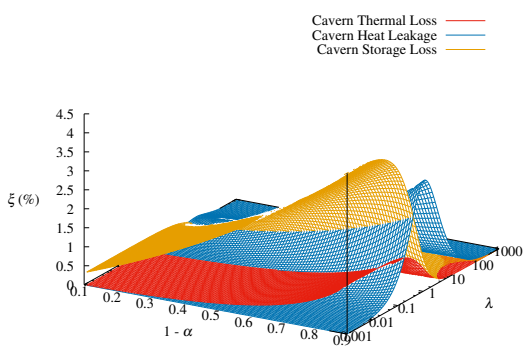

(a) 3D surface graph of the cavern losses

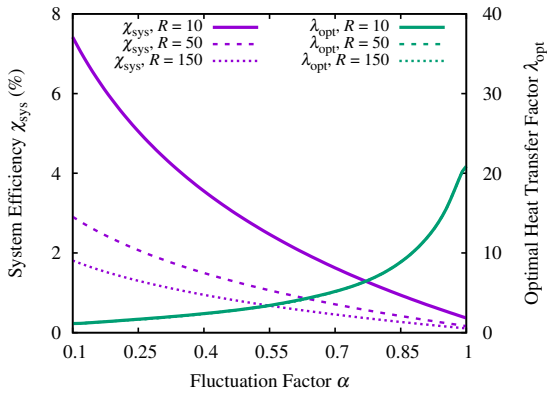

(b) Movement of the cavern heat leakage loss peak

Figure 5.8: Coupled impact of the fluctuation factor α and dimensionless heat transfer coefficient λ on the cavern losses (with storage loss): (a) 3D surface graph of the cavern losses (b) Movement of the cavern heat leakage loss peak.

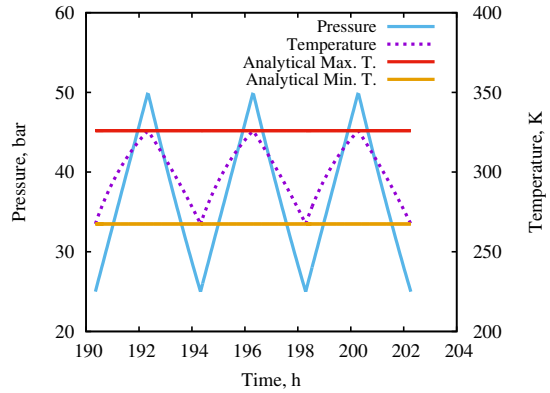

(a) no cooling

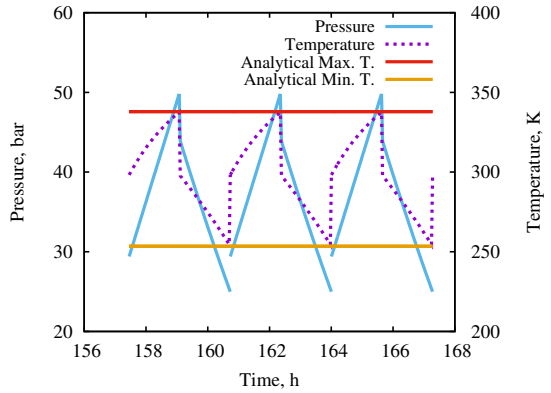

(b) complete cooling

Figure 5.9: The pressure and temperature variations within the cavern which has (a) no cooling and (b) complete cooling during storage

the discharged state is approximately 1.22 in this case. From Fig. 5.9b, it can be noted that the cavern pressure and temperature change abruptly during storage. This is because after storage, the cavern temperature is returned to ambient T_0 and the cavern pressure also varies accordingly. The temperature ratio of charged state to the discharged state is approximately 1.33 in this case, which is larger than the result in Fig. 5.9a.

5.6.5 The effects of cavern parameters on energy density

From the above sections, it can be noted that the cavern parameters have significant effects on the system efficiency. In this section, the effects of the cavern parameters on the energy density will be examined. In most A-CAES systems, part of the available energy is stored as the thermal potential in the TES, whilst the rest is stored as the pressure potential in the cavern (or air reservoirs), as discussed in the previous chapter. In this chapter, the analytical expressions of cavern energy density have been derived for each type of air reservoir. For example, the energy density of an isobaric cavern is:

$$D_{\mathrm{P}} = p_{\max} \ln \frac{p_{\max}}{p_0} \tag{5.34}$$

Similarly, the energy density of an isochoric and isothermal cavern is:

$$D_{\mathrm{VT}} = (p_{\max} - p_{\min}) \left(\ln \frac{p_{\max}}{p_0} - 1 \right) - p_{\min} \ln \frac{p_{\min}}{p_{\max}} \tag{5.35}$$

The energy density of an isochoric and adiabatic cavern is not shown here due to its excess complicity. However, both the analytical and numerical results of all types of air reservoirs are shown in Figs. 5.10, 5.11 and 5.12, where the analytical and numerical results are shown as dots and lines respectively.

Fig. 5.10 shows the cavern energy densities as functions of the maximum pressure $p_{\max}$. The fluctuation factor α of the isochoric cavern is fixed at 0.5 in this case. From Fig. 5.10, it can be noted that all the cavern energy densities increase monotonically with the maximum pressure $p_{\max}$ and reveal similar trends with each other. It is also notable that the isobaric air reservoir has higher energy density than the isochoric ones, and amongst the isochoric caverns, the isothermal cavern has higher energy density than the adiabatic ones. The energy density of an actual cavern always falls between the ranges set by the isothermal and adiabatic limits, as shown by the intermediate case ($\lambda = 5$) in Fig. 5.10. Therefore, the analytical results developed in Section 5.5 and this section can be used to determine the ranges quickly for an actual cavern.

The cavern energy densities D as functions of the fluctuation factors α are shown in Fig.

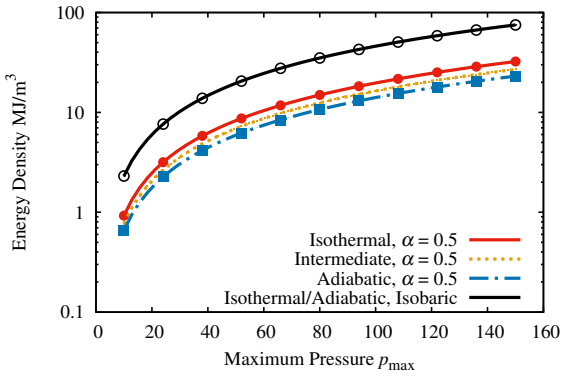

Figure 5.10: Cavern energy densities as functions of the system pressure ratio

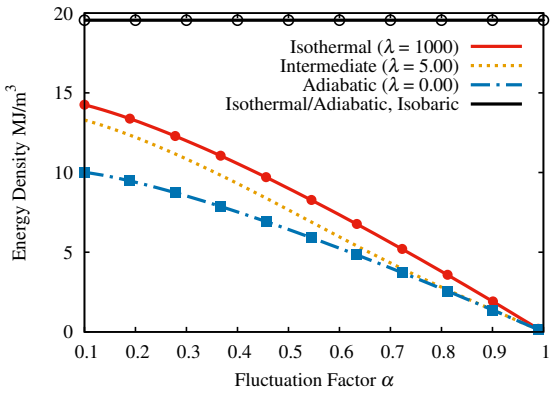

Figure 5.11: Cavern energy densities as functions of the fluctuation factor

5.11, from which it can be noted that whatever the α is, the isobaric cavern always has the highest energy density, which is in accord with Eqs. (5.34) and (5.35). For the isochoric caverns, all the energy densities decrease monotonically with the fluctuation factor α increasing, which is opposite to the trends of system efficiencies discussed in Section 5.6.2. This is because as α increases, the pressure range becomes narrower and the stored mass and available energy decrease accordingly. Therefore, there is a tradeoff between the system efficiency χ and the energy density D with respect to the fluctuation factor α.

Fig. 5.12 shows the cavern energy densities D as functions of the heat transfer coefficient λ. The maximum pressure $p_{\max}$ is still 50 bar whilst the two cases of α (e.g., $\alpha = 0.1$ and $\alpha = 0.5$) are shown for comparison. From Fig. 5.12, it can be noted that the energy densities of isochoric caverns with and without cooling during storage both increase monotonically with λ. It is also notable that when λ is low, the cavern with cooling has even lower energy density than the one without.

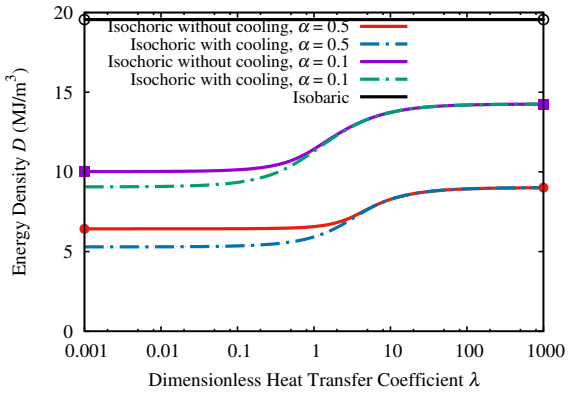

Figure 5.12: Cavern energy densities as functions of the dimensionless heat transfer coefficient

5.7 Case study of the Huntorf CAES cavern

In Section 5.6, the effects of cavern parameters on the A-CAES have been analyzed individually. However, some simplifications are made to find the losses caused by the cavern parameters, which will inevitably make the final results depart from the reality. Therefore, in order to compensate for the limitations of the previous analysis, a more detailed and realistic case study based on Huntorf CAES plant is carried out and the role of the cavern in real A-CAES is revealed in this section.

The A-CAES of this case study is a hypothetical system based on Huntorf CAES plant. The cavern parameters of the Huntorf plant are extracted from Ref. [71] whilst the effective heat transfer coefficient h_{eff} of the Huntorf cavern is taken from Ref. [72], which is given by:

$$h_{eff} = a + b\,|\dot{m}_{\text{in}} - \dot{m}_{\text{out}}|^{0.8} \tag{5.36}$$

where the constant a and b stand for the effective heat transfer coefficient caused by the natural convection and the forced convection respectively, $a = 0.2356$ and $b = 0.0149$. This equation has been validated by comparing it with the experimental data of the Huntorf plant. In order to use this equation reliably, the cavern parameters of the A-CAES are set as the same with the Huntorf plant, which is summarized in Table 5.4. Other parameters including the polytropic efficiency and heat exchanger effectiveness are mainly cited from Ref. [77], which are also summarized in Table 5.4.

By using Eq. (5.5), it can be calculated that the dimensionless heat transfer coefficient λ of the Huntorf cavern during charge and discharge are 2.4 and 1.5 respectively. This value falls into the range between 1.0 and 10 and shows that the Huntorf cavern is in an intermediate state, therefore, the cavern losses and temperature variation are very important and should not

Table 5.4: Basic parameters of the hypothetical A-CAES

Cavern Parameters	Value	Unit	Other Parameters	Value	Unit
Charge Flowrate	108	kg/s	H. Ex. Effectiveness	0.80	-
Discharge Flowrate	417	kg/s	TES Insulation Factor	0.99	-
Minimum Pressure	46	bar	Polytropic Efficiency	0.90	-
Maximum Pressure	66	bar	heat Leakage Factor	0.01	-
Cavern Volume	300000	m3	Heat Capacity Ratio	1.00	-
Cavern Wall Temperature	50	°C	Friction Factor	0.01	-

be overlooked in the numerical study. During storage, there's no compressed air flowing into or out of the cavern, therefore, the effective heat transfer coefficient is a constant 0.2356. The cavern temperature variation during storage could be approximated by the following equation [126]:

$$mc_v \frac{\mathrm{d}T}{\mathrm{d}t} = -U_0 A \left(T - T_0\right) \tag{5.37}$$

where m is the mass of compressed air in the cavern and U_0 is the heat transfer coefficient during storage, $U_0 = h_{eff} V/A$. If we assume the initial temperature of the cavern is T_s, then after the storage process, the final temperature T_f could be calculated by:

$$T_\mathrm{f} = T_0 + (T_\mathrm{s} - T_0) \exp\left(-\frac{t}{\tau}\right) \tag{5.38}$$

where τ is the time constant, which is given by: $\tau = mc_v/U_0 A$.

It can be proved that if $t = \tau$, then the final temperature difference will be 36.8 % of the initial temperature difference and for the Huntorf CAES cavern, the time constant is 57.52 hours, roughly 2.4 days, Therefore, if the storage system is operated on a weekly or monthly basis, then the assumption in Section 5.6.4 is valid. On the other hand, if the storage time only lasts for a few hours, then the assumption in Section 5.6.3 seems more reasonable. The Huntorf CAES plant, for example, is operated on a daily basis and uses 8 hours a day for charge and 2 hours a day for discharge, hence, the storage time after charge/discharge is roughly 7 hours, which leads to 13 % reduction of the final temperature difference. The storage loss is added to the numerical model, and the loss distributions of the hypothetical A-CAES system and the Huntorf CAES cavern are shown in Figs. 5.13a and 5.13b.

Fig. 5.13a and Fig. 5.13b show the losses distribution of the hypothetical A-CAES and the Huntorf cavern respectively. From Fig. 5.13a, it can be noted that the cavern losses play a minor role in the system efficiency when compared to the losses of other components, such as the compressor/expander and TES. However, it can not be concluded the cavern parameters are

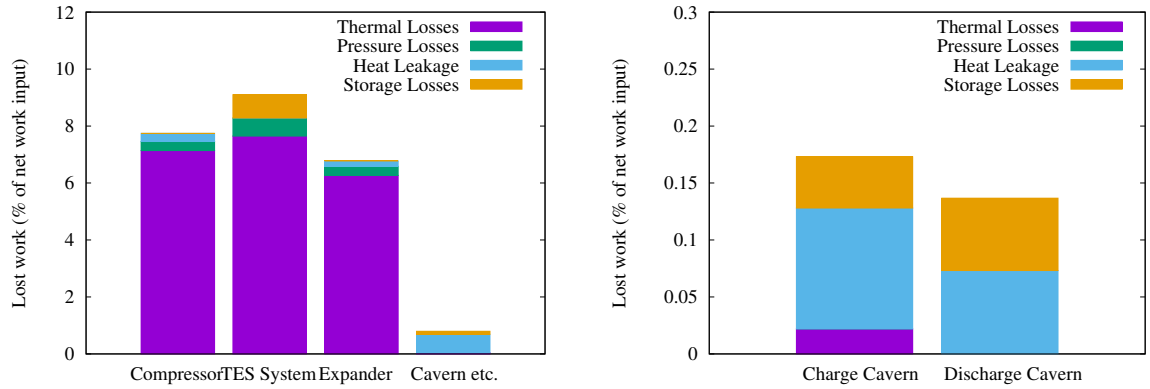

(a) Hypothetical A-CAES system

(b) Huntorf CAES cavern

Figure 5.13: The loss distributions of the hypothetical A-CAES and Huntorf CAES cavern: (a) Hypothetical A-CAES system; (b) Huntorf CAES cavern

not important to the A-CAES system, because it has been proven in Section 5.6 that both the maximum pressure $p_{\max}$ and fluctuation factor α can affect the system efficiency indirectly by changing the losses of other components. These losses are not cavern losses (or "direct losses") but are affected by cavern parameters. Therefore, these losses are referred to as the "indirect losses" in this chapter. In addition, the cavern parameters also have significant effects on the cavern energy density, as shown in Section 5.6.5. Therefore, it's still necessary to study the effects of cavern parameters on the A-CAES even if the cavern losses themselves are negligible.

The detailed cavern losses distribution is shown in Fig. 5.13b. It can be noted from Fig. 5.13b that the storage loss is comparable to the heat leakage losses and should not be ignored, whilst the thermal loss is the least of the three. In addition, it can be noted from Fig. 5.13b that the storage losses after discharge is larger than the storage losses after charge. That's because for the same temperature deviations from the ambient value, the temperature below the ambient value will usually result in more storage loss during a fixed period of time. For example, the exergy losses of cavern during storage can be calculated by:

$$\frac{\mathrm{d}B}{\mathrm{d}t} = -U_0 A \frac{(T - T_0)^2}{T} \tag{5.39}$$

where B is the available energy of the cavern and U_0 is the overall heat transfer coefficient during storage. It can be noted from Eq. (5.39) that with the same temperature difference $\Delta T = |T - T_0|$, discharging cavern at temperature below ambient value ($T = T_0 - \Delta T$) tends to have higher storage loss than the charging cavern at temperature above ambient temperature ($T = T_0 + \Delta T$), which is in accord with the discovery in Fig. 5.13b.

Table 5.5: The nominal, minimum and maximum design variable values of A-CAES for the parametric and optimization study

	p_{max} (bar)	p_{min}/p_{max}	λ	NTU	η	Π	d_p (mm)	L/D
Nominal	120	0.60	10.00	9.00	0.85	0.80	15.0	1.00
Minimum	40	0.30	0.001	1.00	0.80	0.50	2.00	0.20
Maximum	200	0.90	1000	49.0	0.90	1.50	30.0	6.00

5.8 The impact of TES on A-CAES

Before embarking on the parametric study of different A-CAES with solid, liquid and hybrid TES, it is useful to first consider the connection between maximum permissible temperature and stage number. The number of stages for solid, hybrid and liquid systems is set at two, three and four respectively, with each solid TES roughly equivalent to two liquid ones. This is a consequence of the higher maximum permissible temperature for solid systems. Other design variables and their ranges are summarized in Table 5.5. As each parameter is varied, all other parameters are held at their nominal values. The effect of these parameters on performance is evaluated in terms of efficiency $\chi = W_{dis}/W_{chg}$ and unit storage cost $Z = Z_{tot}/W_{dis}$, where W_{chg} and W_{dis} are the work input and output, obtained by integrating power over the charge and discharge times respectively. The total cost Z_{tot} is simply the sum of the various component costs. Mechanical (friction) losses and electrical losses are not accounted for, so χ constitutes a "thermodynamic" round-trip efficiency. Likewise, the costs are limited to the "thermodynamic" components, as Z_{tot} does not include motor and generator costs. However, as shown in Ref. [119], these are usually a simple function of rated power and will therefore remain constant across the different designs considered here.

5.8.1 Effect of cavern parameters

Figs. 5.14a, 5.14b and 5.14c show respectively the impacts of maximum pressure (p_{max}), pressure fluctuation (p_{min}/p_{max}) and cavern heat transfer rate (λ) on the efficiency and cost. It is notable that the efficiency increases with p_{max} for all A-CAES types (liquid, solid and hybrid), which is due to the fact that exergetic losses are dominated by the compression and expansion processes. IN the case of polytropic compression, the specific entropy increase per stage may be written as $\Delta s_c = (1/\eta - 1)R_g \ln \beta_c$, whereas the specific work input per stage, w_c, is given by $w_c = mc_pT_0\left(\beta_c^{\phi_c} - 1\right)$. The ratio $(T_0\Delta s_c/w_c)$ is a decreasing function of pressure ratio. A similar results hold for expansion, thus leading to the observed trend of χ with p_{max}. Fig. 5.14a also shows that the unit storage cost of solid A-CAES increases rapidly

with maximum pressure $p_{\max}$, whereas that of the liquid system decreases slightly. This is due to the dominant impact of pressure vessel costs for the second stage solid TES thermal reservoir. For liquid systems, costs are influenced strongly by the air mass flowrate which decreases with $p_{\max}$ for a given power rating. The hybrid A-CAES shows a tradeoff between these opposing trends but has the lowest cost of all systems.

Increasing the ratio of the minimum to maximum pressure in the cavern improves the efficiency slightly, but significantly increases the cost (Fig. 5.14b). The increase in χ stems mainly from reduced cavern losses, whereas the higher unit cost is a consequence of reduced storage density since the cavern is only partially emptied with each cycle.

The dimensionless heat transfer coefficient λ is not really a design parameter (except possibly in the case of artificial air reservoir) but rather a function of the cavern size, geometry and surrounding rock type. Increasing values of λ makes the cavern more isothermal, allowing more air to be stored per unit volume and thereby decreasing the unit storage cost, as shown in Fig. 5.14c. Thermal exergetic losses occur within the cavern due to mixing of inlet air with cavern air (which is generally at a different temperature) and due to heat leakage to and from the surroundings at temperature different to T_0. Mixing losses tend to dominate for adiabatic caverns ($\lambda = 0$) whereas the sum of these two loss components tends to peak for the mid-range values of λ which, estimates suggest, are likely to be representative of real caverns [2]. The impact on efficiency is, however, relatively small.

5.8.2 Effect of heat exchanger size for liquid and hybrid systems

The effects of varying the NTU rating of the main heat exchangers is shown in Fig. 5.14d. Increasing NTU improves heat exchanger effectiveness but with diminishing returns, as shown by $\varepsilon = \mathrm{NTU}/(\mathrm{NTU}+1)$. Consequently, the round-trip efficiency increases with NTU for the hybrid system, but the improvement is marginal beyond NTU ~ 10, whereas the cost rises in accord with $Z_{\mathrm{hex}} = C_{\mathrm{hex}}(\dot{m}\cdot\mathrm{NTU})^{0.6}$. For liquid systems, more of the heat exchange occurs at low air pressure where the density is lower and pressure losses are more significant. These losses outweigh the small improvement in ε at high NTU such that the efficiency reaches a maximum at NTU ~ 20. Since all heat transfer to the storage media occurs via the heat exchangers for liquid systems, the cost increases more rapidly than for hybrid A-CAES.

5.8.3 Effect of compression and expansion efficiency

Increasing the polytropic efficiency of compressors and expanders results in a more or less linear increase in overall efficiency, with χ increasing by roughly 1.5 percentage points for each percentage point increase in turbomachineray efficiency, as shown in Fig. 5.15a. The

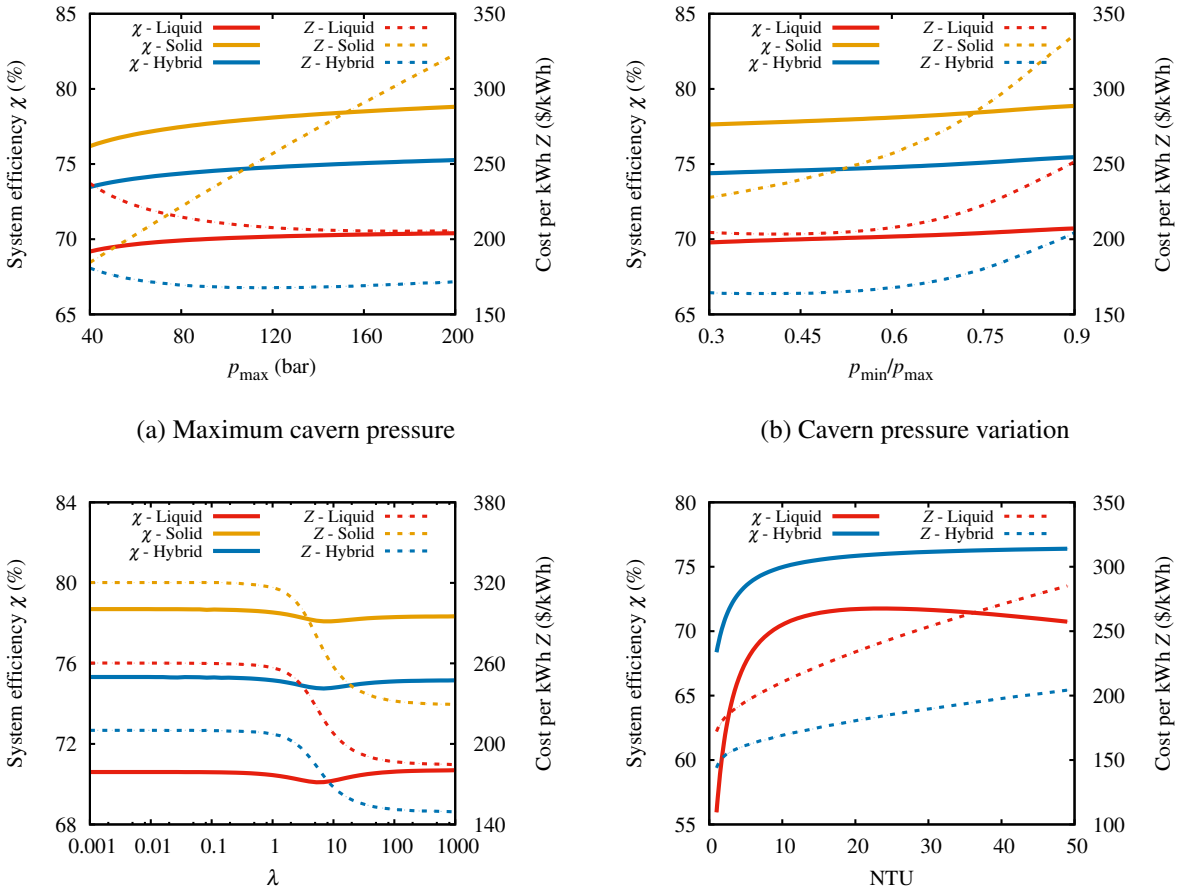

(a) Maximum cavern pressure

(b) Cavern pressure variation

(c) Cavern dimensionless heat transfer rate

(d) Heat exchanger NTU rating

Figure 5.14: Variation of system efficiency and unit cost with cavern and heat exchanger parameters: (a) Maximum cavern pressure (b) Cavern pressure variation (c) Cavern dimensionless heat transfer rate (d) Heat exchanger NTU rating

designer has the choice between cheap, low-efficiency compressors and expanders, or expensive high-efficiency ones. The rise in cost is dramatic for turbomachineray efficiencies greater than about 86 %, but the shape of these curves is of course dependent on the cost equation of compressor/expander which, as already noted, is subject to some uncertainty.

5.8.4 Effect of packed bed parameters for solid and hybrid systems

The effects of packed bed utilization factor Π, particle diameter d_p and aspect ratio L/D on the round-trip efficiency and unit cost are shown in Figs. 5.15b, 5.15c and 5.15d. Recall that Π is the ratio between the actual and nominal charge times for the solid thermal reservoir, so as Π increases more of the reservoir's capacity is exploited. The system cost therefore falls as Π rises, but beyond $\Pi \sim 1$ the reservoir is fully charged with each cycle and any attempt to charge it further simply results in hot air issuing from the exit and hence a decrease in efficiency. As discussed in Ref. [41], greater utilization also leads to steeper temperature gradients in the packed bed and consequently higher losses due to irreversible heat exchange between the air and storage media. The cost may continue to fall beyond $\Pi = 1$ because this implies a smaller thermal reservoir, but eventually the impact of increased losses on the returned work, W_{dis}, begins to dominate such that the curve flattens out.

The effective particle diameter d_p determines the balance between thermal and pressure losses within the packed bed: small particles provide more surface area thereby decreasing heat transfer losses, but at the expense of a larger pressure drop. There is thus an optimum particle size at which the efficiency is maximum (see Figs. 5.15c). This optimum will depend on the air mass flow per unit area G and hence on the reservoir aspect ratio. The cost of the packing materiel and the volume it occupies is assumed independent of d_p and therefore the improvement in χ obtained with smaller particles results in a slight decrease in unit cost Z. This is one of the few areas where there is no conflict between cost and efficiency.

In conjunction with the particle size, the aspect ratio L/D also affects the balance between thermal and pressure losses, with long thin reservoirs having efficient heat transfer but larger pressure drop. Again there is an optimum, as shown in Fig. 5.15d, which will in turn depend on d_p. This time there is, however, a rapid increase in cost at low values of L/D which is due to "end effects" - i.e., the high surface-to-volume ratio, requiring more insulation and therefore a larger vessel, and the wasted space in the domed end caps of the pressure vessel (which reflect the cost of flanges and high-tensile bolts).

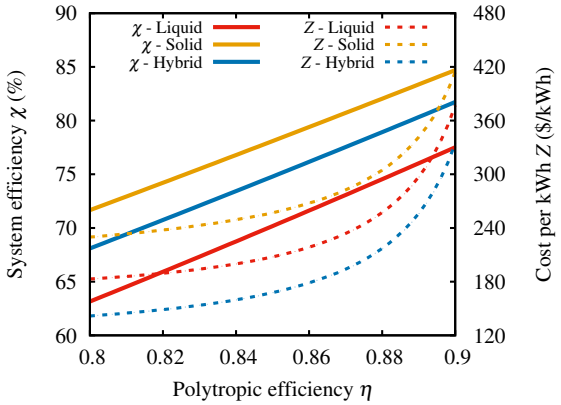

(a) Compression and expansion efficiency

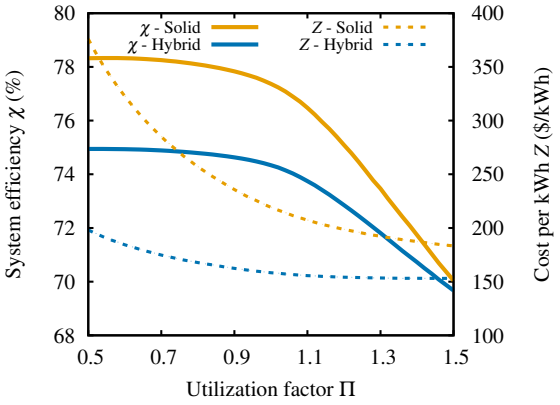

(b) Reservoir utilization factor

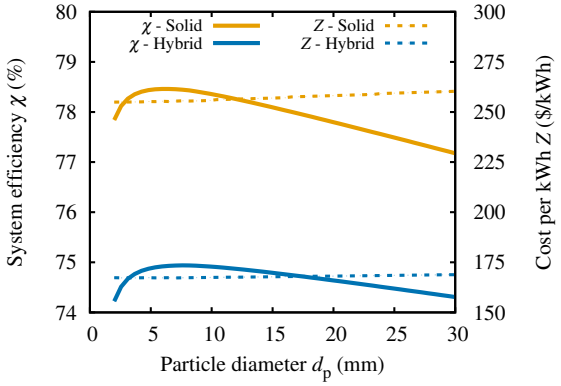

(c) Effective particle diameter

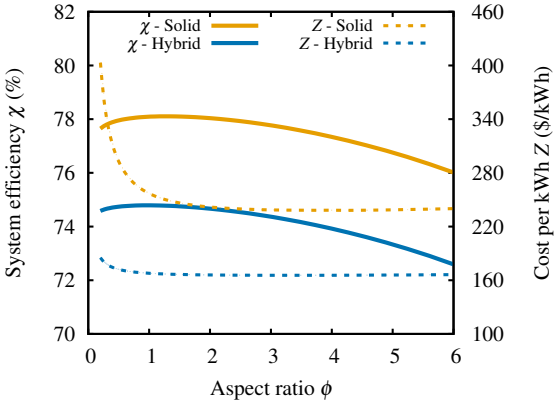

(d) Reservoir aspect ratio

Figure 5.15: Variation of system efficiency and unit cost with turbomachinery efficiency and packed bed parameters: (a) Compression and expansion efficiency (b) Reservoir utilization factor (c) Effective particle diameter (d) Reservoir aspect ratio

Table 5.6: Main results for the nominal designs

	Liquid CAES	Solid CAES	Hybrid CAES
System Efficiency	70.2 %	78.1 %	74.8 %
Cost per kWh	219 $/kWh	257 $/kWh	170 $/kWh
Capital Cost	63 M$	72 M$	48 M$
Net Output Work	289 MWh	279 MWh	284 MWh
Net Input Work	413 MWh	358 MWh	379 MWh

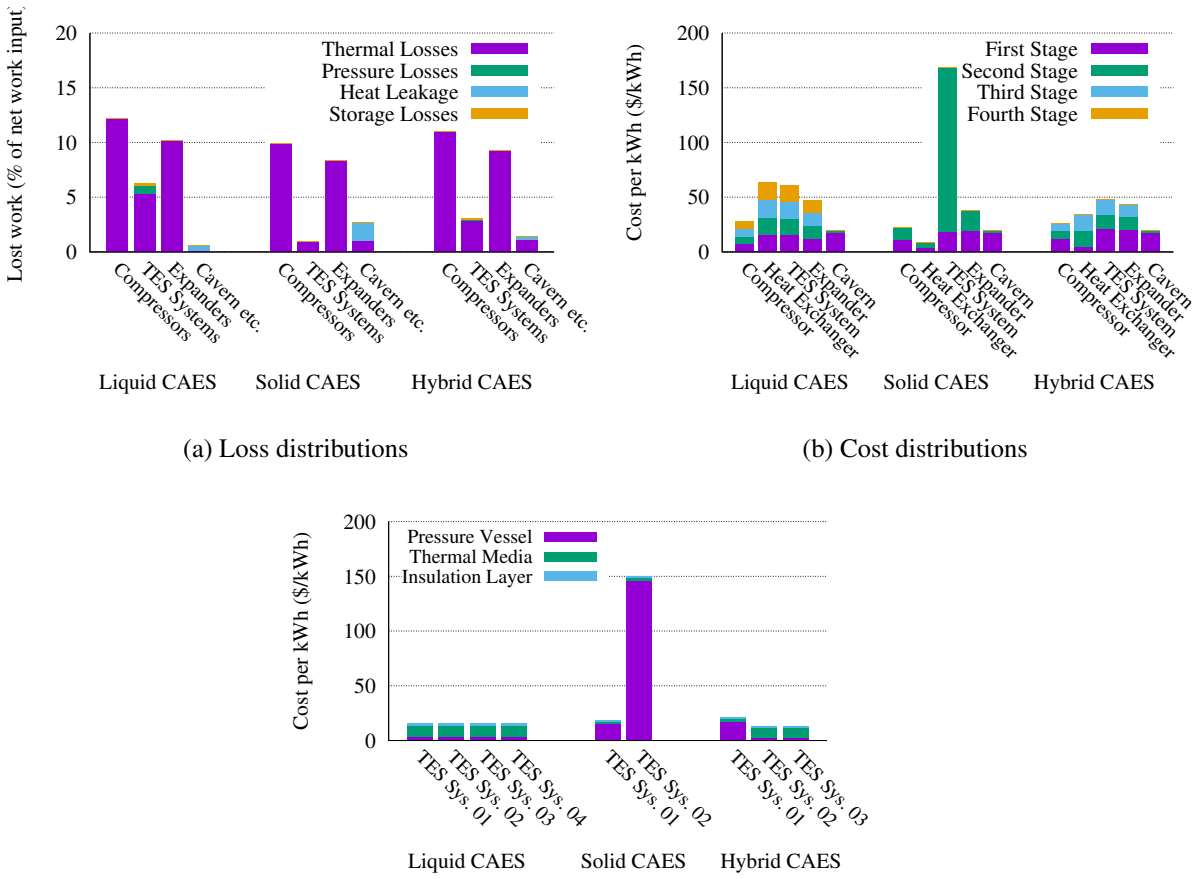

(a) Loss distributions

(b) Cost distributions

(c) TES cost distributions

Figure 5.16: Loss and cost distributions of different A-CAES with nominal designs: (a) Loss distributions (b) Cost distributions (c) TES cost distributions

5.9 Comparison of the results for the nominal designs

After the parametric study, the main results for the nominal designs of liquid, solid and hybrid A-CAES are summarized in Table 5.6, from which it can be noted that the hybrid A-CAES has the lowest cost per kWh and it will be interesting to see how this has been achieved. Therefore, the loss and cost distributions for the nominal designs of the three systems are shown in Figs. 5.16a and 5.16b respectively for more detailed analysis.

Fig. 5.16a shows the loss distributions for the nominal designs, from which it can be noted that the losses of all A-CAES are dominated by the compressor/expander losses and the compressor losses are slightly larger than the expander ones. This is mainly because the polytropic efficiencies of compressor and expander are assumed to be the same, and it can be proved that with the same polytropic efficiency, the compressor loss $\xi_c = (1/\eta - 1)k\ln\beta$ is always higher than the expander one $\xi_e = (1-\eta)k\ln\beta$. From Fig. 5.16a, it can also be noted that the TES losses of the solid A-CAES are much lower than those of the liquid A-CAES. This is because the thermal reservoir usually have smaller temperature difference than the heat exchangers since it is relatively easier for thermal reservoir to achieve very large heat transfer area without significantly increasing the cost. It can also be noted from Fig. 5.16a that the liquid A-CAES has the lowest cavern losses, which include the exit loss and the auxiliary heat exchanger loss. This is because there is no thermal reservoirs in the liquid A-CAES, which avoids the associated exit losses when the thermal front comes out the thermal reservoir.

The cost distributions for the nominal designs are shown in Fig. 5.16b, from which it can be clearly noted that the unit storage cost of the solid A-CAES is the highest, mainly due to its exorbitantly expensive high pressure (second stage) thermal reservoir. In fact, the cost of the containment vessel increases linearly with the pressure p, as shown in Eq. (4.28), which makes the thermal reservoir only suitable for first stage TES. Meanwhile, the cost of the low pressure (first stage) thermal reservoir is lower than the liquid TES, whilst its maximum allowable temperature is higher, which makes it ideal for the first-stage TES. The hybrid A-CAES, which combines the merits of low-pressure solid TES and high-pressure liquid TES, becomes the cheapest A-CAES as a result. The distribution of costs between different components of the TES systems is shown in Fig. 5.16c, from which it is clear that the pressure vessel cost and thermal fluid cost are the dominant part for the solid and liquid TES respectively. It is also notable that the pressure vessel cost varies significantly for different stages, whilst the thermal fluid cost is evenly distributed among different stages.

5.10 Summary

In this chapter, the thermodynamic and economic models have been devised for various air reservoirs and A-CAES systems, and the appropriate materials selected for solid and liquid thermal stores. The effects of various air reservoir parameters on the system efficiency and energy density has been analyzed individually. A more realistic case study of the Huntorf CAES cavern has also been carried out. After that, a hybrid A-CAES system is proposed that combines low-pressure solid TES with liquid TES for the high pressure compression stages. This has been compared with other systems that use just liquid or just solid TES. A combination of parametric studies and loss/cost distributions has been used to undertake this comparison. It can be concluded from this chapter that:

1. The trend system efficiency χ varies with maximum pressure $p_{\max}$ and stage number N is mainly determined by the dominating loss of this A-CAES system. With different dominating losses, the system efficiencies χ as functions of maximum pressure $p_{\max}$ and stage number N will show different trends.

2. The maximum pressure $p_{\max}$ and fluctuation factor α can indirectly affect the system efficiency χ by changing the losses of other components. Even if the direct cavern losses are zero, the caver parameters are still critical for the optimal operation of other components.

3. The cavern parameters may have significant effects on the energy density. The energy density of an isochoric cavern can be increased by reducing fluctuation factor α, increasing heat transfer coefficient λ or minimizing cavern storage loss. However, the energy density of an isochoric cavern is always lower than that of an isobaric cavern under the same operating conditions.

4. The heat transfer coefficient λ of Huntorf CAES cavern is between 1.0 and 10, therefore, it is more close to an intermediate cavern and the impact of heat transfer are important. The time constant of Huntorf CAES cavern during storage is roughly two days, therefore, if an A-CAES is operated on a weekly or monthly basis, then its cavern is more close to the model with complete cooling.

5. The main factors controlling the cost-efficiency trade off are the polytropic efficiency of compressors and turbines, the NTU of the heat exchangers (for liquid and hybrid systems), the reservoir "utilization factor" Π and reservoir aspect ratio L/D (for solid and hybrid systems).

6. The hybrid system demonstrates a lower cost than the other two systems for a given efficiency (or higher efficiency for a given cost). Although this conclusion might be affected by different cost assumptions, the margin is reasonably significant - i.e., roughly 20 % lower cost at nominal design. The main reason for this advantage is that solid TES is cheap when operated at low pressure and does not require indirect heat exchange, whereas at high pressure it is much more expensive than liquid TES.

Chapter 6

Isothermal Compressed Air Energy Storage

6.1 Introduction

The compression and expansion of A-CAES are usually achieved in staged manners, with intermediate cooling and heating respectively between stages. Isothermal Compressed Air Energy Storage (I-CAES) may be considered as the limiting case of this process, wherein heat is extracted continuously during compression, and added during expansion at close to ambient temperature, thereby obviating the need for separate thermal storage [81]. In practice, some of the proposed I-CAES systems make use of cheap, low-grade thermal storage by means of, for example, a warm water pool [130]. Proposals of I-CAES have been published by SustainX, LightSail and General Compression, most of which require continuous heat exchange between the air and some other substance to remove/add heat during compression/expansion [130, 131]. Water is often used as the heat-exchange fluid due to its highly suitable properties and it can be in various forms (such as bubbles, foams and droplets etc.) to increase the two-phase contact area [5].

Besides the attention from industry, research on isothermal compression/expansion is also very active in academia. Numerical models on mass and heat transfer within the two-phase flow have been presented numerous times in the literature [6, 89], and their applications have been extended to wet compression cycles [132], liquid-flooded Ericsson cycles [86], and liquid piston compression [6]. However, due to the complicated and coupled processes of mass and heat transfer, most of the numerical models can only be applied to specific cases with given compressor/expander geometry and operating conditions. A simplified yet universal model that can integrate easily with other CAES components has so far been lacking. A generalized

Figure 6.1: Comparison of three methods for creating large contact area between a liquid and gas: spraying, foaming and bubbling [5]

model of I-CAES is therefore proposed in this chapter. Parametric studies are carried out to analyze the impact of various parameters on the system performance of I-CAES. Both the loss and cost distributions are provided for the nominal case, and these I-CAES systems will be optimized and compared in Chapter 8.

6.2 Cycle layouts

The layouts of I-CAES are similar to that of the A-CAES, as shown in Figs. 6.2 and 6.3. However, the compressor/expander and the heat exchanger are replaced with an isothermal compressor/expander, wherein heat is continuously subtracted from the air along the compression and continuously added along the expansion, by injecting large quantities of atomized (or foamed) water into the cylinder. Water's properties make it a highly suitable heat exchange fluid: it is non-toxic and low-cost, has extraordinarily high heat capacity, and is almost incompressible. To increase the heat transfer area, water can be in different forms, such as liquid spay, aqueous foam and air bubbles, as shown in Fig. 6.1, depending on the air to water volume ratio [5, 131]. When the air pressure is high whilst the air to water volume ratio is low (1.5 to 50), it is reported that foaming is the best choice [5, 131]. However, despite the various forms of water, the ultimate goal is to make sure the heat exchange occurs quickly enough relative to the density change. In the ideal case, the air and water reach thermal equilibrium and the results should be the same.

In the I-CAES shown in Fig. 6.2, the water tanks are used to recycle the thermal energy generated during charge and therefore, it is referred to as I-CAES with Heat Recycling (I-CAES-HR). This system can be viewed as a transition between the A-CAES and the Pure I-CAES (I-CAES without any heat recycling). Due to the heat recycling, the roundtrip efficiency of I-CAES-HR is expected to be higher than the Pure I-CAES. However, ambient water must be pumped to the same pressure with the air before mixing them up. In theory, any energy added to the air-water mixture may be recoverable, but in practice most of the energy spent on

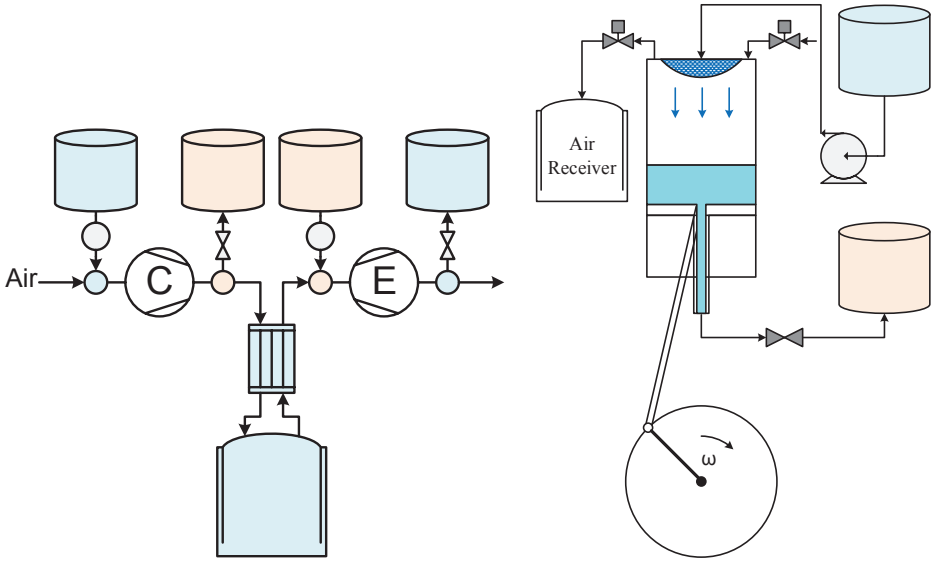

(a) I-CAES-HR (b) Isothermal compressor

Figure 6.2: Schematic diagrams of the I-CAES with heat recycling (I-CAES-HR) and the isothermal compressor: (a) I-CAES-HR (b) Isothermal compressor

pumping is lost [5]. As a result, after the air-water mixture is separated downstream, the water can be stored in ambient-pressure tanks. During discharge, the same amount of pumping work will be consumed, which is given by:

$$W_{\mathrm{pmp}} \approx \int_{\mathrm{d}}^{\mathrm{c}} \frac{p - p_0}{\rho_{\mathrm{f}} \eta} \mathrm{d}m_{\mathrm{f}} \tag{6.1}$$

where ρ_{f} and m_{f} are the density and mass of the thermal fluid respectively, and η is the isentropic efficiency of the hydraulic pump.

Another variant of the I-CAES is shown in Fig. 6.3, from which it can be noted that the water tanks are replaced with an external heat exchanger. This continuously dissipates the absorbed thermal energy into the environment, thus avoiding the large water tanks. Meanwhile, the inlet and outlet pressure of the hydraulic pump will be the same if the friction loss is negligible. Therefore, the water in Pure I-CAES can be viewed as a medium to transport the thermal energy between the compressor/expander and the external heat exchanger, and it is not consumed but reused within a closed loop. This system is called Pure I-CAES in this thesis because all of its exergy is stored in the form of pressure potential of the air reservoir. Due to the lack of heat recovery, its roundtrip efficiency may be lower than that of I-CAES-HR, but the wasted pumping work and expensive water tanks can be avoided. In addition, the external heat exchanger of I-CAES makes it possible for waste heat or solar energy to be integrated into the system, which may offset its disadvantage of lack of heat recovery to some extent.

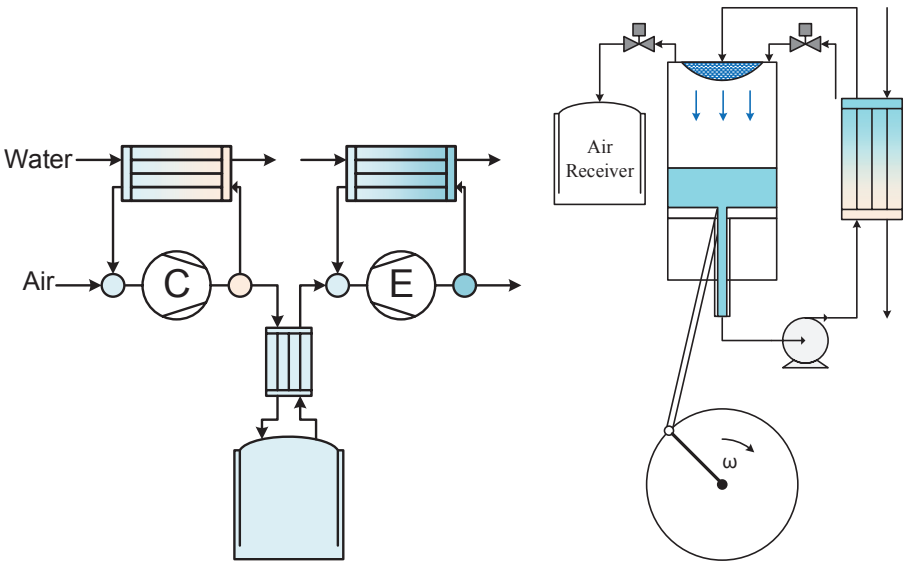

(a) Pure I-CAES (b) Isothermal compressor

Figure 6.3: Schematic diagrams of the I-CAES without heat recycling (Pure I-CAES) and the isothermal compressor: (a) Pure I-CAES (b) Isothermal compressor

Hence, a more detailed thermo-economic analysis and comparison is necessary.

6.3 Approximate model for the isothermal compressor/expander

6.3.1 Thermodynamic modelling

In I-CAES, the average pressure $\bar{p}$ is high whilst the average temperature $\bar{T}$ is low, which suggests that the impact of vaporisation is small and the sensible heat transfer is the dominant force in achieving isothermality. Therefore, most studies on isothermal compressor/expander and I-CAES only considered the effects of sensible heat transfer [35, 36, 90] and in the rest studies where the impact of vaporisation is included, it is believed that if the gas humidity is high, the mass transfer rate will also tend to be zero [6]. As a result, in this thesis, only the effects of sensible heat transfer are included in the approximate thermodynamic model and the calculation results can be viewed as a conservative estimate accordingly. The maximum impacts of vaporisation on the calculation results will be estimated in Section. 6.3.3.

For the isothermal compressor/expander, a two-stage method is adopted to calculate the outlet temperature of air and liquid [6, 90]. The air is first assumed to be compressed by a small pressure ratio and then immediately transfer the generated thermal energy to the ad-

jacent liquid droplets (or foams). This two-stage process continues infinitely until the air reaches its outlet pressure. Therefore, if we assume the pressure ratio of the isothermal compressor/expander is β and this ratio is equally partitioned among the n steps, then after the first stage of each step, the intermediate temperature of air and liquid is:

$$\begin{pmatrix} T^i_{\mathrm{m,a}} \\ T^i_{\mathrm{m,f}} \end{pmatrix} = \begin{pmatrix} \beta^{\frac{\phi}{n}} & 0 \\ 0 & 1 \end{pmatrix} \begin{pmatrix} T^i_{\mathrm{in,a}} \\ T^i_{\mathrm{in,f}} \end{pmatrix} \tag{6.2}$$

where the subscripts a and f denote the air and liquid respectively; m and in denote the intermediate and inlet state and i denote the i-th time step.

After the compression, the air has higher temperature than the liquid and starts to transfer its heat to the adjacent liquid droplets. If the liquid droplets and their surrounding vapour are in thermal equilibrium, and there is only heat transfer between the liquid droplets and the main body of gas, then the liquid droplet temperature can be expressed as:

$$m_{\mathrm{f}} c_{p,\mathrm{f}} \frac{\mathrm{d}T_{\mathrm{f}}}{\mathrm{d}t} = hA^*_{\mathrm{f}} \left(T_{\mathrm{g}} - T_{\mathrm{f}}\right) \tag{6.3}$$

where $c_{p,\mathrm{f}}$ is the specific heat capacity of the liquid droplets and A^*_{f} is the actual heat transfer area between air and water, $A^*_{\mathrm{f}} = \alpha_s A_{\mathrm{f}}$. A_{f} is the total surface area of the water droplets, $A_{\mathrm{f}} = V_{\mathrm{f}} S_v$ and α_s denotes the fraction of droplets that is suspended in the air. Most of the rest droplets are deposited on the surface of piston, as shown in Figs. 6.2b and 6.3b. S_v is the surface-to-volume ratio of the water droplets, and if the water is in the shape of sphere, then $S_v = 6/d$ and d is the droplet diameter. h is the convective heat transfer coefficient which can be calculated from the well validated Ranz - Marshall relationship [6].

$$\mathrm{Nu} = 2 + 0.6\mathrm{Re}^{1/2}\mathrm{Pr}^{1/3} \tag{6.4}$$

where the Prandtl number Pr is almost constant at room temperature while the Reynolds number Re is a function of the average diameter d and velocity u of the water droplets, $\mathrm{Re} = \rho u d/\mu$.

After discretization, Eq. (6.3) can be expressed as:

$$T^{i+1}_{\mathrm{out,f}} = \frac{hA^*_{\mathrm{f}}\Delta t}{m_{\mathrm{f}} c_{p,\mathrm{f}}} T^i_{\mathrm{m,g}} + \left(1 - \frac{hA^*_{\mathrm{f}}\Delta t}{m_{\mathrm{f}} c_{p,\mathrm{f}}}\right) T^i_{\mathrm{m,f}} \tag{6.5}$$

and similar expression can be derived for the air temperature. Here, if we introduce the concept of heat exchanger effectiveness $\varepsilon = hA^*_{\mathrm{f}}\Delta t/\dot{m}_{\mathrm{a}} c_{p,\mathrm{a}}$ and heat capacity ratio $C_r = \dot{m}_{\mathrm{a}} c_{p,\mathrm{a}}/\dot{m}_{\mathrm{f}} c_{p,\mathrm{f}}$

by using the analogy to a heat exchanger, then Eq. (6.5) can be further simplified to:

$$\begin{pmatrix} T_{\mathrm{out,a}}^{i+1} \\ T_{\mathrm{out,f}}^{i+1} \end{pmatrix} = \begin{pmatrix} 1-\varepsilon & \varepsilon \\ \varepsilon C_r & 1-\varepsilon C_r \end{pmatrix} \begin{pmatrix} T_{\mathrm{m,a}}^{i} \\ T_{\mathrm{m,f}}^{i} \end{pmatrix} \tag{6.6}$$

where $\varepsilon C_r = \Delta t/\tau$. τ is the droplet relaxation time, $\tau = \rho_{\mathrm{f}} c_{\mathrm{f}}/h\alpha_s S_v$ and Δt is the time interval for heat transfer. Although a two-stage method is assumed for the isothermal compression/expansion, the actual heat transfer time Δt is a fraction of the total time of each rotation of the isothermal compressor/expander Δt^*, $\Delta t = \alpha_f \Delta t^*$. Therefore, if the frequency of the isothermal compressor/expander is f, then the time interval Δt is:

$$\Delta t = \frac{\alpha_f}{nf} \tag{6.7}$$

After some algebra, we could get:

$$\varepsilon C_r = \frac{6\mathrm{Nu}\lambda\alpha_f\alpha_s}{\rho_{\mathrm{f}} c_{\mathrm{f}} d^2 f n} = \frac{1}{\dot{p}\tau n} \tag{6.8}$$

where $\dot{p}$ is the compression rate, which is defined by $\dot{p} = \mathrm{d}p/(p\mathrm{d}t) = f/\alpha_f$. From Eq. (6.8), it can be noted that f and d^2 are equivalent, and the isothermal efficiency is only determined by the combination $d^2 f$ (or $\dot{p}\tau$).

After substituting Eq. (6.2) into Eq. (6.6) and then multiplying it n times, we will get the final outlet temperature of the air and water.

$$\begin{pmatrix} T_{\mathrm{out,a}} \\ T_{\mathrm{out,f}} \end{pmatrix} = \lim_{n\to\infty} \begin{bmatrix} (1-\varepsilon)\beta^{\frac{\phi}{n}} & \varepsilon \\ \varepsilon C_r \beta^{\frac{\phi}{n}} & 1-\varepsilon C_r \end{bmatrix}^n \begin{pmatrix} T_{\mathrm{in,a}} \\ T_{\mathrm{in,f}} \end{pmatrix} \tag{6.9}$$

where the step number n is usually a very large number to make sure the calculation results are converged. For the numerical calculations in this thesis, n is set as 10^{10} but the powers of matrix $\mathbf{A}$ (like the one in Eq. (6.9)) can be solved easily by diagonalizing it into $\mathbf{A} = \mathbf{S}\Lambda\mathbf{S}^{-1}$ so that $\mathbf{A^n} = \mathbf{S}\Lambda^{\mathbf{n}}\mathbf{S}^{-1}$, where Λ is a diagonal matrix and its power can be simply raised by raising its diagonal entries to the same power. Therefore, it actually takes two steps to obtain the final results and the speed of calculation is very fast.

Then the actual power input/output of the isothermal compressor/expander can be calculated by the following equation:

$$W_{\mathrm{ac}} = \dot{m}_{\mathrm{a}} c_{p,\mathrm{a}} \left(T_{\mathrm{out,a}} - T_{\mathrm{in,a}}\right) + \dot{m}_{\mathrm{f}} c_{p,\mathrm{f}} \left(T_{\mathrm{out,f}} - T_{\mathrm{in,f}}\right) \tag{6.10}$$

If the droplet diameter d or the frequency f is infinitely small, then we have $\dot{p}\tau \to 0$, as shown by Eq. (6.8). Meanwhile, since $n \to \infty$, then both ε and εC_r are indeterminate numbers.

If they happen to be multiplied by the factor $\beta^{\phi/n}$ which tends to be one when $n \to \infty$, then the value of factor $\beta^{\phi/n}$ can be approximated by one in the case of $\dot{p}\tau \to 0$ to further simplify the analytical expression of $\mathbf{A^n} = \mathbf{S}\Lambda^{\mathbf{n}}\mathbf{S^{-1}}$. By applying the limit $n \to \infty$ to each part of the expression $\mathbf{A^n} = \mathbf{S}\Lambda^{\mathbf{n}}\mathbf{S^{-1}}$ and making the above mentioned approximation, then it can be proved that Eq. (6.9) can be simplified to:

$$\begin{pmatrix} T_{\text{out,a}} \\ T_{\text{out,f}} \end{pmatrix} = \beta^{\kappa\phi} \begin{pmatrix} \kappa & 1-\kappa \\ \kappa & 1-\kappa \end{pmatrix} \begin{pmatrix} T_{\text{in,a}} \\ T_{\text{in,f}} \end{pmatrix} \tag{6.11}$$

where κ is the heat capacity ratio of the air to the air-water mixture, which is given by:

$$\kappa = \frac{C_r}{C_r + 1} = \frac{\dot{m}_{\text{a}} c_{p,\text{a}}}{\dot{m}_{\text{a}} c_{p,\text{a}} + \dot{m}_{\text{f}} c_{p,\text{f}}}$$

From Eq. (6.11), it can be noted that the outlet temperature of the air and the water are the same, which means the equilibrium state has been reached. Therefore, the irreversible heat transfer loss is limited to the beginning of this process and is also termed as the mixing loss in this thesis. After the mixing process, the initial temperature of the compression/expansion is:

$$T_{\text{in}} = \kappa T_{\text{in,a}} + (1-\kappa)\, T_{\text{in,f}} \tag{6.12}$$

and then Eqs. (6.11) and (6.10) can also be written as:

$$T_{\text{out}} = T_{\text{in}} \beta^{\kappa\phi} \tag{6.13}$$

$$W_{\text{th}} = \frac{\dot{m} c_p}{\kappa} T_{\text{in}} \left(\beta^{\kappa\phi} - 1 \right) \tag{6.14}$$

By comparing the Eqs. (6.13) and (6.14) with the Eqs. (4.18) and (4.19) in Chapter 4, it can be noted that the κ in the I-CAES system is equivalent to the $1/N$ in the A-CAES system. Further analysis reveals that for each unit of water-to-air mass flowrate ratio $\dot{m}_{\text{f}}/\dot{m}_{\text{a}}$ increase in the I-CAES, it is equivalent to roughly 4 additional stages of compression/expansion in the A-CAES, as shown in Eq. (6.15). This is the reason why the required stage number N of the I-CAES is usually less than that of the A-CAES system.

$$N \propto 1/\kappa \approx 4\dot{m}_{\text{f}}/\dot{m}_{\text{a}} + 1 \tag{6.15}$$

If we further assume that the mass of water droplets is also infinite, in other words, both C_r and κ approach 0, then in this case, the isothermal compression work can be expressed as:

$$W_{\infty} = \dot{m} c_p T_{\text{in}} \phi \ln \beta \tag{6.16}$$

From Eqs. (6.13) and (6.16), it can be noticed that although the air/water temperatures remain constant in the case of infinite water droplets, the compression work W_∞ still depends on the polytropic efficiency η of the compressor. Therefore, in order to derive the expression for ideal isothermal compression work W_{iso}, the polytropic efficiency η should be set as one, and hence:

$$W_{\text{iso}} = \dot{m} R_g T_0 \ln \beta \tag{6.17}$$

The isothermal efficiency is defined as:

$$\eta_{\text{iso}} = \frac{W_{\text{iso}}}{W_{\text{ac}}} \times 100\% \tag{6.18}$$

6.3.2 Cost modelling

Estimating the cost of an isothermal compressor/expander is a very uncertain and challenging task since the I-CAES technology is still at an early stage of development. Therefore, the concept of cost ratio k_r is introduced here to evaluate its relative cost to a similar conventional compressor/expander.

$$Z_{\text{ICE}} = k_r Z_{\text{CE,std}} \frac{f_{\text{std}}}{f} \tag{6.19}$$

where Z_{ICE} and Z_{CE} denote the capital cost of an isothermal and conventional compressor/expander respectively, the subscript std denotes the standard state as shown in Table 6.2. For example, the polytropic efficiency in the cost equation $Z_{\text{CE,std}}$ is fixed at its standard value $\eta_{\text{std}} = 0.85$. Therefore, Eq. (6.19) essentially uses the capital cost of a conventional compressor/expander with an 85 % polytropic efficiency as the approximate for the cost of an isothermal compressor/expander. The effect of rotation frequency f on the capital cost is also considered in the factor f_{std}/f: the higher the rotation frequency is, the lower the capital cost will be. It is obvious that this cost equation is subject to some levels of uncertainty, and therefore, the effect of cost ratio k_r on the optimized system performance will be studied in Chapter 8.

By referencing the cost equation of a conventional compressor/expander in Chapter 4, it can be noted that $Z_{\text{CE,std}}$ is proportional to the mass flowrate $\dot{m}$ and the log nature of pressure ratio β, so that $Z_{\text{CE,std}} \propto \dot{m} \ln \beta$ if its polytropic efficiency is fixed. From Eq. (6.17), it can be noted that the ideal work of an isothermal compressor/expander W_{iso} is also proportional to $\dot{m} \ln \beta$. Therefore, the cost of an isothermal compressor/expander Z_{ICE} is also proportional to its ideal power input/output W_{iso}, $Z_{\text{ICE,std}} \propto W_{\text{iso}}$, which is reasonable to some extend.

6.3.3 Estimating the impact of evaporation

In order to accurately determine the temperatures of gas and liquid within the isothermal compressor/expander, it is usually necessary to evaluate the mass transfer as well because mass and heat transfer processes are strongly coupled. Actually there is a lot of publications about droplet evaporation model and its application in wet compression cycles [84, 85, 132], but the working conditions of isothermal compressors/expanders in I-CAES are a bit different. For example, during the charge of I-CAES, ambient air is compressed near-isothermally to a high pressure, so the average pressure $\bar{p}$ is higher than that for wet compression cycles whilst the average temperature $\bar{T}$ is lower. The latter corresponds to a low saturated vapour pressure p_s, and therefore, the mass of vapour carried by unit mass of dry air ω_v is also lower than that for wet compression cycles, due to the low fraction of partial pressure p_s/p. Meanwhile, the mass of liquid carried by each unit mass of dry air f_l is very high as large quantities of water droplets are injected into the gas cylinder throughout the compression process. As a result, the mass ratio between vapour and liquid ω_v/f_l is very low in I-CAES, which suggests the sensible heat cooling effect plays a dominant role in achieving isothermal compression/expansion, but the impacts of vaporization will still be estimated here.

The normal condition for a combined heat and mass transfer problem (e.g., droplet evaporation) is that the water vapour is saturated at the surface of the droplet. In other words, at the droplet surface, we have $p_\mathrm{v} = p_s(T_\mathrm{f})$ where T_f is the droplet temperature. The droplets are colder than the surrounding gas because there is heat exchange from the gas to the droplet. As a result, the droplets are tending to evaporate, so the vapour fraction at the surface of the droplets is higher than that in the main body of the gas. Therefore, the maximum possible vapour content is given by $p_\mathrm{v} \leq p_s(T_\mathrm{f})$, and in the worst case, we will have the following equation according to the Dalton's law of partial pressure [132]:

$$\frac{p_\mathrm{v}}{p} = \frac{\omega_\mathrm{v}}{\omega_\mathrm{v} + M_\mathrm{v}/M_\mathrm{a}} = \frac{p_s(T_\mathrm{f})}{p} \tag{6.20}$$

where T_f is droplet temperature, and M is the molecular weight. From Eq. (6.20), the mass of vapour carried by unit mass of dry air ω_v can be derived easily:

$$\omega_\mathrm{v} = \frac{M_\mathrm{v}}{M_\mathrm{a}} \frac{p_s(T_\mathrm{f})}{p - p_s(T_\mathrm{f})} \tag{6.21}$$

Since the saturated vapour pressure p_s increases with the droplet temperature T_f, it can be noted from Eq. (6.21) that the mass of vapour ω_v increases with the droplet temperature T_f but decreases with the pressure p.

For each unit mass of dry air, there is ω_v kg vapour and f_l kg liquid corresponding to it. If we apply the first law of thermodynamics to the f_l kg liquid and its thin interface with the

vapour (not the vapour itself), the following equation can be obtained:

$$\delta Q = \mathrm{d}H = f_l c_{p,\mathrm{f}} \mathrm{d}T_\mathrm{f} + L\mathrm{d}\omega_\mathrm{v} \tag{6.22}$$

where L is the specific enthalpy of vaporisation. The increment in specific humidity ω_v can be obtained by differentiating the right hand side of Eq. (6.20) and introducing the Clausius - Claperyon equation in the following form [132]:

$$\frac{\mathrm{d}p_s}{p_s} \approx \frac{L}{R_{g,\mathrm{v}} T_\mathrm{f}} \frac{\mathrm{d}T_\mathrm{f}}{T_\mathrm{f}} \tag{6.23}$$

After some simplification, we can get [132]:

$$\mathrm{d}\omega_\mathrm{v} = \omega_\mathrm{v} \left(1 + \frac{M_\mathrm{a}}{M_\mathrm{v}} \omega_\mathrm{v}\right) \left(\frac{L}{R_{g,\mathrm{v}} T_\mathrm{f}} \frac{\mathrm{d}T_\mathrm{f}}{T_\mathrm{f}} - \frac{\mathrm{d}p}{p}\right) \tag{6.24}$$

By introducing Eq. (6.24) into Eq. (6.22) and applying the definition of isobaric heat capacity gives:

$$C_{p,\mathrm{f}} = \left(\frac{\partial H}{\partial T}\right)_p = f_l c_{p,\mathrm{f}} + \left(1 + \frac{M_\mathrm{a}}{M_\mathrm{v}} \omega_\mathrm{v}\right) \frac{L^2 \omega_\mathrm{v}}{R_{g,\mathrm{v}} T_\mathrm{f}^2} = \left(f_l + f_l^*\right) c_{p,\mathrm{f}} = f_l c_{p,\mathrm{f}}^* \tag{6.25}$$

where $c_{p,\mathrm{f}}^*$ is the effective value for the specific heat capacity of the liquid, $c_{p,\mathrm{f}}^* = \left(1 + f_l^*/f_l\right) c_{p,\mathrm{f}}$, and f_l^* is the equivalent mass of liquid due to vaporisation, which is given by:

$$f_l^* = \left(1 + \frac{M_\mathrm{a}}{M_\mathrm{v}} \omega_\mathrm{v}\right) \frac{L^2 \omega_\mathrm{v}}{R_{g,\mathrm{v}} T_\mathrm{f}^2 c_{p,\mathrm{f}}} \tag{6.26}$$

From Eqs. (6.25) and (6.26), it can be noted that the effect of vaporisation is equivalent to adding extra f_l^* kg liquid for each unit mass of dry air, and once the average temperature and pressure is fixed, the equivalent liquid mass f_l^* is constant and independent of the actual mass of liquid f_l, which is $f_l = c_{p,\mathrm{a}} C_r / c_{p,\mathrm{f}}$. On the other hand, the equivalent specific heat capacity of the liquid $c_{p,\mathrm{f}}^*$ is dependent on the actual mass of liquid f_l: the higher the liquid mass f_l is, the less effect of vaporisation will have on $c_{p,\mathrm{f}}^*$. For example, the effective heat capacity $c_{p,\mathrm{f}}^*$ and equivalent liquid mass f_l^* of the isothermal compressor with direct injection in Ref. [6] are 4800 J/ kg and 0.143 kg respectively, and these values are obtained by comparing the results of the approximate model in Section 6.3.1 with the more detailed numerical results in Ref. [6]. In this thesis, the average pressure is much higher than that in Ref. [6], therefore, the impact of vaporisation is negligible and can be ignored without causing too much error.

From Eq. (6.25), it can be noted that although the effect of vaporization changes the equiv-

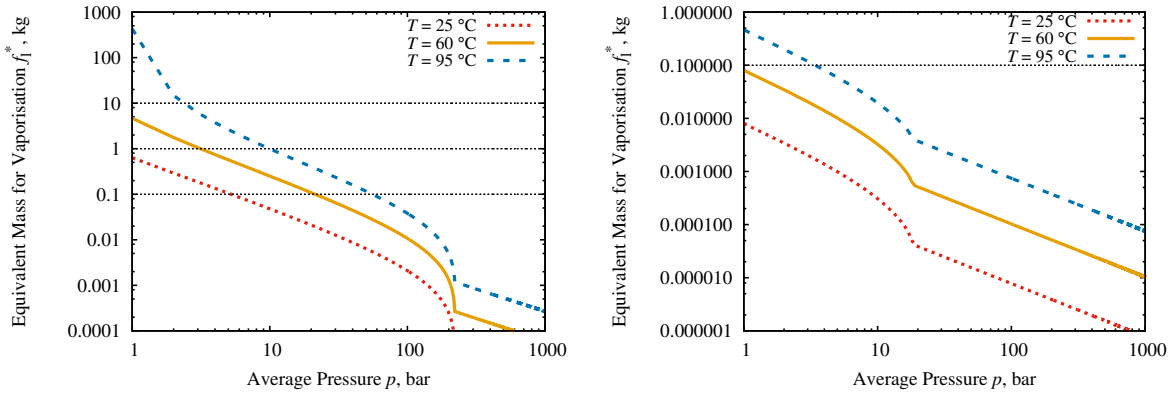

(a) water (H_2O) (b) dodecane ($C_{12}H_{26}$)

Figure 6.4: The impacts of temperature T and pressure p on the equivalent liquid mass for vaporisation f_l^* of (a) water and (b) dodecane ($C_{12}H_{26}$)

alent heat capacity $c^*_{p,\mathrm{f}}$ of thermal fluid, the liquid droplets can still be viewed as incompressible fluid since its temperature does not change much with the pressure. On the other hand, both air and vapour are treated as ideal gas and their temperature are assumed the same, so that the air/vapour mixture is considered as the gas phase. Since the mass fraction of vapour ω_v is usually negligible in the I-CAES, the thermophysical properties of dry air are used instead for the air/vapour mixture. Therefore, the analysis in Section 6.3.1 is still valid.

The impact of temperature T_f and pressure p on the equivalent liquid mass for vaporisation f_l^* of water and dodecane ($C_{12}H_{26}$) are shown in Figs. (6.4a) and (6.4b) respectively. (Note that dodecane can be viewed as the major components of mineral oil, which has been widely used in liquid-flooded compression and expansion.) Since the actual liquid mass f_l is always in the range of 0.1 ~ 10, the relative value of equivalent liquid mass f_l^* can be viewed as an indicator of relative dominance of latent and sensible heat transfer. For example, if $f_l^* > 10$, which means the equivalent liquid mass f_l^* is higher than 10 kg for each unit mass of dry air, then the heat transfer is dominated by the latent heat transfer. Similarly, if $f_l^* < 0.1$, which means the equivalent liquid mass f_l^* is less than 0.1 kg for each unit mass of dry air, then the heat transfer is dominated by the sensible heat transfer, and hence the analytical model developed here can be applied with confidence. If $0.1 < f_l^* < 10$, then the mass and sensible heat transfer make similar contribution to the temperature change.

As mentioned before, the compression and expansion of I-CAES can also be achieved in stages. For example, an I-CAES with a pressure ratio of 100 can have two stages, with the low pressure stage compressing from 1 to 10 bar and the high pressure stage from 10 to 100 bar. From Fig. 6.4a, it can be noted that in the low pressure stage, the mass and heat transfer have similar effects on the energy exchange whilst in the high pressure stage, the sensible heat

Table 6.1: Comparison of three methods for creating large contact area between a liquid and gas: spraying, foaming and bubbling [5]

	Liquid Spray	Aqueous Foam	Air Bubbles
Air to water volume ratio	>20:1	1.5:1 to 50:1	<1.5:1
Stability for port injection	poor	excellent	good
Energy for generation	moderate	low	low
Liquid surface area	sphere	shell	sphere

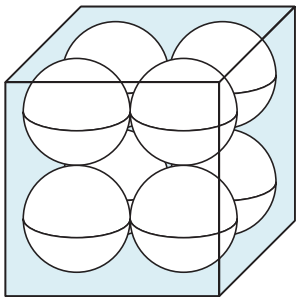

Figure 6.5: Schematic diagram of the wet aqueous foam

transfer is dominant. Therefore, in the I-CAES with water as the thermal fluid, the effect of mass transfer should not be ignored altogether, and the mass or heat capacity of liquid should be corrected to account for this effect, as discussed above. On the other hand, for I-CAES with mineral oil as the thermal fluid, the impact of mass transfer on the energy exchange is insignificant, as shown in Fig. 6.4b. Therefore, the effect of mass transfer can be ignored and the model developed here can be used with confidence. In fact, in the liquid-flooded compression and expansion, the effect of mass transfer is seldom considered in the literature [86].

6.4 Validation and discussion of the approximated model

6.4.1 Different forms of the injected liquid

In addition to water droplets, the water can also in the shape of aqueous foam and air bubbles depending on the air-to-water mass ratio. For water droplets with sphere shape, $S_v = 6/d$ and d is in the range of $10\,\mu$m to $1000\,\mu$m.

The air-to-water volume ratio V_a/V_f, as shown in Table 6.1, is a good indicator of the heat

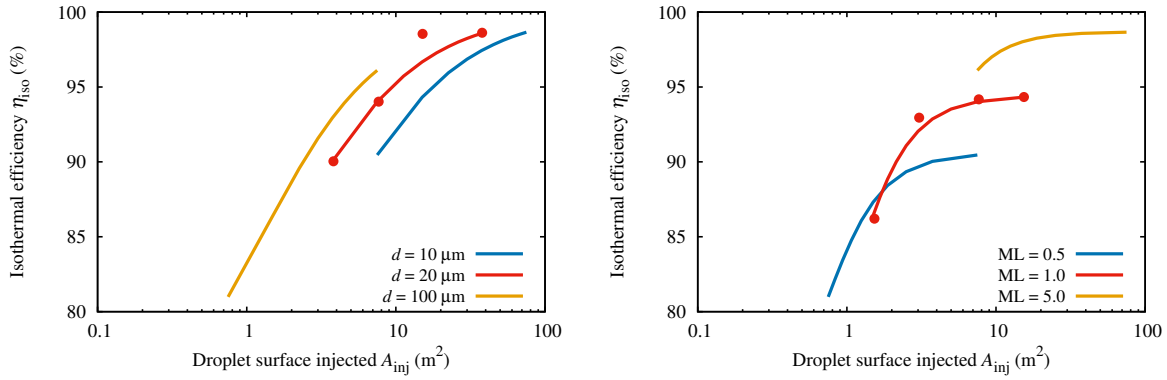

(a) droplet diameters d

(b) mass flowrate ratio ML

Figure 6.6: Isothermal efficiency as a function of the total droplet surface injected at different (a) droplet diameters d and (b) mass flowrate ratio ML (Lines denote the approximate results from Section 6.3.1 and points denote the accurate results from Ref. [6])

capacity ratio C_r of the I-CAES systems:

$$C_r = \left(\frac{V_a}{V_f}\right)\left(\frac{\rho_0 c_p}{\rho_f c_f}\right)\left(\frac{p_{max}}{p_0}\right) \tag{6.27}$$

where ρ_0 is the ambient air density and p_{max}/p_0 is the system pressure ratio. From Eq. (6.27), it can be noted that the the heat capacity ratio C_r increases with the air-to-water volume ratio V_a/V_f and the system pressure ratio p_{max}/p_0. Therefore, when the required heat capacity ratio C_r is low but the pressure ratio p_{max}/p_0 is high, it might be difficult to keep the liquid spray stable due to its low air-to-water volume ratio V_a/V_f. In this case, the aqueous foam should be used instead to further reduce V_a/V_f without impairing the stability. A simplified model for the wet aqueous foam is illustrated in Fig. 6.5, where the white spheres denote the air bubbles whilst the blue background denotes the water. If there are n^3 air bubbles within the cubic space with a side length of a, then the average diameter of the air bubble is $d = a/n$ and the surface-to-volume ratio of the liquid S_v is:

$$S_v = \frac{n^3 \pi d^2}{a^3 - n^3 \pi d^3/6} \approx \frac{6}{d} \tag{6.28}$$

It can be noted from Eq. (6.28) that the surface-to-volume ratio S_v also increases with the average bubble size d decreasing, and d can vary from 10 μm to 1000 μm as well.

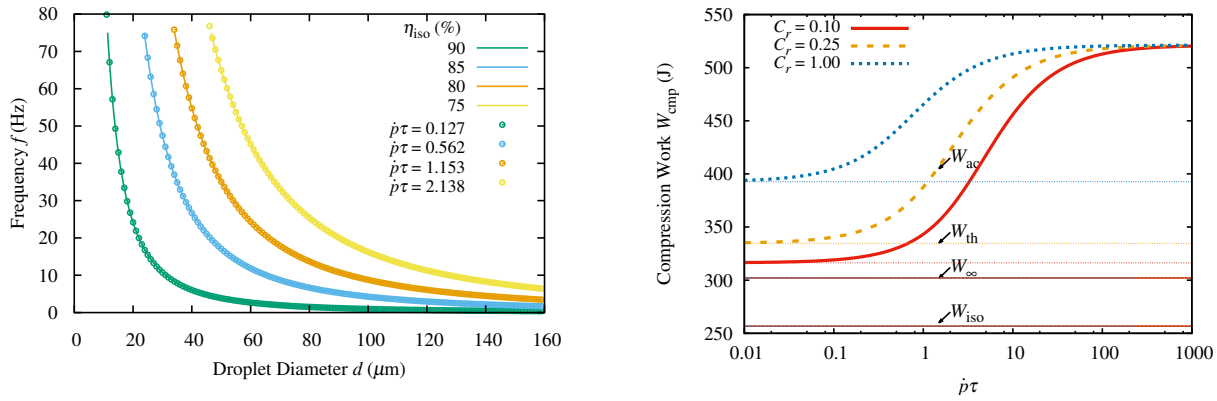

(a) Contours of η_{iso} and $\dot{p}\tau$

(b) Impacts of C_r and $\dot{p}\tau$ on W_{cmp}

Figure 6.7: Impacts of the heat capacity ratio C_r, system frequency f and droplet diameter d on the isothermal efficiency η_{iso}: (a) Contours of η_{iso} and $\dot{p}\tau$ (b) Impacts of C_r and $\dot{p}\tau$ on W_{cmp}

6.4.2 Validation of the isothermal model

The numerical model of isothermal compressor/expander developed in Section 6.3 is validated with the one with direct injections from Ref. [6], and the results are shown in Fig. 6.6. It is notable that the results of this numerical model agree very well with those of isothermal compressor with direct injections from Ref. [6]. The constants α_s and α_f of Section 6.3 are set as 0.6 and 0.2 respectively, which are also in accord with the ones from Ref. [6]. The former is used to adjust the heat transfer area of the water droplets because not all droplets participate in the heat transfer, whilst the latter is for the adjustment of heat transfer time because the compression/expansion is just a fraction of each rotation time. ω denotes the mass of water vapour carried by unit mass of dry air and is determined by comparing the results of the approximate model in Section 6.3.1 with the more accurate numerical results in Ref. [6], as discussed in Section 6.3.3.

The nominal frequency of the isothermal compressor/expander is set as 1 Hz, which is the same with the value in Ref. [6]; whilst the range of system frequency is from 0.5 to 50 Hz. Other parameters of the isothermal compressor/expander are summarized in Table 6.2, and the impact of these isothermal compressor/expander parameters on the system performance will be addressed in later sections.

6.4.3 Temperature difference and water amount

From Section 6.3, it suggests that the system frequency f and the square of droplet diameter d^2 have equivalent effect on the isothermal efficiency η_{iso} which is only determined by the combination $\dot{p}\tau$. To confirm this conclusion, contours of the isothermal efficiency η_{iso} and functions $\dot{p}\tau$ are shown in Fig. 6.7a, from which it can be noted that these exactly overlap. In Fig. 6.7a, the heat capacity ratio C_r is fixed at 0.25 and the droplet velocity is zero so that the Nu (Eq. (6.4)) in Eq. (6.8) is a constant 2. The effects of C_r and $\dot{p}\tau$ on the compression work W_{cmp} are shown in Fig. 6.7b, from which it is notable that even if $\dot{p}\tau \to 0$, the actual compression work W_{cmp} is still higher than the ideal value W_{iso}. In order to further increase η_{iso}, it is essential to further reduce C_r and increase the polytropic efficiency η, as shown by the faint lines in Fig. 6.7b.

From Eqs. (6.10), (6.14), (6.16) and (6.18), it can be noted that the isothermal efficiency η_{iso} can be written as:

$$\eta_{\text{iso}} = \frac{W_{\text{iso}}}{W_\infty}\frac{W_\infty}{W_{\text{th}}}\frac{W_{\text{th}}}{W_{\text{ac}}} = \eta_{\text{ae}}\eta_\infty\eta_{\text{th}} \tag{6.29}$$

where W_{th} denotes the compression work when the temperature difference between the air and water is zero (e.g., $\dot{p}\tau \to 0$, no thermodynamic loss), W_∞ denotes the isothermal work when the water supply is also infinite (e.g., $C_r \to 0$), whilst W_{iso} denotes the ideal isothermal work when the compressor is also free from any loss (e.g., $\eta \to 1$, no aerodynamic loss). Therefore, η_{ae}, η_∞ and η_{th} measures the effect of η, C_r and $\dot{p}\tau$ respectively, and if $\eta_{\text{th}} = 100\,\%$, some parameters such as particle velocity u, α_s and α_f have no impacts on η_{iso}, since the heat transfer between air and water can no longer be enhanced further due to the absence of temperature difference.

From Eq. (6.29) and Fig. 6.7, it can also be noted that an ideal I-CAES should have low system frequency f, droplet diameter d and heat capacity ratio C_r. However, these requirements usually conflict with the economic objectives. For example, large and expensive compressors/expanders are required for I-CAES with low system frequency f, so that the same rated power P and mass flowrate $\dot{m}$ can be reached, as shown by Eq. (6.19). Similarly, expensive nozzles and higher pumping losses are necessary for I-CAES with low droplet diameter d; whilst larger thermal fluid tanks are essential for I-CAES with low heat capacity ratio C_r. Therefore, it can be noted that there is a tradeoff between system efficiency χ and unit storage cost Z with respect to these parameters, and a more detailed thermo-economic analysis on their effects will be carried out in later sections.

6.4.4 Loss analysis

There are mainly two types of losses within the isothermal compressor/expander: the aerodynamic losses stemming from the viscosity and the thermodynamic losses stemming from the temperature heterogeneity. The former is caused by the aerodynamic irreversibility of the device itself. For example, if the polytropic efficiency η of the compressor/expander is not unity, then the aerodynamic loss will be generated. It can be proved analytically that the aerodynamic loss is independent of the heat transfer between the dry air and its surrounding, which includes the liquid-vapour mixture. Therefore, application of the first and second law of thermodynamics to the dry air as an adiabatic system results in the following expression of the aerodynamic loss:

$$\xi_{\mathrm{A}} = \left(\frac{1}{\eta} - 1\right) m R_g T_0 \ln \beta \tag{6.30}$$

where η is the polytropic efficiency of the compressor; whilst for the expander, the term $(1/\eta - 1)$ in Eq. (6.30) should be replaced by $(1-\eta)$. From Eq. (6.30), it can be noticed that the aerodynamic loss is also independent of the inlet temperature of air. Instead, it is only determined by the polytropic efficiency η of the device and the pressure ratio β of the compression process.

The thermodynamic loss is caused by the irreversible heat transfer between the air and liquid-vapour mixture. This may be determined either by calculating the gas-liquid mixture entropy and then subtracting the changes due to aerodynamic effects, or by computing the loss production rate directly, as shown by the following expression:

$$\xi_{\mathrm{T}} = \int \delta Q \frac{(T_{\mathrm{a}} - T_{\mathrm{f}})\, T_0}{T_{\mathrm{a}} T_{\mathrm{f}}} \tag{6.31}$$

It can be noticed from Eq. (6.31) that the thermodynamic loss is mainly determined by two factors: the heat exchange between the gas and liquid δQ and the average temperature difference between the gas and liquid $(T_{\mathrm{a}} - T_{\mathrm{f}})$.

Fig. 6.8 compares the "aerodynamic" ξ_{A} and "thermodynamic" losses ξ_{T} for the compression and expansion processes, where Fig. 6.8a shows the impact of $\dot{p}\tau$ on the losses of compressors at different C_r. It is notable that the thermodynamic loss ξ_{T} of compressor first increases and then decreases with $\dot{p}\tau$, which leads to a peak of ξ_{T}. This is because as $\dot{p}\tau$ increases, the heat exchange δQ between gas and liquid reduces whilst the temperature difference $(T_{\mathrm{a}} - T_{\mathrm{f}})$ increases, resulting in a maximum of the product of the two factors. It is also notable that as C_r increases, the peak of ξ_{T} moves leftward and becomes flatter, which means both $\xi_{\mathrm{T,max}}$ and $(\dot{p}\tau)_{\mathrm{max}}$ decreases with C_r increasing. This is because as C_r increases, the heat exchange δQ will reduce whilst the temperature difference $(T_{\mathrm{a}} - T_{\mathrm{f}})$ will increase. In

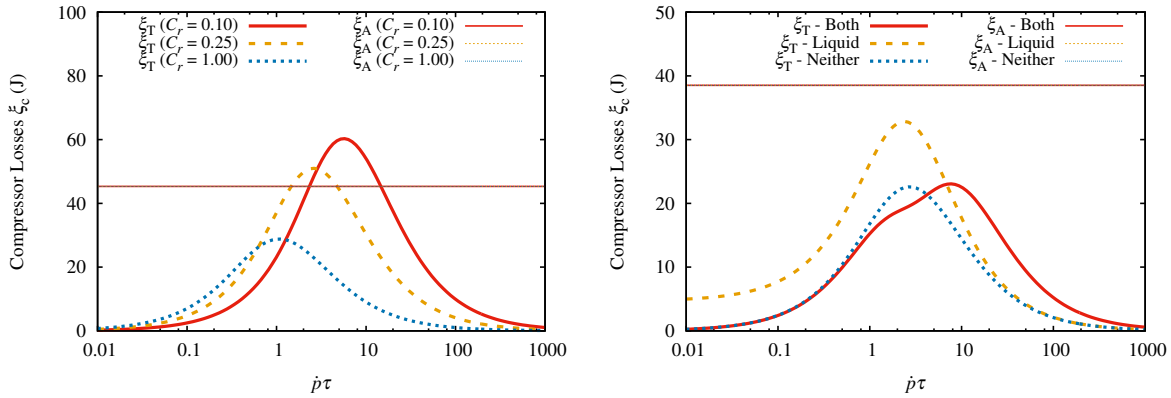

(a) Compressor with different heat capacity ratio C_r (b) Expander with different heat recycling conditions

Figure 6.8: Impact of $\dot{p}\tau$ on the losses of compressor and expander: (a) Compressor with different heat capacity ratio C_r (b) Expander with different heat recycling conditions

order to counteract this effect, the $(\dot{p}\tau)_{\max}$ should be reduced accordingly to make δQ higher and $(T_a - T_f)$ lower. Meanwhile, the heat exchange δQ of $\xi_{T,\max}$ decreases with C_r increasing, which reduces $\xi_{T,\max}$ and and makes the peak flatter. From Fig. 6.8a, it can also be noticed that the aerodynamic loss ξ_A is independent of C_r and $\dot{p}\tau$, which is in accord with the prediction by Eq. (6.30).

According to the definition of isothermal efficiency η_{iso}, only the pressure potential of compressed air is considered as useful work, whilst the thermal energy of both air and liquid are considered as losses. These losses are called storage losses ξ_S and are the main reasons for the low η_{iso} (e.g., $\eta_{iso} = 1 - \xi_A - \xi_T - \xi_S$). However, this assumption is only valid for the Pure I-CAES, whilst for the I-CAES-HR, the thermal energy of the liquid can be partly reused in the isothermal expander during discharge. In the ideal case, both the thermal energy of liquid and air can be recovered, which is actually the "Both" case in Fig. 6.8b. The "Liquid" case refers to the I-CAES-HR, where only the thermal energy of liquid can be recovered; whilst the "Neither" cases refers to the Pure I-CAES, where both the thermal energy of air and liquid are lost.

From Fig. 6.8b, it can be noted that in all cases, there is a peak of ξ_T, which is similar to the cases of the compressors. However, the peak of ξ_T in "Both" case is different from the others due to its coupled interaction with the isothermal compressor. Therefore, analyzing the impact of $\dot{p}\tau$ and C_r on its system performance will be difficult. Actually, it will be impractical to recycle both the thermal exergy of liquid and air. The "Liquid" and "Neither" cases have similar peak shapes, with the exception that the ξ_T in "Liquid" case is not zero when $\dot{p}\tau$ is zero. This is because the inlet temperature of air and water are different, therefore, even if $\dot{p}\tau$ is zero, ξ_T still exists due to the mixing of the inlet fluids. This loss is also referred to as the

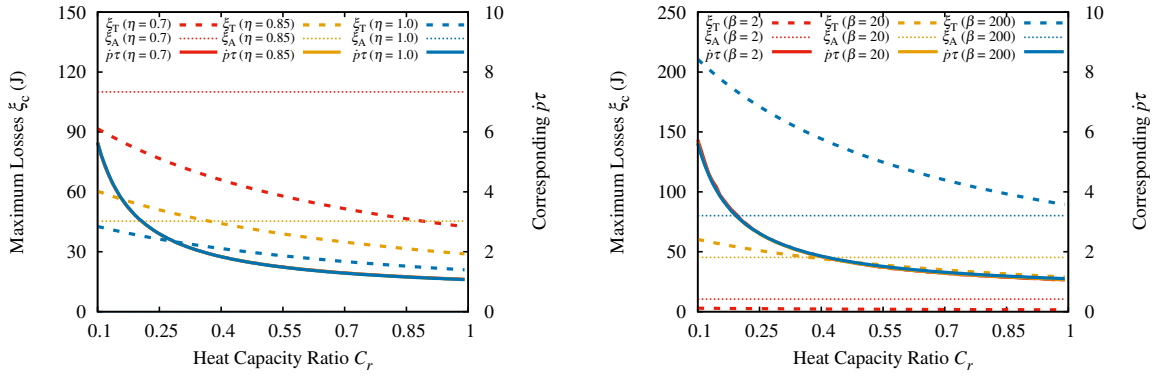

(a) polytropic efficiency η (b) pressure ratio β

Figure 6.9: Variation of $(\dot{p}\tau)_{\max}$ and $\xi_{T,\max}$ with C_r at different (a) polytropic efficiency η and (b) pressure ratio β.

mixing loss and can be calculated by:

$$\xi_T = \ln \frac{T_{in}}{T_{in,a}} + \frac{1}{C_r} \ln \frac{T_{in}}{T_{in,f}} \tag{6.32}$$

where T_{in} is the initial temperature of the air-water mixture after the mixing process, as shown in Eq. (6.12).

As shown by Eq. (6.30), the aerodynamic losses ξ_A of isothermal expanders are also independent of the inlet temperate, so the three cases have exactly the same ξ_A despite of their different inlet temperatures. From Figs. 6.8a and 6.8b, it can also be noted that both ξ_A and ξ_T of isothermal expanders are lower than those of the isothermal compressors.

Fig. 6.9 shows the impact of C_r on the location $(\dot{p}\tau)_{\max}$ and value $\xi_{T,\max}$ of the thermodynamic loss peak, where Fig. 6.9a also shows the impact of polytropic efficiency η whilst Fig. 6.9b also shows the impact of pressure ratio β. In addition, the aerodynamic losses ξ_A at these peaks are also shown for comparison. It can be noted from Fig. 6.9 that both $\xi_{T,\max}$ and $(\dot{p}\tau)_{\max}$ decreases with C_r increasing, but the $(\dot{p}\tau)_{\max}$ is independent of η and β. It can also be noted from Fig. 6.9 that $\xi_{T,\max}$ decreases with η, but increases with β. This is because increasing η or reducing β will lead to lower air temperature T_a and temperature difference $(T_a - T_f)$, therefore, the maximum $\xi_{T,\max}$ will also decrease. In Fig. 6.9, it should be noted that the aerodynamic loss ξ_A also decreases with η and increases with β. Therefore, the variation of η and β has an impact on both ξ_A and ξ_T.

Table 6.2: The standard, minimum and maximum design variable values of I-CAES for the parametric and optimization study

	N_{stg}	$p_{\max}$	$p_{\min}/p_{\max}$	NTU	C_r	f	d	u	η	α_{leak}	f_{p}	T_{f}
Standard	3	80	0.50	9.00	0.25	1.0	20	0	0.85	0.00	0.01	25.0
Minimum	1	80	0.50	1.00	0.10	0.5	10	0	0.80	0.00	0.01	25.0
Maximum	9	200	0.99	49.0	1.00	50	300	30	0.90	0.10	0.10	95.0

6.5 Parametric study

After building the thermo-economic models for each system component, it is useful to consider the effect of varying the various design parameters on both system efficiency and cost of the I-CAES and I-CAES-HR. The results of A-CAES are also included here for comparison. For all three CAES, the nominal stage number N_{stg} is set as three stages, with ambient water as the thermal fluid for each stage. Accordingly, the maximum allowable temperature for each TES is set as $T_{\max} = 100\,^{\circ}\mathrm{C}$, and a relatively low nominal heat capacity ratio $C_r = 0.25$ is selected to prevent the thermal fluid from boiling. Other design variables and their ranges are summarized in Table 6.2. As each parameter is varied, all others are held at their nominal values. The effects of these parameter variations on performance are evaluated in terms of efficiency $\chi = W_{\mathrm{dis}}/W_{\mathrm{chg}}$ and unit storage cost $Z = Z_{\mathrm{tot}}/W_{\mathrm{dis}}$, where W_{chg} and W_{dis} are the work input and output, obtained by integrating power over the charge and discharge time respectively. The total cost Z_{tot} is simply the sum of the various component costs. Mechanical (friction) losses and electrical losses are not accounted for, so χ constitutes a "thermodynamic" roundtrip efficiency. Likewise, the costs are limited to the "thermodynamic" components, as Z_{tot} does not include motor and generator costs.

6.5.1 Effect of cavern and heat exchanger parameters

Figs. 6.10a, 6.10b and 6.10c show respectively the impact of number of stages N_{stg}, maximum cavern pressure $p_{\max}$ and pressure fluctuation $p_{\min}/p_{\max}$ on efficiency and cost. It is notable that the efficiency of A-CAES and I-CAES increase with the number of stage N_{stg}, which is due to the fact that exergetic losses are dominated by the heat exchange process. In the case of heat exchanger with $C_r = 1$, the specific entropy increase may be written as $\Delta s_{\mathrm{hx}} = \varepsilon(1-\varepsilon)\left(\tau + \tau^{-1} - 2\right)$, whereas the specific work input per stage w_{c} is given by Eq. (6.14). The ratio $T_0 \Delta s_{\mathrm{hx}}/w_{\mathrm{c}}$ is an increasing function of temperature ratio τ. A similar result hold for cases with $C_r < 1$, thus leading to the observed trend of χ with N_{stg}, as higher N_{stg} leads to lower τ. This trend is also valid for I-CAES-HR, however, its pumping loss increases rapidly

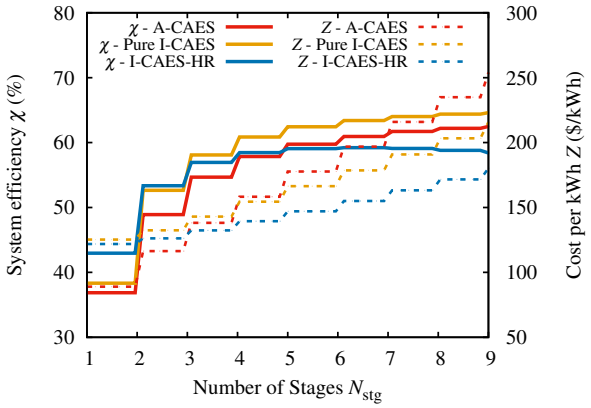

(a) Number of stages N_{stg}

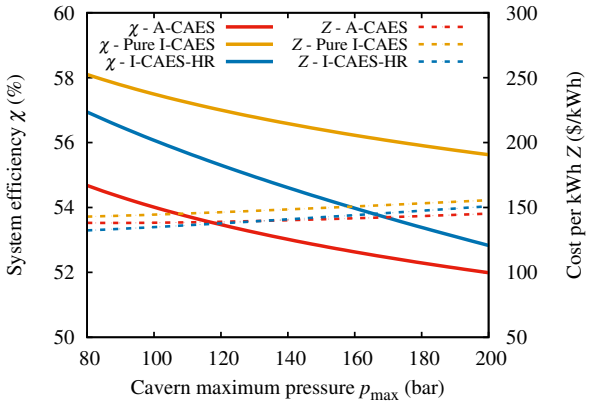

(b) Cavern maximum pressure p_{max}

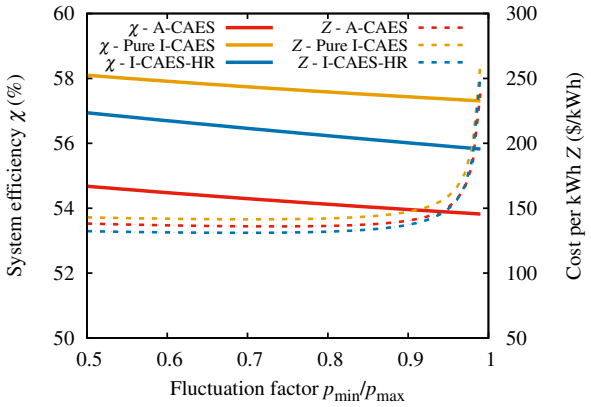

(c) Fluctuation factor $p_{\text{min}}/p_{\text{max}}$

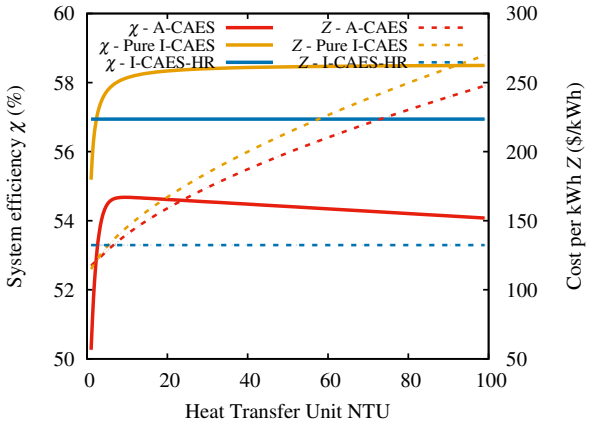

(d) Heat transfer unit NTU

Figure 6.10: Variation of system efficiency and unit cost with various system parameters: (a) Number of stages N_{stg} (b) Cavern maximum pressure p_{max} (c) Fluctuation factor $p_{\text{min}}/p_{\text{max}}$ (d) Heat transfer unit NTU

with N_{stg} and eventually drags down its efficiency at high N_{stg}. Fig. 6.10a also shows that the unit storage cost of all CAES increase with the number of stages N_{stg}, whereas that of the I-CAES-HR increases slightly. This is because the cost of both heat exchangers and thermal fluid tanks increase with N_{stg}, whilst there is only cheap thermal fluid tanks in I-CAES-HR, which reduces the increase rate.

Fig. 6.10b shows that with the maximum cavern pressure $p_{\max}$ increasing, the system efficiency of all CAES decreases monotonically. This is also due to the dominant heat exchange losses, which increases with the temperature ratio τ. The I-CAES-HR has the largest reduction because of its additional pumping loss. From Fig. 6.10c, it can be noted that increasing the ratio of the minimum to maximum pressure $p_{\min}/p_{\max}$ in the cavern reduces the efficiency slightly, but significantly increases the cost. The reduction in χ mainly stems from the increased average pressure and heat exchange losses, whereas the higher unit cost is a consequence of reduced storage density since the cavern is only partially emptied with each cycle.

The effect of varying the NTU rating of the heat exchangers is shown in Fig. 6.10d. Increasing NTU improves heat exchanger effectiveness ε but with diminishing returns, as shown by the $\varepsilon-$NTU model. Consequently, the roundtrip efficiency increases with NTU for the A-CAES and I-CAES systems, but the improvement is marginal beyond NTU ~ 10, whereas the cost rises in accord with heat exchanger cost equation. For A-CAES, the density of its working fluid (air) is relatively low and the pressure losses are more significant. These losses outweigh the small improvement in ε at high NTU such that the efficiency reaches its maximum at NTU ~ 10.

6.5.2 Effect of isothermal compressor/expander parameters

Fig. 6.11a shows the impact of heat capacity ratio C_r on efficiency and cost, from which it can be noted that as C_r decreases, the system efficiency χ of A-CAES decreases monotonically, the χ of pure I-CAES increases monotonically, whilst the χ of I-CAES-HR increases at first but begins to decrease after C_r reaches its optimal value. This is because the heat capacity ratio C_r has different meanings for different CAES systems. For A-CAES, lower C_r means lower TES temperature, unnecessary irreversibility and higher heat transfer and auxiliary losses. Therefore, C_r should always be fixed at one for A-CAES. For pure I-CAES, however, lower C_r means less temperature variation and higher isothermal efficiency η_{iso}, which then increases the system efficiency χ. For I-CAES-HR, though lower C_r also means higher isothermal efficiency η_{iso} and lower auxiliary losses, it increases the pumping work as well, which lead to an optimal C_r for I-CAES-HR due to the two conflicting effects. The unit storage cost Z of each CAES generally increases with the heat capacity ratio C_r, as more thermal fluid and

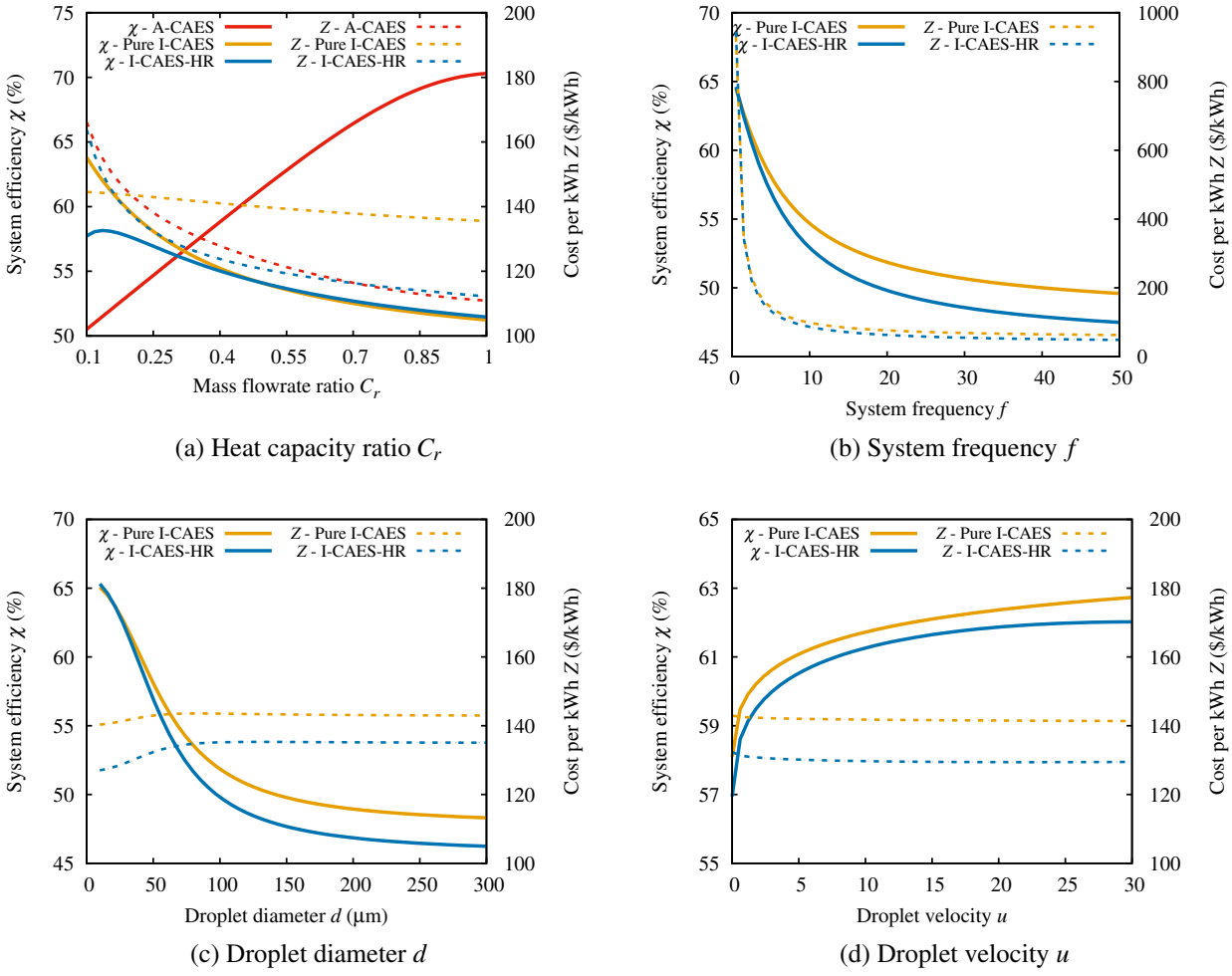

(a) Heat capacity ratio C_r

(b) System frequency f

(c) Droplet diameter d

(d) Droplet velocity u

Figure 6.11: Variation of system efficiency and unit cost with various isothermal compressor/expander parameters: (a) Heat capacity ratio C_r (b) System frequency f (c) Droplet diameter d (d) Droplet velocity u

more expensive TES is required for lower C_r. However, it is worth mentioning that the pure I-CAES needs far less thermal fluid than the other two CAES systems, as thermal energy is not stored within the pure I-CAES. Therefore, the increase in Z is less significant for pure I-CAES system.

The effects of system frequency f, droplet diameter d and droplet velocity u on roundtrip efficiency and unit cost are shown in Figs. 6.11b to 6.11d. Recall that the temperature difference between air and water is determined by these variables, so as $\dot{p}\tau$ decreases, I-CAES will enjoy lower heat transfer losses and higher efficiency η_{I}. Unsurprisingly, the system efficiency of both I-CAES systems decrease with system frequency f and droplet diameter d, as shown in Figs. 6.11b and 6.11c respectively, but increases with the droplet velocity u, as shown in Fig. 6.11d. This is due to the increase in equivalent heat exchanger effectiveness ε, as shown in Eq. (6.8). Figs. 6.11b and 6.11c also show that the I-CAES-HR is more sensitive to $\dot{p}\tau$ than I-CAES. This is because the I-CAES-HR recycles part of its thermal energy at the expense of higher pumping loss, therefore, as $\dot{p}\tau$ increases, the stored thermal energy cannot be fully used but the pumping loss remains high, which makes its efficiency χ lower than that of I-CAES. Increasing the droplet velocity u not only increases the efficiency η_{th} but also the pumping loss ξ_{pmp}, as higher pressure difference $\Delta p = \rho u^2/2$ is required for droplets injection. Therefore, there is a tradeoff between η_{th} and ξ_{pmp}, as well as an optimal u for this tradeoff. As for the unit storage cost Z, it is notable that Z decreases rapidly with frequency f, as indicated by Eq. (6.19), but generally remains constant as u and d varies.

6.5.3 Effect of compressor/expander parameters

Figs. 6.12a to 6.12c show respectively the impact of polytropic efficiency η, heat leakage factor α_{leak} and pressure loss factor f_p on efficiency and cost. It is notable that increasing the polytropic efficiency of compressors and expanders results in a more or less linear increase in overall efficiency, with the I-CAES systems slightly more sensitive to this increase than the A-CAES, as shown in Fig. 6.12a. The unit storage cost of I-CAES systems, however, reveals an opposite trend to that of the A-CAES. This is because the compressor/expander cost of A-CAES increases with the polytropic efficiency η; whilst the compressor/expander cost of I-CAES systems is independent of η, as shown in Eq. (6.19). However, the shape of these curves is of course dependent on the form of compressor/expander cost equations which, as already noted, are subject to some uncertainty. The impacts of nominal polytropic efficiency η_{nom} and cost ratio k_r on the optimization results will be analyzed in Chapter 8.

The heat leakage factor α_{leak} is included in this chapter (whilst ignored in other chapters) because heat leakage is useful for improving the I-CAES performance, and liquid piston and reciprocating devices are often deployed to enhance α_{leak}. From Fig. 6.12b, it can be noted

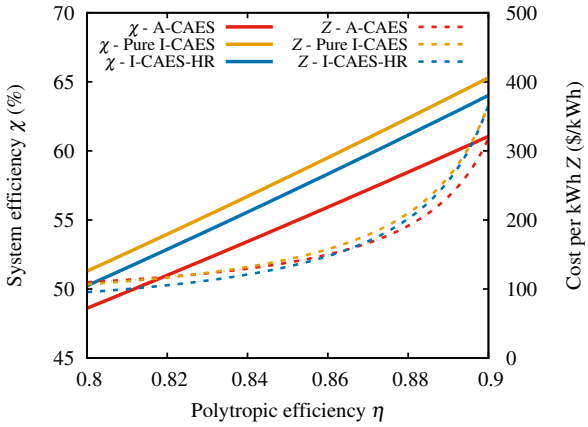

(a) Polytropic efficiency η

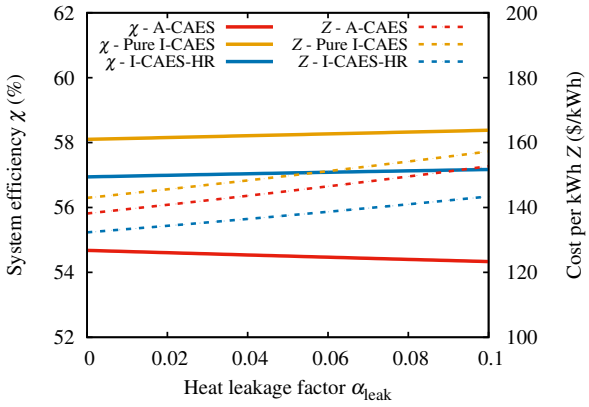

(b) Heat leakage factor α_{leak}

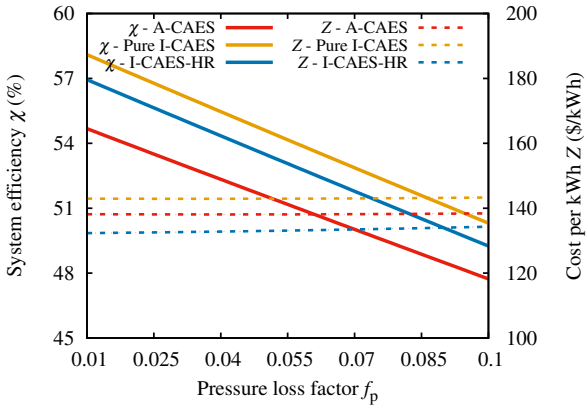

(c) Pressure loss factor f_p

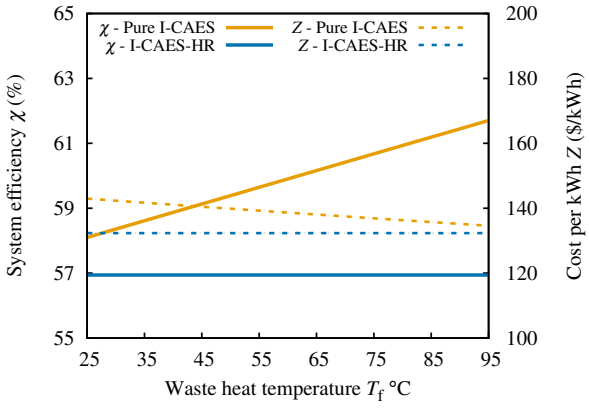

(d) Waste heat temperature T_{f}

Figure 6.12: Variation of system efficiency and unit cost with various compressor/expander parameters: (a) Polytropic efficiency η (b) Heat leakage factor α_{leak} (c) Pressure loss factor f_p (d) Waste heat temperature T_{f}

that the efficiency of A-CAES decreases slightly with the heat leakage factor α_{leak}; whilst the efficiency of I-CAES systems increases slightly with it. This is because A-CAES can recycle the thermal energy generated during compression and higher α_{leak} means more heat leakage loss; whilst the I-CAES systems can only recycle part (or none) of the thermal energy and higher α_{leak} only makes it closer to ideal isothermal processes. Meanwhile, the unit storage cost of all CAES increases slightly with α_{leak} because higher α_{leak} means lower specific work and higher mass flowrate $\dot{m}$, which then increases the capital cost of isothermal compressor/expander. It is worth mentioning that the impact of α_{leak} on efficiency and cost are relatively insignificant, which means increasing α_{leak} is not an ideal method for improving isothermal efficiency η_{iso}.

The pressure loss factor f_p is included in this chapter because reciprocating devices are often employed as the isothermal compressor/expander, the value loss of which are often too large to be ignored. Increasing the pressure loss factor f_{p} of compressors and expanders results in more or less linear decrease in system efficiency, with χ reducing by roughly 1.0 percentage point for each percentage point increase in pressure loss factor f_{p}, as shown in Fig. 6.12c. The reduction rate actually depends on the pressure ratio per stage β, with more rapid reduction at low β and high N_{stg}. Therefore, A-CAES might have the highest pressure loss due to its high N_{stg} and low β in reality. However, it should be noted that the pressure loss factor f_{p} is only significant for reciprocating devices but becomes negligible in turbomachinery. The unit storage cost of all CAES generally remains unchanged with f_{p}, despite the rapid reduction in χ.

The impact of waste heat recovery on I-CAES are shown in Fig. 6.12d, from which it can be noted that the improvement in efficiency is significant even if the waste heat temperature T_{f} is relatively low. It is worth mentioning that the waste heat integration cannot be easily applied to A-CAES and I-CAES-HR, because there is already a TES system within them.

6.6 Loss and cost distributions of the standard designs

The main results for the nominal designs of the three CAES are shown in Table 6.3. In the nominal cases, the I-CAES-HR has higher efficiency and lower cost than the Pure I-CAES, and the A-CAES has the worst performance of the three CAES systems. It will be useful to see how this has been achieved, and how the losses and costs are distributed amongst the different components. This information is provided in the histogram of Fig. 6.13.

For both the I-CAES and I-CAES-HR, losses are dominated by the irreversibility in the compressors and expanders. Compression losses are slightly greater than expansion losses because it has been assumed that these processes have the same polytropic efficiency ($\eta_{\text{c}} =$

Table 6.3: Main results for the standard designs

	A-CAES	Pure I-CAES	I-CAES-HR
System Efficiency	54.1 %	63.9 %	66.3 %
Cost per kWh	151 $/kWh	139 $/kWh	121 $/kWh
Capital Cost	41.4 M$	41.1 M$	36.1 M$
Net Output Work	274 MWh	296 MWh	298 MWh
Net Input Work	506 MWh	464 MWh	449 MWh

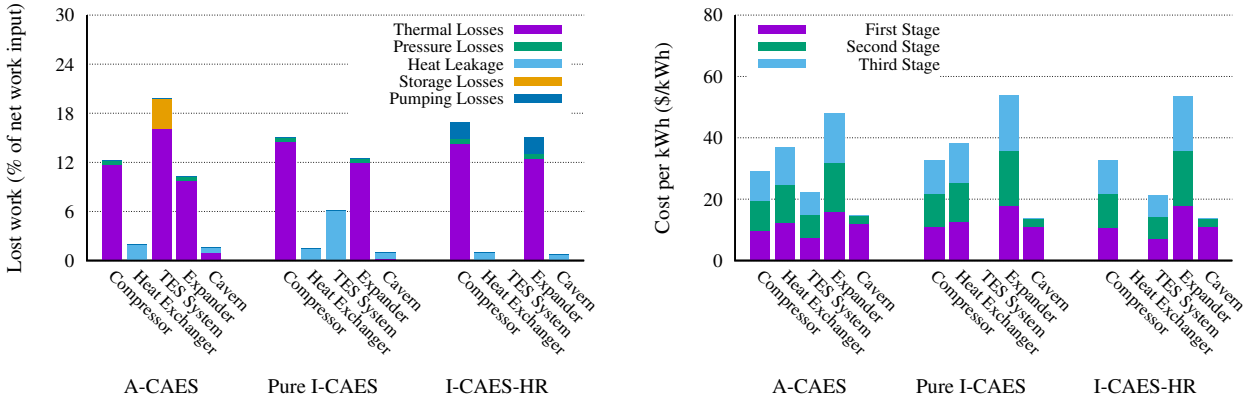

(a) Loss distributions

(b) Cost distributions

Figure 6.13: Loss and cost distributions of different I-CAES and A-CAES with standard designs: (a) Loss distributions (b) Cost distributions

$\eta_e = \eta$), which gives (for a given pressure ratio) $\Delta s_c/\Delta s_e = 1/\eta$. It is possible that slightly better designs might be realized if this assumption were relaxed. For the A-CAES, the largest loss is associated with the TES and is mainly due to the irreversible heat exchange caused by the low C_r. This TES loss is also the second largest one for Pure I-CAES, however, it is caused by the heat leakage instead because thermal exergy is not stored but simply dissipated into the environment in the Pure I-CAES. For I-CAES-HR, the TES loss is negligible because there is neither heat exchange nor leakage loss in its TES and the water is simply stored in it at near ambient temperature. Instead, the next biggest loss for I-CAES-HR is the pumping loss because the ambient water need to be pumped to high pressures before being injected into the isothermal compressor/expander, and this work can hardly be recycled. Finally, the loss category labeled "cavern" includes direct cavern losses plus exergetic losses due to air being returned to atmosphere after discharge at a temperature above/below T_0. This category is slightly larger for A-CAES because during discharge, its exit temperature is below ambient due to the inefficient heat exchange of TES system.

Fig. 6.13b shows that the isothermal compressor/expander cost forms a dominant part in the I-CAES-HR, whilst the heat exchanger cost of A-CAES and I-CAES is comparable to that of its compressor/expander. However, the heat exchanger cost of I-CAES can be significantly reduced because cheap heat exchangers with low NTU but $C_r \approx 0$ can achieve high effectiveness ε and efficiently dissipate the waste heat, whilst in the A-CAES, a large portion of its input exergy is stored in the TES and the heat capacity ratio C_r should be fixed at one. It is also notable that there is no TES cost in the Pure I-CAES, as all of its thermal exergy is dissipated via the auxiliary heat exchangers. On the other hand, the thermal exergy of water is recycled and stored in the TES in I-CAES-HR. Therefore, there is no heat exchanger cost but only TES cost in I-CAES-HR. It is worth mentioning that the TES cost is relatively low because the thermal fluid (ambient water) and the containment vessel (water tanks) are both very cheap.

6.7 Summary

In this chapter, an approximate thermodynamic model has been built for the isothermal compressor/expander, and this model is integrated into the I-CAES with and without heat recycling. The expressions of isothermal efficiency, aerodynamic and thermodynamic losses are derived and this model is validated with more detailed and accurate numerical models. After that, parametric studies are carried out for both Pure I-CAES and I-CAES with heat recycling (I-CAES-HR), and their results are compared with each other. It is found that some parameters of the I-CAES, such as k_r, η_{nom} and $\dot{p}\tau$, is subject to significant uncertainty, and the impacts of these parameters on the final optimization results will be dealt with in Chapter 8. From this chapter, it can be concluded that:

1. The isothermal efficiency η_{iso} is determined by three factors, namely the combination $\dot{p}\tau$, the heat capacity ratio C_r and the polytropic efficiency η. The combination $\dot{p}\tau$ is further determined by the system frequency f, droplet diameter d and droplet velocity u. If the droplet velocity u is negligible, then the system frequency f and the square of droplet diameter d^2 has the same effect on the system efficiency.

2. The losses within the isothermal compressor/expander can be divided into the aerodynamic and thermodynamic loss. The aerodynamic loss is only determined by the polytropic efficiency η and the pressure ratio β, and is independent of the heat transfer with water and the inlet temperature of air. The thermodynamic loss first increases but then decreases with $\dot{p}\tau$, resulting in a peak $\xi_{\text{T,max}}$ at $(\dot{p}\tau)_{\text{max}}$. With the heat capacity ratio C_r increasing, both $\xi_{\text{T,max}}$ and $(\dot{p}\tau)_{\text{max}}$ decreases accordingly.

3. The effect of mass transfer on the isothermal compression/expansion depends on the type of fluid as well as the average temperature and pressure. The effect of mass transfer is less significant at high pressure and low temperature operating conditions. For water, the effect of mass transfer should be considered and the liquid mass should be adjusted accordingly, whilst for the mineral oil, the effect of mass transfer can be ignored without causing much error.

4. The heat transfer loss is the dominant loss within the I-CAES system, therefore, in order to achieve higher system efficiency, the pressure ratio per stage β should be reduced, which means lower cavern maximum pressure $p_{\max}$ and more stages N_{stg}. For the I-CAES with heat recycling (I-CAES-HR), the pumping loss and capital cost of water tanks should be considered separately. The system efficiency of I-CAES can also be increased by reducing $\dot{p}\tau$, however, changing any factor of $\dot{p}\tau$ may cause an increase in capital cost, and the tradeoff between efficiency and cost must be considered.

5. For both I-CAES and I-CAES-HR, the losses are dominated by the compressor/expander ones, and the next largest loss for I-CAES is the heat leakage loss within auxiliary heat exchangers; whilst for I-CAES-HR the second largest loss is the pumping loss within the isothermal compressor/expander.

Chapter 7

Liquid Air Energy Storage

7.1 Introduction

Liquid Air Energy Storage (LAES) refers to the process of cryogenically cooling and liquefying air using off peak energy and then allowing its expansion through a series of turbines when the energy demand exceeds its supply. Compared with CAES, LAES is not bound by the specific geographical and geological requirements, and the energy density of liquid air is much higher than that of the compressed air. A key milestone for LAES was the completion and testing of a 350 kW/2.5 MWh demonstration plant by Highview, which is based on a Claude liquefaction cycle during charge and a Rankine cycle during discharge. Since then, there is a number of literature on the thermodynamic analysis and performance improvement of LAES [37–39, 97, 98, 102]. However, some earlier LAES designs (particularly those before 2000) cannot efficiently recycle and reuse the "hot energy" generated by compression during charge and the "cold energy" released by the liquid air during discharge, which impairs their roundtrip efficiency. In addition, some LAES systems make use of a complicated multi-stream heat exchanger (or a "cold box"), which could be beneficial for the heat transfer loss reduction but will inevitably make the system more complicated and the results more difficult to interpret.

As a result, in this chapter, a simple but efficient LAES has been introduced, and its stable operation requirements have been analyzed in detail. Both the packed bed thermal reservoir and the heat exchanger with thermal fluid tanks have been used as the cold TES, and their performance are compared with each other. The phenomena unique to the LAES, such as the pinch point problem and thermal shock wave, have been studied in depth, and the impacts of TES materials and operating pressure on these phenomena are also considered. After that, parametric studies are conducted to find the relative sensitivity of LAES performance to various parameters. Finally, the drawbacks of LAES are pointed out and the methods for potential

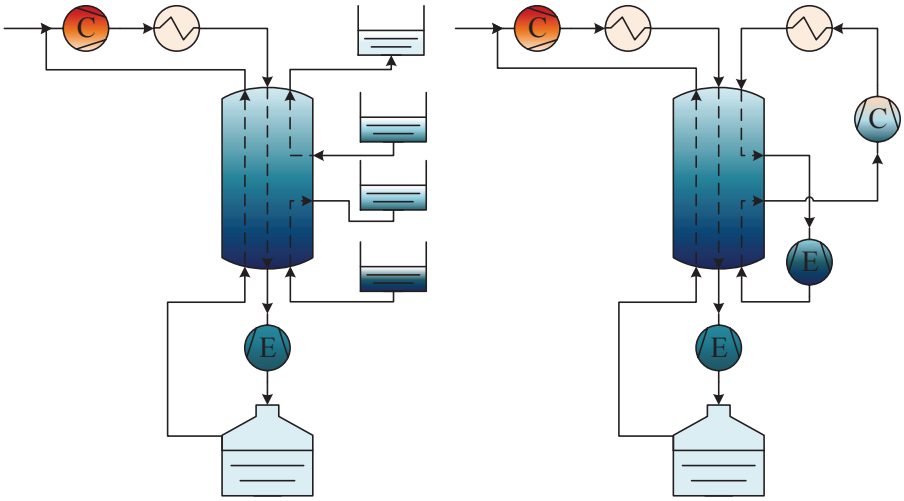

(a) Linde-Hampson system (b) Claude system

Figure 7.1: Schematic diagram of the various air liquefaction systems: (a) Linde-Hampson system (b) Claude system

improvement are also given. In Chapter 8, the LAES with liquid TES will be optimized and compared with other energy storage systems.

7.2 Cycle layouts

A typical LAES comprises of three primary processes: air liquefaction, energy storage and power recovery. Depending on the types of air liquefaction unit, LAES can be further divided into the Linde-Hampson and the Claude system. The Linde-Hampson system is shown in Fig. 7.1a, from which it can be noted that if there is no pre-stored "cold energy" available, then it will use the flash gas (unliquified air vapour) to liquefy the incoming gas. As a result, it suffers from low efficiency due to the throttling losses and the compression of flash-gas. However, since the LAES is an integrated system, a Cryogenic Energy Storage (CES) system, or a cold TES, can be deployed to recycle the "cold energy" of liquid air and enhance the system efficiency. The cold TES operates over a wide temperature range between 80 K to 300 K. Therefore, it usually employs a large multi-stream heat exchanger system with several different thermal fluids to cover the temperature range and minimize the heat transfer loss.

The schematic diagram of the Claude system is shown in Fig. 7.1b. It uses the cold generated from the expansion of compressed air to liquefy the mainstream air, and is claimed to be much more efficient than the Linde - Hampton system. However, as mentioned above, this is due to the fact that there is no pre-stored "cold energy" available in a stand-alone air

liquefaction plant, which is not the case for an "adiabatic" LAES system. Therefore, during the stable operations of an adiabatic LAES, it is unnecessary to use additional expansion to get extra cold, and the Claude cycle may only be useful for the starting process of LAES when the cold TES is completely discharged.

Therefore, a modified Linde - Hampson LAES with an efficient CES will be analyzed in detail in this chapter. Its schematic diagram is shown in Fig. 7.2. During charge, the ambient air is compressed in the compressor, stores its thermal exergy in the hot TES and finally releases its extra heat in the auxiliary heat exchanger to reduce its temperature to ambient value. This process is usually repeated one or two times before the compressed air is split into two flows: the mainstream flow absorbs the "cold energy" from the cold TES and the rest auxiliary flow absorbs the "cold energy" from the flash-gas. Finally, the two flows are mixed and expanded in a cryogenic expander (or throttled through a valve) to further reduce its temperature. The generated liquid-vapor mixture is then separated: the liquid air is stored in a cryogenic tank whilst the vapor (flash-gas) is circulated through an auxiliary heat exchanger to recycle its "cold energy". After that, the ambient temperature flash-gas is mixed with the incoming air for the next cycle. For the liquid LAES (LAES with liquid TES only), the cold TES and auxiliary auxiliary heat exchanger in Fig. 7.2 could be replaced by a multi-stream heat exchanger (or a "cold box"). For the solid LAES (LAES with solid TES only), however, the multi-stream heat exchanger cannot be employed. Therefore, in order to better compare these two types of LAES systems, the auxiliary heat exchanger is separated from the cold TES, and the compressed air is separated before entering these two components, as shown in Fig. 7.2.

7.3 System modelling

7.3.1 Modelling of the heat exchanger

Unlike other energy storage systems, the working fluid (supercritical air) of LAES is operated around its critical point in the cold TES. Therefore, the ideal gas assumption is no longer valid and the pinch point problem caused by heat capacity variation must be considered. This challenge has been well addressed by Pau Farres-Antunez [7, 49], and his method is included here for the sake of completeness. Similar to the heat exchanger introduced in Chapter 4, the counterflow concentric-tube design and the $\varepsilon - \mathrm{NTU}$ method are still adopted, and the heat capacity ratio C_r is still set as one, but the heat exchanger effectiveness ε is defined as:

$$\varepsilon = \frac{\dot{Q}}{\dot{Q}_{\max}} \tag{7.1}$$

where $\dot{Q}_{\max}$ represents the maximum heat transfer rate - i.e. that of an infinitely large heat exchanger. If the working fluid is ideal gas and the heat capacity variation is negligible, then $\varepsilon = 1$ means there is no temperature difference everywhere within the heat exchanger and the $\varepsilon - \text{NTU}$ method here is essentially the same with that in Chapter 4. However, if the fluids exhibit c_p variation, then $\varepsilon = 1$ means the temperature difference is zero just at the pinch point but not elsewhere, which implies that the process is still irreversible. In this study, $\dot{Q}_{\max}$ is therefore found by imposing zero temperature difference at the pinch point for the give mass flowrate and inlet conditions. As shown by Fig. 7.5, the pinch point appears either somewhere in the middle of the heat exchanger or at points $Q = 0$ (left end) or $Q = 1$ (right end). If it happens in the middle, then the temperature difference $\Delta T\left(\dot{Q}\right) = T_{\text{h}}\left(\dot{Q}\right) - T_{\text{c}}\left(\dot{Q}\right)$ has a local minimum at that point, which implies:

$$\frac{\mathrm{d}T_{\text{h}}\left(\dot{Q}\right)}{\mathrm{d}\dot{Q}} = \frac{\mathrm{d}T_{\text{c}}\left(\dot{Q}\right)}{\mathrm{d}\dot{Q}} \tag{7.2}$$

If the changes in kinetic and potential energy within each stream is neglected, then the steady-flow energy equation can be written in the following differential form:

$$\mathrm{d}\dot{Q} = \dot{m}\mathrm{d}h = \dot{m}\left[\left(\frac{\partial h}{\partial T}\right)_p \mathrm{d}T + \left(\frac{\partial h}{\partial p}\right)_T \mathrm{d}p\right] \approx \dot{m}c_p\mathrm{d}T \tag{7.3}$$

where the right hand side of Eq. (7.3) is exact for perfect and semi-perfect gases, and a good approximation for real fluid as long as the pressure loss within the heat exchanger is small. Therefore, combining Eq. (7.2) with Eq. (7.3) leads to:

$$\dot{m}_{\text{h}}c_{p,\text{h}}T_{\text{p,h}} = \dot{m}_{\text{c}}c_{p,\text{c}}T_{\text{p,c}} \tag{7.4}$$

Since there is no temperature difference at the pinch point when $\varepsilon = 1$, the possible pinch point temperature T_{p} could be find through Eq. (7.4) by examining the $\dot{m}c_p$ variation between T_{c} and T_{h}. T_{c} and T_{h} corresponds to the minimum and maximum temperature limit respectively:

$$T_{\text{c}} = \max\left(T_{\text{c},1}, T_{\text{liq,min}}\right)$$

$$T_{\text{h}} = \min\left(T_{\text{h},2}, T_{\text{liq,max}}\right)$$

where $T_{\text{liq,min}}$ and $T_{\text{liq,max}}$ are the minimum and maximum allowable temperature of the thermal fluid respectively, whereas $T_{\text{c},1}$ and $T_{\text{h},2}$ are the inlet temperature of the cold fluid and hot fluid respectively. The subscripts 1 and 2 respectively correspond to the left and right hand

side of a $T-Q$ diagram during a heating process, such as Figs. 7.5b and 7.5d. If the thermal fluid has a wide allowable temperature range, then the inlet temperature of the two fluids will be used as range to search for T_p and $\dot{Q}_\mathrm{max}$; otherwise, the allowable temperature of thermal fluids will place a limit on the search range in order to prevent the thermal fluid from boiling or freezing.

If the pinch point temperature T_p is found in the middle of T_c and T_h, then the heat transfer rate $\dot{Q}_\mathrm{T,p}$ could be calculated by:

$$\dot{Q}_\mathrm{T,p} = \dot{m}_\mathrm{c} \int_{T_\mathrm{c}}^{T_\mathrm{p}} c_{p,\mathrm{c}} \mathrm{d}T_\mathrm{c} + \dot{m}_\mathrm{h} \int_{T_\mathrm{p}}^{T_\mathrm{h}} c_{p,\mathrm{h}} \mathrm{d}T_\mathrm{h} \tag{7.5}$$

The heat transfer rate $\dot{Q}_\mathrm{T,p}$ given by Eq. (7.5) could be the maximum heat transfer rate $\dot{Q}_\mathrm{max}$ if the equal local heat capacity rate indeed represents the minimum of $\Delta T\left(\dot{Q}\right)$. However, the condition of equal local heat capacity rate could also represent a maximum of $\Delta T\left(\dot{Q}\right)$, in which case Eq. (7.5) would not be valid and the pinch point would occur at either 1 (left end) or 2 (right end) instead. Suppose that the pinch point occurs at 1, then the outlet temperature of the hot fluid $T_\mathrm{h,1}$ equals T_c and the heat transfer rate $\dot{Q}_\mathrm{T,1}$ is:

$$\dot{Q}_\mathrm{T,1} = \dot{m}_\mathrm{h} \int_{T_\mathrm{c}}^{T_\mathrm{h,2}} c_{p,\mathrm{h}} \mathrm{d}T_\mathrm{h} \tag{7.6}$$

Similarly, if the pinch point occurs at 2, then the outlet temperature of the cold fluid $T_\mathrm{c,2}$ equals T_h and the heat transfer rate $\dot{Q}_\mathrm{T,2}$ is:

$$\dot{Q}_\mathrm{T,2} = \dot{m}_\mathrm{c} \int_{T_\mathrm{c,1}}^{T_\mathrm{h}} c_{p,\mathrm{c}} \mathrm{d}T_\mathrm{c} \tag{7.7}$$

It can be shown that the actual value of the maximum heat transfer rate must be the minimum of the three integrals, which in turn indicates the actual pinch point location.

$$\dot{Q}_\mathrm{max} = \min\left(\dot{Q}_\mathrm{T,1}, \dot{Q}_\mathrm{T,2}, \dot{Q}_\mathrm{T,p}\right) \tag{7.8}$$

Then the actual value of total heat transfer rate $\dot{Q}$ can be calculated from Eq. (7.1), and the outlet temperature of the hot and cold fluids can be calculated from the enthalpy change indicated by the total heat transfer rate $\dot{Q}$.

7.3.2 Modelling of the cryogenic system

Since the cryogenic pump and the cryo-turbine operate in (or near) the liquid phase, where the density change with pressure is insignificant, the simple isentropic efficiency η is used to model their performance. The work consumed by the cryogenic pump w_pmp or extracted by

the cryo-turbine w_{turb} is given by:

$$w_{\text{pmp}} = \int_{p_0}^{p_{\text{d}}} \frac{\mathrm{d}p}{\eta\rho} \tag{7.9}$$

$$w_{\text{turb}} = \int_{p_0}^{p_{\text{c}}} \frac{\eta \mathrm{d}p}{\rho} \tag{7.10}$$

where ρ is the average density of saturated liquid air.

The costs of a cryogenic pump and a cryo-turbine are respectively [119]:

$$Z_{\text{pmp}} = 3540 W_{\text{pmp}}^{0.71} \tag{7.11}$$

$$Z_{\text{turb}} = 6000 W_{\text{turb}}^{0.7} \tag{7.12}$$

where W_{pmp} and W_{turb} are the power output of the cryogenic pump and cryo-turbine respectively (Unit: kW), which can be obtained by multiplying Eqs. (7.9) and 7.10 with the discharging and charging mass flowrate respectively; whilst Z_{pmp} and Z_{turb} are the purchase cost of the cryogenic pump and cryo-turbine respectively (Unit: USD).

The purchase cost as well as the isentropic efficiency of the cryogenic pump and cryo-turbine are subject to significant uncertainty. However, since the corresponding work term is very small, their impact on the unit storage cost Z is negligible.

7.4 System analysis

In order for the LAES to operate stably and sustainably, the "cold exergy" released by 1 kg of liquid air during discharge must be sufficient for producing (at least) the same amount of liquid air during charge, or otherwise the produced liquid air will become less and less after cycles of operation and the LAES will stop working eventually. This operating stability challenge will be addressed in Section 7.4.1, where it is found that for each 1 kg of liquid air, there should be $(1+\alpha)$ kg of air being compressed and cooled in the hot TES, then 1 kg of the compressed air is liquefied by the cold TES whilst the rest α kg is liquefied by the flash-gas. That way, the cold TES will get replenished by the 1 kg of liquid air during discharge, and the "hot exergy" for 1 kg of air will also be absorbed from the hot TES. The excess "hot exergy" for α kg of air will simply be dissipated as storage losses in this thesis, though it has been pointed out in Ref. [133] that this exergy can also be used for organic Rankine cycle (ORC). The impact of storage media and operating pressure on the solid and liquid TES will also be discussed in Sections 7.4.2 and 7.4.3 respectively.

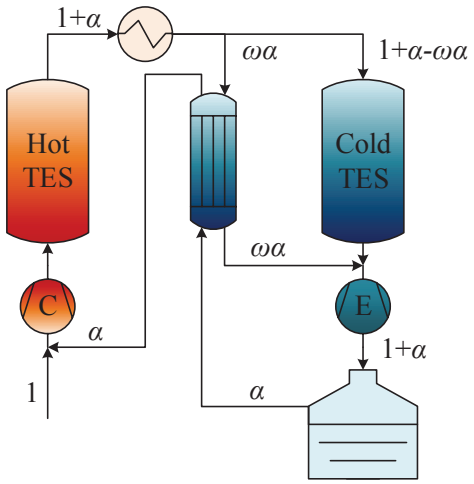

Figure 7.2: Schematic diagram of an adiabatic LAES system

7.4.1 Stability analysis

Most energy storage systems, such as CAES and PTES, store electricity in the form of pressure or thermal potential during charge; whilst during discharge, the stored available energy is completely released and converted back into electricity. The LAES, however, must charge up the cold TES during discharge and then release the pre-stored "cold exergy" during charge, which is opposite to the desired direction. This characteristic of LAES not only drags down its energy density but also gives rise to the challenge of stable operation. For example, if a LAES always uses more "cold exergy" during charge than it can replenish during discharge, then the pre-stored cold exergy will finally be depleted after several cycles of operation. Therefore, in order for LAES to operate stably and sustainably, at least the same amount of cold exergy must be replenished during discharge as the amount consumed during charge.

Fig. 7.2 shows an adiabatic LAES with both "hot" and "cold" thermal energy recycling. The hot and cold TES are employed for the recycling task respectively, however, they are always operated in the opposite direction. For example, during charge the hot TES is storing exergy whilst the cold TES is releasing exergy for air liquefaction. Due to the irreversibility of the LAES system, the air cannot be fully liquefied after the cryogenic turbine (or throttle valve) and the leftover vapour (flash-gas) will be recirculated through the auxiliary heat exchanger and mixed with the incoming ambient air. The efficiency of the liquefaction process is measured by the vapour quality x, which refers to the vapour fraction in a saturated mixture, $x = m_{\mathrm{v}}/(m_{\mathrm{v}} + m_{\mathrm{l}})$. Since there is no air accumulators or buffer tanks in the LAES system, as shown in Fig. 7.2, for each unit of ambient air flowing into the system, it will finally be liquefied and store in the liquid air tank. Therefore, if we assume the incoming ambient air is

1 kg and the flash-gas is α kg, then the vapour quality can be expressed as:

$$x = \frac{\alpha}{1+\alpha} \tag{7.13}$$

After some simple transformation, the mass of flash-gas is $\alpha = x/(1-x)$. From Fig. 7.2, it can be noted that the mass of air flowing through the compressor and hot TES is $(1+\alpha)$ kg, whilst the mass of air flowing through the cold TES is $(1+\alpha-\omega\alpha)$, as long as we assume the mass ratio between the supercritical air and flash-gas is ω for the auxiliary heat exchanger. During discharge, the stored 1 kg liquid air will be pumped to p_d before flowing through the cold TES to replenish cold exergy for it. If the cold TES consists of heat exchangers and liquid tanks, then the cold fluid replenished during discharge ω_d must be larger or at least equal to the cold fluid consumed during charge $\omega_\mathrm{c}(1+\alpha-\omega\alpha)$ in order for the system to operate stably. After some simplification, we have:

$$\omega_\mathrm{d} = \omega_\mathrm{c}\left[1+(1-\omega)\frac{x}{1-x}\right] \tag{7.14}$$

where ω_d and ω_c refers to the mass ratio between the cold thermal fluid and supercritical air of the main heat exchangers of cold TES during discharge and charge respectively. From Eq. (7.14), it can be noted that the discharging mass ratio ω_d should be adjusted for different x, if the auxiliary heat exchanger is operated at its optimal mass ratio $\omega_\mathrm{opt} = \overline{c_{p,\mathrm{flash}}}/\overline{c_{p,\mathrm{critical}}} < 1$. This is especially difficult if the vapour quality x is not precisely known before the calculation or the value of x keeps varying during charge, such as the LAES with solid TES where the thermal front may come out of the reservoir. Therefore, in this thesis, the mass ratio of auxiliary heat exchanger ω is fixed at one so that the mass ratio of cold TES is always the same during charge and discharge, $\omega_\mathrm{d} = \omega_\mathrm{c}$. As a result, the auxiliary heat exchanger may not operate at its optimal mass ratio ω_opt and thus impairs the system efficiency. But it lends more stability to the LAES and makes different LAES more comparable. Hence, if the cold TES is enough efficient, which means most of supercritical air will flow through the cold TES rather than the auxiliary heat exchanger, the penalty on system efficiency caused by $\omega = 1$ is insignificant and outweighed by the benefits it brings to the LAES systems.

The charging mass ratio of the main heat exchanger in liquid TES ω_c is set as its optimal value $\omega_\mathrm{c,opt} = \overline{c_{p,\mathrm{critical}}}/\overline{c_{p,\mathrm{fluid}}}$ whilst the discharging mass ratio ω_d is equal to the charging one, $\omega_\mathrm{d} = \omega_\mathrm{c}$. Therefore, if the operating condition of discharging process is different from the charging one, ω_d may also deviate from its optimal value $\omega_\mathrm{d,opt}$. However, setting $\omega_\mathrm{d} = \omega_\mathrm{c}$ can ensure the LAES will not rely on external supply of cold fluid (or cold exergy) and thus make the system operation much simpler.

7.4.2 Impact of the storage media

Thermal front of the solid TES

In order to increase the energy density and reduce the cost of the solid TES, materials with high volumetric heat capacity $\rho_{\mathrm{m}} c_{p,\mathrm{m}}$, which is the product of molar heat capacity $c_{p,\mathrm{m}}$ and molarity ρ_{m}, is preferred as the packing materials. In 1819, Dulong and Petit discovered that the molar heat capacity $c_{p,\mathrm{m}}$ of many solid elements is about $3R$, where R is the universal gas constant, and their molarity ρ_{m} (the reciprocal of molar volume v_{m}) is also very roughly constant. This means the volumetric heat capacity of many solid elements is constant at room temperature. However, the Dulong-Petit law is only valid when the temperature is significantly higher than the Debye temperature θ_D of the solid elements, and in the cryogenic temperature region, the volumetric heat capacity $\rho_{\mathrm{m}} c_{p,\mathrm{m}}$ begins to drop rapidly to zero, as shown in Fig. 7.3a, and the Debye model works well under such condition. For example, the variation of volumetric heat capacity of boron, iron and lead are shown in Fig. 7.3a, from which it can be noted that the heat capacity $\rho_{\mathrm{m}} c_{p,\mathrm{m}}$ of boron begins to drop at high temperature whilst that of lead only begins to fall at very low temperature. This is because the Debye temperature of boron (θ_D = 1362 K) is much higher than that of the lead (θ_D = 87 K), and that of the iron (θ_D = 373 K) is in the middle of the two.

The variation of volumetric heat capacity $\rho_{\mathrm{m}} c_{p,\mathrm{m}}$of solid materials not only has an impact on the size and cost of the solid TES, it also influences the shape of the thermal front in the reservoir, which then determines the TES losses and system efficiency. For example, the thermal fronts of solid TES with boron, iron and lead are shown in Figs. 7.3b, 7.3c and 7.3d respectively, from which it can be noted that there is a thermal wave 'catch-up' phenomenon in each cold TES, and the solid TES with boron as the packing materials has the sharpest thermal front and highest temperature difference. As shown in Ref. [59], the thermal wave speed $\vec{U}$ is given by:

$$\vec{U} = \frac{G c_{p,\mathrm{g}}}{\rho_{\mathrm{s}} c_{\mathrm{s}} (1-\varepsilon)} \tag{7.15}$$

From Eq. (7.15) it can be noted that the lower the volumetric heat capacity $\rho_{\mathrm{s}} c_{\mathrm{s}} = \rho_{\mathrm{m}} c_{p,\mathrm{m}}$, the higher the thermal wave speed $\vec{U}$. Therefore, since the boron has the fastest volumetric heat capacity $\rho_{\mathrm{s}} c_{\mathrm{s}}$ reduction of the three within the temperature range (83 ~ 298 K) considered here, the losses caused by its thermal shock wave is also the highest, as shown by the temperature difference in Fig. 7.3b. From Figs. 7.3c and 7.3d it can be found that the losses of the iron-packed and lead-packed thermal reservoir are relatively similar, but the former has much smaller size than the latter, as shown by the reservoir length in Figs. 7.3c and 7.3d. This is because the average volumetric heat capacity of iron $\overline{\rho_{\mathrm{s}} c_{\mathrm{s}}}$ is almost twice that of lead and

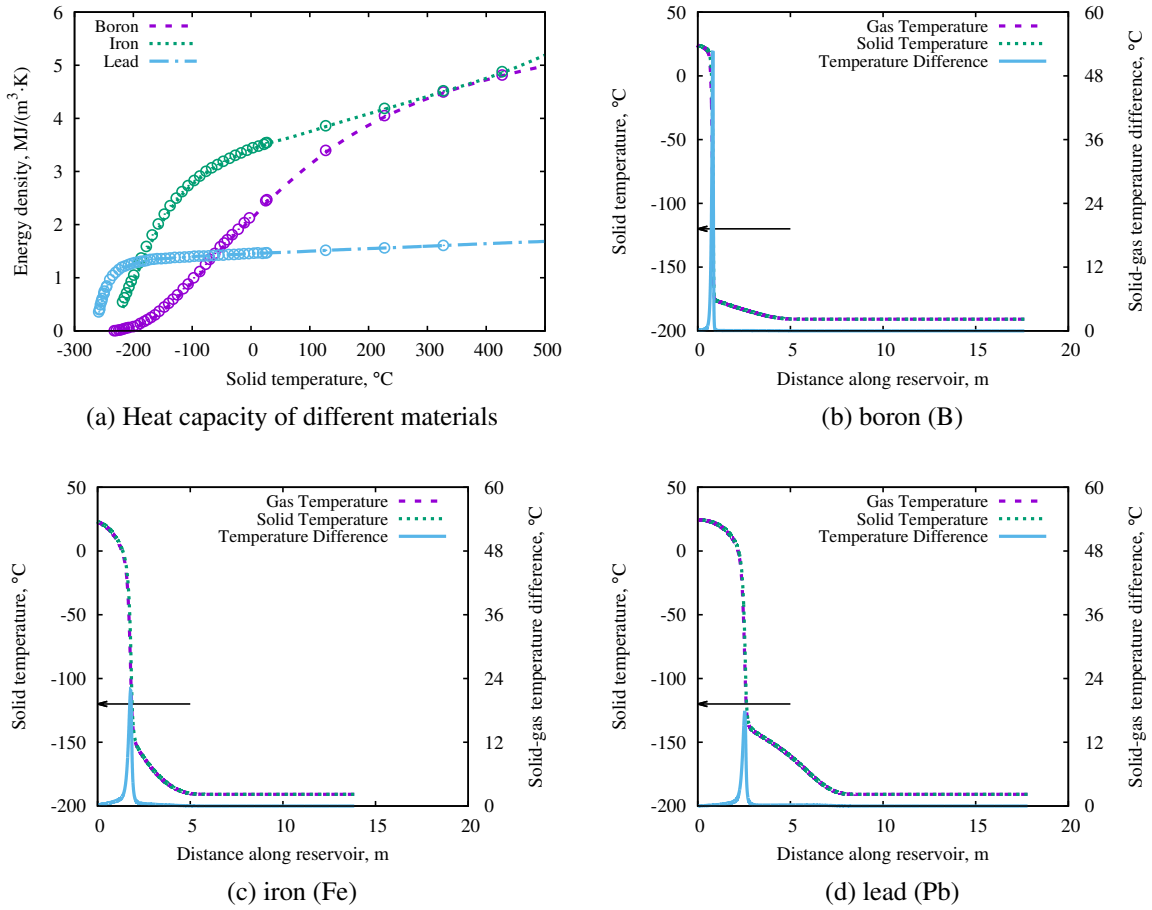

(a) Heat capacity of different materials

(b) boron (B)

(c) iron (Fe)

(d) lead (Pb)

Figure 7.3: Heat capacity of different materials (Fig. 7.3a) and thermal wave propagation of cold TES with (b) boron (B), (c) iron (Fe) and (d) lead (Pb)

boron within the temperature range considered (83 ~ 298 K), as shown in Fig. 7.3a. There is evidence that the oxide of metal has even higher volumetric heat capacity [134, 135], therefore, haematite (Fe_2O_3) is selected as the packing materials for both the hot and cold TES due to its high volumetric heat capacity $\overline{\rho_s c_s}$, low heat capacity variation at cryogenic temperature, wide temperature range and low capital cost. The magnetite (Fe_3O_4) is not used here due to an erratic point caused by crystalline phase transition at cryogenic temperature (around 115 K) [136].

Pinch points of liquid TES

Unlike the packing materials of solid TES which have wide temperature range and varying volumetric heat capacity $\rho_s c_s$, the thermal fluids usually have much narrower operating temperature range but relatively constant heat capacity, as shown in Fig. 7.4a. Meanwhile, the

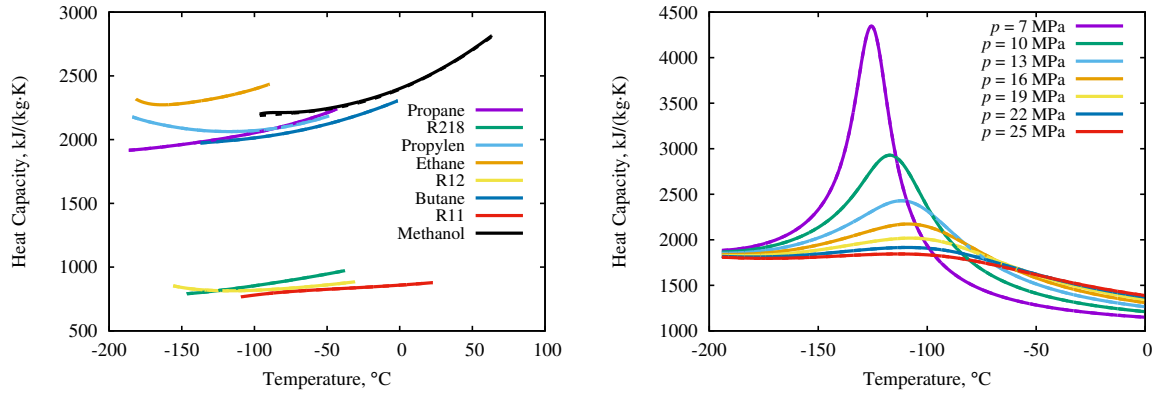

(a) different thermal fluids

(b) supercritical air at difference pressure levels

Figure 7.4: Specific heat capacity variation of (a) different thermal fluids and (b) supercritical air at different pressure levels

heat capacity of supercritical air (the working fluid) varies significantly as it approaches the critical temperature (T_{crit} = 132.5 K) and critical pressure (p_{crit} = 37.9 bar), as shown in Fig. 7.4b. This heat capacity variation gives rise to the pinch point problem in the heat exchanger of liquid TES, which limits the maximum heat transfer rate Q_{max} and causes irreversibility even in an infinitely large heat exchanger with $\varepsilon = 1$, as discussed in Section 7.3.1. It can also be noted from Fig. 7.4a that there is no single fluid that can cover the temperature range required for the supercritical air cooling (or heating) process by itself, therefore, at least two main heat exchangers and two types of thermal fluids are used in series as the cold TES. In this thesis, methanol (177 ~ 336 K) and propane (87 ~ 230 K) are selected as the thermal fluid and used together to cover the cold TES temperature range, as proposed in Ref. [101, 102]. They enjoy the merits of low cost, wide availability and environmental benignity.

Fig. 7.5 shows the temperature distribution inside the two heat exchanger of the cold TES. The operating parameters of this LAES are summarized in Table 7.1, with the exception that the heat exchanger effectiveness ε is set as one here to better illustrate the pinch point problem. From Figs. 7.5a and 7.5c it can be noted that the charging mass ratios ω_{c} are at their optimal value $\omega_{\text{c,opt}}$ so that the temperature difference is zero at the pinch points whilst the discharging mass ratio ω_{d} slightly deviate from its optimal value $\omega_{\text{d,opt}}$ for the sake of system stability, which are in accord with the analysis in Section 7.4.1. It can also be noted from Fig. 7.5 that both propane and methanol varies within the same temperature range during charge and discharge, which means the LAES system has reached equilibrium after several cycles of operation.

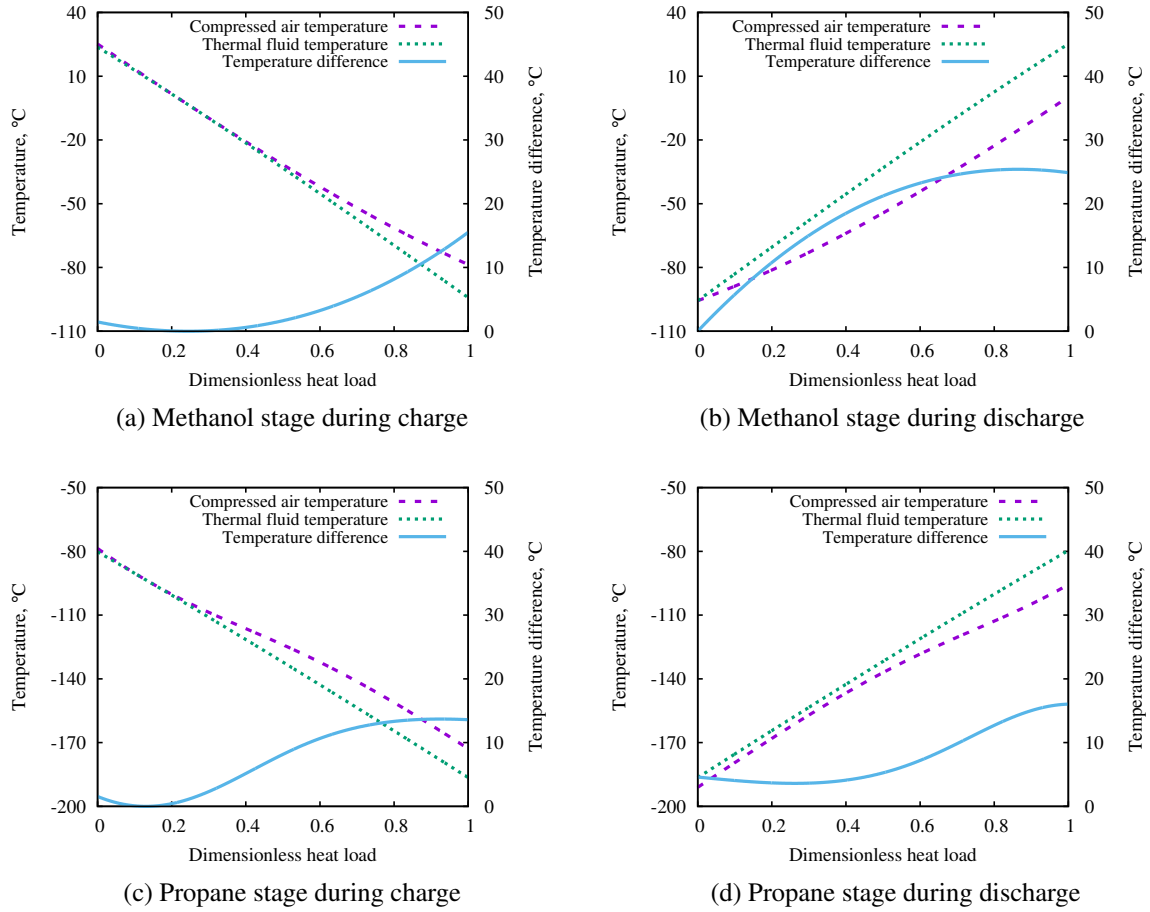

(a) Methanol stage during charge

(b) Methanol stage during discharge

(c) Propane stage during charge

(d) Propane stage during discharge

Figure 7.5: Temperature distribution inside the main heat exchanger of cold TES: (a) Methanol stage during charge (b) Methanol stage during discharge (c) Propane stage during charge (d) Propane stage during discharge

7.4.3 Impact of pressure on the TES

Thermal front of the solid TES

The temperature profile of the solid TES not only depends on its initial or previous state but also depends on the propagation speed of the thermal wave. Therefore, estimating its impact on the system efficiency is not an easy task. From Eq. (7.15) and Section 7.4.2, we know that the variation of solid heat capacity c_s influences the speed and shape of the thermal front. In fact, the variation of supercritical air heat capacity $c_{p,g}$ with pressure and temperature, as discussed in Section 7.4.2, also has an important impact on the thermal wave speed $\vec{U}$. For example, the thermal front speed $\vec{U}$ of the cold TES as a function of temperature at different pressure levels are shown in Fig. 7.6, from which it can be noted that the propagation speed $\vec{U}$ of the cold region tends to be higher than that of the hot region, which means there tends to be a thermal wave 'catch-up' in the cold TES. Besides, it can also be noted that there is a peak in the propagation speed $\vec{U}$ around the critical temperature (T_{crit} = 132.5 K) at low pressure levels, and the peak gradually flattens as the charging pressure p_c increases. This is in accord with the prediction in Eq. (7.15) and Fig. 7.4b, and the impact of speed variation on the thermal fronts of solid TES are shown in Fig. 7.7.

Figs. 7.7a and 7.7c show the thermal fronts of a charging cold TES at 50 bar and 200 bar respectively. The utilization factor of both TES are set as $\Pi = 1.0$ and other parameters are summarized in Table 7.1. From Figs. 7.7a and 7.7c, it can be noted that the thermal front at 50 bar is much steeper than the one at 200 bar, which prevents the thermal front from coming out of the cold TES and reduces the recirculation losses to some extent. The thermal fronts have different shape is because the thermal wave speed $\vec{U}$ at 50 bar has a peak around the critical temperature T_{crit}, as shown in Fig. 7.6, which prevent the thermal front from spreading out and becoming too flat. Meanwhile, it can be noted that the cold TES at 50 bar is larger than the one at 200 bar. This is because the size of the cold TES is determined by the mass m and average heat capacity $\overline{c_{p,g}}$ of the supercritical air, $V_s = m\overline{c_{p,g}}/\rho_s\overline{c_s}$. As the operating pressure p increases, more exergy will be stored in the hot TES and the mass of liquid air m will decrease. Meanwhile, the average heat capacity $\overline{c_{p,g}}$ of supercritical air also decreases with operating pressure p, as shown in Fig. 7.4b, which results in smaller cold TES and higher outlet temperature. Therefore, the average outlet temperature of cold TES at 200 bar is higher than that at 50 bar, which means higher vapour quality x and recirculation losses.

Figs. 7.7b and 7.7d show the thermal fronts of cold TES at 50 bar and 200 bar respectively near the end of the discharging process, from which it can be noted that the thermal front at 200 bar is much steeper than the one at 50 bar, meaning the temperature difference and thermal losses at 200 bar are much higher. This is also due to the difference in thermal front

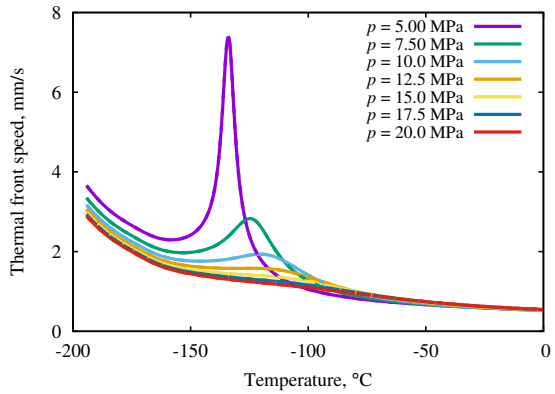

Figure 7.6: Thermal front speed $\vec{U}$ as a function of temperature at different pressure levels

speed $\vec{U}$, as shown in Fig. 7.6. At 200 bar, the propagation speed of thermal wave at low temperature region is always higher than that at high temperature region, which means the cold front will finally catch up with the hot one and thus results in the formation of thermal shock wave, as shown in Fig. 7.7d. On the other hand, the propagation speed of thermal wave at 50 bar peaks around the critical temperature T_{crit}, which means the 'catch-up' phenomenon will only happen in the intermediate temperature region and thus avoid the formation of full-scale thermal shock wave, as shown in Fig. 7.7b. Therefore, the thermal losses of cold TES at 200 bar during discharge is also higher than the one at 50 bar, meaning the losses caused by the cold TES always increases with the operating pressure p.

Pinch point of the liquid TES

As discussed in Section 7.4.2, the pinch point is caused by the difference of the heat capacity variation of the supercritical air and thermal fluid. Therefore, the higher the operating pressure is, the less heat capacity variation will the supercritical air have (as shown in Fig. 7.4b), and the lower losses will be caused by the pinch point. This is in accord with the findings in Fig. 7.8, where the temperature profiles of the heat exchanger with propane as the thermal fluid are shown. The operating pressures in Figs. 7.8a and 7.8b are fixed at 50 bar whilst the pressure in Figs. 7.8c and 7.8d are 200 bar. Other operating parameters are summarized in Table 7.1. From Fig. 7.8, it can be noted that the average temperature difference between air and fluid at 50 bar is much higher than that at 200 bar, which means the thermal losses of cold TES are higher at low operating pressure. Meanwhile, it can also be noted from Figs 7.8a and 7.8c that the outlet temperature of the cold TES at 50 bar is much higher than that at 200 bar, which means the vapour quality x and recirculation losses are much higher at low operating pressure. Therefore, even if the heat exchanger effectiveness ε is fixed, the thermal losses caused by the

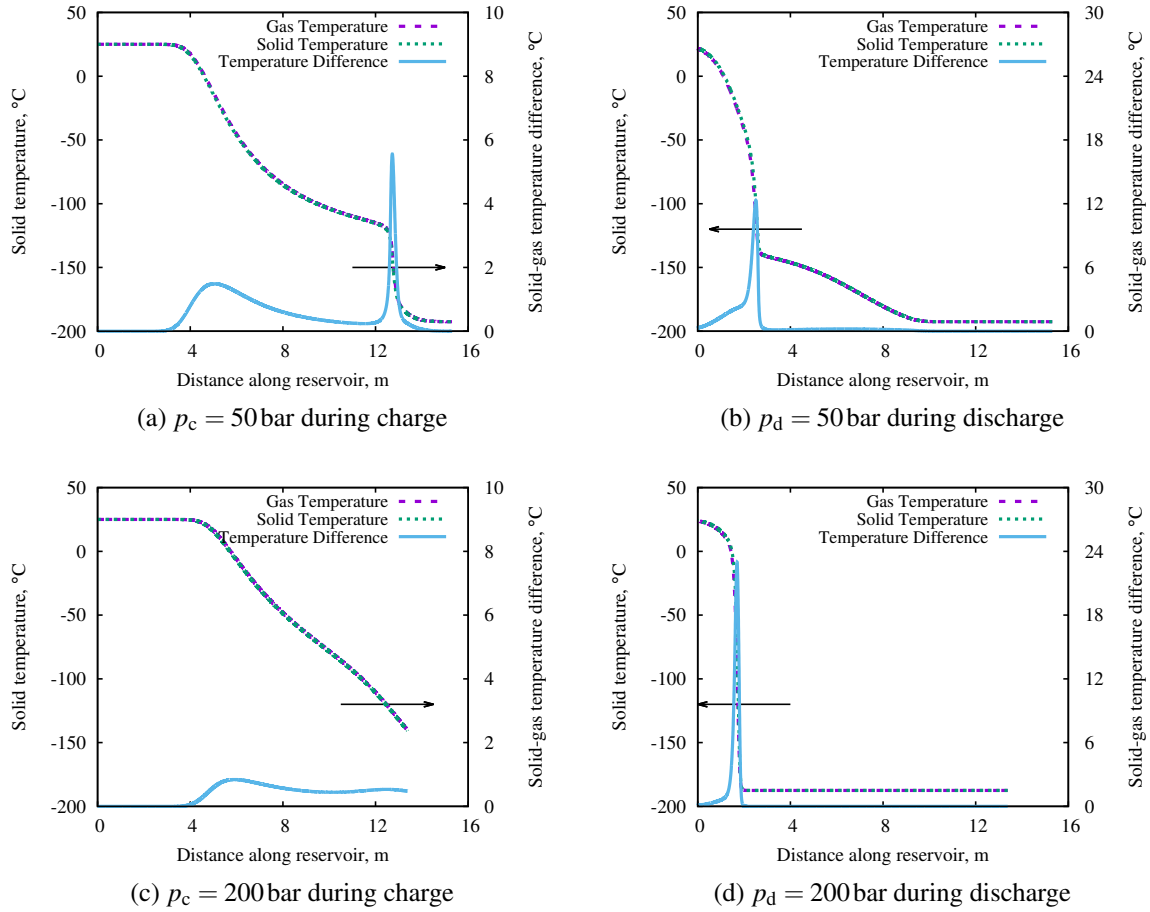

(a) $p_c = 50\,\text{bar}$ during charge

(b) $p_d = 50\,\text{bar}$ during discharge

(c) $p_c = 200\,\text{bar}$ during charge

(d) $p_d = 200\,\text{bar}$ during discharge

Figure 7.7: The impact of operating pressure on the thermal front of solid TES: (a) $p_c = 50\,\text{bar}$ during charge (b) $p_d = 50\,\text{bar}$ during discharge (c) $p_c = 200\,\text{bar}$ during charge (d) $p_d = 200\,\text{bar}$ during discharge

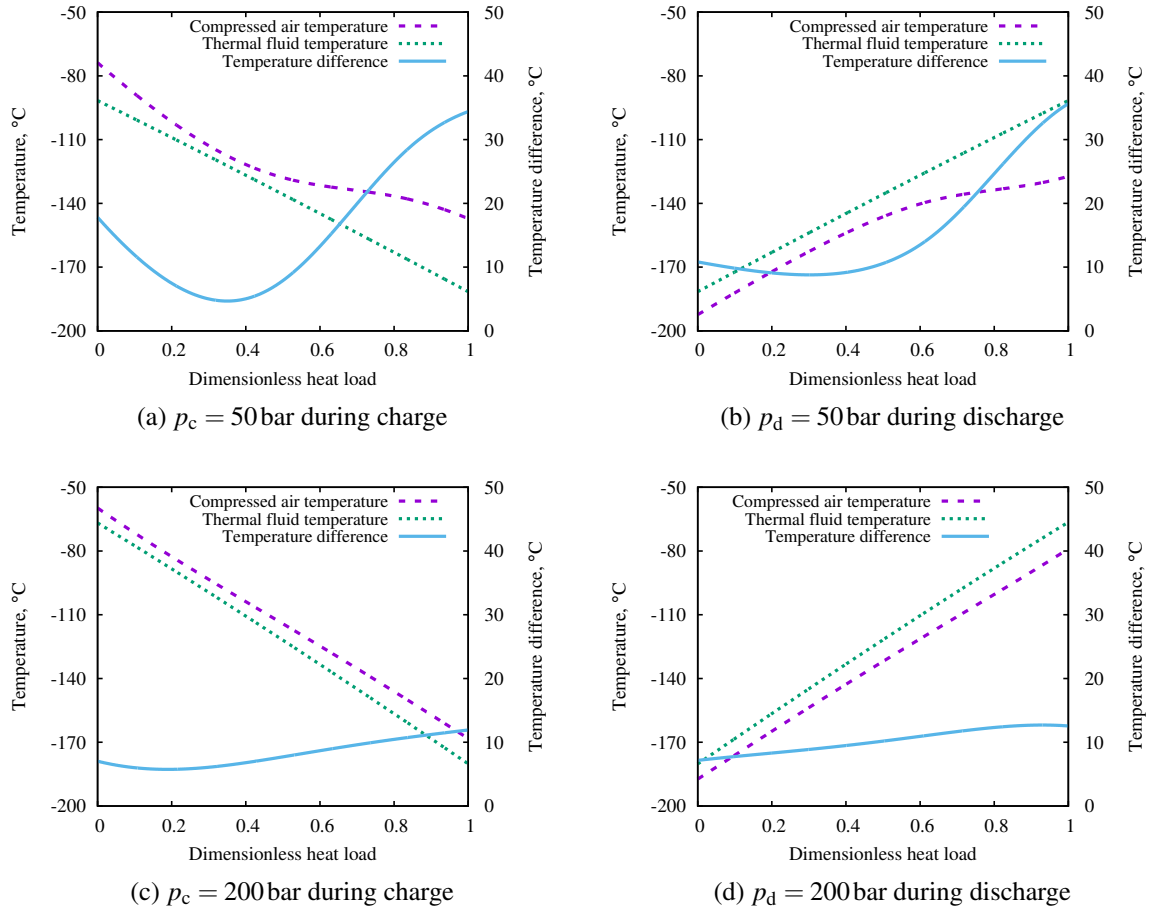

(a) $p_c = 50\,\text{bar}$ during charge

(b) $p_d = 50\,\text{bar}$ during discharge

(c) $p_c = 200\,\text{bar}$ during charge

(d) $p_d = 200\,\text{bar}$ during discharge

Figure 7.8: The impact of operating pressure on the pinch points of propane stage heat exchanger: (a) $p_c = 50\,\text{bar}$ during charge (b) $p_d = 50\,\text{bar}$ during discharge (c) $p_c = 200\,\text{bar}$ during charge (d) $p_d = 200\,\text{bar}$ during discharge

pinch point will still decrease monotonically with the operating pressure.

7.5 Impact of pressures on the system efficiency

7.5.1 Operating pressure p

The impact of operating pressure p on the system efficiency χ of LAES with solid and liquid TES are shown in Figs. 7.9a and 7.9b respectively. The charging and discharging pressure are assumed equal here ($p_d/p_c = 1$) and the nominal values of other parameters are summarized in Table 7.1. From Fig. 7.9a it can be noted that the system efficiency χ of solid LAES (LAES with solid TES) first decreases but then increases with the operating pressure p. This is due to two conflicting variation of losses: the cold TES losses increases with the operating pressure

Table 7.1: The nominal, minimum and maximum design variable values of LAES for the parametric and optimization study

	p_c (bar)	p_d/p_c	NTU	η	Π	d_p (mm)	L/D
Nominal	100	1.00	19.00	0.85	1.00	15.0	1.00
Minimum	50	0.50	9.00	0.80	0.50	5.00	0.20
Maximum	200	2.00	99.0	0.90	1.50	30.0	5.00

p, as discussed in Section 7.4.3; whilst the auxiliary heat exchanger losses decreases with the operating pressure p. As p increases, the average heat capacity of supercritical air $\overline{c_{p,\text{critical}}}$ decreases, and the optimal mass ratio of the auxiliary heat exchanger $\omega_{\text{opt}} = \overline{c_{p,\text{flash}}}/\overline{c_{p,\text{critical}}}$ increases accordingly, thus making the actual mass ratio $\omega = 1$ closer to its optimal value. The unit storage cost Z of the solid LAES increases monotonically with the operating pressure p because the capital cost of pressure vessel increases linearly with p. Therefore, the solid LAES should be operated at low pressure for better thermo-economic performance.

Fig. 7.9b shows that the system efficiency χ of liquid LAES (LAES with liquid TES) increases monotonically with the operating pressure p, mainly because of the reduction in cold TES losses, as discussed in Section 7.4.3. The unit storage cost Z of liquid LAES, however, decreases monotonically with the operating pressure p. This is because as p increases, the hot TES temperature increases, and as a result, the mass and mass flowrate of supercritical air decreases accordingly. Since the capital cost of compressor/expander and TES system is proportional to the mass and mass flowrate of the working fluid, the capital cost of liquid LAES decreases with p, hence resulting in an increase in unit storage cost Z. Therefore, the liquid LAES should be operated at high pressure for better thermo-economic performance.

It can also be noted from Fig. 7.9 that both the system efficiency χ and unit storage cost Z of solid LAES tends to be higher than those of liquid LAES. At low pressure (50 bar), the unit storage cost Z of solid LAES and liquid LAES are relatively similar.

7.5.2 Pressure ratio p_d/p_c

The impact of pressure ratio p_d/p_c on the system efficiency χ and unit storage cost Z of solid and liquid LAES are shown in Figs. 7.10a and 7.10b respectively, from which it can be noted that the system efficiency χ of both solid and liquid LAES first increases but then decreases with the pressure ratio, resulting in an optimal p_d/p_c at around 1.5. This is because although more work W_{dis} can be extracted at higher discharging pressure p_d, the average heat capacity of supercritical air $\overline{c_{p,\text{critical}}}$ decreases with p_d, which means the stored exergy within the cold TES will decrease accordingly and eventually leads to more charging work W_{chg} and lower

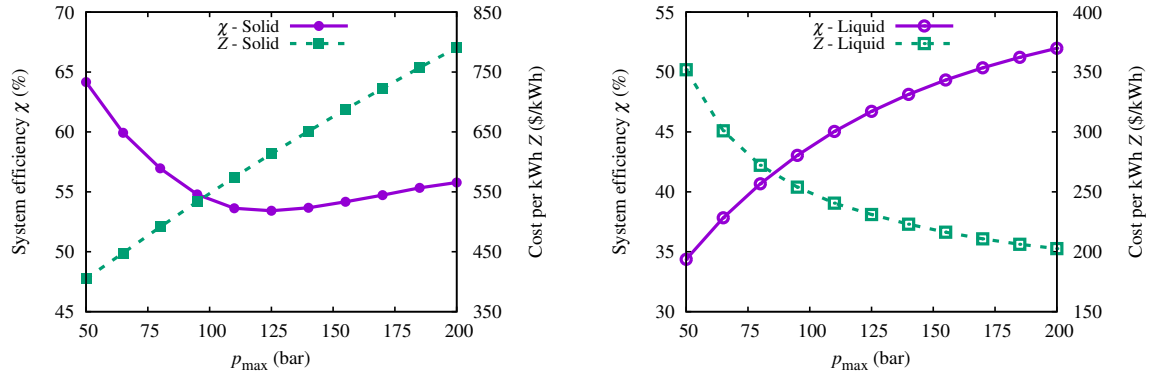

(a) LAES with solid TES

(b) LAES with liquid TES

Figure 7.9: The impact of operating pressure p on the system efficiency χ and unit cost Z of the LAES with (a) solid TES and (b) liquid TES

system efficiency χ. In theory, any energy storage system should be made as reversible as possible, and the discharging and charging pressure should be the same in an ideal LAES without losses. In practice, the discharging pressure p_d should be slightly higher than the charging one p_c in order to counteract the effect of irreversibility if the LAES is dominated by the compressor/expander losses.

The unit storage cost Z of the solid LAES first decreases but then increases with the pressure ratio, resulting in an minimal Z at round 1.0. This is because the pressure vessel of solid TES is built according to the maximal pressure of the charging and discharging process. Therefore, when $p_d/p_c \leq 1$, the capital cost of solid LAES Z_{tot} is constant whilst the the work output W_{dis} increases with p_d, which causes the unit storage cost Z to decrease at first. When $p_d/p_c > 1$, however, the capital cost of solid LAES Z_{tot} begins to increase rapidly, which offsets the increase in W_{dis} and causes the unit cost Z to rise steadily, as shown in Fig. 7.10a. On the other hand, the capital cost Z_{tot} of liquid LAES is independent of the operating pressure, and the unit storage cost Z decreases monotonically with p_d as the work output W_{dis} increases with it.

7.6 Impact of TES and C/E on system efficiency

7.6.1 Heat exchanger effectiveness ε

The impacts of heat exchanger effectiveness ε on the system efficiency χ and unit cost Z of solid and liquid LAES are shown in Figs. 7.11a and 7.11b respectively. For the solid LAES, the heat exchanger effectiveness ε is only for the auxiliary heat exchanger which is

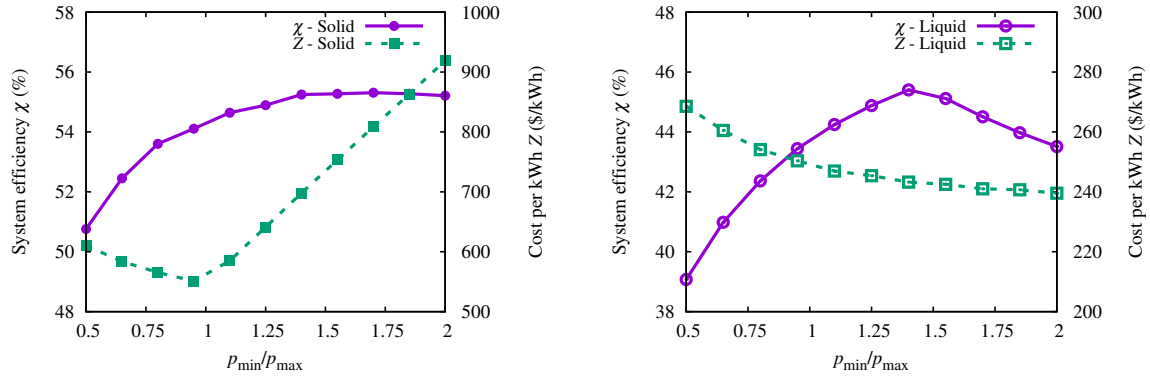

(a) LAES with solid TES

(b) LAES with liquid TES

Figure 7.10: The impact of pressure ratio p_d/p_c on the system efficiency χ and unit cost Z of the LAES with (a) solid TES and (b) liquid TES

used for recycling the cold exergy of flash-gas; whilst for the liquid LAES, the heat exchanger effectiveness ε is for all heat exchangers, including those in the hot and cold TES. From Fig. 7.11, it can be noted that the system efficiency χ of both solid and liquid LAES is a linear function of the heat exchanger effectiveness ε, but the system efficiency χ of liquid LAES is much more sensitive to ε than that of the solid LAES. In addition, the unit storage cost Z of liquid is also much more sensitive to ε than that of the solid LAES, which is due to their difference in the number of heat exchangers. Increasing the heat exchanger effectiveness ε can increase the work output W_{dis} but will also increase the system cost Z_{tot}, and the combination of these two effects determines the variation of unit storage cost Z. From Fig. 7.11, it can also be noted that when the heat exchanger effectiveness ε is very high, the system efficiency χ and unit storage cost Z of liquid and solid LAES are comparable.

7.6.2 Thermal reservoir parameters

The impact of various thermal reservoir parameters on the system efficiency χ and unit storage cost Z of solid LAES are shown in Fig. 7.12. Similar to the A-CAES, the utilization factor Π, particle diameter d_p and aspect ratio L/D are still used to model the performance of thermal reservoir. Fig. 7.12a shows the effect of utilization factor Π on the system performance. As Π increases, more of the reservoir's capacity is exploited, and the unit storage cost Z falls as a result. Meanwhile, the system efficiency χ decreases with Π rising, because in an over-exploited thermal reservoir, the hot or cold air will issue from the exit and cause losses in the auxiliary heat exchangers. As discussed in Ref. [41], greater utilization also leads to steeper temperature gradients in the packed bed and consequently higher losses due to irreversible

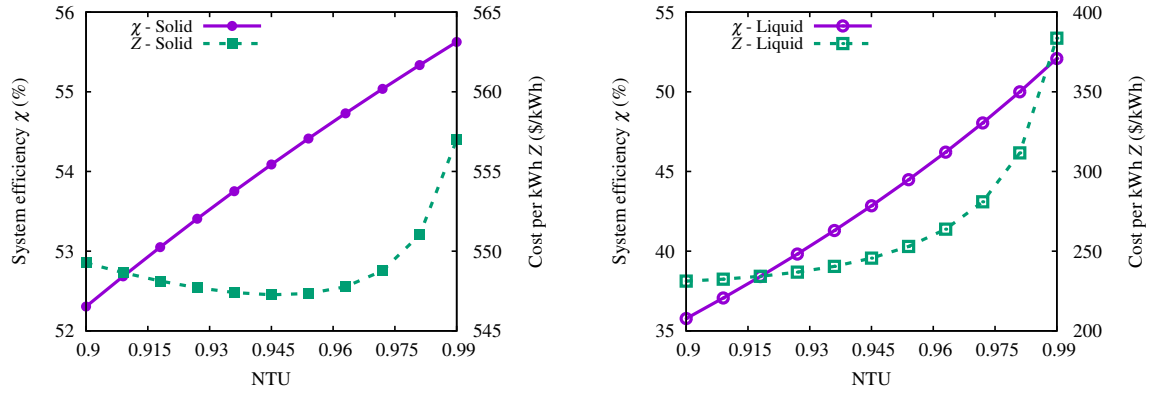

(a) LAES with solid TES

(b) LAES with liquid TES

Figure 7.11: The impact of heat exchanger effectiveness ε on the system efficiency χ and unit cost Z of LAES with (a) solid TES and (b) liquid TES

heat exchange between the air and storage media. The cost may continue to fall at high Π, but eventually the impact of increased losses on the system efficiency χ begins to dominate such that the curve flattens out.

The effective particle diameter determines the balance between thermal and pressure losses within the packed bed: smaller particles provide more surface area thereby decreasing heat transfer losses, but at the expense of a larger pressure drop. Therefore is thus an optimal particle size at which the efficiency is maximum, as shown in Fig. 7.12b. This optimum will depend on the air mass flow per unit area G and hence on the reservoir aspect ratio L/D. The cost of the packing material and the volume it occupies is assumed independent of d_p and therefore the improvement in χ results in a slight decrease in unit storage cost Z.

In conjunction with the particle size, the aspect ratio L/D also affects the balance between thermal and pressure losses, with long thin reservoirs having efficient heat transfer but larger pressure drop. Again there is an optimum, as shown in Fig. 7.12c, which will in turn depend on d_p. However, this time there is a rapid increase in cost at low values of L/D which is due to the "end effects" - i.e., the high surface-to-volume ratio (requiring more insulation and therefore a larger vessel) and the wasted space in the domed end caps of the pressure vessel.

7.6.3 Compressor/Expander (C/E) polytropic efficiency

The impacts of the polytropic efficiency η of compressors and expanders on the system efficiency χ and unit storage cost Z of solid and liquid LAES are shown in Figs. 7.13a and 7.13b respectively. The isentropic efficiency of cryogenic expander of both LAES systems are assumed to be the same with the polytropic efficiency η of other compressors and expanders.

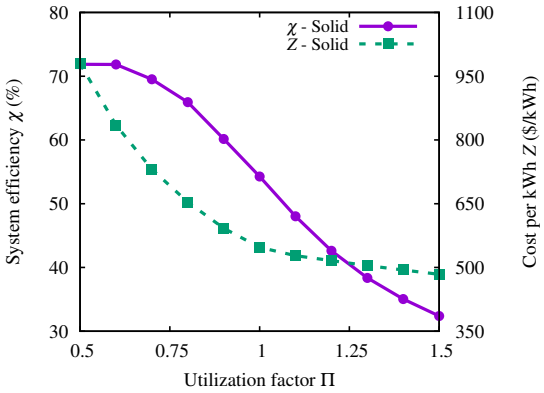

(a) Reservoir utilization factor Π

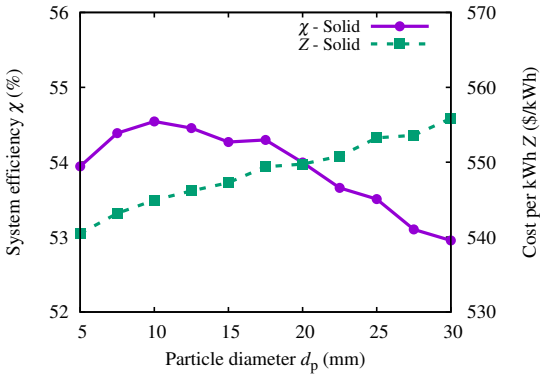

(b) Reservoir particle diameter d_p

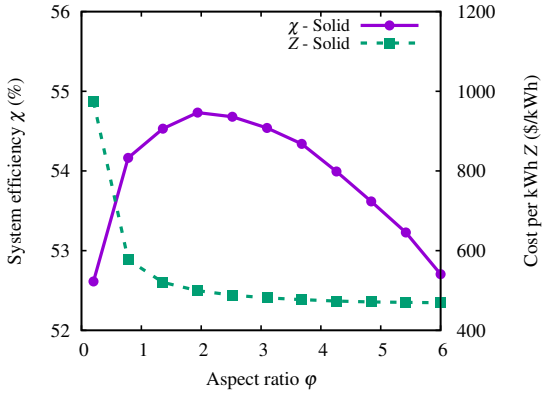

(c) Reservoir aspect ratio L/D

Figure 7.12: The impact of thermal reservoir parameters on the system efficiency χ and unit cost Z of LAES with solid TES: (a) Reservoir utilization factor Π (b) Reservoir particle diameter d_p (c) Reservoir aspect ratio L/D

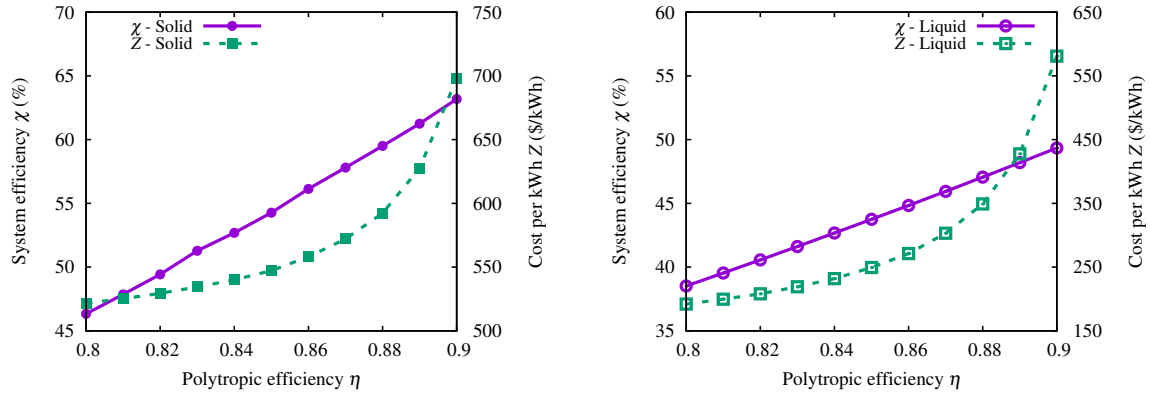

(a) LAES with solid TES

(b) LAES with liquid TES

Figure 7.13: The impact of polytropic efficiency η on the system efficiency χ and unit cost Z of LAES with (a) solid TES and (b) liquid TES

From Fig. 7.13, it can be noted that the system efficiency χ of both liquid and solid LAES is a linear function of the polytropic efficiency η, but the system efficiency χ of solid LAES is more sensitive to η than that of the liquid LAES. This is mainly because of the relative high efficiency of the solid TES and as a result, the compressor/expander losses become the dominant losses in the solid LAES. Therefore, the system efficiency χ of solid LAES is more sensitive to the polytropic efficiency η. On the other hand, due to the expensive pressure vessel of solid TES, the compressor/expander cost becomes a minor part in the capital cost Z_{tot} of solid LAES. Therefore, the unit storage cost Z of solid LAES is not as sensitive to η as that of the liquid LAES. As a result, it can be concluded from Fig. 7.13 and Fig. 7.11 that the polytropic efficiency η is more important to solid LAES than the liquid one, whilst the heat exchanger effectiveness ε is more important to liquid LAES than the solid one.

7.6.4 Throttle valve and cryo-expander

The impacts of heat exchanger effectiveness ε and polytropic efficiency η on the system efficiency χ of liquid LAES with cryogenic expander and throttle valve are shown in Figs. 7.14a and 7.14b respectively. The isentropic efficiency of cryogenic expander is assumed to be the same with the polytropic efficiency η of other compressor/expander, whilst the isentropic efficiency of throttle valve is assumed to be zero, which corresponds to an isenthalpic expansion in an adiabatic throttle valve. From Fig. 7.14, it can be clearly noted that the throttle valve severely impairs the system efficiency χ of LAES system, with an average of more than 40 % reduction in χ. This is not only because of the increased losses in the throttle valve itself, but also due to the huge losses associated with the inefficient cold recovery system and the flash-

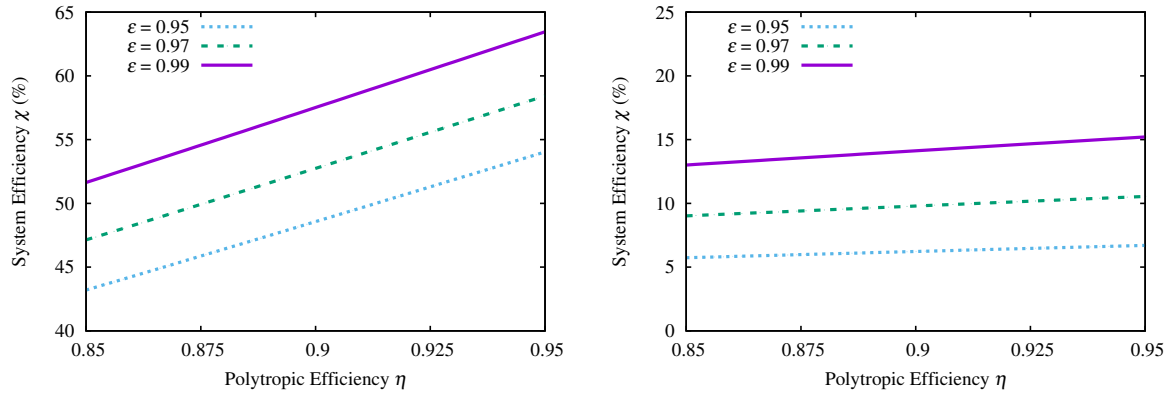

(a) cryogenic expander (b) throttle valve

Figure 7.14: The impact of different air expansion devices on the system efficiency χ of liquid LAES with (a) cryogenic expander and (b) throttle valve

gas re-compression system. For example, the mass ratio ω of the auxiliary heat exchanger for flash-gas cold recovery system is not set as its optimum ω_{opt} for the sake of better operation stability, and the extra thermal energy generated during the flash-gas re-compression cannot be used during discharge. Therefore, an efficient cryogenic expander is critical for the success of any LAES discussed in this thesis. From Fig. 7.14, it can also be noted that due to the huge losses associated with the throttle valve, the liquid LAES becomes less sensitive to the polytropic efficiency η of other compressors and expanders.

7.7 Loss and cost analysis of specific cases

From Section 7.5, we know the optimal pressure for solid and liquid LAES should be 50 bar and 200 bar respectively, and the heat exchanger effectiveness ε of liquid LAES should be increased in order to better compete with solid LAES. Therefore, these parameters are used as input and the results for this specified case are summarized in Table 7.2. The loss and cost distributions of this specific case are shown in Figs. 7.15 and 7.16 respectively.

7.7.1 Loss analysis for different LAES

The loss distributions of solid and liquid LAES are shown in Figs. 7.15a and 7.15b respectively. The losses of "auxiliary etc." is the sum of the auxiliary heat exchangers as well as the inlet mixing losses and system exit losses. There are two types of auxiliary heat exchangers in the LAES: the one for flash-gas cold recovery placed next to the cold TES, and the ones for heat dissipation placed after each hot TES, as shown in Fig. 7.2. Since the heat exchange for

Table 7.2: Main results for the specified designs

	Solid LAES	Liquid LAES
Operating Pressure	50	200
H.X. Effectiveness	0.90	0.99
Polytropic Efficiency	0.85	0.85
System Efficiency	64.2 %	61.7 %
Cost per kWh	405 $/kWh	308 $/kWh
Capital Cost	103.6 M$	105.5 M$
Net Output Work	255.8 MWh	342.2 MWh

flash-gas cold recovery takes place within the system, whilst the heat dissipation simply goes into the surroundings, the losses of these two types of auxiliary heat exchanger can be distinguished in Fig. 7.15 as the thermal losses and heat leakage losses respectively. The losses of "cryogenic etc." is the sum of the cryogenic pump and expander as well as the mixing losses at the outlet of cold TES and auxiliary heat exchanger. Unlike the losses of "auxiliary etc.", these cryogenic component related losses are all thermal losses.

From Fig. 7.15, it can be noted that although the heat exchanger effectiveness ε of liquid LAES has been raised to its upper limit, its cold TES loss is still slightly higher than that of the solid LAES. This means when compared with the heat exchangers, thermal reservoir tends to be more efficient, especially at cryogenic temperature range. It can also be noted that the compressor/expander losses of solid LAES are higher than that of the liquid LAES. This is simply because the operating pressure of liquid LAES is much higher than that of the solid LAES, whilst the compressor/expander losses is a decreasing function of the operating pressure. From Fig. 7.15, it can also be noted that in solid LAES, a large portion of heat leakage losses are generated in the auxiliary heat exchangers after the hot TES; whilst in liquid LAES, an even larger portion of storage losses are generated in the hot TES. Storage losses refer to the cooling losses during storage. As discussed in Section 7.4.1, there are $(1+\alpha)$ kg of air flowing through the hot TES during charge, whilst only 1 kg of air flowing through the hot TES during discharge, the extra thermal exergy for α kg of air must be dissipated in the form of storage losses after discharge.

Unlike the liquid TES where there is always abundant thermal fluids in reserve, the size and shape of a solid TES is fixed before operating, and the stored thermal exergy cannot be easily dissipated during operating. As a result, after the solid TES is fully charged, the extra hot air will simply issue from the exit of the hot reservoir and dissipate its thermal exergy in the auxiliary heat exchanger after hot TES. Therefore, the storage losses of liquid LAES and the heat leakage losses of solid LAES essentially refers to the same loss, which is the

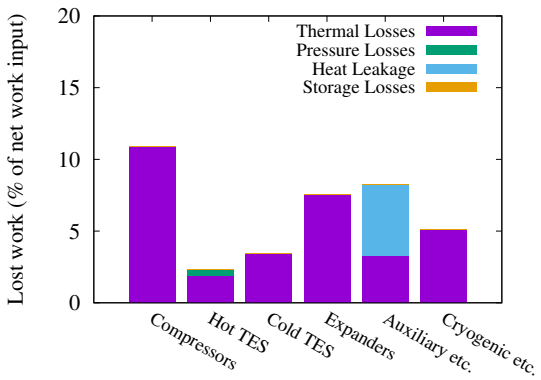

(a) Solid LAES

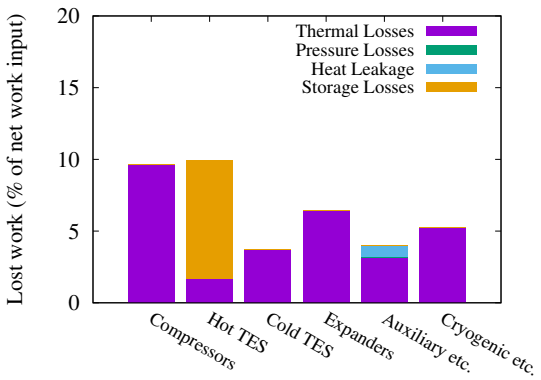

(b) Liquid LAES

Figure 7.15: Loss distributions of the solid and liquid LAES: (a) Solid LAES (b) Liquid LAES

extra thermal exergy due to the α kg of flash-gas re-compression. From Fig. 7.15 it can also be noted that the storage loss of the liquid LAES is higher than the heat leakage loss of solid LAES. This is because the heat exchanger is relatively inefficient due to the pinch point problem when compared with the thermal reservoir, therefore, there will be more flash-gas being re-compressed and thus causes more losses.

7.7.2 Cost analysis and comparison

The cost distributions of solid and liquid LAES are shown in Figs. 7.16a and 7.16b respectively. The first, second, third and fourth stage of the costs of "Cryogenic etc." respectively refers to the cost of cryogenic tank, auxiliary heat exchanger for cold recovery, cryogenic pump and cryogenic expander. From Fig. 7.16a, it can be noted that the solid TES itself forms roughly 78 % of the total cost, though its low operating pressure already makes it the cheapest option of all solid LAES. The first, second and third stage of the solid TES respectively forms 4 %, 20 % and 55 % of the total cost, therefore, the high pressure hot TES and cold TES are the components responsible for the high cost of solid LAES. Further analysis reveals that most of the component cost is for the pressure vessel, which increases linearly with the operating pressure. Meanwhile, the cold TES is even more expensive than the high pressure hot TES because the average heat capacity of the packing materials $\overline{\rho_s c_s}$ at cryogenic temperature range is much lower than that at high temperature range, therefore, more packing materials and larger pressure vessel are required for the same amount of stored exergy.

From Fig. 7.16b, it can be noted that the heat exchanger forms roughly 53 % of the total

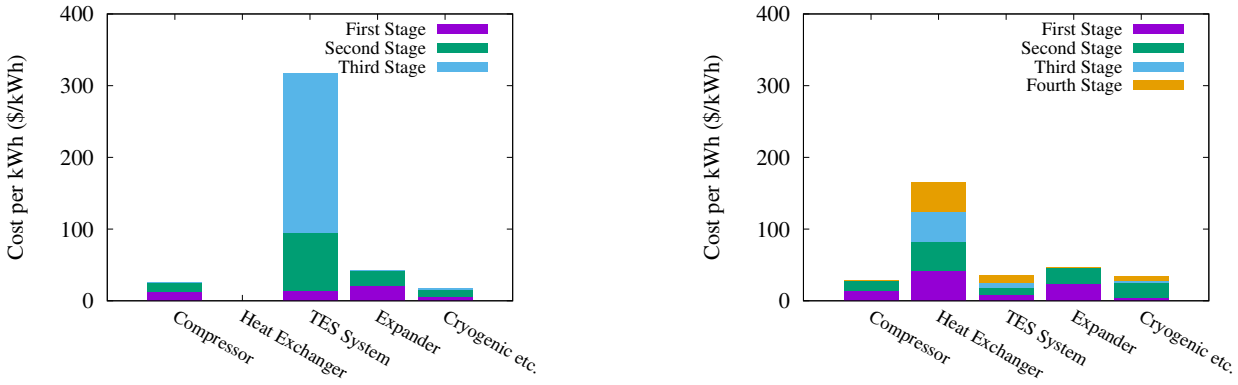

(a) Solid LAES

(b) Liquid LAES

Figure 7.16: Cost distributions of the solid and liquid LAES: (a) Solid LAES (b) Liquid LAES

cost of liquid LAES, after its heat exchanger effectiveness ε being raised to the upper limit. For similar reason, the second stage of "cryogenic" cost (for auxiliary heat exchanger) is also higher than that of the solid LAES. Unlike the solid TES, the capital costs of liquid TES and heat exchanger are independent of its pressure and therefore, the liquid LAES tends to be operated at high pressure to increase the system efficiency χ and reduce the unit storage cost Z. Generally speaking, the cost of cryogenic pump and expander forms a small fraction of the total cost, mainly because of the high density and low power consumption (or output) at low temperature range. However, they play a critical role in the LAES and an efficient and reliable cryogenic pump/expander is essential for a successful LAES. In this specific case, the compressor/expander cost also forms a relatively small fraction of the total cost. However, this is simply because the polytropic efficiency η of this case is relatively low and the compressor/expander cost will rise rapidly with the input polytropic efficiency η.

7.8 Energy distribution and density

7.8.1 Energy distribution of solid and liquid LAES

The stored energy distribution between each component as a function of system pressure p for solid and liquid LAES are shown in Figs. 7.17a and 7.17b respectively. From Fig. 7.17, it can be noted that the stored available energy in both solid and liquid LAES are fixed at $E = 400\,\text{MWh}$ and is independent of the operating pressure p. It can also be noted that the

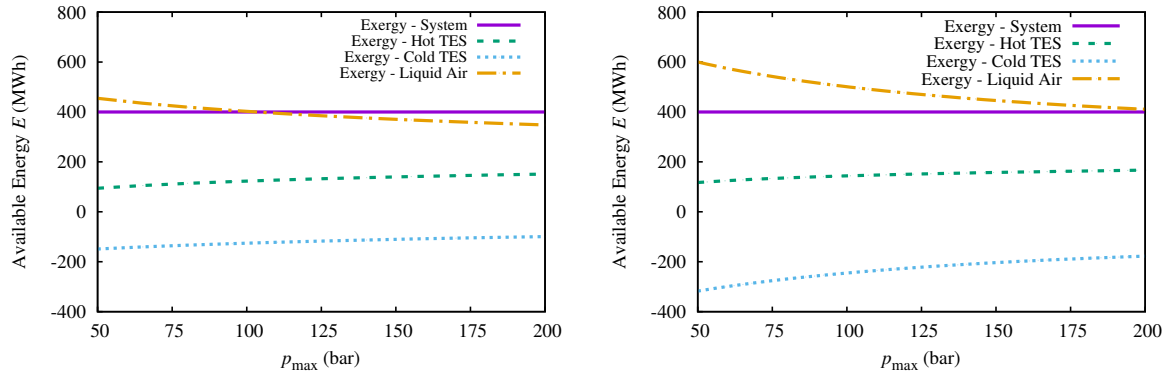

(a) solid LAES

(b) liquid LAES

Figure 7.17: Energy distribution between each component for (a) solid LAES and (b) liquid LAES

available energy stored in the liquid air E_{L} is roughly equal to the rated stored available energy in the LAES system E, and the available energy stored in the hot TES E_{H} and cold TES E_{C} are relatively similar but with opposite signs. This is because the available energy stored in the cold TES is consumed during charge and get replenished during discharge, which is opposite to the desired energy flowing direction of the LAES system, as discussed in Section 7.4.1. Therefore, the stored available energy of each component within the LAES must satisfy the following equation: $E = E_{\mathrm{H}} - E_{\mathrm{C}} + E_{\mathrm{L}}$.

From Fig. 7.17, it can also be noted that with the system pressure p increasing, E_{L} and E_{C} decreases whilst E_{H} increases accordingly. This is because the energy density D_{H} and stored exergy E_{H} of hot TES increase with the temperature ratio τ and system pressure p. Meanwhile, the mass ratio of the cold TES $\omega_{\mathrm{c,opt}} = \overline{c_{p,\mathrm{g}}}/\overline{c_{p,\mathrm{f}}}$ decreases with the pressure p (see Fig. 7.4b), which means less thermal fluid m_{C} and exergy E_{C} will be stored in cold TES. As a result, $E_{\mathrm{H}} - E_{\mathrm{C}}$ increases with p, and E_{L} decreases accordingly. It is also notable that the E_{C} of liquid LAES is higher than that of the solid LAES. This is because in order to cover the cryogenic temperature range of liquid LAES, there are two sets of thermal fluids (propane and methanol) working in series, and the stored available energy increases as a result.

7.8.2 Energy density of solid and liquid LAES

The stored energy density of each component as a function of system pressure p for solid and liquid LAES are shown in Figs. 7.18a and 7.18b respectively. From Fig. 7.18, it can be noted that the energy density of liquid air D_{L} is constant and high, $D_{\mathrm{L}} = 641\,\mathrm{MJ/m^3}$. However, the system energy density D of the solid LAES is only around $200\,\mathrm{MJ/m^3}$ and that of the liquid

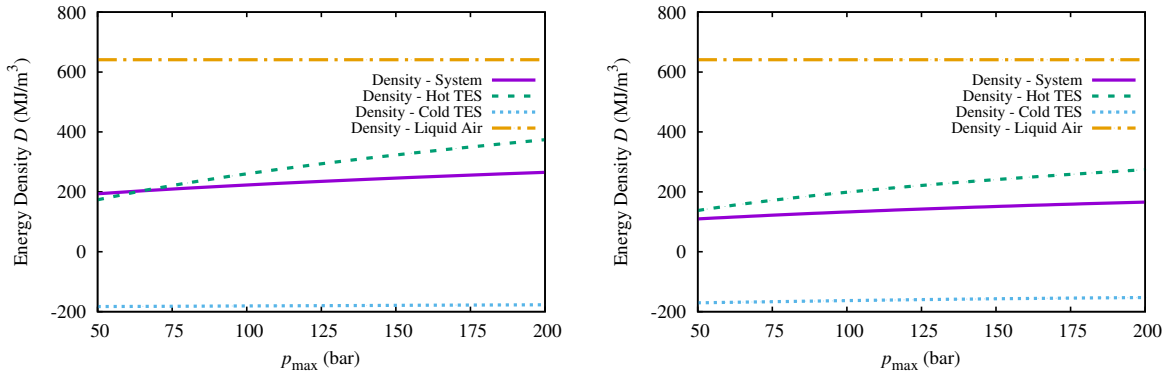

(a) solid LAES

(b) liquid LAES

Figure 7.18: Energy density of each component for (a) solid LAES and (b) liquid LAES

LAES is even lower. This is because although the specific energy of liquid air E_L is high, the specific energy after cold TES $E_L - E_C$ is relatively low. Meanwhile, the cold TES increases the cold storage volume from V_L to $V_L + V_C$ and thus significantly drags down the system energy density of LAES, as shown by the following equation:

$$D_{LAES} = \frac{E_L - E_C + E_H}{V_L + V_C + V_H} \tag{7.16}$$

The cold TES of liquid LAES has two sets of thermal fluids working in series, therefore, its volume of cold TES V_C is even higher and system energy density D_{LAES} is lower. From Fig. 7.18, it can also be noted that the energy density of hot TES D_H increases with pressure p; whilst the energy density of cold TES D_C is almost constant. This is because the supercritical air is more close to ideal gas at high temperature, therefore, the temperature and energy density of hot TES increases with the pressure p. On the other hand, the supercritical air is more close to liquid at very low temperature, therefore, the temperature and energy density of cold TES is almost independent of p.

7.9 Comparison with PTES and potential improvement

One of the major attractions of LAES is the high energy density of liquid air. However, only half of its stored exergy can be extracted during discharge and the rest is used to charge up the cold TES. Besides, the heat capacity of cold TES is usually very low due to the cryogenic effect, which leads to a large and expensive cold TES and drags down the system energy density. To deal with this challenge, a combined cycle of PTES and LAES has been proposed by Pau Farres-Antunez recently [7]. During charge, the cold exergy required for air liquefaction

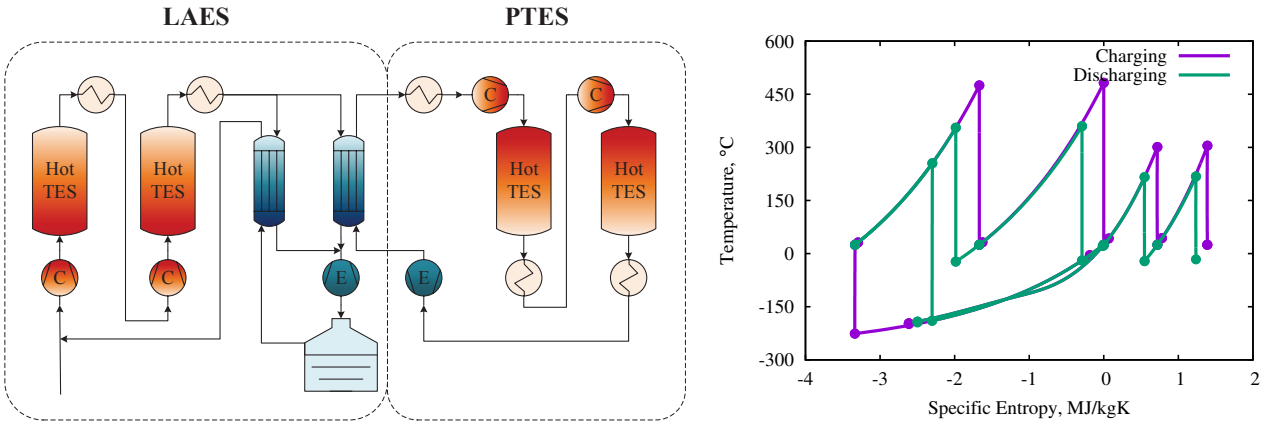

(a) Schematic diagram

(b) T-s diagram

Figure 7.19: Schematic and T-s diagrams of the combined cycle: (a) Schematic diagram (b) T-s diagrams

is provided by the PTES topping cycle, whilst during discharge, the cold exergy stored in the liquid air can also be released via the PTES. Therefore, there is no need for a cold TES for both LAES and PTES, and these two cycles operate in the same direction.

The schematic and T-s diagrams of the combined cycle are shown in Figs. 7.19a and 7.19b respectively. Both LAES and PTES sub-cycle is assumed to start at ambient temperature T_0 and pressure p_0. Both flows start with a compression followed by cooling, where the working fluids transfer heat into the storage media. For LAES and PTES sub-cycle, the compression and cooling process are repeated three times and twice respectively before the LAES sub-cycle reaching the top pressure of 150 bar. Then the working fluid of PTES sub-cycle undergoes a single expansion back to p_0 before entering the "coupler", which is the main counterflow heat exchanger linking the two cycles and cools the supercritical air down to cryogenic temperatures. Helium is selected here as the working fluid of the PTES sub-cycle mainly due to its low boiling point, which is essential for air liquefaction. Finally the air flows through a cryo-expander (rather than a throttle), resulting in a 100 % liquid air yield. The liquid air is then stored at ambient pressure, while the helium return to the starting point of the closed cycle. During discharge, all processes are reversed.

The combined cycle has several important features that distinguish it from the separate cycles. Firstly, the cold thermal reservoirs of the two systems have been replaced by a single heat exchanger, thus economizing significantly on the storage media. Secondly, the supercritical air can be cooled to temperatures that are low enough for it to be fully liquefied upon expansion. That affords several advantages, including: (a) a mechanical expansion devices is more readily employed (because the damage associated with two-phase flow has been eliminated), thereby avoiding the significant irreversibility associated with throttling. (b) there is no need

Table 7.3: Comparison between the stand-alone PTES, LAES and the combined cycle [7]

Parameter	Single PTES	Single LAES	Combined Cycle
Efficiency (%)	61.8	61.0	60.4
Energy density (kWh/m^3)	45.9	27.4	65.7
Work ratio (dis)	3.3	27.3	2.64 (PTES), 28.2 (LAES)
Specific work (dis)	1.44	0.49	0.85 (PTES), 0.50 (LAES)

for flash gas recirculation system (c) the same quantity of air is processed during discharge and charge, thus providing better heat integration with the thermal stores. Lastly, the energy density of the combined cycle is higher than any of its individual sub-cycle. To better demonstrate this advantage, the energy density of the PTES and the combined cycle have been given as follows:

$$D_{\mathrm{PTES}} = \frac{E'_{\mathrm{C}} + E'_{\mathrm{H}}}{V'_{\mathrm{C}} + V'_{\mathrm{H}}} \tag{7.17}$$

$$D_{\mathrm{CC}} = \frac{E_{\mathrm{L}} + E_{\mathrm{H}} + E'_{\mathrm{H}}}{V_{\mathrm{L}} + V_{\mathrm{H}} + V'_{\mathrm{H}}} \tag{7.18}$$

where the subscript CC denotes the combined cycle and the prime symbol ($'$) refers to the parameters of the PTES sub-cycle. Other parameters without the prime symbol refer to those of the LAES sub-cycle. The energy density of the LAES has been given by Eq. (7.16). From Eqs (7.16) and (7.18), it can be easily noted that the energy density of the combined cycle is higher than that of the LAES, $D_{\mathrm{CC}} > D_{\mathrm{LAES}}$. This is because if we assume the energy density of the hot TES of the combined cycle and LAES are roughly the same, which means $(E_{\mathrm{H}} + E'_{\mathrm{H}}) / (V_{\mathrm{H}} + V'_{\mathrm{H}}) \approx E_{\mathrm{H}}/V_{\mathrm{H}}$, then the combined cycle will have higher energy density of the cold part than that of the LAES because $E_{\mathrm{L}} > E_{\mathrm{L}} - E_{\mathrm{C}}$ whilst $V_{\mathrm{L}} < V_{\mathrm{L}} + V_{\mathrm{C}}$. Similarly, it can be noted from Eqs. (7.17) and (7.18) that the energy density of liquid air $E_{\mathrm{L}}/V_{\mathrm{L}}$ is higher than that of the cold TES $E_{\mathrm{C}}/V_{\mathrm{C}}$ because the volumetric heat capacity of liquid air is higher whilst the temperature is lower. Hence, it has been proved analytically that the combined cycle has the highest energy density of the three systems.

The results of the comparative study are summarized in Table 7.3. The efficiency of the combined cycle is around 60 %, similar to that of both PTES and LAES. The table also highlights that the combined cycle gives a significant improvement in energy density, exceeding that of PTES by about 43 % and more than doubling that of LAES, which is in accord with the above analysis.

It should be noted that, due to the difficulties associated with operating expanders in the

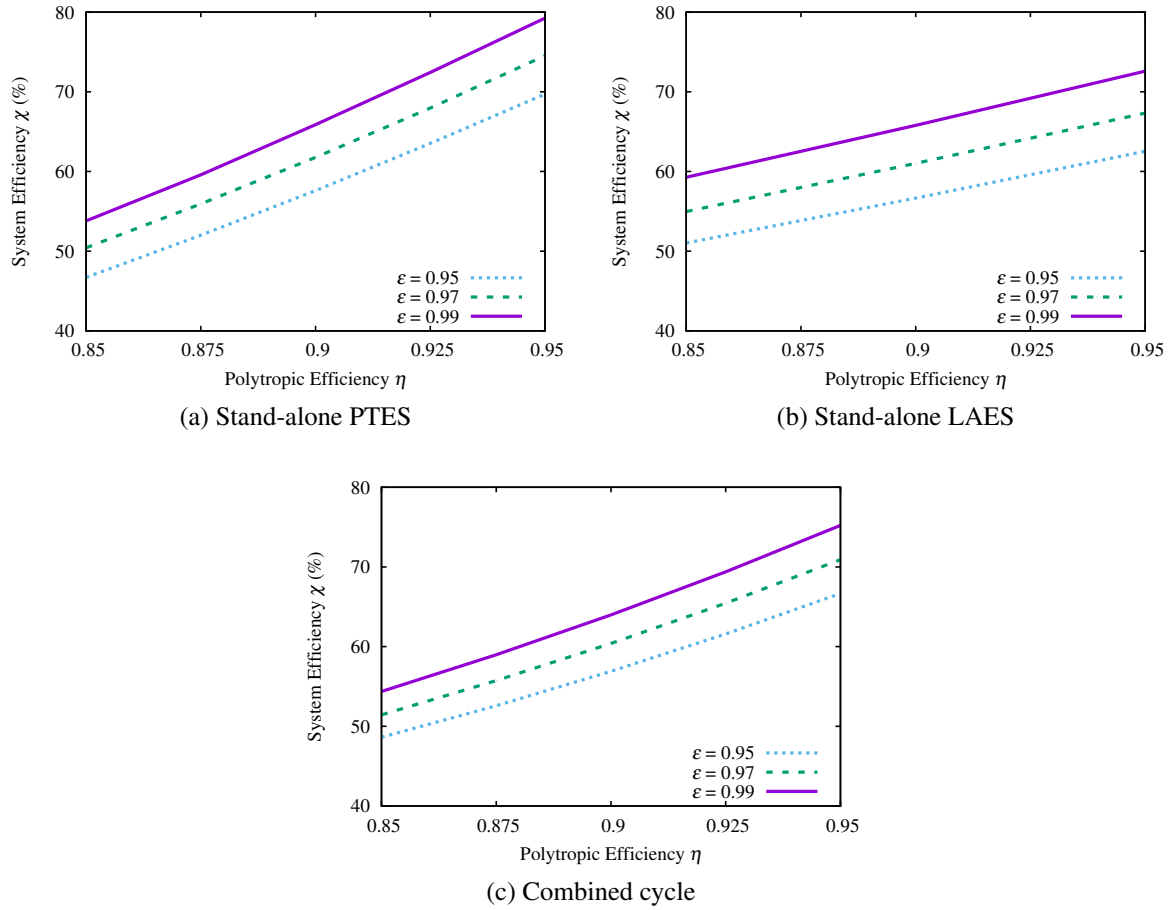

(a) Stand-alone PTES

(b) Stand-alone LAES

(c) Combined cycle

Figure 7.20: Sensitivity study of the stand-alone PTES, LAES and the combined cycle: (a) Stand-alone PTES (b) Stand-alone LAES (c) Combined cycle [7]

two-phase region, practical (stand-alone) LAES might employ a throttle instead of a mechanical expander, and in this case the efficiency would fall dramatically, by more than 20 %, due to the reduced liquid air yield during charge. For comparison, where a throttle to be employed in the combined cycle, it would incur a much smaller efficiency penalty of just 3 %. This is because conditions downstream of the throttle remain in the fully liquid state for the combined cycle case.

Results thus far have been obtained with fixed values of compression and expansion polytropic efficiency η and heat exchanger effectiveness ε. The effect of varying these parameters is shown in Fig. 7.20. It is notable that the stand-alone LAES is the least sensitive to variation in η, this being due to its high work ratio, whereas the combined cycle is the least sensitive to ε, due to heat transfer irreversibility being dominated by the pinch point in the coupler. Conclusions regarding the relative merits of the different systems are, however, unaffected by

the values of η and ε.

7.10 Summary

In this chapter, a simple yet efficient LAES is proposed, and its requirements for stable operation is analyzed. Both the packed bed thermal reservoir and the heat exchanger with thermal fluid tanks have been used as the cold TES, and their performance are compared with each other. Unique phenomena such as pinch point and thermal shock wave have been discovered in the liquid and solid LAES respectively, and the impacts of TES materials and operating pressure on these phenomena are studied in detail. Parametric studies are also carried out for both solid and liquid LAES, in order to study the variation of system efficiency, unit storage cost and energy density due to various parameters. Both the loss and cost distributions are given, and the drawbacks of LAES are also pointed out. Finally, a feasible combined cycle with PTES for enhancing the energy density of LAES is also proposed and their performance are compared with each other. From this chapter, the following conclusions could be reached.

1. The pinch point problem and thermal front management are respectively the major challenges of the liquid and solid TES. The thermal fluid of liquid TES tends to have narrower temperature range but constant heat capacity, whilst the packing material of solid TES have wide temperature range but decreasing heat capacity. In addition, the pressure vessel of solid LAES makes it more expensive than liquid LAES, but the solid LAES is usually more efficient than liquid LAES.

2. For the solid LAES, its efficiency decreases with the pressure but the unit cost increases with it; whilst for the liquid LAES, its efficiency increases with pressure but the unit cost decreases with it. Meanwhile, for the solid LAES, its cost is dominated by the TES system but the efficiency by the compressor/expander; whilst for the liquid LAES, its cost is dominated by the compressor/expander but the efficiency by the TES system.

3. The performance of cryogenic expander significantly affects the system efficiency but its capital cost is relatively low, therefore, it is worthwhile to deploy efficient yet expensive cryo-turbine for LAES.

4. The exergy stored in the liquid air is roughly equal to the rated energy of the LAES system and the exergy stored in the hot TES and cold TES are roughly the same but of opposite signs. The energy density of hot TES increases with pressure whilst the energy density of cold TES and liquid air is independent of it. The system energy density of solid LAES tends to be higher than that of liquid LAES.

5. the combined cycle has higher energy density than both PTES and LAES and can avoid the two-phase working condition and flash-gas challenge faced by LAES.

Chapter 8

Comparison and optimisation of the technologies

8.1 Description of optimisation method

Optimization can assist designers and engineers to find the best solution to a problem, by allowing them to maximize the potential of their work whilst minimizing the cost. There are a wide range of optimization algorithms, such as the golden section method, the steepest descent method, the Newton-Rhapson method and the conjugated gradient method [120]. However, these algorithms generally rely on the function being defined analytically and differentiable, and are thus limited to tacking certain types of problems. In practical scenarios, the optimization problems can become extremely complex due to the following reasons [8]:

1. The objective function and its derivative cannot be obtained in analytical form. They may be the output of a complex numerical model.

2. The objective function may be a function of many design variables and therefore, the search space is large and multidimensional.

3. There may be multiple competing optimization objectives, and an improvement in one objective is often obtained at the cost of deterioration in another one.

4. The problem can be highly constrained, so that the search space is often disjoint.

5. The problem may include many local optima which can easily trap the optimization process.

An appropriate approach to such difficult optimization problems is to use a stochastic search method, such as Simulated Annealing (SA), Genetic Algorithm (GA), Evolution Strategies

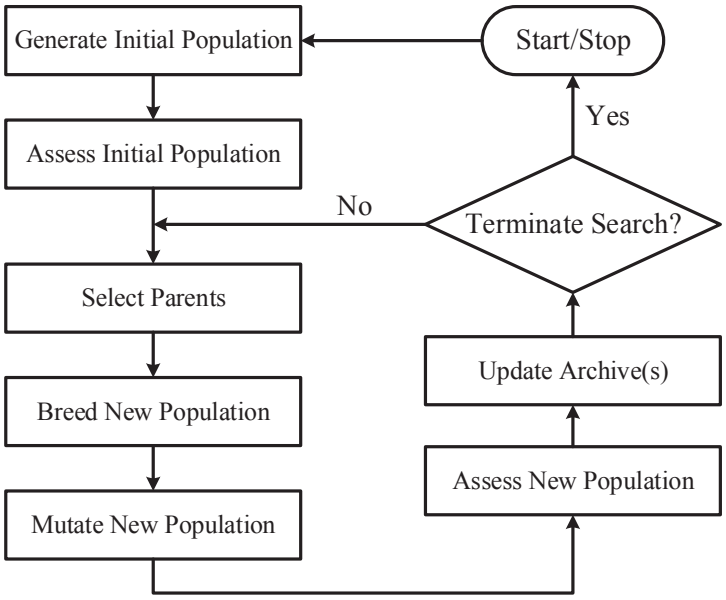

Figure 8.1: Basic structure of GA

(ES), Hook and Jeeves Search (HJS) and Tabu Search (TS). These stochastic algorithms searches the entire design space in a random manner with less risk of becoming trapped in local optima, and are well suited to solving complex real-world problems. Amongst these stochastic optimizations, evolutionary algorithm such as GA is a popular branch, which attempts to simulate the phenomenon of natural evolution first observed by Darwin. GA differs from traditional optimization algorithms in four important aspects [120]:

1. They work using an encoding of the control variables, rather than the variables themselves.

2. They search from one population of solutions to another, rather than from individual to individual.

3. They use only objective function information, not derivatives.

4. They use probabilistic, not deterministic, transition rules.

The basic structure of a GA is shown in Fig. 8.1. One minor change from the standard optimization routine flow diagram is the use of the word “population” rather than “solution”. A more major difference is that the usual operation of generating a new solution has been replaced by three separate activities - selection, recombination and mutation.

8.1.1 Parent Selection

The initial population for a GA is usually selected randomly if no knowledge-based selection is available. Then a popular selection algorithm, know as the tournament selection, is used to randomly create a small subset of solutions and then pick up the best two from it as parents. The parent selection is based on the principle of "survival of the fittest" and the fitness implies how good a candidate is in terms of the objective functions. Other factors, such as diversity, are also considered during the selection. Then two offspring are produced from each pair of parents and the "child" population is thus generated. Finally, the "child" population is merged with the "parent" population, from which the new "parent" population is generated for the next generation. Compared with other selection algorithm, tournament solution is less susceptible to takeover by strong individuals and the selection pressure can be adjusted by controlling the size of the subsets used.

8.1.2 Population recombination

After the best two solutions from each subset are selected as parents, their good existing features are combined to construct better solutions, and this procedure is called crossover. There are mainly two types of crossover in GA, one for binary (or integer) number and the other for real number. The former can be further divided into one point, two points and multiple points crossovers, whilst for the latter, many problem-specific solution representations and crossover operations have been developed, which can substantially improve algorithm performance. For example, Simulated Binary Crossover (SBX) is used for the real number in this thesis.

8.1.3 Population mutation

The purpose of mutation is to provide insurance against the irrevocable loss of genetic information and hence to maintain diversity within the population. For instance, if every solution in the population has 0 as the value of a particular bit, then no amount of crossover will produce a solution with a 1 there instead. As a result, binary mutation and real polynomial mutation are introduced here for the integer and real number respectively. In the NSGA-II used in this thesis, each bit is subjected to a simulated weighted coin toss with a probability of mutation p_{m}, which is usually very low. If mutation is approved, the bit changes value.

8.2 Multi-objective optimisation and Pareto fronts

Most real-world design problems are actually multi-objective optimization problems where designers seek to optimize simultaneously several performance attributes of the design and an improvement in one objectives is often only obtained at the cost of deterioration in other objectives [45, 120]. Therefore, tradeoffs are common and necessary in multi-objective optimisation.

There are two standard methods for treating multi-objective problems, if a traditional optimization algorithms which minimizes a single objective is to be employed. One is to construct a composite objective:

$$\text{Minimize } \tilde{f} = \sum_{i=1}^{N} a_i f_i \tag{8.1}$$

where the f_i are the N objectives to be minimized and the a_i are positive-valued weightings.

The other is to place constraints on all but one of the objectives, i.e:

$$\text{Minimize } f_j \text{ subject to } f_i \leq C_i \; \forall \, i = 1,N; \; i \neq j \tag{8.2}$$

where the C_i are the constraint limits.

No matter which of these approaches is used, the solution of single-objective problem results in a single point on the tradeoff surface, the position of which depends on the designer's preconceptions (the values of a_i or C_i chosen) as illustrated in Fig. 8.2. In order to further explore the tradeoff surface, numerous different optimizations must be conducted, each with different weightings or constraints. It will be a potentially time-consuming and computationally expensive exercise if ever attempted.

Although a single solution must be chosen eventually, it is evident that the designer will make better-informed decision if the tradeoff surface between the conflicting objectives can be inspected before this choice is made. By using suitably adapted stochastic optimization methods it is possible to reveal the tradeoff surface of a multi-objective optimization problem in a single run. The appropriate adaptions to the standard Genetic Algorithm (GA) will be explained in detail because GAs search from population to population rather than from one individual solution to another, which makes them well suited to performing multi-objective optimization. In fact, the only modification required for turning a single-objective GA into a multi-objective one, is by applying the multi-objective archiving and non-dominated sorting in the selection process.

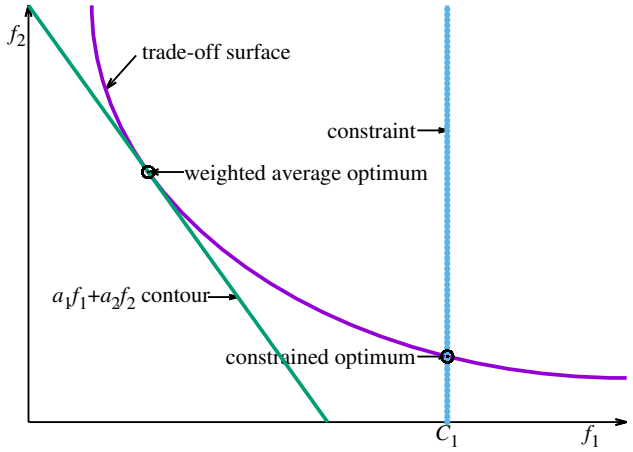

Figure 8.2: Types of multi-objective optimum

8.2.1 Multi-objective archiving

Adapting any stochastic optimization algorithms to perform multi-objective optimization will inevitable required a common change to the method of archiving. In multi-objective optimization solutions lying on the tradeoff surfaces (or Pareto fronts as it is also known) are sought.

Any solution on the Pareto front can be identified formally by the fact that it is not dominated by any other possible solution. A solution X is said to be dominated by solution Y if Y is at least as good as all counts (objectives) and better on at least one, i.e., assuming all M objectives are to be minimized if:

$$f_i(Y) \leq f_i(X) \ \forall i = 1, M \text{ and } f_i(Y) < f_i(X) \text{ for some } i \tag{8.3}$$

Thus, in multi-objective optimization, an archive of the best (i.e. the non-dominated) solutions found should be maintained. A suitable archiving scheme, illustrated in Fig. 8.3, is as follows:

1. All feasible solution generated are candidates for archiving.
2. If a candidate solution dominates any existing members of the archive, those are removed and the new solution is added (Case 1)
3. If the new solution is dominated by any existing members of the archive, it is not archived (Case 2)
4. If the new solution neither dominates nor is dominated by any members of the archive, it is added to the archive (Case 3)

Using this scheme, it is hoped that the archive will converge onto the true trade-off surface between the objectives as the search progresses.

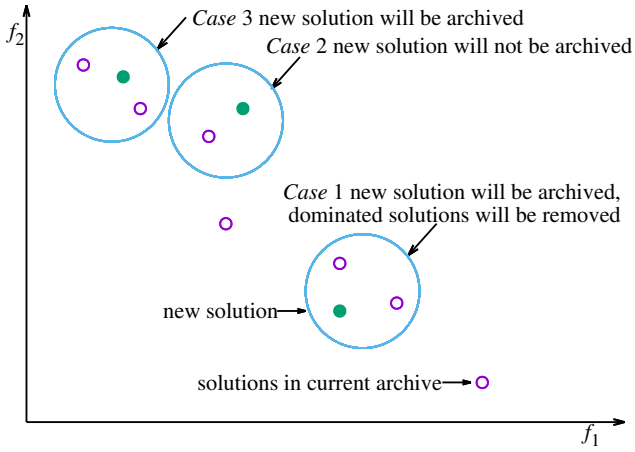

Figure 8.3: Multi-objective archiving

8.2.2 Archiving diversity

In addition to maintaining dominance over other solutions in terms of optimisation objectives, it is also critical to maintain diversity in the design variable and objective function space. This is because members of a diverse population will generate equally diverse offspring therefore helping the design space to be more fully explored. The objectives of converging archives to Pareto fronts and maximizing diversity may be at odds and there are many methods of achieving both objectives. For example, the Genetic Diversity Evolutionary Algorithm (GDEA) [137] explores this conflict by making diversity an additional objective in the problem. The Non-dominated Sorting Genetic Algorithm (NSGA-II) [45] encourages diversity along the Pareto front by calculating the crowding distance between each member on the Pareto front. Therefore, if all the members are non-dominated solutions, then the ones with the largest crowding distance will be selected. In another algorithm called Strength Pareto Evolutionary Algorithm (SPEA) [138], a ranking procedure based on the number of solutions that a given solution dominates is used. Therefore, the fewer points a solution dominates, the more this solution is preferred because it is located in a less-explored area. Comparisons of various algorithms have shown that the NSGA-II generally have the best performance, and therefore, it is also used in this thesis for multi-objective optimization.

8.3 Optimization study

The objective functions of all thermo-economic optimizations are the system efficiency χ and the unit storage cost Z, which are defined by:

System efficiency:

$$\chi = \frac{W_{\text{dis}}}{W_{\text{chg}}} \tag{8.4}$$

Unit storage cost:

$$Z = \frac{Z_{\text{tot}}}{W_{\text{dis}}} \tag{8.5}$$

where W_{chg} and W_{dis} are the net work input during charge and net work output during discharge respectively, and Z_{tot} is the total cost of the system components. W_{chg} and W_{dis} are calculated by numerically integrating the power over the durations of charge-discharge cycle, and Z_{tot} is obtained by summing up all the component cost. As mentioned in Chapter 5, the mechanical and electrical losses are not accounted for, so χ constitutes a thermodynamic roundtrip efficiency. Likewise, the costs are limited to thermodynamic components, as Z_{tot} does not include motor/generator costs and maintenance cost.

8.3.1 Comparison of liquid, solid and hybrid A-CAES

The parametric study in Chapter 5 suggests that hybrid A-CAES has the lowest unit cost whilst the solid system has the highest efficiency. However, strictly this is only the case for the points associated with the nominal design. To find out the best designs across the full design space and provide a thorough comparison between the liquid, solid and hybrid systems, a multi-objective optimization has been carried out for each A-CAES system. A stochastic optimization algorithm called NSGA-II, as described in Ref. [45, 46], has been used for this task. The objectives are to maximize the efficiency χ and minimize the unit cost Z. Boundaries are placed on the design variables to aid the search for the optimum solutions, as summarized in Table 5.5. In addition, the maximum allowable temperatures of the TES materials are also used as constraints, these being 340 °C for mineral oil and 600 °C for magnetite. The best designs emerging from the optimization are shown in Fig. 8.4a, where the nominal design points of the three systems are also shown for comparison.

Cost and efficiency tradeoffs and general design trends

Fig. 8.4a shows so-called Pareto fronts for the three types of A-CAES. These constitutes the "leading edge" solutions, with all other designs lying either below or to the right (as in the case of the nominal designs). The Pareto fronts clearly demonstrate the tradeoffs between cost and efficiency stemming from the various factors discussed in Chapter 5. Based on the underlying assumptions in the model, it is clear from Fig. 8.4a that the solid and liquid systems

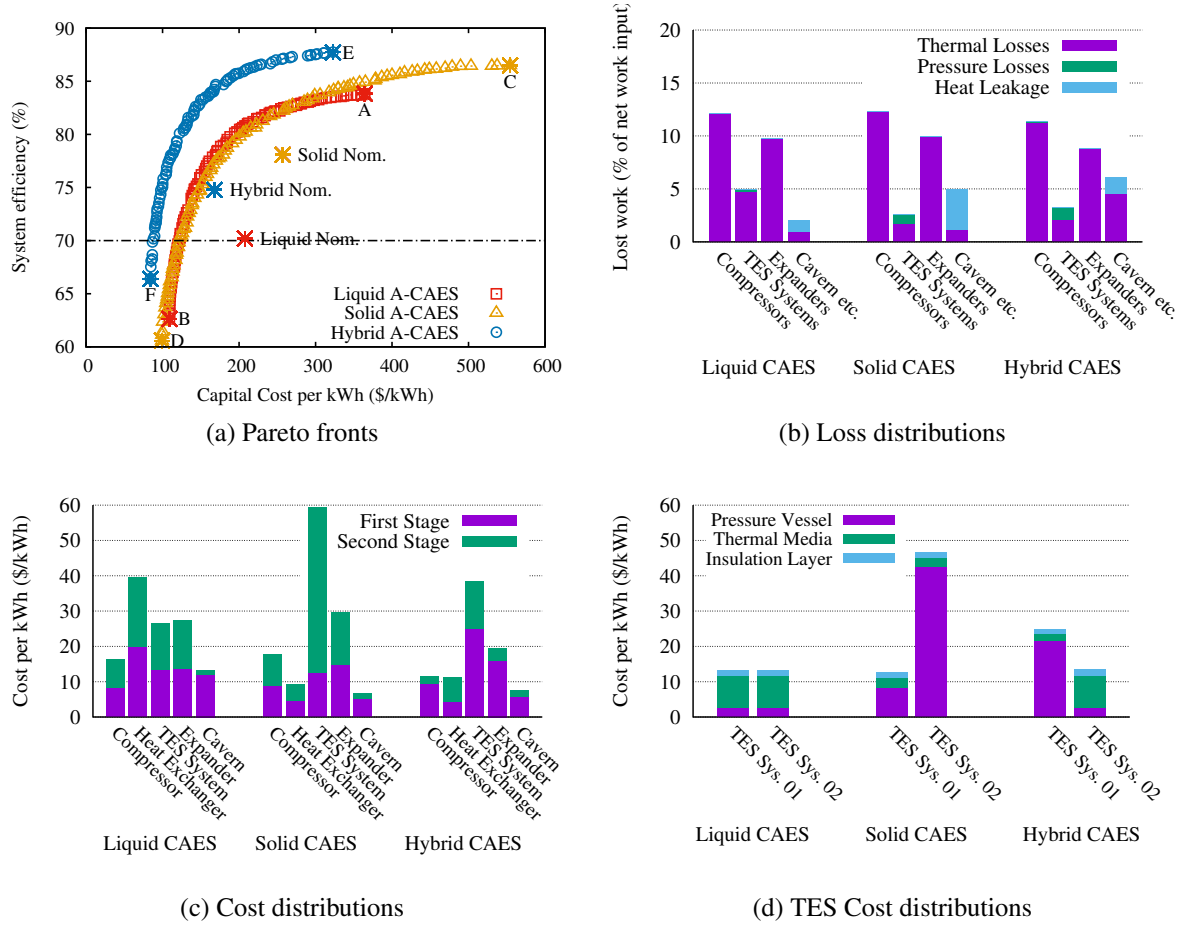

(a) Pareto fronts

(b) Loss distributions

(c) Cost distributions

(d) TES Cost distributions

Figure 8.4: Pareto fronts and loss and cost distributions of the three systems: (a) Pareto fronts (b) Loss distributions (c) Cost distributions (d) TES Cost distributions. (loss and cost distributions are for designs with thermodynamic round-trip efficiency $\chi = 70\%$.)

demonstrate similar performance but the hybrid system is superior in that it is either cheaper for the same efficiency, or more efficient for the same cost. It is also notable that there are diminishing returns in trying to further increase χ when Z is very high, or to further reduce Z when χ is very low. The tradeoff is thus more significant at the "knee" of the curves where χ and Z have moderate values (e.g. $Z = 100 - 200\,\$/\text{kWh}$ or $\chi = 75 - 85\,\%$ for the hybrid system).

Table 8.1 summarizes the design variables and resulting performance for the nominal cases and for the six points labeled A through F in Fig. 8.4a, each of these being at either the highest efficiency or the lowest cost for the three systems. All of these solutions (and in fact all designs on the Pareto fronts) converge to having just two stages in order to reduce costs. On the other hands, there is significant spread in many of the other variables. As would be expected, high values of $\eta_{c/e}$ and NTU correlate with efficient but expensive designs, but

Table 8.1: Design variables and main results for the nominal and optimal designs indicated in Fig. 8.4a

	Liquid A-CAES			Solid A-CAES			Hybrid A-CAES		
	Nom.	A	B	Nom.	C	D	Nom.	E	F
N_{stg}	4	2	2	2	2	2	3	2	2
p_{max} (bar)	120	100	79	120	195	40	120	40	42
$p_{\text{min}}/p_{\text{max}}$	0.60	0.89	0.44	0.60	0.87	0.30	0.60	0.86	0.54
NTU	9	49	7	-	-	-	9	36	1
$\eta_{\text{c/e}}$	0.85	0.90	0.80	0.85	0.90	0.80	0.85	0.90	0.80
p_{m}	-	-	-	-	-	-	10	30	20
Π	-	-	-	1.0	1.0	1.5	1.0	1.0	1.3
d_p (mm)	-	-	-	15	2.6	22.6	15	2.1	5.0
L/D	-	-	-	1.0	0.4	2.6	1.0	0.4	3.1
$\chi(\%)$	70.2	83.8	62.6	78.1	86.5	60.6	74.8	87.7	66.4
Z (\$/kWh)	208	364	109	257	554	99	168	323	84

Table 8.2: Main results for the 70 % efficiency cases of A-CAES

	Liquid A-CAES	Solid A-CAES	Hybrid A-CAES
System Efficiency	70.3 %	70.2 %	70.2 %
Cost per kWh	123 \$/kWh	123 \$/kWh	88 \$/kWh
Capital Cost	37 M\$	39 M\$	26 M\$
Net Output Work	303 MWh	320 MWh	298 MWh
Net Input Work	431 MWh	456 MWh	425 MWh

different preferences are exhibited by the three systems for other parameters. For example, liquid systems tend to select the highest value of p_{max} consistent with the limit on liquid storage temperature, whereas the hybrid systems opt for the lowest cavern pressure and solid systems show a strong cost-efficiency tradeoff, as discussed in Chapter 5.

Comparison of designs with fixed efficiency

The main results for optimized designs at a fixed round-trip efficiency of 70 % are shown in Table 8.2. For this level of efficiency the capital cost per kWh for the hybrid system is some 15 - 25 % below that of the other two A-CAES types, and the margin is even greater at higher efficiencies. It is of interest to see how this has been achieved, and how the losses and costs are distributed amongst the different components. This information is provided in the histograms of Figs. 8.4b to 8.4d.

For all three systems, losses are dominated by irreversibility in the compressors and expanders. Compression losses are slightly greater than expansion losses because it has been assumed that these processes have the same polytropic efficiency ($\eta_c = \eta_e = \eta$), which gives (for a given pressure ratio) $\Delta s_c / \Delta s_e = 1/\eta$. The next largest loss for liquid system is associated with the TES and is due mainly to irreversible heat exchange. This loss is much smaller for solid TES because of the direct nature of heat exchange and possibility of using small particles with large heat-transfer area. At additional cost, losses in liquid TES might be reduced further by the use of compact heat exchangers that have channel sizes smaller than 3 mm. Finally, the loss category labeled "cavern etc." includes direct cavern losses (as described in Chapter 5) plus exergetic losses due to heat rejection from the auxiliary heat exchangers and the exit loss due to air being returned to atmosphere after discharge at a temperature above T_0. This category of loss is larger for solid systems, particularly when the packed bed is undersized relative to the cavern because significant quantities of heat must then be rejected via the auxiliary heat exchangers.

Fig. 8.4c shows that the solid A-CAES system is the most expensive. As previously noted, this is due to the very high cost of the second-stage thermal reservoir. Meanwhile, the cost of the first-stage thermal store is lower than that of the liquid system and has a higher allowable top temperature. These are the main factors that provide the motivation for the hybrid system. Note that the turbomachinery (and other) costs are unequally distributed between the first and second stages for the hybrid systems because the pressure ratios are different, in accord with the different maximum temperatures for solid and liquid TES. (Note that first and second stage refer to well and mining costs respectively in the case of the cavern costs.) The distribution of costs between different components of the TES systems is shown in Fig. 8.4d from which it is clear that containment vessel costs dominate for solid systems (due to pressurization) whilst the mineral oil is the most expensive part of liquid TES.

Choice of storage media for liquid TES

Fig. 8.5 compares Pareto fronts for liquid systems obtained with different storage media. The cost and main thermodynamic properties of these liquids are summarized in Table 4.2. From the figure it is clear that mineral oil is the best candidate with other fluids being inferior for a variety of reasons. For example, ambient water has a low boiling point and therefore requires too many stages to achieve a reasonable cavern pressure. The temperature range can be extended by pressuring the storage vessel, but this quickly becomes very expensive. Therminol VP is more expensive than mineral oil despite its boiling point and heat capacity being lower. Saltstream XL (nitrate salt) has the highest boiling point and heat capacity, whilst the lowest cost. However, it solidifies at room temperature (the temperature at which the compressed

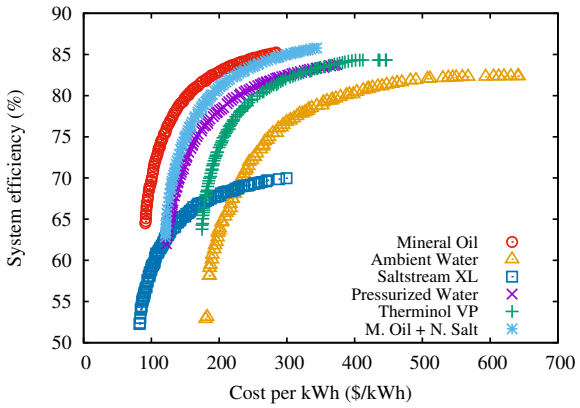

Figure 8.5: Pareto fronts of the liquid A-CAES with different thermal fluids

air is stored) and air existing from the main heat exchanger must therefore be hotter than the melting point (120 °C). This requires subsequent heat rejection to the environment, leading to significant exergetic loss and a reduction in roundtrip efficiency. It may be possible to get round this problem by "recuperation" (i.e., using an additional heat exchanger to preheat atmospheric inlet air during charge and cool the exhaust air during discharge) but the discussion of this possibility will be postponed to Section 8.3.2. Other nitrate salts have similar problems but with even higher melting points. In principle, it would be possible to extend the temperature range by operating these salts in series with a second thermal fluid, but this roughly doubles the TES costs. Mineral oil alone therefore emerges as the most economical option.

Sensitivity to cost assumptions

The impact of using optimistic, nominal and pessimistic cost factors (see Table 4.1) on the Pareto fronts for the liquid system is shown in Fig. 8.6a. Unsurprisingly, these factors have no impact on the system efficiency χ, and the three curves are simply shifted relative to one another along the cost axis. This serves to show that unit costs (i.e., per kWh storage capacity) might be expected to fall within the range of 70 to 100 $/kWh (ex. motor/generator, control and electrical connection costs) for a 70 % efficient hybrid system with a nominal rating of 100 MW and four hours capacity.

Effect of the stored energy-to-power ratio

The capital cost of some components (compressors, expanders and heat exchangers) is roughly proportion to the rated power, whereas that of others (the cavern and TES systems) depends

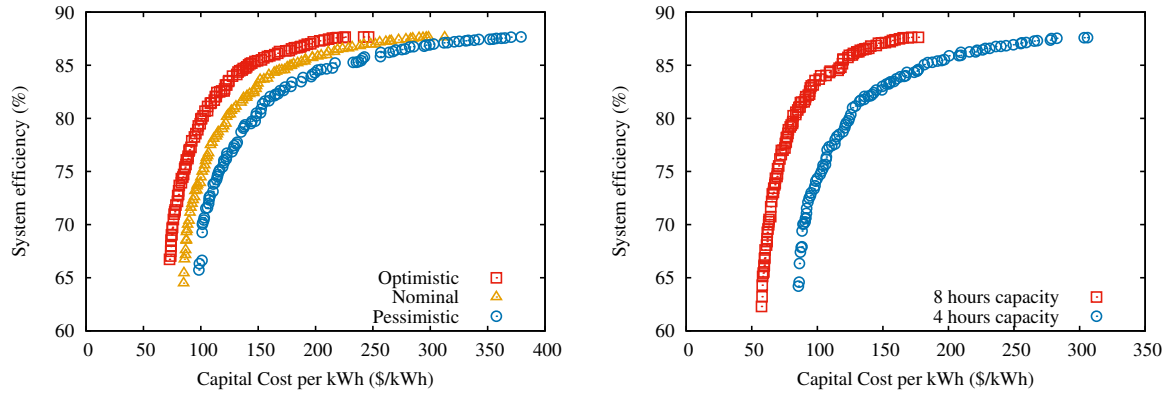

(a) Impacts of the cost equation constants

(b) Impacts of the stored energy W_{dis}

Figure 8.6: Pareto fronts of the liquid A-CAES systems: (a) with different cost factor scenarios (nominal, optimistic and pessimistic cases) and (b) with different stored energy W_{dis} at fixed power P using nominal cost factors.

mainly on the stored energy. An approximation to the total system cost is therefore given by:

$$Z_{\text{tot}} \simeq C_{\text{P}} P + C_{\text{E}} W_{\text{dis}} \tag{8.6}$$

where P and W_{dis} are the power and discharged work, and C_{P} and C_{E} are corresponding cost factors in \$/kW and \$/kWh respectively. The overall unit cost Z, as previously defined, is thus:

$$Z \simeq C_{\text{P}}/\tau_{\text{dis}} + C_{\text{E}} \tag{8.7}$$

where $\tau_{\text{dis}} = W_{\text{dis}}/P$ is the discharge duration, which reflects the storage capacity and has been set at four hours for the system considered so far. Eqs. (8.6) and (8.7) are not quite exact: for example, the cost per kWh of the TES is influenced slightly by its size via the level of insulation required.

Fig. 8.6b shows the Pareto fronts for two hybrid systems, both rated at 100 MW but one with four and the other with eight hours of storage. It is evident from Eq. (8.7) that the unit cost Z will be lower for the larger system. On the basis of Fig. 8.6b, estimates of C_{P} and C_{E} for a liquid system with $\chi = 70\%$ are ~250 \$/kW and ~20 \$/kWh respectively.

8.3.2 Comparison of A-CAES and PTES

The parametric study in Chapter 4 has shown that the Recuperated PTES tends to have higher system efficiency and lower sensitivity to various operating parameters than other PTES systems. However, this is realized at the expense of higher capital cost, and the parametric study

is only valid for the points associated with the nominal design. In order to find the optimal designs for each PTES and compare them with the counterparts of A-CAES, thermo-economic optimizations are applied to the PTES and A-CAES. Boundaries are placed on each design variable to aid the optimization, which are summarized in Table 4.3. In addition, the discharged hot and cold TES temperatures, T'_{H} and T'_{C}, also place constraints on the discharging temperature ratio τ' of some PTES variants, as shown in Eqs. (4.4) and (4.6). Unlike the PTES in Chapter 4, which are unpressurized and use air as the working fluid, all the PTES in this section are pressurized to a maximum allowable pressure of $p_{\max} = 500\,\mathrm{bar}$, use helium as the working fluid, and can reuse the compressor (or expander) for charge as the expander (or compressor) for discharge. With these assumptions, the PTES in this section are referred to as the PTES (Optimistic) whilst the PTES in Chapter 3 and Chapter 4 are referred to as the PTES (Pessimistic), and the comparison of these two cases will be discussed in Section 8.3.4. Similar to the PTES in Chapter 4, mineral oil and solar salts are still used as thermal fluids in the hot TES, and the propane and methanol are still employed by the cold TES. Therefore, the maximum and minimum allowable temperatures, $T_{\max}$ and $T_{\min}$, are set as 550 °C and −185 °C respectively.

Cost and efficiency tradeoffs and general design trends

The optimization results of the various PTES and A-CAES systems are summarized in Figs. 8.7a to 8.7c, from which it can be noted that the Pareto fronts of each A-CAES and PTES are relatively similar. The returns of further increasing χ when Z is high, or further reducing Z when χ is low gradually diminished, meaning the tradeoff is more significant when χ and Z are in moderate ranges. The Pareto fronts of the four PTES systems are relatively close to each other, as all PTES have managed to fully exploit the allowed temperature range, and minimize the losses and costs after the optimization. The Baseline PTES has the best performance when the unit storage cost Z is low, whilst the Recuperated PTES has the best performance when the system efficiency χ is high. This suggests the two recuperators enhances the thermodynamic efficiency χ at the cost of increasing the unit storage cost Z. Meanwhile, it should be noted that the Preheated and Precooled PTES have no advantages over the Baseline PTES. Therefore, the Baseline PTES should be deployed instead when lower capital cost is preferred.

From Fig. 8.7a, it can also be noted that with pressurization, the PTES can be almost as cheap as the CAES, provided that the compressor/expander costs indeed decrease with the system inlet pressure p_{in} increasing, as shown in Eq. (4.31). However, it will be difficult for PTES to achieve the same round-trip efficiency as the CAES, as long as the same components are used for both systems. In fact, the highest efficiency of the Baseline PTES is almost equal to the lowest efficiency of the Baseline CAES. However, it should be noted that the PTES enjoy

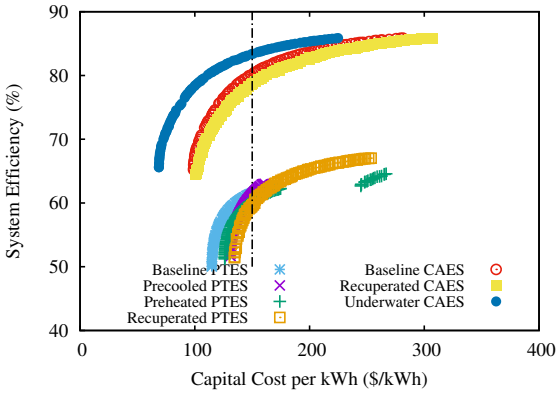

(a) Comparison of different A-CAES and PTES

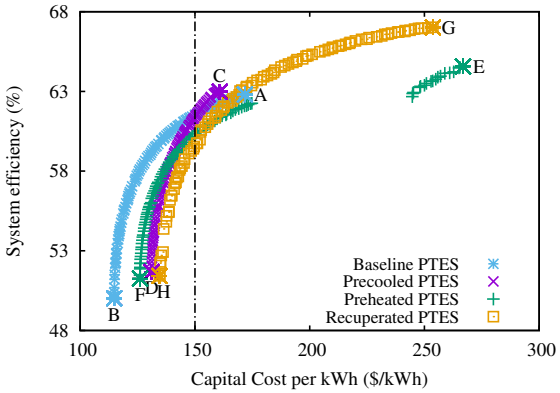

(b) Comparison of different PTES

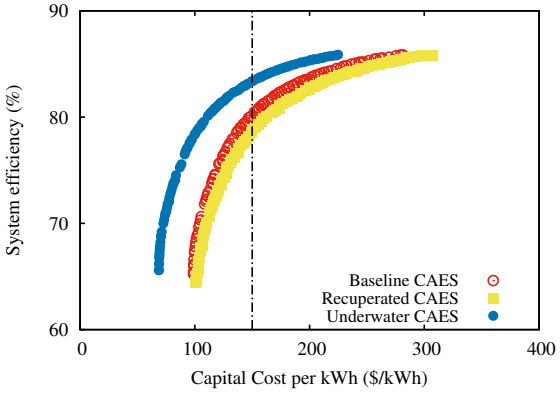

(c) Comparison of different A-CAES

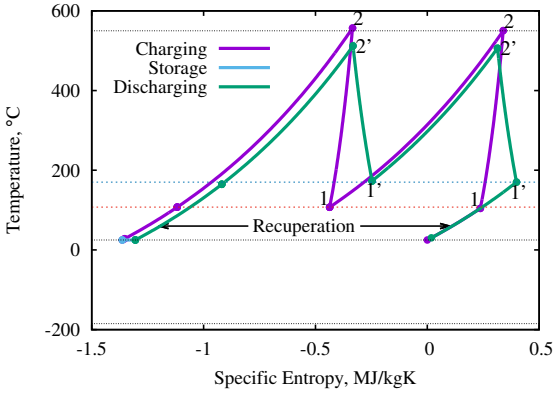

(d) $T-s$ diagram of the Recuperated CAES

Figure 8.7: Pareto fronts of different A-CAES and PTES: (a) Comparison of PTES and CAES (b) Comparison of PTES (c) Comparison of CAES (d) T-s diagram of the Recuperated CAES

Table 8.3: Design variables and main results for the optimal designs indicated in Fig. 8.7b

	Baseline		Precooled		Preheated		Recuperated	
	A	B	C	D	E	F	G	H
N_{hot}	1	1	1	1	1	1	1	1
N_{cold}	1	1	1	1	1	1	1	1
p_{max}	9.77	9.78	9.78	9.78	2.54	9.74	9.24	7.58
p_{min}	7.19	5.69	5.16	3.93	2.92	6.20	5.74	3.45
NTU	99	16	99	29	99	21	99	13
$\eta_{\text{c/e}}$	0.90	0.90	0.90	0.90	0.90	0.90	0.90	0.80
$\chi(\%)$	62.8	50.0	63.0	51.7	64.6	51.2	67.0	51.4
Z (\$/kWh)	172	115	161	131	267	126	254	134

more siting freedom than the CAES, as they have no specific requirements for the geology (or geographical) conditions of the site. If the CAES is required to have the same siting freedom, it will become unacceptably expensive as long as the pressure vessels are used as the air receivers. Actually, due to its sensitivity to various loss factors, the PTES usually employ novel and more efficiency devices, such as the efficient reciprocating compressors/expanders and segmented packed beds, to enhance its roundtrip efficiency, as discussed in Section 3.5.1.

As for the CAES, it can be noted from Fig. 8.7a that the round-trip efficiency ranges of these CAES are identical, whilst the Underwater CAES has the lowest unit storage cost. This is because the air accumulators of the Underwater CAES are isobaric and can store more energy within the same volume. However, the conclusions on cost comparison are at the mercy of the cost equations of the air accumulators from Ref. [30], therefore, these results should be treated with caution. From Fig. 8.7a, it can also be noted that the Pareto fronts of the Recuperated CAES and Baseline CAES almost overlap with each other, with the Recuperated CAES slightly more expensive due to the additional cost of hot recuperator, as shown in Fig. 8.7d. This means unlike PTES, the recuperation cannot enhance the efficiency of CAES. This characteristic of CAES can be noted from Eqs. (3.10) and (3.29), from which we know that increasing the charging compressor $T_{\text{c,in}}$ and discharging expander $T'_{\text{e,in}}$ inlet temperature simultaneously without changing the ratio between them has no impact on the roundtrip efficiency χ.

Comparison of designs with fixed unit storage cost

In order to better demonstrate the difference in thermal-economical performance, the loss and cost distributions of all PTES and A-CAES at $Z = 150$ \$/kWh are shown in Figs. 8.8a and

Table 8.4: Main results for the 150 $/kWh cost cases of PTES

	Baseline	Precooled	Preheated	Recuperated
System Efficiency	61.5 %	61.4 %	60.3 %	59.7 %
Cost per kWh	150 $/kWh	150 $/kWh	150 $/kWh	150 $/kWh
Capital Cost	44 M$	42 M$	43 M$	46 M$
Net Output Work	294 MWh	284 MWh	284 MWh	303 MWh
Net Input Work	477 MWh	462 MWh	471 MWh	508 MWh

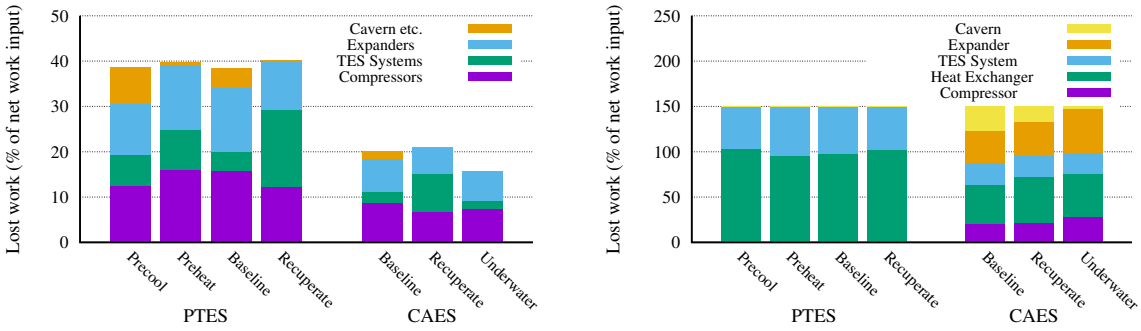

(a) Loss Distributions

(b) Cost Distributions

Figure 8.8: Loss and cost distributions of different A-CAES and PTES systems: (a) Loss distribution (b) Cost distribution

8.8b respectively, and the main calculation results of all PTES variants are summarized in Tables 8.4.

Fig. 8.8a shows the loss distributions of all CAES and PTES variants, from which it can be noted that the losses of CAES are always lower than that of the PTES, and the losses of PTES are very similar. From Fig. 8.8a, it can also be noted that the Precooled PTES has the highest auxiliary losses (which are included in the cavern losses) whilst the Recuperated PTES has the lowest ones. This is because unlike the Precooled PTES where the waste heat is dissipated into the environment via an auxiliary heat exchanger, this thermal energy is recycled in the Recuperated PTES. Therefore, the Recuperated PTES has the lowest auxiliary losses but the highest TES losses since most recycled thermal energy need to be cooled during storage to avoid over-heating, as mentioned in Section 4.6.

The cost distributions of all CAES and PTES variants are shown in Fig. 8.8b, from which it can be easily noted that the unit storage cost of all CAES and PTES variants are the same, and the compressor and expander cost of all PTES variants are close to zero. This is because the compressor/expander cost of PTES variants reduces rapidly with the pressurization, whilst

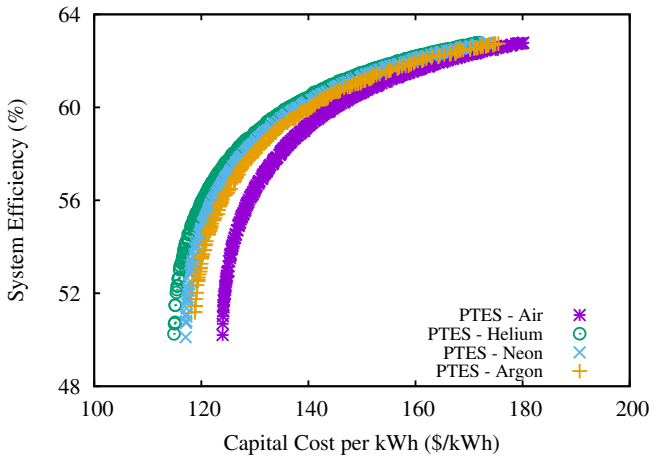

Figure 8.9: Pareto fronts of the Baseline PTES with different working fluids

the TES and heat exchanger cost remain constant. As a result, the TES and heat exchanger cost becomes dominant after optimization for the PTES variants. From Fig. 8.8b it can also be noted that the Recuperated CAES has higher heat exchanger cost, whilst the Underwater CAES has the lowest air reservoir cost.

Choice of working fluid for PTES

As mentioned before, the PTES usually enjoy more design freedom and can employ non-conventional gases, such as helium, neon, and argon, as the working fluids. In order to analyze their impacts on the thermal-economic performance of PTES, the Pareto fronts of the Baseline PTES with different working fluids are shown in Fig. 8.9. The efficiency ranges of various PTES are quite similar whilst the PTES with helium as the working fluid enjoys the lowest unit storage cost. This is because the input power of all PTES are fixed at $P = 100\,\mathrm{MW}$ in this thesis, and as a result, under the same temperature ratio τ, the higher the heat capacity c_p of the working fluid is, the lower mass flowrate $\dot{m}$ and component cost Z_i are required, as indicated by Eqs. (4.31) and (4.33). Meanwhile, since helium is a kind of monatomic gas which has relatively high adiabatic index γ, a lower pressure ratio β is required for the same temperature ratio τ. Although the gas constant R_g of helium is high, which increases its compressor/expander cost according to Eq. (4.31), the above two factors make helium the best working fluid for PTES systems. However, it should be noted that the helium is also more expensive than other gases, but the mass and cost of different working fluids are not considered here. Besides, the validity of these results and conclusions are also subject to the accuracy of the cost equations of the system components.

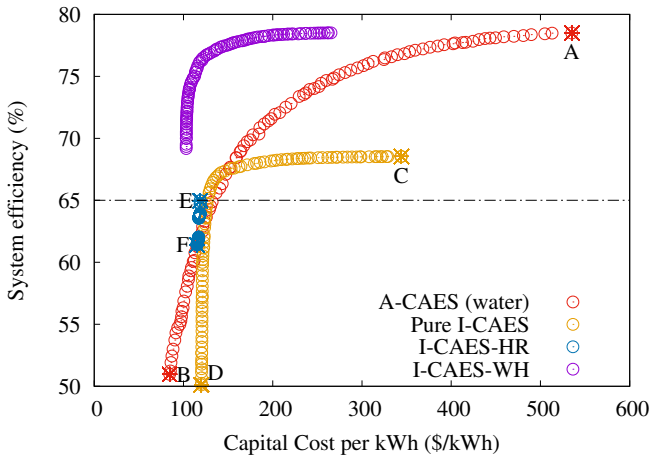

Figure 8.10: Pareto fronts (trade-off surfaces) for the A-CAES, Pure I-CAES and I-CAES-HR systems

8.3.3 Comparison of A-CAES and I-CAES

The parametric study in Chapter 6 shows that different CAES may reveal different trends as each parameter varies. Therefore, it is difficult to find out the best designs across the full design spaces and provide a thorough comparison between these CAES systems without thermo-economic optimizations. As mentioned before, NSGA-II is used for this task and the objectives are to maximize the efficiency χ whilst minimizing the unit cost Z. Boundaries are placed on the design variables to aid the search for the optimum solutions, as summarized in Table 6.2. In addition, the maximum allowable temperatures of the TES material is also used as the constraint, this being 100 °C for water at ambient pressure. The polytropic efficiency η, system frequency f and droplet diameter d are fixed at 85 %, 1 Hz and 20 μm respectively throughout the optimization. The best designs emerging from the optimization are shown in Fig. 8.10, where the nominal points of these three systems are also shown for comparison

Cost and efficiency trade-offs and general design trends

Fig. 8.10 shows Pareto fronts for the three types of CAES. The Pareto fronts clearly demonstrate the trade-offs between cost and efficiency stemming from the various factors discussed in Chapter 6. Based on the underlying assumptions in the model, it is clear from Fig. 8.10 that the A-CAES and I-CAES systems demonstrate similar performance at moderate efficiency χ and unit cost Z regions (e.g. $Z = 100 - 150\,\mathrm{kW/h}$ or $\chi = 62 - 68\,\%$) but the A-CAES is superior to the I-CAES at high efficiency χ or low unit cost Z regions. It is also notable that the Pareto front of I-CAES has sharper edge (or lower curvature radius) than that of A-CAES because the polytropic efficiency η of isothermal compressor/expander is fixed at its nominal

Table 8.5: Design variables and main results for the nominal and optimal designs indicated in Fig. 8.10

	A-CAES			Pure I-CAES			I-CAES-HR		
	Std.	A	B	Std.	C	D	Std.	E	F
N_{stg}	3	7	4	3	3	1	3	1	3
$p_{\max}$	80	169	80	80	80	80	80	80	80
$p_{\min}/p_{\max}$	0.50	0.85	0.50	0.50	0.88	0.50	0.50	0.50	0.50
NTU	9	30	1	9	81	2	-	-	-
Cr	0.25	0.99	1.00	0.25	0.10	0.19	0.25	0.19	0.94
η	0.85	0.90	0.80	0.85	0.85	0.85	0.85	0.85	0.85
$\chi(\%)$	54.7	78.5	51.0	58.1	68.5	50.1	56.4	65.0	61.40
Z (\$/kWh)	138	535	85	143	344	120	174	119	115

value $\eta_{\text{std}} = 85\,\%$ throughout the optimizations, and as a result, the heat transfer unit NTU becomes the sole dominant parameter in the efficiency cost trade-offs. Since there is no heat exchangers in the I-CAES-HR, the tradeoff between efficiency χ and unit cost Z is weak and its Pareto front becomes very narrow, as shown by the blue circles in Fig. 8.10. In I-CAES-HR, the only parameter that controls the efficiency cost trade-off is the heat capacity ratio C_r, as discussed in Section 6.5.2, and the gaps within its Pareto front is due to the variation of stage number N.

From Fig. 8.10, it can also be noted that the waste heat can significantly boost the system efficiency χ of I-CAES, thus making it the best CAES even if the temperature of waste heat T_{f} is not very high ($T_{\text{f}} = 95\,^{\circ}\text{C}$). However, this waste heat recovery can only be applied to pure I-CAES directly. This is because only the pure I-CAES has the externals heat exchangers that can be integrated into a fluid circulation system easily. Therefore, if free low-grade waste heat is available, the pure I-CAES might be a good choice.

Table 8.5 summarized the design variables and resulting performance for the nominal cases and for the six points labeled A through F in Fig. 8.10, each of these being at either the highest efficiency or the lowest cost for the three CAES systems. A pressure loss factor $f_p = 0.01$ is assumed for the isothermal compressor/expander because reciprocating devices are likely to be deployed which tend to have high valve losses. From Table 8.5, it can be noted that high values of $\eta_{\text{c/e}}$ (for A-CAES only) and NTU (for A-CAES and Pure I-CAES) correlate with efficient but expensive designs. It is also notable that A-CAES tends to select the highest value of C_r in order to minimize the heat transfer losses, whereas the Pure I-CAES opt for the lowest heat capacity ratio C_r and I-CAES-HR show a weak cost-efficiency trade-off with respect to C_r , as discussed in Section 6.5.2.

Table 8.6: Main results for the 65 % efficiency cases of I-CAES and A-CAES

	A-CAES	Pure I-CAES	I-CAES-HR
System Efficiency	64.9 %	64.7 %	65.0 %
Cost per kWh	132 $/kWh	126 $/kWh	119 $/kWh
Capital Cost	39.2 M$	33.6 M$	30.6 M$
Net Output Work	297 MWh	266 MWh	258 MWh
Net Input Work	457 MWh	411 MWh	397 MWh

From Table 8.5 it can also be noted that the optimal NTU of A-CAES tends to be lower than that of the I-CAES. This is because the stage number N_{stg} of A-CAES is higher, making it more sensitive to heat exchanger cost. Both Pure I-CAES and I-CAES-HR tend to minimize its cavern pressure p_{max}, which indicates the heat transfer loss is dominant in I-CAES and aligns with the analysis in Section 6.5.1. When C_r is low and the efficiency is high, the I-CAES-HR tends to minimize its stage number N_{stg} to reduce the pumping loss; whilst when C_r is high and the efficiency is low, the I-CAES-HR tends to maximize the stage number N_{stg} to prevent the water from boiling. For the Pure I-CAES, higher stage number N_{stg} means higher isothermal efficiency η_{iso} but also higher capital cost Z_{tot} (due to the external heat exchangers), so there is an efficiency-cost tradeoff with respect to N_{stg} for the Pure I-CAES.

Comparison of designs with fixed efficiency

The main results for optimized designs at a fixed system efficiency of 65 % are shown in Table 8.6. For this level of efficiency, the unit cost of all three CAES are similar, with I-CAES-HR slightly cheaper than the I-CAES which is then slightly cheaper than A-CAES. It is of interest to see how this has been achieved, and how the losses and costs are distributed amongst the different components. This information is provided in the histogram of Fig. 8.11.

For all three CAES, losses are dominated by the irreversibility in the compressors and expanders. Compression losses are slightly greater than expansion losses because it has been assumed that these processes have the same polytropic efficiency ($\eta_c = \eta_e = \eta$), which gives (for a given pressure ratio) $\Delta s_c / \Delta s_e = 1/\eta$. The next biggest loss for A-CAES is associated with the TES and is mainly due to irreversible heat exchange. This TES loss is also the second largest one for Pure I-CAES, however, it is caused by the heat leakage loss since thermal energy is not stored but simply dissipated in the Pure I-CAES. For I-CAES-HR, the TES loss is negligible because there is neither exchange nor leakage loss in its TES and the water is simply stored in it at near ambient temperature. Instead, the next biggest loss for I-CAES-HR is associated with the auxiliary heat exchanger, where the relatively hot compressed air at the outlet of isothermal compressor is cooled to ambient temperature to prevent from

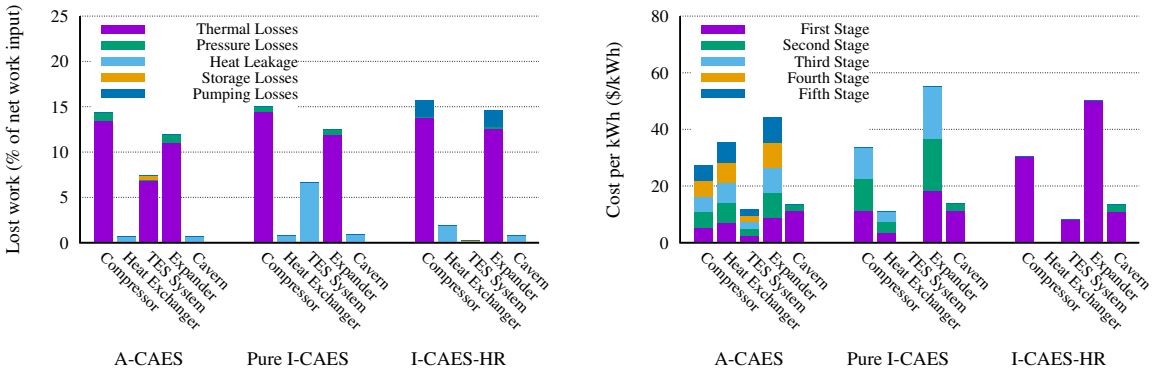

(a) Loss distributions

(b) Cost distributions

Figure 8.11: Loss and cost distributions for the three A-CAES when $\chi = 65\,\%$: (a) Loss distributions (b) Cost distributions

influencing next stages. In addition, there is a high pumping loss in I-CAES-HR since the ambient water need to be pumped to high pressures before being injected into the isothermal compressor/expander, and this work can hardly be recycled. Finally, the loss category labeled "cavern etc." includes direct cavern losses plus exergetic losses due to air being returned to atmosphere after discharge at a temperature above/below T_0. This category is slightly larger for pure I-CAES because during discharge, its exit temperature is below ambient due to the absence of TES system.

Fig. 8.11b shows that the isothermal compressor/expander cost forms a dominant part in the two I-CAES systems, whilst the heat exchanger cost of A-CAES is comparable to that of its compressor/expander. This is because for A-CAES, a large portion of its input exergy is stored in the TES and the effectiveness of its "main" heat exchangers is critical for its efficiency, whilst for Pure I-CAES, the heat exchange takes place within the isothermal compressor/expander and therefore, the expensive "main" heat exchangers are avoided. In addition, the "external" or "auxiliary" heat exchanger is just to dissipate the heat into the ambient so that cheap heat exchangers with lower C_r and NTU can be used. It is also notable that there is no TES cost in the Pure I-CAES because there is no thermal fluids and liquid tanks, and all of its "heat of compression" is simply dissipated into the environment. On the other hand, there is no heat exchanger cost in the I-CAES-HR because there is no "main" or "external" heat exchangers and all of its heat exchange takes place within the isothermal compressor/expander. It is worth mentioning that its TES cost is relatively low because the thermal fluid (ambient water) and the containment vessel (water tanks) are both very cheap.

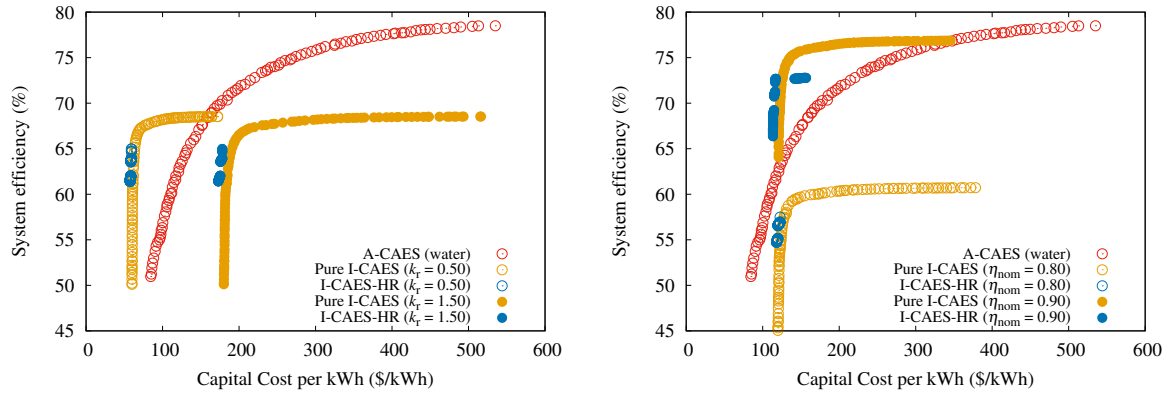

(a) Impacts of the cost equation constants k_r (b) Impacts of the nominal polytropic efficiency η_{std}

Figure 8.12: Pareto fronts of the I-CAES and A-CAES: (a) with different cost factor scenarios (k_r = 0.5 or 1.5 for optimistic or pessimistic cases) and (b) with different nominal efficiency scenarios (η_{std} = 0.90 or 0.80 for optimistic or pessimistic cases).

Sensitivity to standard efficiency η_{std} and cost factor k_r assumptions

The impacts of using optimistic ($k_r = 0.5$) and pessimistic ($k_r = 1.5$) cost factors on the Pareto fronts of Pure I-CAES and I-CAES-HR are shown in Fig. 8.12a, whilst the nominal case is shown in Fig. 8.10. Unsurprisingly, the cost factor k_r have no impact on the system efficiency χ, and the three groups of curves are simply shifted relative to one another along the cost axis. This serves to show that the unit storage costs might be expected to fall within the range of 70 to 180 \$/kWh for a 65 % efficient I-CAES systems with a nominal rating of 100 MW and four hours of capacity. It should be noted that even for A-CAES, there is still $\pm 30\,\%$ uncertainty about its capital cost, therefore, the performance of A-CAES and I-CAES are relatively similar. Additional information on k_r and more detailed analysis are required to determine which system is actually the best.

Fig. 8.12b shows the impacts of using pessimistic ($\eta_{\text{std}} = 0.8$) and optimistic ($\eta_{\text{std}} = 0.9$) nominal polytropic efficiency on the Pareto fronts of Pure I-CAES and I-CAES-HR. Similar to the cost factors k_r, the nominal polytropic efficiency η_{std} have little impact on the unit storage cost Z, and the three groups of curves are simply shifted relative to one another along the efficiency axis. This serves to show that the system efficiency χ might be expected to fall within the range of 58 to 75 % for a 125 \$/kWh I-CAES systems with a nominal rating of 100 MW and four hours of capacity. Therefore, it can be noted that the performance of I-CAES is highly dependent on the assumed nominal polytropic efficiency η_{std} and the cost factors k_r, and it is critical to make an accurate estimate of their values before making any comparison.

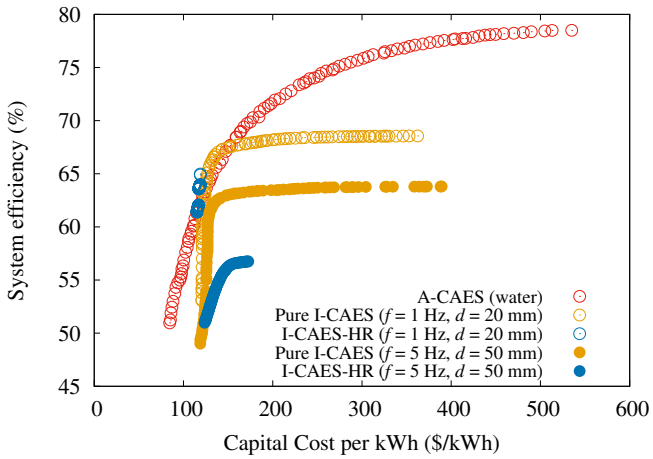

Figure 8.13: Impacts of the system frequency f and droplet diameter d

Sensitivity to system frequency f and droplet diameter d assumptions

From Section 6.4, it has been proved that the system frequency f and the square of droplet diameter d^2 have the same effect on the isothermal efficiency η_{iso}, and this combination of $d^2 f$ (or $\dot{p}\tau$) determines the temperature difference between air and water. In the previous analysis of Section 8.3.3, the system frequency f and droplet diameter d are fixed at 1 Hz and 20 μm respectively, so that $\dot{p}\tau = 0.00526$ and η_{th} is very close to 100 %, as shown in Fig. 6.7b. In this section, the impact of frequency f and droplet diameter d on the system efficiency χ will be examined. Since χ is a function of $\dot{p}\tau$, only one additional case is shown in Fig. 8.13, with f and d fixed at 5 Hz and 50 μm respectively, so that $\dot{p}\tau = 0.1645$.

From Fig. 8.13, it can be noted that increasing $\dot{p}\tau$ has a negative effect on the system efficiency χ of both Pure I-CAES and I-CAES-HR, with roughly 5 % reduction for Pure I-CAES and 10 % for I-CAES-HR. The latter is more sensitive to $\dot{p}\tau$ because the poor heat transfer at large $\dot{p}\tau$ makes it difficult to store and recycle any thermal exergy, which renders I-CAES-HR more similar to Pure I-CAES, where a large stage number N_{stg} is preferred. Meanwhile, the pumping loss of I-CAES-HR increases with the stage number N_{stg}, which results in a large reduction in its system efficiency χ, as shown in Fig. 8.13. The wider selection range of I-CAES-HR at large $\dot{p}\tau$ is also due to its large stage number N_{stg}.

It can be concluded from Fig. 8.13 that the system efficiency χ of I-CAES is also very sensitive to the assumed system frequency f and droplet diameter d, and it is essential to make an accurate estimate of their values before making any comparison. All other conditions being the same, it is likely that the A-CAES has better performance than the I-CAES, whilst pure I-CAES is superior to I-CAES-HR when $\dot{p}\tau$ is very large.

8.3.4 Comparison of LAES and PTES

Cost and efficiency trade-offs and general design trends

LAES and PTES are similar in several aspects. For example, they both store the electricity in the forms of temperature potential and do not rely on specific geography and geology condition. Therefore, multi-objective optimizations are carried out for LAES and PTES to compare their performance from a thermo-economic perspective, and the results are shown in Fig. 8.14. The PTES (Optimistic) refers to the PTES with helium as the working fluid, with pressurization ($p_{\max} = 500\,\text{bar}$), and its compressors/expanders able to be switched freely between different modes and reused for discharge. Therefore, the PTES (Optimistic) is essentially the Baseline PTES is Section 8.3.2. On the other hand, the PTES (Pessimistic) refers to the PTES with air as the working fluid, without pressurization ($p_{\min} = 1\,\text{bar}$), and with separate compressor/expander for charge and discharge. Therefore, the PTES (Pessimistic) refers to the Baseline PTES discussed in Chapter 3 and Chapter 4. These two scenarios are included because although single molecule gas (such as helium) is generally considered to enjoy better thermo-economic performance than the air, the cost equations of compressor/expander with non-conventional working fluid, such as helium, may not have been validated with the cost data [111]. Therefore, they are subject to a high level of uncertainty. Meanwhile, it is generally believed that more stages are required to compress helium due to its high heat capacity, which may actually increase the capital cost. The same reason applies to the pressurization and compressor/expander re-usage. It is still uncertain how much cost reduction will pressurization bring to the compressor/expander and what the maximum allowable pressure $p_{\max}$ can be, and although compressor/expander re-usage has been proposed by Isentropic Ltd. [19], none of these novel devices are available off the shelf, and PTES with conventional devices are still developed by Saipem Ltd. [60]. Therefore, two scenarios are provided to demonstrate the uncertainty with PTES costing.

From Fig. 8.14, it can be noted that at around 60 % system efficiency, the PTES (Optimistic) is superior to the LAES (Liquid TES), which is then superior to PTES (Pessimistic). This means the above assumptions on PTES have a significant impact on its cost, and the potential of cost reduction is large for conventional PTES. It can also be noted that the PTES (Optimistic) has much narrower range of selection than the other two systems, and the LAES (Liquid TES) can reach higher system efficiency than the PTES. This is probably because the Rankine cycle is employed in the LAES whilst the Brayton cycle is used in the PTES, which makes the LAES less sensitive to the compressor/expander losses due to the large work ratio of Rankine cycle. Although LAES may suffer from more serious pinch point problem, its effect can be minimized by maximizing the operating pressure p and the heat transfer unit NTU,

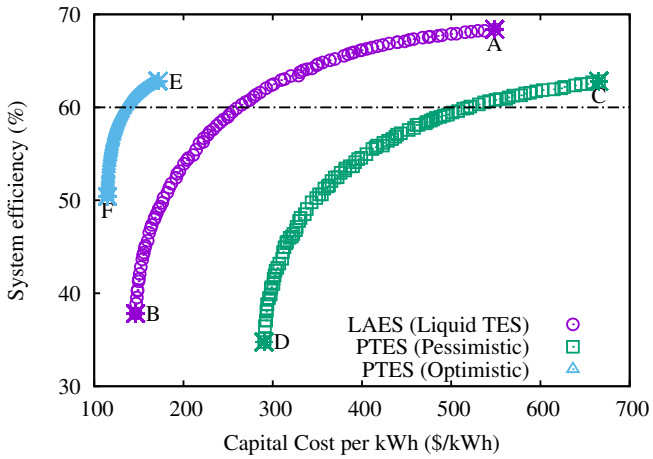

Figure 8.14: Pareto fronts of the LAES and PTES

Table 8.7: Design variables and main results for the nominal and optimal designs indicated in Fig. 8.14

	LAES (Liquid TES)			PTES (Pessimistic)			PTES (Optimistic)		
	Nom.	A	B	Nom.	C	D	Nom.	E	F
N_{hot}	2	2	2	1	1	1	1	1	1
N_{cold}	-	-	-	1	1	1	1	1	1
p_{max}	100	200	200	20	24.5	18.5	10	9.8	9.8
p_{min}	100	200	200	20	16.0	6.5	10	7.2	5.8
NTU	19	99	9	19	99	26	19	99	16
$\eta_{\text{c/e}}$	0.85	0.90	0.80	0.85	0.90	0.82	0.85	0.90	0.90
$\chi(\%)$	49.4	68.4	37.8	32.4	62.8	34.8	35.3	62.8	50.4
Z ($/kWh)	585	549	146	419	665	290	143	172	115

as shown in Table 8.7. Therefore, LAES can have similar thermo-economic performance with the PTES, and both of them have the potential to become the energy storage systems with high efficiency, low cost and high siting freedom.

Comparison of designs with fixed efficiency

The main results for optimized designs at a fixed roundtrip efficiency of 60 % are shown in Table 8.8, and the loss and cost distributions of these designs are shown in Figs 8.15a and 8.15b respectively. From Fig. 8.15a, it can be noted that although the system efficiencies are all 60 %, the loss distributions of LAES and PTES are quite different. For example, the losses of LAES are evenly distributed among the system components, whilst the losses of PTES are

Table 8.8: Main results for the 60 % efficiency cases of LAES and PTES

	LAES (Liquid TES)	PTES (Pessimistic)	PTES (Optimistic)
System Efficiency	60.3 %	60.1 %	60.1 %
Cost per kWh	265 $/kWh	563 $/kWh	143 $/kWh
Capital Cost	91 M$	165 M$	41 M$
Net Output Work	566 MWh	486 MWh	482 MWh
Net Input Work	341 MWh	292 MWh	290 MWh

centered on the compressors/expanders and auxiliary devices. This means the PTES is very sensitive to the compressor/expander losses due to its low work ratio, and significant amount of heat is dissipated through the auxiliary heat exchangers due to the system irreversibilities. It can also be noted that the loss distributions of PTES (Pessimistic) and PTES (Optimistic) are relatively similar, which means the change of cost equations has little impact on the system losses. The pressure losses of PTES tend to be higher than that of LAES, mainly because of the low pressure of its cold reservoir. Therefore, pressurization can help reduce the pressure loss of PTES to some extend. The LAES, on the other hand, is mainly operated at high pressure and low temperature region, which means its pressure loss is negligible.

From Fig. 8.15b, it can be noted that the cost of LAES is within the range of the two scenarios of PTES, and the costs of LAES are evenly distributed among the various components. For the unpressurized PTES, compressors and expanders are the most expensive components because the PTES is sensitive to the polytropic efficiency η whilst the cost increases rapidly with η. However, the compressor/expander cost of the pressurized PTES is almost zero, mainly because the pressurization can significantly reduce the volumetric flowrate of the compressor/expander and thus their size and cost. As a result, the heat exchange and TES cost become the dominant cost, which is comparable to that of the LAES. The auxiliary cost mainly includes the cost of cryogenic tank, cryogenic pump/expander and auxiliary heat exchanger for flash-gas recuperation, and therefore, it is absent in the PTES systems.

8.3.5 Comparison of all technologies considered

The Pareto fronts of the four thermal-mechanical energy storage systems (A-CAES, PTES, I-CAES and LAES) are shown in Fig. 8.16. Only some of the representatives are shown here to avoid over-crowding. From Fig. 8.16, it can be noted that of all the systems discussed, the Underwater CAES and the Hybrid CAES seem to have the best thermal-economic performance. This is because the Underwater CAES employs an isobaric air reservoir, which has higher energy density and lower volume and cost. The Hybrid CAES combines the merits

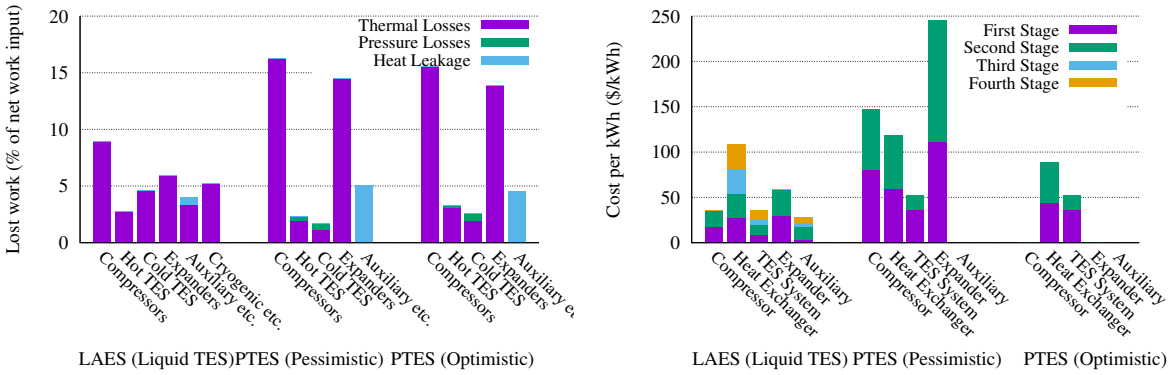

(a) Loss distributions

(b) Cost distributions

Figure 8.15: Loss and cost distributions for the three LAES when $\chi = 60\,\%$: (a) Loss distributions (b) Cost distributions

of low-pressure solid TES and high-pressure liquid TES, and therefore, it tends to be more efficient and cheaper than the Liquid CAES. However, it should be noted that both Underwater and Hybrid CAES are reliant on specific geology and geographic conditions, and their thermal-economic performances are subject to the assumptions made on their cost equations.

Although the I-CAES has similar thermo-economic performance with the A-CAES with ambient water as the thermal fluid. After replacing the ambient water with mineral oil, it seems that the Liquid A-CAES tends to have higher system efficiency and similar unit storage cost. However, this conclusion is based upon the assumption that the polytropic efficiency of an isothermal compressor/expander is fixed at 85 %. After increasing the nominal polytropic efficiency to 90 %, the I-CAES still enjoys comparable performance with the A-CAES. It is reported that some novel isothermal compressors/expanders, such as liquid piston, tend to have very higher polytropic efficiency [6, 90]. As a result, the I-CAES still remains an attractive option as long as novel efficient isothermal compressor/expanders can be invented. Moreover, the system efficiency of Pure I-CAES can be further enhanced with waste heat (or solar heat) integration, as discussed in Section 8.3.3.

Both LAES and PTES enjoy full siting freedom and their thermo-economic performance are also similar. From Fig. 8.16, it seems that the pressurization can significantly reduce the unit storage cost of PTES, thereby making it superior to the LAES and comparable to the A-CAES in terms of unit storage cost. Of course this conclusion is at the mercy of the assumptions on the impacts of pressurization on the cost equations. It is also notable that a system efficiency of 50 - 60 % is typical for the PTES and LAES, and the LAES can achieve slightly higher efficiency than the PTES. On the other hand, a system efficiency of 70 - 80 % is typical for the A-CAES, and the system efficiency of I-CAES tends to be in the middle of

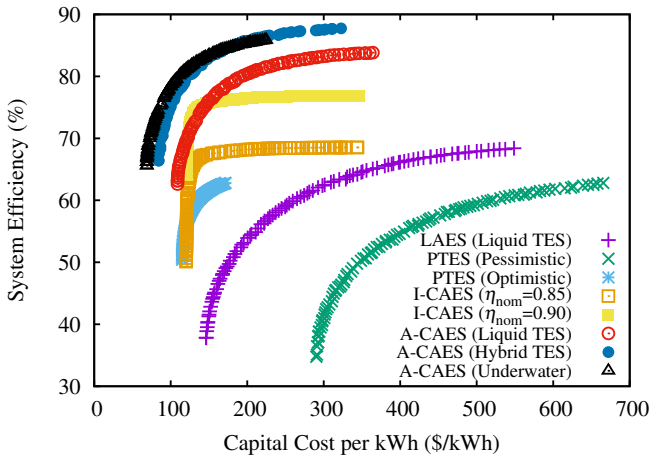

Figure 8.16: Pareto fronts of the representative energy storage systems

Table 8.9: The efficiency, unit cost and energy density of the representative energy storage systems

	Efficiency [%]	Unit Cost [$/kWh]	Energy Density [MJ/m^3]
A-CAES (Liquid)	70 - 80	123 - 194	~27
A-CAES (Hybrid)	70 - 80	88 - 122	~8
PTES (Optimistic)	50 - 60	115 - 145	~200
PTES (Pessimistic)	50 - 60	350 - 565	~200
I-CAES (η_{std}=0.85 -0.90, k_r=1.0-1.5)	64 - 72	138 - 225	~12
LAES (Liquid)	50 - 60	180 - 270	~150

those of the PTES and A-CAES. In addition, the unit storage cost of an A-CAES also tends to be lower than that of LAES and PTES even with pressurization, which makes it very difficult for PTES and LAES to beat A-CAES in terms of thermal-economic performance. However, in places where A-CAES and I-CAES are unfeasible, the PTES or LAES remains an attractive option.

Other results on the system efficiency, unit cost and energy density of the four representative energy storage systems can be found in Table 8.9. It can be noted that the energy density of the PTES and LAES tends to be an order of magnitude higher than that of the A-CAES and I-CAES. The low energy density of A-CAES and I-CAES is mainly caused by the large volume of cavern which is further determined by the maximum pressure p_{max} and variation factor p_{min}/p_{max}. After optimization, the maximum pressure p_{max} of Hybrid A-CAES is lower than that of Liquid A-CAES, therefore, its energy density is also much lower.

8.4 Summary

In this chapter, stochastic optimization algorithms are introduced and the working principles of multi-objective genetic algorithm are explained in detail. The objectives, boundaries and constraints of optimization are introduced for each system, and then the thermo-economic optimizations are carried out individually. The optimization results are placed together and compared with each other. Loss and cost distributions are provided for some representative cases and the reasons for their differences are explained. The impacts of some undecided factors, such as the cost assumptions and stored energy-to-power ratio, on the optimization results are also studied. From this chapter, it can be concluded that:

1. There are rapidly diminishing returns at the extremes of low cost and high efficiency (i.e., the Pareto fronts become vertical and horizontal respectively) such that the cost-efficiency trade off is most pronounced in the intermediate range, typically with χ around 80 % for CAES and 60 % for LAES and PTES. The main factors controlling the cost-efficiency tradeoff are the polytropic efficiency η of compressors and turbines, NTU of the heat exchangers (for systems with liquid TES), the reservoir "utilization factor" Π and reservoir aspect ratio L/D (for systems with solid TES).

2. The Hybrid A-CAES demonstrates a lower cost than the other two A-CAES for a given efficiency (or higher efficiency for a given cost). Although this conclusion might be affected by different cost assumptions, the margin is reasonably significant - i.e., typically 15 to 25 % lower cost at fixed χ. The main reason for this advantage is that solid TES is cheap when operated at lower pressure, whereas at high pressure it is much more expensive than liquid TES.

3. Mineral oil was found to be the best thermal fluid for Liquid A-CAES due to its relative high allowable temperature and low unit cost. Helium seemed to be the best working fluid for the PTES. The unit storage cost decreases monotonically with the discharge duration τ_{dis}, which means longer discharge time or higher energy-to-power ratio W_{dis}/P leads to lower unit storage cost.

4. The Baseline PTES has the best thermo-economic performance at low-cost region, whilst the Recuperated PTES has the best performance at at high-efficiency region. With pressurization, the PTES can achieve similar unit storage cost as the A-CAES, but hardly the same efficiency as long as the same system components are deployed. With recuperation, the system efficiency of A-CAES cannot be enhanced but the unit cost will increase and therefore, recuperation should be avoided in A-CAES.

5. The thermal-economic performance of I-CAES is highly dependent on the assumptions of nominal polytropic efficiency η_{std}, cost factor k_r and the combination $\dot{p}\tau$, which is then a function of droplet diameter d and system efficiency f, and it is essential to make an accurate estimate of all these values before making any reasonable comparison. For the Pure I-CAES, there is a clear tradeoff between efficiency and cost whilst for the I-CAES-HR, this tradeoff is much weaker due to its absence of heat exchangers. If the waste heat or solar energy is available, the efficiency of Pure I-CAES can be significantly enhanced even if its temperature is relatively low.

6. The thermo-economic performance of LAES and PTES are relatively similar. Pressurization can significantly reduce the capital cost of PTES and makes it superior to LAES and comparable to A-CAES in terms of cost. The LAES can achieve slightly higher system efficiency than the PTES due to the Rankine cycle it employed.

Chapter 9

Conclusions and Suggestions for Future Work

9.1 Conclusions of this thesis

In this thesis, different thermo-mechanical EES technologies are introduced and reviewed. Parametric study and loss/cost distribution analysis are carried out for each individual technology. Important components and their influence on system performance are studied separately and analyzed in detail. Thermo-economic optimizations are introduced and applied to each variant of EES system, and the optimization results are compared with each other. Through this comparative study, some important conclusions are obtained and summarized in later part of this section.

In Chapter 1, the general background to EES technologies are introduced and the outline description of various thermo-mechanical energy storage systems are provided. The motivation, scope and contribution of this comparative study are also clarified in this chapter.

In Chapter 2, the contribution of EES technologies to the current energy systems are reviewed and emphasized. Then the various thermo-mechanical energy storage systems are explained and reviewed individually. Finally, the methods for cost estimation and thermo-economic optimization are also reviewed.

In Chapter 3, a simple analytical model has been built for baseline A-CAES and PTES respectively and these two systems are compared from an analytical perspective. The expression of system efficiency, energy distribution and energy density are derived and their sensitivity to various parameters are also studied. Finally, a simple numerical model is introduced to support the analytical model.

In Chapter 4, a detailed numerical model with due consideration for both thermodynamic

and economic factors has been developed for each system component. Different variants of PTES are introduced and numerical models are built for each of them. Then parametric study and loss/cost distribution analysis are conducted for the PTES variants, and the reasons for their difference in thermo-economic performance are explained in detail.

In Chapter 5, detailed analytical, numerical and economic models have been developed for various types of air reservoirs, and then integrated to the A-CAES systems. The impact of various air reservoir parameters on the system performance of A-CAES are analyzed in detail. A more realistic case study based on Huntorf CAES cavern is also carried out. Finally, a hybrid A-CAES with low-pressure solid TES and high-pressure liquid TES is proposed and compared with the other A-CAES with just liquid or just solid TES. A combination of parametric study and loss/cost distribution analysis has been used to undertake this comparison.

In Chapter 6, a simple and general thermo-economic model has been built for the isothermal compressor/expander and I-CAES. The expressions for isothermal efficiency, aerodynamic and thermodynamic loss are derived and validated with more accurate results from the literature. Finally, parametric study and loss/cost analysis are conducted for both pure I-CAES and I-CAES-HR, and their results are compared with the A-CAES with ambient water as liquid TES.

In Chapter 7, a simple and efficient LAES with both "hot" and "cold" thermal energy recovery is proposed and the requirements for its stable operation is studied in detail. Both solid and liquid TES are used as the cold TES, and their thermo-economic performance are compared with each other. Unique phenomena such as pinch point problem and thermal front management are discovered and studied separately. Parametric study and loss/cost analysis are also carried out for solid and liquid LAES and their merits and weakness are revealed and compared. Finally, a combined cycle for overcoming the weakness of LAES is proposed and its thermo-economic performance is compared to LAES and PTES.

In Chapter 8, different algorithms for stochastic optimization are introduced and the working principles of multi-objective genetic algorithm are explained. The objectives, boundaries and constraints of optimization are introduced and the thermo-economic optimizations are conducted for each individual system. Finally, the optimization results are compared with each other, and the impacts of some undecided factors (e.g., the cost factor k_r and energy-to-power ratio W_{dis}/P) are also studied.

Therefore, it can be concluded from this thesis that:

1. Compared with the CAES, PTES is generally more sensitive to various losses and has lower efficiency. For the baseline PTES, its efficiency increases monotonically with the temperature ratio τ, whilst for the baseline CAES, it depends on the tradeoff between different losses. With τ increasing, more energy will be stored in the hot TES for both

CAES and PTES, and their energy densities also increase monotonically. However, the energy density of PTES tends to be an order of magnitude higher than that of A-CAES.

2. Of all PTES variants considered, the baseline PTES is most sensitive to the temperature ratio τ and least sensitive to the pressure loss f_p. It also has higher freedom than other PTES by allowing independent temperature ratios for charge and discharge. The precooled PTES is most sensitive to heat exchanger effectiveness ε and least sensitive to the polytropic efficiency η; whilst the preheated PTES is the opposite, being most sensitive to η and least sensitive to ε. In addition, the precooled PTES has the highest auxiliary losses, the recuperated PTES has the highest TES losses and the preheated PTES has a decreasing system efficiency χ with τ increasing, which is different from all other PTES. With the same ε and η, recuperated PTES usually has the highest χ but also the highest cost.

3. Cavern parameters may affect system performance through "direct" cavern losses and "indirect" losses of other components. For example, increasing the maximum pressure $p_{\max}$ will increase the thermodynamic losses and reduce the mechanical losses, whilst decreasing the fluctuation factor α will increase the TES mixing loss and system exit loss. As for the "direct" cavern losses, they are determined by the coupled effects of α and λ. As the cavern insulation factor λ increases, the cavern storage and thermodynamic losses decrease monotonically, whilst the heat leakage loss increases first and decreases later. For the A-CAES with liquid TES, the NTU of the heat exchangers controls the cost-efficiency trade-off; whilst for the A-CAES with solid TES, the reservoir "utilization factor" Π and aspect ratio L/D fulfill the same function; and the polytropic efficiency of compressors and turbines are important for any A-CAES. It is also found that the hybrid A-CAES tends to be cheaper than the A-CAES with only liquid or only solid TES.

4. The isothermal efficiency η_{iso} of an isothermal compressor/expander is determined by three factors, namely the polytropic efficiency η_{std}, heat capacity ratio C_r and the combination $\dot{p}\tau$, which corresponds to the aerodynamic loss, storage loss and thermodynamic losses respectively. The combination $\dot{p}\tau$ is further determined by the system frequency f, droplet diameter d and velocity u. If $u = 0$, then f and d^2 have the same effect on $\dot{p}\tau$ and η_{iso}. As $\dot{p}\tau$ increases, the thermodynamic losses increases first and decreases later, resulting in a peak. If $\dot{p}\tau \to 0$, then both the temperature difference and thermodynamic loss will disappear. If $C_r \to 0$, then both the temperature variation and storage loss (which is essentially the thermal energy loss) will disappear. If $\eta_{\text{std}} \to 1$, then the aerodynamic loss will also disappear. An ideal isothermal process requires all of the

three conditions to be met. In I-CAES, it is found that the thermal losses of isothermal compressor/expander are always dominant, therefore, a low maximum pressure $p_{\max}$ is preferred for I-CAES. It is also found that the the pumping loss of I-CAES-HR and heat exchanger cost of Pure I-CAES tend to prevent the I-CAES from having many stages.

5. The pinch point problem and thermal front management are respectively the major challenges for the liquid and solid TES of LAES. The liquid TES tends to have constant heat capacity but a narrow temperature range; whilst the solid TES tends to have a wide temperature range but a varying heat capacity. In addition, the liquid TES can be pressurized easily but becomes expensive when the required effectiveness is high; whilst the solid TES is efficient but becomes expensive at high pressures. As a result, it is found that solid LAES prefers low pressure whilst the liquid LAES prefers high pressure. It is also found that the efficiency of cryogenic expander significantly affects the system performance whilst its capital cost is relatively low. Finally, a combined cycle of LAES and PTES is studied and it can achieve higher energy density and avoid the two-phase working condition and flash-gas challenge.

6. There are rapidly diminishing returns at the extremes of low cost and high efficiency (i.e., the Pareto fronts become vertical and horizontal respectively) such that the cost-efficiency trade off is most pronounced in the intermediate range, typically with χ around 80 % for A-CAES and 60 % for LAES and PTES. With pressurization, the unit cost of PTES can be significantly reduced, making it superior to LAES and comparable to A-CAES. PTES (and LAES) can hardly be as efficient as A-CAES, as long as the same components are employed, but they both enjoys higher energy density and more siting freedom. The unit cost of A-CAES can be further decreased through the use of hybrid TES and underwater air accumulators. The performance of I-CAES depends on the assumptions of polytropic efficiency η_{std}, cost factor k_r and the combination $\dot{p}\tau$, and it is essential to make an accurate estimate for all of these before making any reasonable comparison.

9.2 Suggestions for future work

Although some preliminary results and conclusions have been obtained in this study, a thorough and rigorous comparison of all variants of EES technologies requires a number of challenges to be addressed. Future works are necessary to better understand the advantages and disadvantages of each EES technology and devise novel EES systems that combine the merits of existing ones. The suggestions for future work are summarized as follows:

1. More rigorous comparisons on a level playing field should be conducted. The assumptions of the thermo-economic models should be justified and the uncertainties of the optimization results should be estimated.

2. Dynamic simulations should be carried out to study the off-design behavior of each energy storage system. The starting process and varying operating conditions of each system should be analyzed in more detailed manner.

3. The mechanism of different types of losses and their varying trends should be studied in details. For example, the mechanical losses caused by viscosity and the thermodynamic losses caused by irreversible heat transfer have revealed opposite trends with pressure ratio, and more fundamental research are required to unveil the underlying reasons for this difference.

4. In-depth comparative studies of the regenerative and recuperative heat exchangers are necessary to reveal their fundamental differences. For example, the packed bed thermal reservoir and counterflow concentric-tube heat exchanger are typical regenerative and recuperative heat exchangers respectively, and their differences in thermo-economic performance are stressed several times in this thesis. However, the fundamental reason for their difference remains unclear.

5. More rigorous studies should be conducted for the economic models. For example, more cost data should be collected and more quantitative methods, such as hypothesis testing and regression analysis, should be employed to develop the cost equations. The confidence intervals of the cost estimates should also be provided.

6. Exergoeconomic analysis, which assigns a cost for each exergy flow, should be employed for the comparative study, and the comparison could be extended to include the electrical and chemical energy storage systems as a result.

7. Axial conduction, heat leakage and reservoir segmentation should be added to the thermal reservoir model and validated with the experiential data. More detailed numerical models should be developed for the heat exchanger to relate the heat transfer loss and pressure loss to the capital cost.

8. Numerical models for indirect contact thermal reservoir should be developed and incorporated into the Rankine-cycle PTES program. Thermo-economic analysis and optimization should be carried out and the optimization results compared with other EES technologies.

9. More detailed and accurate numerical models should be developed for the isothermal compressor/expander which takes into account of the mass and heat transfer simultaneously and used to validated the simple model in this thesis. The expression of $\dot{p}$ and τ should be derived for this general case.

10. Novel I-CAES based on latent heat transfer (e.g. vapour injection and condensation) should be proposed and compared with the I-CAES based on sensible heat transfer. The impacts of different thermal fluids on the thermo-economic performance should also be studied.

11. Mass transfer models should be developed for the packed bed thermal reservoir and applied to some special combined cycles. For example, Rankine-cycle PTES with CO_2 as the working fluid may also be used for Supercritical Fluid Extraction (SFE) and packed bed reactor will become the central component for this combined cycle.

Bibliography

[1] Gridwatch. G.B. National Grid Status. https://www.gridwatch.templar.co.uk/, 2018. [Online; accessed 1-September-2018].

[2] Alexander J. White. A exergetic analysis of cavern-related phenomena for CAES, 12-14 July 2017. Offshore Energy and Storage Symposium 2017.

[3] Haisheng Chen, Chunqing Tan, Jia Liu, and Yujie Xu. Energy storage system using supercritical air, December 22 2015. US Patent 9,217,423.

[4] Robert B. Schainker and Abhi Rao. Compressed Air Energy Storage (CAES) scoping for California, USA. Report CEC-500-2008-069, California Energy Commission, 2008.

[5] T McBride, A Bell, and D Kepshire. ICAES innovation: foam-based heat exchange. *Seabrook, TX, USA*, 2013.

[6] Chao Qin and Eric Loth. Liquid piston compression efficiency with droplet heat transfer. *Applied Energy*, 114:539–550, 2014.

[7] Pau Farres-Antunez, Haobai Xue, and Alexander J White. Thermodynamic analysis and optimisation of a combined liquid air and pumped thermal energy storage cycle. *Journal of Energy Storage*, 18:90–102, 2018.

[8] Joshua McTigue. *Analysis and optimisation of thermal energy storage*. PhD thesis, Department of Engineering, University of Cambridge, 2016.

[9] Wolf-Dieter Steinmann. Thermo-mechanical concepts for bulk energy storage. *Renewable and Sustainable Energy Reviews*, 75:205–219, 2017.

[10] S Ushak, AG Fernández, and M Grageda. Using molten salts and other liquid sensible storage media in Thermal Energy Storage (TES) systems. *Advances in Thermal Energy Storage Systems: Methods and Applications, 1st ed.; Cabeza, LF, Ed*, pages 49–63, 2014.

[11] W-D Steinmann. Thermal energy storage systems for Concentrating Solar Power (CSP) technology. In *Advances in Thermal Energy Storage Systems*, pages 511–531. Elsevier, 2015.

[12] James Macnaghten. Commercial potential of different large scale thermal storage technologies under development globally, 8 June 2016. UK Energy Storage Conference 2016.

[13] Michael E Van Valkenburg, Robert L Vaughn, Margaret Williams, and John S Wilkes. Thermochemistry of ionic liquid heat-transfer fluids. *Thermochimica Acta*, 425(1):181–188, 2005.

[14] Haisheng Chen, Thang Ngoc Cong, Wei Yang, Chunqing Tan, Yongliang Li, and Yulong Ding. Progress in electrical energy storage system: A critical review. *Progress in Natural Science*, 19(3):291–312, 2009.

[15] Xing Luo, Jihong Wang, Mark Dooner, and Jonathan Clarke. Overview of current development in electrical energy storage technologies and the application potential in power system operation. *Applied energy*, 137:511–536, 2015.

[16] David MacKay. *Sustainable energy - without the hot air*. UIT Cambridge, 2009.

[17] Marcus Budt, Daniel Wolf, Roland Span, and Jinyue Yan. A review on compressed air energy storage: Basic principles, past milestones and recent developments. *Applied Energy*, 170:250–268, 2016.

[18] Alexander White, Geoff Parks, and Christos N Markides. Thermodynamic analysis of pumped thermal electricity storage. *Applied Thermal Engineering*, 53(2):291–298, 2013.

[19] Jonathan Howes. Concept and development of a pumped heat electricity storage device. *Proceedings of the IEEE*, 100(2):493–503, 2012.

[20] Jonathan Sebastian Howes and James MacNaghten. Energy storage, February 25 2014. US Patent 8,656,712.

[21] J Ruer. Installation and methods for storing and recovering electric energy. Technical report, WO/2008/148962, 12-Dec-2008.

[22] Hemrle Jaroslav, Mercangoez Mehmet, Kaufmann Lilian, and Ohler Christian. Thermoelectric energy storage based on transcritical CO2 cycle, 24-25 May 2011. Supercritical CO2 Power Cycle Symposium 2011.

[23] MJ Hobson. Conceptual design and engineering studies of adiabatic Compressed Air Energy Storage (CAES) with thermal energy storage. Technical report, Pacific Northwest Lab., Richland, WA (USA); Acres American, Inc., Columbia, MD, 1981.

[24] Chris Bullough, Christoph Gatzen, Christoph Jakiel, Martin Koller, Andreas Nowi, and Stefan Zunft. Advanced Adiabatic Compressed Air Energy Storage for the integration of wind energy, 2004.

[25] RWE Power. ADELE - Adiabatic compressed air energy storage for electricity supply. Report, 2012.

[26] Daniel Wolf and Marcus Budt. LTA-CAES - A low-temperature approach to adiabatic compressed air energy storage. *Applied Energy*, 125:158–164, 2014.

[27] Lukas Geissbühler, Viola Becattini, Giw Zanganeh, Simone Zavattoni, Maurizio Barbato, Andreas Haselbacher, and Aldo Steinfeld. Pilot-scale demonstration of Advanced Adiabatic Compressed Air Energy Storage, Part 1: Plant description and tests with sensible thermal-energy storage. *Journal of Energy Storage*, 17:129–139, 2018.

[28] V Becattini, L Geissbühler, G Zanganeh, A Haselbacher, and A Steinfeld. Pilot-scale demonstration of Advanced Adiabatic Compressed Air Energy Storage, Part 2: Tests with combined sensible/latent thermal-energy storage. *Journal of Energy Storage*, 17:140–152, 2018.

[29] Andrew J Pimm, Seamus D Garvey, and Maxim de Jong. Design and testing of energy bags for underwater compressed air energy storage. *Energy*, 66:496–508, 2014.

[30] Brian C Cheung, Rupp Carriveau, and David SK Ting. Multi-objective optimization of an underwater compressed air energy storage system using genetic algorithm. *Energy*, 74:396–404, 2014.

[31] Hydrostor. World's first underwater air energy storage system launched. http://www.imeche.org/news/news-article/world's-first-underwater-compressed-air-energy-storage-system-launched, 2015. [Online; accessed 11-December-2015].

[32] Opubo N Igobo and Philip A Davies. Review of low-temperature vapour power cycle engines with quasi-isothermal expansion. *Energy*, 70:22–34, 2014.

[33] Troy O McBride, Benjamin R Bollinger, Michael Izenson, Weibo Chen, Patrick Magari, Benjamin Cameron, Robert Cook, and Horst Richter. Systems and methods for energy

storage and recovery using rapid isothermal gas expansion and compression, July 24 2012. US Patent 8,225,606.

[34] Karl E Stahlkopf, Stephen E Crane, Edwin P Berlin Jr, AmirHossein POURMOUSA ABKENAR, et al. Compressed Air Energy Storage system utilizing two-phase flow to facilitate heat exchange, May 7 2013. US Patent 8,436,489.

[35] Adewale Odukomaiya, Ayyoub M Momen, Ahmad Abu-Heiba, Kyle Gluesenkamp, Omar Abdelaziz, and Samuel Graham. Transient thermofluids analysis of a Ground-Level Integrated Diverse Energy Storage (GLIDES) system. In *ASME 2015 International Mechanical Engineering Congress and Exposition*, pages V06BT07A038–V06BT07A038. American Society of Mechanical Engineers, 2015.

[36] Adewale Odukomaiya, Ahmad Abu-Heiba, Kyle R Gluesenkamp, Omar Abdelaziz, Roderick K Jackson, Claus Daniel, Samuel Graham, and Ayyoub M Momen. Thermal analysis of near-isothermal compressed gas energy storage system. *Applied Energy*, 179:948–960, 2016.

[37] EM Smith. Storage of electrical energy using supercritical liquid air. *Proceedings of the Institution of Mechanical Engineers*, 191(1):289–298, 1977.

[38] Kenji Kishimoto, K Hasegawa, and T Asano. Development of generator of liquid air storage energy system. *Mitsubishi Juko Giho*, 35:60–63, 1998.

[39] Kooichi Chino and Hidefumi Araki. Evaluation of energy storage method using liquid air. *Heat Transfer - Asian Research*, 29(5):347–357, 2000.

[40] Robert Morgan, Stuart Nelmes, Emma Gibson, and Gareth Brett. Liquid air energy storage-analysis and first results from a pilot scale demonstration plant. *Applied Energy*, 137:845–853, 2015.

[41] Alexander J White. Loss analysis of thermal reservoirs for electrical energy storage schemes. *Applied Energy*, 88(11):4150–4159, 2011.

[42] Alexander J White, Joshua D McTigue, and Christos N Markides. Analysis and optimisation of packed-bed thermal reservoirs for electricity storage applications. *Proceedings of the Institution of Mechanical Engineers, Part A: Journal of Power and Energy*, 230(7):739–754, 2016.

[43] Joshua D McTigue, Alexander J White, and Christos N Markides. Parametric studies and optimisation of pumped thermal electricity storage. *Applied Energy*, 137:800–811, 2015.

[44] Joshua D McTigue and Alexander J White. Segmented packed beds for improved thermal energy storage performance. *IET Renewable Power Generation*, 2016.

[45] Kalyanmoy Deb, Amrit Pratap, Sameer Agarwal, and TAMT Meyarivan. A fast and elitist multiobjective genetic algorithm: NSGA-II. *IEEE transactions on evolutionary computation*, 6(2):182–197, 2002.

[46] Kalyanmoy Deb. Multi-objective NSGA-II code in C. https://www.iitk.ac.in/kangal, 2015. [Online; accessed 17-November-2015].

[47] Pau Farres-Antunez. Modelling of thermal energy storage systems for bulk electricity storage. First year report of PhD study, 28 August 2015.

[48] Pau Farres-Antunez. Thermodynamic strategies for Pumped Thermal Exergy Storage (PTES) with liquid reservoirs, 1 December 2016. UK Energy Storage Conference 2016.

[49] Pau Farres-Antunez. Optimization of heat exchangers operating with real fluids for thermo-mechanical energy storage. Offshore Energy and Storage Symposium 2016, 13-15 July 2016.

[50] Yuan Zhang, Ke Yang, Xuemei Li, and Jianzhong Xu. The thermodynamic effect of air storage chamber model on Advanced Adiabatic Compressed Air Energy Storage system. *Renewable Energy*, 57:469–478, 2013.

[51] Michael Money. Thermodynamic losses in Compressed Air and Pumped Thermal Energy Storage. Fourth-year undergraduate project, 30 May 2012.

[52] Haobai Xue and Alexander White. A comparative study of liquid, solid and hybrid adiabatic compressed air energy storage systems. *Journal of Energy Storage*, 18:349–359, 2018.

[53] C Bueno and Jose A Carta. Wind powered pumped hydro storage systems, a means of increasing the penetration of renewable energy in the Canary Islands. *Renewable and Sustainable Energy Reviews*, 10(4):312–340, 2006.

[54] Sam Koohi-Kamali, VV Tyagi, NA Rahim, NL Panwar, and H Mokhlis. Emergence of energy storage technologies as the solution for reliable operation of smart power systems: A review. *Renewable and Sustainable Energy Reviews*, 25:135–165, 2013.

[55] William F Pickard. The history, present state, and future prospects of underground pumped hydro for massive energy storage. *Proceedings of the IEEE*, 100(2):473–483, 2012.

[56] Nasim Uddin. Geotechnical issues in the creation of underground reservoirs for massive energy storage. *Proceedings of the IEEE*, 100(2):484–492, 2012.

[57] YM Kim, DG Shin, and D Favrat. Operating characteristics of constant-pressure Compressed Air Energy Storage (CAES) system combined with Pumped Hydro Storage based on energy and exergy analysis. *Energy*, 36(10):6220–6233, 2011.

[58] BBC Brown Boveri. Huntorf air storage gas turbine power plant. Technical Report D GK 90202 E, BBC Brown Boveri.

[59] Alexander White, Joshua McTigue, and Christos Markides. Wave propagation and thermodynamic losses in packed-bed thermal reservoirs for energy storage. *Applied Energy*, 130:648–657, 2014.

[60] Tristan Desrues, Jacques Ruer, Philippe Marty, and JF Fourmigué. A thermal energy storage process for large scale electric applications. *Applied Thermal Engineering*, 30(5):425–432, 2010.

[61] Fan Ni and Hugo S Caram. Analysis of Pumped Heat Electricity Storage process using exponential matrix solutions. *Applied Thermal Engineering*, 84:34–44, 2015.

[62] JD McTigue and Alexander John White. A comparison of radial-flow and axial-flow packed beds for thermal energy storage. *Applied Energy*, 2017.

[63] Mehmet Mercangöz, Jaroslav Hemrle, Lilian Kaufmann, Andreas Z'Graggen, and Christian Ohler. Electrothermal energy storage with transcritical CO2 cycles. *Energy*, 45(1):407–415, 2012.

[64] Matteo Morandin, Mehmet Mercangöz, Jaroslav Hemrle, François Maréchal, and Daniel Favrat. Thermoeconomic design optimization of a thermo-electric energy storage system based on transcritical CO2 cycles. *Energy*, 58:571–587, 2013.

[65] Miles Abarr, Brendan Geels, Jean Hertzberg, and Lupita D Montoya. Pumped thermal energy storage and bottoming system Part A: Concept and model. *Energy*, 120:320–331, 2017.

[66] Miles Abarr, Jean Hertzberg, and Lupita D Montoya. Pumped thermal energy storage and bottoming system Part B: Sensitivity analysis and baseline performance. *Energy*, 119:601–611, 2017.

[67] WD Steinmann. The CHEST (Compressed Heat Energy STorage) concept for facility scale thermo mechanical energy storage. *Energy*, 69:543–552, 2014.

[68] Axel Dietrich, Frank Dammel, and Peter Stephan. Exergoeconomic analysis of a Pumped Heat Electricity Storage system with concrete thermal energy storage. *International Journal of Thermodynamics*, 19(1):43–51, 2016.

[69] Ecofriend. Compressed air energy storage systems could be the next big thing in managing green energy. https://ecofriend.com/compressed-air-energy-storage-systems-could-be-the-next-big-thing-in-managing-green-energy.html, 2018. [Online; accessed 1-September-2018].

[70] Greenage. Compressed air energy storage. https://www.thegreenage.co.uk/tech/compressed-air-energy-storage/, 2018. [Online; accessed 1-September-2018].

[71] Fritz Crotogino, Klaus-Uwe Mohmeyer, and Roland Scharf. Huntorf CAES: More than 20 years of successful operation. *Orlando, Florida, USA*, 2001.

[72] Mandhapati Raju and Siddhartha Kumar Khaitan. Modeling and simulation of compressed air storage in caverns: a case study of the Huntorf plant. *Applied Energy*, 89(1):474–481, 2012.

[73] Giuseppe Grazzini and Adriano Milazzo. Thermodynamic analysis of CAES/TES systems for renewable energy plants. *Renewable Energy*, 33(9):1998–2006, 2008.

[74] Jinchao Liu, Xinjing Zhang, Yujie Xu, Zongyan Chen, Haisheng Chen, and Chunqing Tan. Economic analysis of using above ground gas storage devices for Compressed Air Energy Storage system. *Journal of Thermal Science*, 23(6):535–543, 2014.

[75] Edward Barbour, Dimitri Mignard, Yulong Ding, and Yongliang Li. Adiabatic compressed air energy storage with packed bed thermal energy storage. *Applied Energy*, 155:804–815, 2015.

[76] Hao Peng, Rui Li, Xiang Ling, and Huihua Dong. Modeling on heat storage performance of compressed air in a packed bed system. *Applied energy*, 160:1–9, 2015.

[77] Xing Luo, Jihong Wang, Christopher Krupke, Yue Wang, Yong Sheng, Jian Li, Yujie Xu, Dan Wang, Shihong Miao, and Haisheng Chen. Modelling study, efficiency analysis and optimisation of large-scale Adiabatic Compressed Air Energy Storage systems with low-temperature thermal storage. *Applied Energy*, 162:589–600, 2016.

[78] Francesco Buffa, Simon Kemble, Giampaolo Manfrida, and Adriano Milazzo. Exergy and exergoeconomic model of a ground-based CAES plant for peak-load energy production. *Energies*, 6(2):1050–1067, 2013.

[79] AJ White and AJ Meacock. An evaluation of the effects of water injection on compressor performance. In *ASME Turbo Expo 2003, collocated with the 2003 International Joint Power Generation Conference*, pages 181–189. American Society of Mechanical Engineers, 2003.

[80] AJ White. Thermodynamic analysis of the reverse Joule–Brayton cycle heat pump for domestic heating. *Applied Energy*, 86(11):2443–2450, 2009.

[81] Mahbod Heidari, Sylvain Lemofouet, and Alfred Rufer. On the strategies towards isothermal gas compression and expansion. 2014.

[82] Qun Zheng, Yufeng Sun, Shuying Li, and Yunhui Wang. Thermodynamic analyses of wet compression process in the compressor of gas turbine. In *ASME Turbo Expo 2002: Power for Land, Sea, and Air*, pages 487–496. American Society of Mechanical Engineers, 2002.

[83] Carl Knowlen, John Williams, AT Mattick, Helene Deparis, and A Hertzberg. Quasi-isothermal expansion engines for liquid nitrogen automotive propulsion. Technical report, SAE Technical Paper, 1997.

[84] AJ Meacock and AJ White. The effect of water injection on multispool gas turbine behavior. *Journal of engineering for gas turbines and power*, 128(1):97–102, 2006.

[85] AJ White and AJ Meacock. Wet compression analysis including velocity slip effects. *Journal of Engineering for Gas Turbines and Power*, 133(8):081701, 2011.

[86] Jason Hugenroth, James Braun, Eckhard Groll, and Galen King. Thermodynamic analysis of a liquid-flooded Ericsson cycle cooler. *International Journal of Refrigeration*, 30(7):1176–1186, 2007.

[87] Jason Hugenroth, James Braun, Eckhard Groll, and Galen King. Experimental investigation of a liquid-flooded Ericsson cycle cooler. *international journal of refrigeration*, 31(7):1241–1252, 2008.

[88] Michael W Coney, P Stephenson, A Malmgren, C Linnemann, RE Morgan, RA Richards, R Huxley, and H Abdallah. Development of a reciprocating compressor using water injection to achieve quasi-isothermal compression. 2002.

[89] MW Coney, C Linnemann, and HS Abdallah. A thermodynamic analysis of a novel high efficiency reciprocating internal combustion engine-the isoengine. *Energy*, 29(12-15):2585–2600, 2004.

[90] James D Van de Ven and Perry Y Li. Liquid piston gas compression. *Applied Energy*, 86(10):2183–2191, 2009.

[91] C Qin and E Loth. Simulation of spray direct injection for compressed air energy storage. *Applied Thermal Engineering*, 95:24–34, 2016.

[92] Benjamin R Bollinger. System and method for rapid isothermal gas expansion and compression for energy storage, 2010. US Patent 7,802,426.

[93] Bernd Ameel, Christophe T'Joen, Kathleen De Kerpel, Peter De Jaeger, Henk Huisseune, Marnix Van Belleghem, and Michel De Paepe. Thermodynamic analysis of energy storage with a liquid air Rankine cycle. *Applied Thermal Engineering*, 52(1):130–140, 2013.

[94] Huan Guo, Yujie Xu, Haisheng Chen, and Xuezhi Zhou. Thermodynamic characteristics of a novel supercritical compressed air energy storage system. *Energy Conversion and Management*, 115:167–177, 2016.

[95] Huan Guo, Yujie Xu, Haisheng Chen, Cong Guo, and Wei Qin. Thermodynamic analytical solution and exergy analysis for supercritical compressed air energy storage system. *Applied energy*, 199:96–106, 2017.

[96] Lei Chai, Jia Liu, Liang Wang, Lei Yue, Liang Yang, Yong Sheng, Haisheng Chen, and Chunqing Tan. Cryogenic energy storage characteristics of a packed bed at different pressures. *Applied Thermal Engineering*, 63(1):439–446, 2014.

[97] A Sciacovelli, A Vecchi, and Y Ding. Liquid Air Energy Storage (LAES) with packed bed cold thermal storage-from component to system level performance through dynamic modelling. *Applied Energy*, 190:84–98, 2017.

[98] Yongliang Li. *Cryogen based energy storage: process modelling and optimisation*. PhD thesis, The University of Leeds, 2011.

[99] Yongliang Li, Xiang Wang, and Yulong Ding. An optimal design methodology for large-scale gas liquefaction. *Applied energy*, 99:484–490, 2012.

[100] Yongliang Li, Xiang Wang, Yi Jin, and Yulong Ding. An integrated solar-cryogen hybrid power system. *Renewable energy*, 37(1):76–81, 2012.

[101] Yongliang Li, Hui Cao, Shuhao Wang, Yi Jin, Dacheng Li, Xiang Wang, and Yulong Ding. Load shifting of nuclear power plants using cryogenic energy storage technology. *Applied Energy*, 113:1710–1716, 2014.

[102] Giuseppe Leo Guizzi, Michele Manno, Ludovica Maria Tolomei, and Ruggero Maria Vitali. Thermodynamic analysis of a liquid air energy storage system. *Energy*, 93:1639–1647, 2015.

[103] Piotr Krawczyk, Lukasz Szablowski, Krzysztof Badyda, Sotirios Karellas, and Emmanuel Kakaras. Impact of selected parameters on performance of the adiabatic liquid air energy storage system. *Journal of Power Technologies*, 96(4):238–244, 2016.

[104] Bharath Kantharaj, Seamus Garvey, and Andrew Pimm. Compressed air energy storage with liquid air capacity extension. *Applied Energy*, 157:152–164, 2015.

[105] Bharath Kantharaj, Seamus Garvey, and Andrew Pimm. Thermodynamic analysis of a hybrid energy storage system based on compressed air and liquid air. *Sustainable Energy Technologies and Assessments*, 11:159–164, 2015.

[106] Antonio Valero, Miguel A Lozano, Luis Serra, George Tsatsaronis, Javier Pisa, Christos Frangopoulos, and Michael R von Spakovsky. CGAM problem: definition and conventional solution. *Energy*, 19(3):279–286, 1994.

[107] Randall W Whitesides. Process equipment cost estimating by ratio and proportion. *Course notes, PDH Course G*, 127, 2005.

[108] R Williams. Six-tenths factor aids in approximating costs. *Chemical Engineering*, 54(12):124–125, 1947.

[109] MA Tribe and RLW Alpine. Scale economies and the "0.6 rule". *Engineering Costs and Production Economics*, 10(1):271–278, 1986.

[110] James R Couper, W Roy Penney, and James R Fair. *Chemical Process Equipment-Selection and Design (Revised 2nd Edition)*. Gulf Professional Publishing, 2009.

[111] Alberto Traverso, Aristide F Massardo, Walter Cazzola, and Giovanni Lagorio. WIDGET-TEMP: a novel web-based approach for thermoeconomic analysis and optimization of conventional and innovative cycles. In *ASME Turbo Expo 2004: Power for Land, Sea, and Air*, pages 623–631. American Society of Mechanical Engineers, 2004.

[112] Leandro Galanti and Aristide F Massardo. Micro gas turbine thermodynamic and economic analysis up to 500 kWe size. *Applied Energy*, 88(12):4795–4802, 2011.

[113] Granta Design Ltd. Compressed air energy storage systems could be the next big thing in managing green energy. http://www.grantadesign.com/education/edupack/, 2018. [Online; accessed 1-September-2018].

[114] James Riley Couper. *Process engineering economics*. CRC Press, 2003.

[115] HP Loh, Jennifer Lyons, and Charles W White. Process equipment cost estimation. *National Energy Technology Center, Report No. DOE/NETL-2002/1169*, 2002.

[116] AF Massardo and M Scialò. Thermoeconomic analysis of gas turbine based cycles. *Journal of engineering for gas turbines and power*, 122(4):664–671, 2000.

[117] Andrea Toffolo and Andrea Lazzaretto. Evolutionary algorithms for multi-objective energetic and economic optimization in thermal system design. *Energy*, 27(6):549–567, 2002.

[118] Andrea Lazzaretto and Andrea Toffolo. Energy, economy and environment as objectives in multi-criterion optimization of thermal systems design. *Energy*, 29(8):1139–1157, 2004.

[119] JL Silveira and CE Tuna. Thermoeconomic analysis method for optimization of combined heat and power systems. Part I. *Progress in energy and Combustion Science*, 29(6):479–485, 2003.

[120] Geoff Parks. Notes on Practical Optimisation. Lecture Notes, University of Cambridge, Department of Engineering, 2014.

[121] Carlo A Borghi, Massimo Fabbri, and Pier Luigi Ribani. Design optimization of a microsuperconducting magnetic energy storage system. *IEEE transactions on magnetics*, 35(5):4275–4284, 1999.

[122] Pierfrancesco Palazzo. Thermal and mechanical aspect of entropy-exergy relationship. *International Journal of Energy and Environmental Engineering*, 3(1):4, 2012.

[123] Frank W Schmidt, A John Willmott, et al. *Thermal energy storage and regeneration*. Hemisphere Publishing Corporation Washington, 1981.

[124] J.A. Willmott. *Dynamics of Regenerative Heat Transfer*. Taylor & Francis, 2002.

[125] Richard G Holdich. *Fundamentals of particle technology*. Midland Information Technology and Publishing, 2002.

[126] Ramesh K Shah and Dusan P Sekulic. *Fundamentals of heat exchanger design*. John Wiley & Sons, 2003.

[127] Juan Carlos Ordóñez and Adrian Bejan. Entropy generation minimization in parallel-plates counterflow heat exchangers. *International Journal of Energy Research*, 24(10):843–864, 2000.

[128] Robert B Laughlin. Pumped thermal grid storage with heat exchange. *Journal of Renewable and Sustainable Energy*, 9(4):044103, 2017.

[129] Pierre Berest, Benoît Brouard, and JG Durup. Tightness tests in salt-cavern wells. *Oil & Gas Science and Technology*, 56(5):451–469, 2001.

[130] Alexander G. Fassbender. Compressed Air Energy Storage (CAES) - Past, present, and near future. Technical report, PE, Ecovia Corporation, 2013.

[131] Benjamin Bollinger. Demonstration of isothermal compressed air energy storage to support renewable energy production. Technical report, Sustainx, Incorporated, Seabrook, NH (United States), 2015.

[132] AJ White and AJ Meacock. An evaluation of the effects of water injection on compressor performance. *Journal of engineering for gas turbines and power*, 126(4):748–754, 2004.

[133] Xiaohui She, Xiaodong Peng, Binjian Nie, Guanghui Leng, Xiaosong Zhang, Likui Weng, Lige Tong, Lifang Zheng, Li Wang, and Yulong Ding. Enhancement of round trip efficiency of liquid air energy storage through effective utilization of heat of compression. *Applied Energy*, 206:1632–1642, 2017.

[134] YS Touloukian and EH Buyco. Thermophysical properties of matter - The TPRC Data Series. Volume 5. Specific heat - Nonmetallic solids. Technical report, Thermophysical and Electronic Properties Information Analysis Center Lafayette, 1970.

[135] YS Touloukian and T Makita. Thermophysical properties of matter - The TPRC Data Series. Volume 6. Specific Heat - Nonmetallic liquids and gases. Technical report, Thermophysical and Electronic Properties Information Analysis Center Lafayette, 1970.

[136] Edgar F Westrum Jr and Fredrik Grønvold. Magnetite (Fe3O4) heat capacity and thermodynamic properties from 5 to 350 K, low-temperature transition. *The Journal of Chemical Thermodynamics*, 1(6):543–557, 1969.

[137] Andrea Toffolo and Ernesto Benini. Genetic diversity as an objective in multi-objective evolutionary algorithms. *Evolutionary computation*, 11(2):151–167, 2003.

[138] Eckart Zitzler and Lothar Thiele. Multiobjective evolutionary algorithms: a comparative case study and the strength Pareto approach. *IEEE transactions on Evolutionary Computation*, 3(4):257–271, 1999.

[139] A Anzelius. Heating by means of percolating media. *J Mech Des*, 6:291–294, 1926.

Appendix A

Liquid TES systems

Compared with the packing materials of the solid TES, the thermal fluids of liquid TES generally has much narrower temperature range. Therefore, it is often necessary to operate several heat exchangers with different thermal fluids in series to cover the whole temperature range of liquid TES. For example, in the hot TES of liquid LAES, mineral oil and solar salts are often utilized together to cover the temperature range from ambient to 550 °C. If the inlet temperature of the hot TES system (and the heat exchanger network) is T_{in} ($T_{\mathrm{in}} > T_0$), and the temperature of the second stage (the stage with mineral oil as the thermal fluid) cold fluid tank is fixed at ambient value $T_{\mathrm{c2}} = T_0$, it will be of interest to figure out the temperature of the intermediate thermal fluid tanks, such as that of the first stage (the stage with solar salt as the thermal fluid) cold fluid tank T_{c1} and the second stage hot fluid tank T_{h2}. In fact, any large heat exchanger with heat transfer unit of $\mathrm{NTU_t} = 2\mathrm{NTU}$ can be viewed as two small heat exchanger with heat transfer unit of NTU operating in series. The thermal fluid of cold fluid tank at ambient temperature T_0 flows through the second stage heat exchanger into an intermediate tank at T_{m}, and immediately, it flows through the first stage heat exchanger into

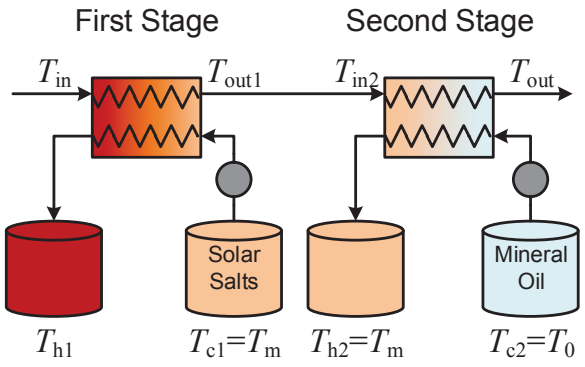

Figure A.1: Schematic diagram of a typical hot TES with two stages

the hot fluid tank. Therefore, the temperature of first stage cold tank T_{c1} and second stage hot tank T_{h2} should be equal for the heat exchanger network to be viewed as one large heat exchanger, which means: $T_{c1} = T_{h2} = T_m$. Then the outlet temperature of the first stage heat exchanger is:

$$T_{out1} = (1-\varepsilon)\, T_{in} + \varepsilon T_{c1} \tag{A.1}$$

Since the outlet of first stage heat exchanger and the inlet of second stage heat exchanger are directly connected, we have $T_{in2} = T_{out1}$. Then the temperature of the second stage hot fluid tank T_{h2} can be expressed as follows:

$$T_{h2} = \varepsilon T_{in2} + (1-\varepsilon)\, T_0 \tag{A.2}$$

By substituting Eq. (A.1) into Eq. (A.2) and solving for T_m, we can get:

$$T_m = \frac{\varepsilon}{1+\varepsilon} T_{in} + \frac{1}{1+\varepsilon} T_0 \tag{A.3}$$

From Eq. (A.3), it can be found that the intermediate temperature T_m is close to the arithmetic average of the inlet T_{in} and ambient temperature T_0, if the heat exchanger effectiveness ε is high. The outlet temperature of the second stage heat exchanger T_{out2} is also the outlet temperature of the hot TES system T_{out}, which is :

$$T_{out} = \frac{1-\varepsilon}{1+\varepsilon} T_{in} + \frac{2\varepsilon}{1+\varepsilon} T_0 \tag{A.4}$$

For a counterflow, concentric tube heat exchanger with $C_r = 1$, the heat exchanger effectiveness ε can be expressed as a simple function of heat transfer unit NTU, which is $\varepsilon = \mathrm{NTU}/(\mathrm{NTU}+1)$, then Eq. (A.4) can be further written as:

$$T_{out} = \frac{1}{2\mathrm{NTU}+1} T_{in} + \frac{2\mathrm{NTU}}{2\mathrm{NTU}+1} T_0 \tag{A.5}$$

It should be noted that for a larger heat exchanger with $\mathrm{NTU_t} = 2\mathrm{NTU}$, the coefficient of the latter part of Eq. (A.5) $2\mathrm{NTU}/(2\mathrm{NTU}+1)$ is essentially its heat exchanger effectiveness ε_t. Therefore, Eq. (A.5) eventually becomes $T_{out} = (1-\varepsilon_t)\, T_{in} + \varepsilon_t T_0$, which is the expression of the outlet temperature for a large heat exchanger with $\mathrm{NTU_t} = 2\mathrm{NTU}$ or $\varepsilon_t = 2\varepsilon/(1+\varepsilon)$. Here, it can be noted that as long as the temperature of the pairs of intermediate thermal fluid tanks is the same ($T_{c1} = T_{h2} = T_m$), how the heat exchanger network is arranged makes no difference to its equivalent heat exchanger effectiveness ε_t and capital cost (which is a function of $\mathrm{NTU_t}$).

The above analysis is very universal and independent of the specific characteristics of

certain thermal fluids, therefore, it is also applicable for TES system with different thermal fluids, such as the hot TES with solar salt and mineral oil. At the initial state of operation, mineral oil at T_0 and solar salt at T_m is prepared in advance and stored in the cold fluid tanks of their respective stages. After each cycle, the temperatures of thermal fluids tend to be higher than their initial values due to the thermal irreversibility and they have to be cooled back to T_m via an external heat exchanger. In the hot liquid TES, the working fluid can be viewed as ideal gas and the impact of heat capacity variation is negligible. Therefore, the intermediate temperature T_m can be easily determined via Eq. (A.3), which is essential for the cooling and the stable operation of hot liquid TES.

Appendix B

Numerical method

B.1 System design

In order to run the numerical model properly, the geometric parameters of each component must be set up at first. In this thesis, it is achieved through a trial-and-error method and the mass of working fluid m becomes the most important parameter. This is because the mass of all TES can be determined through the following equations.

$$m_i = \frac{m\bar{c}_p}{\bar{c}_i} \tag{B.1}$$

where $\bar{c}_p$ and $\bar{c}_i$ are the average heat capacities of the working fluid and TES materials respectively, and the latter is determined by:

$$\bar{c}_i = \frac{e_{\text{out}} - e_{\text{in}}}{T_{\text{out}} - T_{\text{in}}} \tag{B.2}$$

Similar equation can be derived for $\bar{c}_p$ by repacking the internal energy e in Eq. (B.2) with the enthalpy h.

In Eq. (B.2), the subscript in and out denote the inlet and outlet conditions respectively, and therefore, the temperature range of each component must be estimated at first. Take the hybrid A-CAES as an example, the pressure ratio β_i of each stage has been set up by Eqs. (5.1) and (5.2), so that the inlet temperature ratio of each stage can be estimated by:

$$\tau_i = \beta_i^{\phi_c} \tag{B.3}$$

where ϕ_c is the polytropic exponent of compressor which is the same with that in Eq. (4.18). The outlet temperature of each TES is approximately ambient during charge, therefore, the mass m_i and average heat capacity $\bar{c}_i$ of each TES can be estimated from Eqs. (B.1) and (B.2).

Besides, the exergy stored in each TES can also be estimated from the following equation:

$$\begin{aligned} B_i &= m_i \left[(e_i - e_0) - T_0 (s_i - s_0) \right] \\ &= m_i \bar{c}_i T_0 (\tau_i - 1 - \ln \tau_i) \end{aligned} \tag{B.4}$$

where e and s refer to the specific internal energy and entropy respectively; the subscript 0 denotes the ambient state.

In the hybrid A-CAES, all the working fluid is stored in (or released from) a cavern, and as a result, the following equation holds:

$$m = \frac{p_{\max} - p_{\min}}{R_g T_0} V = \frac{p_0 V}{R_g T_0} R (1 - \alpha) \tag{B.5}$$

where the cavern is assumed isochoric (with a volume of V) and isothermal (with a temperature of T_0). This assumption may lead to the underestimation of the cavern volume V if the cavern is not isothermal and therefore, in more accurate calculations, the volume V could be adjusted after initial design process.

The exergy of a closed system with a volume V can be written as:

$$\begin{aligned} B &= (U - U_0) - T_0 (S - S_0) + p_0 (V - V_0) \\ &= V \left(p \ln \frac{p}{p_0} - p + p_0 \right) \end{aligned} \tag{B.6}$$

and the exergy stored in an isothermal cavern of volume V is:

$$\begin{aligned} B_{\text{cave}} &= B_{\text{c}} - B_{\text{d}} \\ &= V \left(p_{\max} \ln \frac{p_{\max}}{p_0} - p_{\min} \ln \frac{p_{\min}}{p_0} - p_{\max} + p_{\min} \right) \end{aligned} \tag{B.7}$$

For the hybrid A-CAES, we have:

$$B_{\text{cave}} + \sum_{i=1}^{N} B_i = E \tag{B.8}$$

where E is the rated energy for all energy storage systems and $E = 400\,\text{MWh}$ in this thesis. By applying bisection method to Eq. (B.8), the mass of the working fluid m can be obtained and then the mass of all TES can be calculated through Eq. (B.1). After that, the geometric

parameters of each TES can be determined through the following equations:

$$V_i = \frac{m_i}{\rho_i \Pi} \tag{B.9}$$

$$D_i = \sqrt[3]{\frac{4V_i}{\pi\,(L/D)}} \tag{B.10}$$

where Π is the utilization factor and L/D is the aspect ratio. For liquid TES, both Π and L/D are set as one; whilst for solid TES, they are provided in Table. 5.5. After the diameter D_i is known, the length of a thermal reservoir is calculated by $L_i = D_i\,(L/D)$.

For the A-CAES and I-CAES systems, the switch between the charge and discharge mode is determined by the cavern pressure p. For example, if the cavern pressure p rises above the maximum pressure $p_{\max}$ during charge, then the discharge mode is started and the inlet and outlet mass flowrate are set as 0 and $\dot{m}$ respectively, whereas if the cavern pressure p falls below the minimum pressure $p_{\min}$ during discharge, then the charge mode is initiated and the inlet and outlet mass flowrate are set as $\dot{m}$ and 0 respectively. The rated mass flowrate $\dot{m}$ can be determined through the following equation.

$$\dot{m} = \frac{P}{\sum_{i=1}^{N}\left(h_{\text{out},i} - h_{\text{in},i}\right)} \tag{B.11}$$

where P is the rated power for all energy storage systems and in this thesis, $P = 100\,\text{MW}$. The charge and discharge modes are switched between each other for several times until the final equilibrium state is reached.

Other energy storage systems follow similar design process, with a major difference in Eq. (B.8). For LAES, the Eq. (B.8) should be replaced by:

$$B_{\text{liquid}} + \sum_{i=1}^{N_{\text{hot}}} B_i - \sum_{i=1}^{N_{\text{cold}}} B_i = E \tag{B.12}$$

whereas for PTES, the Eq. (B.8) should be replaced by:

$$\sum_{i=1}^{N_{\text{hot}}} B_i + \sum_{i=1}^{N_{\text{cold}}} B_i = E \tag{B.13}$$

The switch between charge and discharge mode is determined by the mass of liquid air for LAES and by the mass of thermal fluid for PTES.

For the I-CAES-HR, the Eq. (B.8) is still valid, but the mass of the thermal fluid (Eq.

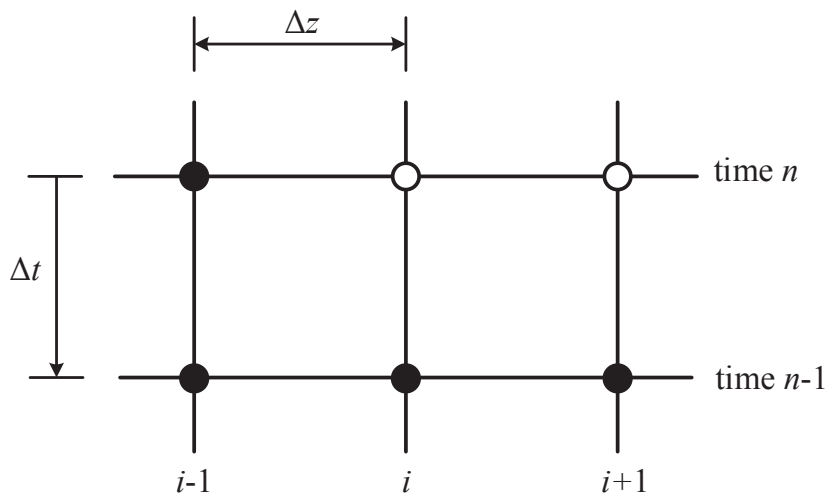

Figure B.1: A section of the computational grid of the thermal reservoir (properties are known at nodes marked • and unknown at those marked ○)

(B.1)) should be determined by:

$$m_i = \frac{m\bar{c}_p}{C_r \bar{c}_i} \tag{B.14}$$

where C_r is the heat capacity ratio of the isothermal compressor/expander, which is usually less than one.

B.2 Solid TES system

The numerical method used to solve Eqs. (4.7) and (4.8) is similar to that described in Refs. [41, 59] where a semi-analytical approach has been employed to improve the stability and computational efficiency. Fig. B.1 shows part of the regular computational grid at two time levels and the task is to calculate the gas and solid temperatures at node (i, n). Meanwhile, temperatures are known at all nodes for the time step $n-1$, and at nodes from 1 to $i-1$ for the time step n. Therefore, the gas temperature T_g at node (i, n) can be obtained by integrating Eq. (4.7) along the z axis, from node $(i-1, n)$ to node (i, n), whilst holding the solid temperature T_s constant at its average value of these two nodes, $\bar{T}_s = \left(T^n_{s,i-1} + T^n_{s,i}\right)/2$.

$$T^n_{g,i} = \bar{T}_s + \left(T^n_{g,i-1} - \bar{T}_s\right) \exp\left(-\Delta z/l\right) = (1-a)\,\bar{T}_s + a T^n_{g,i-1} \tag{B.15}$$

where $a = \exp\left(-\Delta z/l\right)$. Similarly, the solid temperature T_s at node (i, n) can be obtained by integrating Eq. (4.8) along the t axis, from node $(i, n-1)$ to node (i, n), whilst holding the

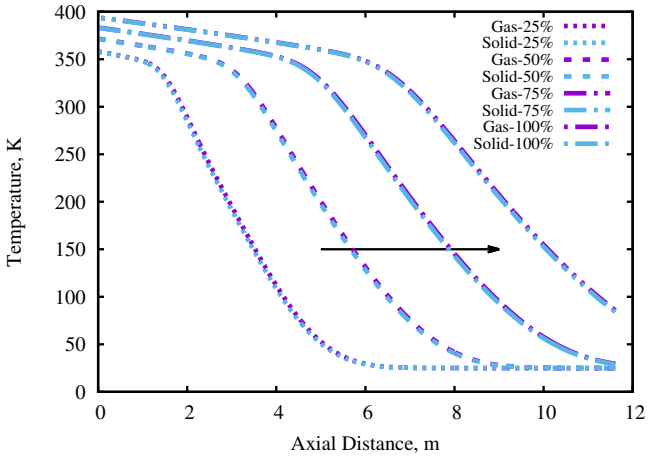

(a) Thermal fronts in the solid TES (Profiles are shown at 25 %, 50 %, 75 %, and 100 % through the charge period)

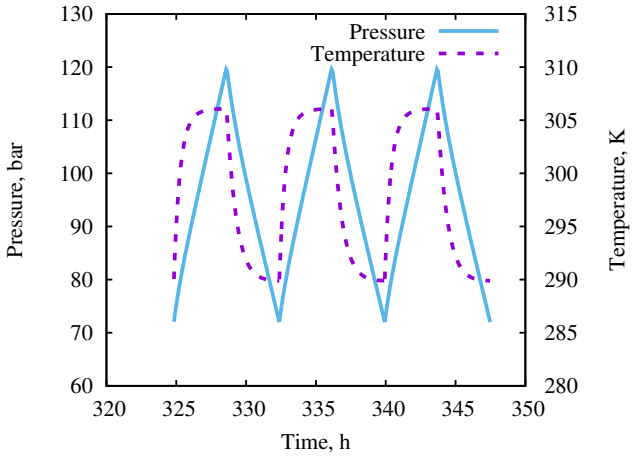

(b) Pressure and temperature variation in the cavern

Figure B.2: Pressure and temperature profiles in the solid TES and isochoric cavern of the nominal hybrid A-CAES in Chapter 5. (a) thermal fronts in the solid TES (b) pressure and temperature variation in the cavern

gas temperature T_g constant at its average value of these two nodes, $\bar{T}_g = \left(T_{g,i}^{n-1} + T_{g,i}^{n}\right)/2$.

$$T_{s,i}^{n} = \bar{T}_g + \left(T_{s,i}^{n-1} - \bar{T}_g\right)\exp\left(-\Delta t/\tau\right) = (1-b)\,\bar{T}_s + bT_{g,i-1}^{n} \tag{B.16}$$

where $b = \exp\left(-\Delta t/\tau\right)$. After substituting the expressions of average temperatures for gas and solid into Eq. (B.15) and Eq. (B.16) respectively, the resulting pair of equations can be expressed in the following form:

$$\begin{bmatrix} 1 & \frac{1}{2}(a-1) \\ \frac{1}{2}(b-1) & 1 \end{bmatrix} \begin{bmatrix} T_{g,i}^{n} \\ T_{s,i}^{n} \end{bmatrix} = \begin{bmatrix} \frac{1}{2}(1-a)\,T_{s,i-1}^{n} + aT_{g,i-1}^{n} \\ \frac{1}{2}(1-b)\,T_{g,i}^{n-1} + bT_{s,i}^{n-1} \end{bmatrix} \tag{B.17}$$

Eq. (B.17) is readily inverted to obtain the two unknown temperatures. The advantage of this method is that the "stiffness" is integrated out of the equations enabling much larger time steps to be taken than with a straightforward difference discretization [41]. This numerical scheme has been validated against the "single-blow" analytical solution first presented by Anzelius [139] for the case of constant gas and solid properties. Details of this validation are given in Ref. [41].

Fig. B.2a shows the thermal front propagation within the first-stage solid TES of the hybrid A-CAES (nominal case) in Chapter 5, which is obtained by calculating Eq. (B.17) for each node (i, n) during the whole charge process.

B.3 Cavern and liquid TES system

The governing equations of the cavern and liquid TES are very similar, and therefore, the same numerical methods are employed for both of them. Take the isochoric cavern as an example, the first-order forward differentiation method can be applied to Eqs. (5.3) and (5.4), and the following equations can be obtained:

$$m_i = m_{i-1} + (\dot{m}_{\text{in}} - \dot{m}_{\text{out}})\,\mathrm{d}t \tag{B.18}$$

$$T_i = T_{i-1} + \left[\dot{Q} + \dot{m}_{\text{in}} c_p T_{\text{in}} - \dot{m}_{\text{out}} c_p T_{i-1} - (\dot{m}_{\text{in}} - \dot{m}_{\text{out}})\, c_v T_{i-1}\right] \frac{\mathrm{d}t}{m_{i-1} c_v} \tag{B.19}$$

where $\dot{Q}$ is the instantaneous heat transfer rate which is given by:

$$\dot{Q} = UA\,(T_0 - T_{i-1}) = \lambda \dot{m} c_p\,(T_{i-1} - T_0) \tag{B.20}$$

Similar equations can be obtained for the Eqs. (4.12) and (4.13) of liquid TES by replacing the heat capacities c_p and c_v with c_{f}.

For an isochoric cavern, its volume is fixed at V, so the pressure within it at time step i can be obtained from the state equations for ideal gas:

$$p_i = m_i R_g T_i / V \tag{B.21}$$

whilst for an isobaric cavern or a liquid TES, its pressure is always fixed at p, so the its volume at time step i is:

$$V_i = m_i / \rho \tag{B.22}$$

where ρ is the density of the compressed air or thermal fluid, which tends to be a constant.

Fig. B.2b shows the temperature and pressure variation within the isochoric cavern of the hybrid A-CAES (nominal case); whilst Figs. B.3a and B.3b show the temperature and mass variation within the hot and cold liquid tanks of the second-stage liquid TES respectively.

B.4 Compressor and expander

Although the outlet temperature T_{out} and work input w_{c} of a compressor with ideal gas as the working fluid can be directly obtained from Eqs. (4.18) and (4.19), these values must be numerically computed step by step for the real gas. For example, if a compressor is adiabatic, then its outlet temperature T_{out} and work input w_{c} can be obtained from its enthalpy increase

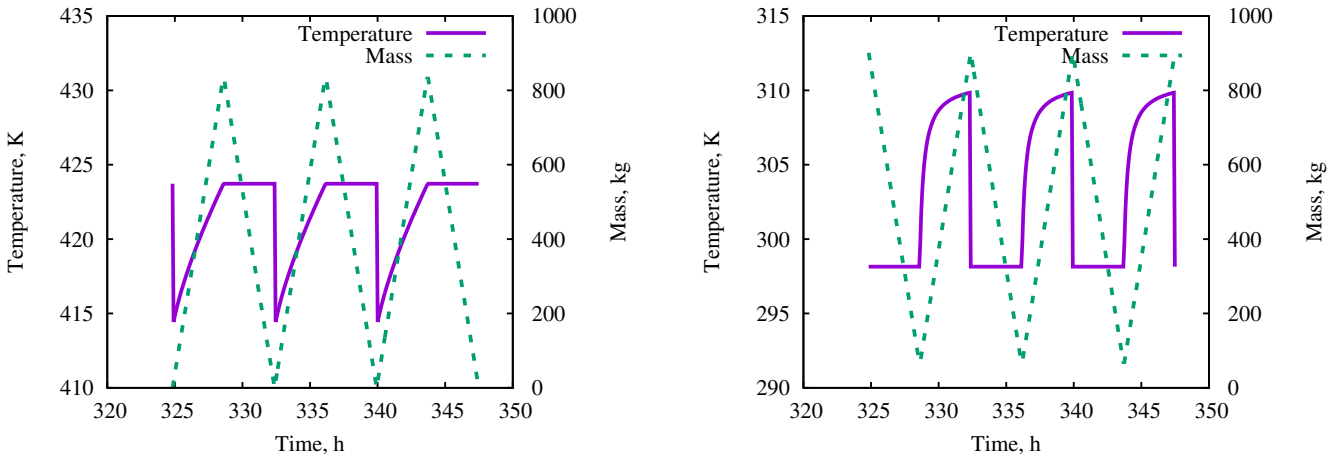

(a) Hot thermal fluid tank

(b) Cold thermal fluid tank

Figure B.3: Temperature and mass variation of the hot and cold thermal fluid tanks within the liquid TES of the nominal hybrid A-CAES in Chapter 5. (a) hot thermal fluid tanks (b) cold thermal fluid tanks

dh since $\mathrm{d}h = -\delta w = v\mathrm{d}p/\eta_\mathrm{c}$ for adiabatic devices. Therefore, by applying first-order forward to the above equation, we have:

$$p_i = p_{i-1} + \mathrm{d}p \tag{B.23}$$

$$h_i = h_{i-1} + v_{i-1}\mathrm{d}p/\eta_\mathrm{c} = h_{i-1} + \mathrm{d}p/\left(\rho_{i-1}\eta_\mathrm{c}\right) \tag{B.24}$$

where dp is the pressure increase for each step which is determined by the outlet pressure of the compressor p_out and the number of steps n, $\mathrm{d}p = \left(p_\mathrm{out} - p_\mathrm{in}\right)/n$; v_{i-1} and ρ_{i-1} are respectively the specific volume and density at step $i-1$, which are obtained through the pressure p_{i-1} and specific enthalpy h_{i-1} at step $i-1$ with the help of Refprop or CoolProp. For the simple forward differentiation, the specific volume v_i and density ρ_i is then calculated and this process continues until p_i reaches the outlet pressure p_out. However, it has been found that this simple forward differentiation method is relatively imprecise and requires more steps n to reach convergence, as shown in Fig. B.4. Therefore, the specific volume or the density in Eq. (B.24) is usually corrected to increase the accuracy and this is achieved by replacing the v_{i-1} or ρ_{i-1} in Eq. (B.24) with the average values $\bar{v}$ or $\bar{\rho}$:

$$\bar{v} = \frac{1}{2}\left(v_{i-1} + v_i^\mathrm{p}\right) \tag{B.25}$$

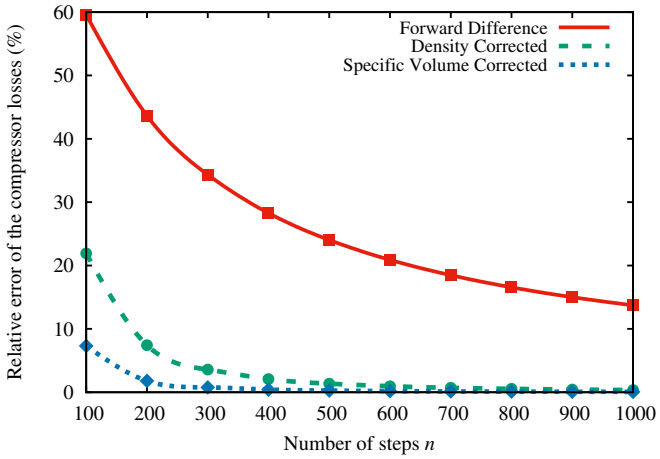

Figure B.4: Comparison of calculation errors of different numerical methods

$$\bar{\rho} = \frac{1}{2}\left(\rho_{i-1} + \rho_i^{\mathrm{p}}\right) \tag{B.26}$$

where the superscript p indicates that the v_i^{p} or ρ_i^{p} obtained from Eqs (B.23) and (B.24) are predicted values and should be updated accordingly after the actual h_i is obtained.

Fig. B.4 compares the converges speed of these numerical methods and it can be noted that the density corrected method (by replacing ρ_{i-1} with $\bar{\rho}$) has the fastest convergence speed. Therefore, it is used as the default numerical method for the compressors and expanders in this thesis.

B.5 Isothermal compressor and expander

In order to get the outlet temperatures and work input (or output) of the isothermal compressor (or expander), Eq. (6.9) must be solved numerically. As mentioned in Chapter 6, the matrix $\mathbf{A}$ should be diagonalized into $\mathbf{A} = \mathbf{S}^{-1}\Lambda\mathbf{S}$, so that $\mathbf{A}^{\mathbf{n}} = \mathbf{S}^{-1}\Lambda^{\mathbf{n}}\mathbf{S}$. If we define $\mathbf{A}$ as:

$$\mathbf{A} = \begin{bmatrix} (1-\varepsilon)\beta^{\frac{\phi}{n}} & \varepsilon \\ \varepsilon C_r \beta^{\frac{\phi}{n}} & 1-\varepsilon C_r \end{bmatrix} = \begin{bmatrix} a & b \\ c & d \end{bmatrix} \tag{B.27}$$

then its two eigenvalues $\lambda_{1,2}$ can be calculated by:

$$|\mathbf{A} - \lambda\mathbf{E}| = \begin{vmatrix} a-\lambda & b \\ c & d-\lambda \end{vmatrix} = 0 \tag{B.28}$$

and the results are:

$$\lambda_{1,2} = \frac{1}{2}(a+d \pm \Delta)$$

where

$$\Delta = \sqrt{(a-d)^2 + 4bc}$$

Therefore, the diagonal matrix Λ is:

$$\Lambda = \begin{bmatrix} \lambda_1 & 0 \\ 0 & \lambda_2 \end{bmatrix} \tag{B.29}$$

After we got the two eigenvalues $\lambda_{1,2}$, the eigenvectors can be calculated by:

$$[\mathbf{A} - \lambda_{1,2}\mathbf{E}] \sim \begin{bmatrix} \frac{1}{2}(a-d \mp \Delta) & b \\ 0 & 0 \end{bmatrix} \sim \begin{bmatrix} -\lambda_{3,4} & 1 \\ 0 & 0 \end{bmatrix} \tag{B.30}$$

where

$$\lambda_{3,4} = -\frac{1}{2b}(a-d \mp \Delta)$$

Therefore, the matrix $\mathbf{S}$ with eigenvectors as its columns can be written as:

$$\mathbf{S} = \begin{bmatrix} 1 & 1 \\ \lambda_3 & \lambda_4 \end{bmatrix} \tag{B.31}$$

and the inverse of matrix $\mathbf{S}$ is:

$$\mathbf{S^{-1}} = \frac{\mathbf{S}^*}{|\mathbf{S}|} = -\frac{b}{\Delta}\begin{bmatrix} \lambda_4 & -1 \\ -\lambda_3 & 1 \end{bmatrix} \tag{B.32}$$

Finally, the n-th power of matrix $\mathbf{A}$ can be expressed as:

$$\begin{aligned} \mathbf{A^n} &= \begin{bmatrix} 1 & 1 \\ \lambda_3 & \lambda_4 \end{bmatrix}\begin{bmatrix} \lambda_1^n & 0 \\ 0 & \lambda_2^n \end{bmatrix}\begin{bmatrix} \lambda_4 & -1 \\ -\lambda_3 & 1 \end{bmatrix}\frac{-b}{\Delta} \\ &= \begin{bmatrix} a_1 & b_1 \\ c_1 & d_1 \end{bmatrix} \end{aligned} \tag{B.33}$$

where

$$a_1 = -\frac{b}{\Delta}(\lambda_4\lambda_1^n - \lambda_3\lambda_2^n)$$

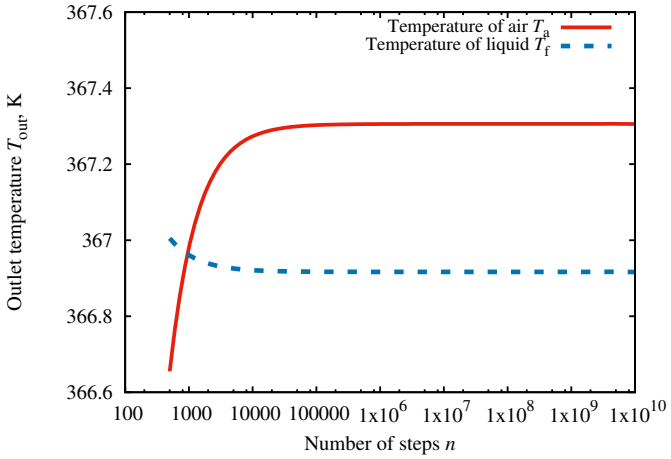

Figure B.5: Illustration of the converging process of the isothermal compressor

$$b_1 = -\frac{b}{\Delta}\left(\lambda_2^n - \lambda_1^n\right)$$

$$c_1 = -\frac{b}{\Delta}\lambda_3\lambda_4\left(\lambda_1^n - \lambda_2^n\right)$$

$$d_1 = -\frac{b}{\Delta}\left(\lambda_4\lambda_2^n - \lambda_3\lambda_1^n\right)$$

The outlet temperatures of the compressed air $T_{a,out}$ and thermal fluid $T_{f,out}$ can therefore be calculated by:

$$T_{a,out} = a_1 T_{a,in} + b_1 T_{f,in} \tag{B.34}$$

$$T_{f,out} = c_1 T_{a,in} + d_1 T_{f,in} \tag{B.35}$$

Fig. B.5 shows the converging process of an isothermal compressor, from which it can be noted that the numerical model has already converged after $n = 10^5$ steps. Therefore, $n = 10^{10}$ is able to guarantee convergence for any isothermal device in this thesis.